Interfaces in disordered media. Scaling growth, avalanche dynamics, and microfluidic fronts

Thesis

Universitat de Barcelona
Departament d'Estructura i Constituents de la Matèria
Programa de doctorat de Física Avançada
Bienni 2004/06

Interfaces in disordered media.

Scaling growth, avalanche dynamics, and microfluidic fronts

Memòria de la tesi presentada el juliol de 2009 per
Marc Pradas Gené
per optar al títol de Doctor en Física
dirigida per la Dra. Aurora Hernández Machado

La realització d'aquesta tesi ha estat possible gràcies a la concessió d'una beca pre-doctoral dins el *Subprograma de ayudas para la Formación de Personal Investigador* (FPI) del *Ministerio de Ciencia e Innovación*.

Contents

Agraïments

En primer lloc voldria agrair a la meva directora de tesi, l'Aurora Hernández Machado, la oportunitat que em va donar per poder realitzar aquesta tesi doctoral. Tots els seus consells i la seva paciència, juntament amb la seva forma sempre tant positiva de veure les coses, han estat sense cap mena de dubte una gran ajuda durant tots aquests anys.

Querría sinceramente dar las gracias a Juan M. López y Miguel A. Rodríguez por la enriquecedora estancia que tuve en el Instituto de Física de Santander las dos veces que estuve de visita. Ha sido todo un placer poder trabajar con ellos, de quien ciertamente he aprendido muchas cosas sobre los exponentes de escala.

A Eugenia Corvera le quiero agradecer la hospitalidad que me brindó durante mi visita en el D.F., así como la agradable colaboración que hemos tenido durante mi último año.

I would like to thank Tapio Ala Nissila for the kind hospitality I received during my stay at TKK in Helsinki, which I really enjoyed, and also for the pleasant collaboration that we had with Teemu Laurila.

Voldria agrair al Jordi Ortín tots els comentaris i discussions que he tingut amb ell, els quals han estat molt útils alhora de comparar els resultats teòrics amb els experimentals. Així mateix, agraeixo també l'Ana Lacasta de la UPC per deixar-me el seu codi del model de camp de fase.

No podré oblidar mai l'ajuda i paciència que sempre he rebut per part del company de despatx i amic Rodrigo Ledesma; tot el seu suport científic i personal han estat molt importants per mi durant tots aquests anys. També vull agrair al Ramon Planet, amic i company del món rugós, per totes les discussions interficials i per l'accés als experiments que sempre he tingut. Així mateix, he de mencionar al Fèlix Campelo, amic i company de grup, perquè

sempre ha estat a punt per resoldre qualsevol dubte. A tots ells els vull agrair tots els magnífics moments passats dins i fora de la facultat. També vull recordar al Jaume López amb qui he compartit tots els anys de carrera i doctorat, i sempre ha tingut un moment per resoldre qualsevol problema que he patit sobre temes de Linux o LaTeX.

Tampoc vull deixar de mencionar a tota aquella gent que he anat coneixent durant aquests anys amb qui he compartit hores de cafès, dinars, sopars,... i amb qui sens dubte he tingut moments molt divertits. El Toni Ramírez, el Guillem Anglada i el Pau Cervera, durant els primers anys; i més recentment, l'Isaac Llopis, el Xavifú, l'Albert Solernou, el Jordi Soriano, el Pau Bitlloch, la Laura Casanellas, el Xavi Moya, l'Enric Álvarez i la Marta Manzanares. En aquest sentit, també vull fer esment de la Mireia Torralba i el Xavi Illa, ara ja de postdoc, de l'Àngel Gómez, amb qui he compartit despatx i congressos, de la Maria Queralt, amb qui he treballat durant l'últim any, i del Pol Lloveras, per l'ajut en el Laboratori de Termodinàmica.

A nivell més personal vull agrair tot el suport que sempre he rebut per part de la meva família, els meus pares, la meva àvia, els meus germans i cunyats. Finalment, dono les gràcies a l'Anna per tota la seva paciència, comprensió i per haver estat sempre allà.

Barcelona, juliol de 2009

Part I Introduction

1
General introduction

The surface of the Moon is not smooth, uniform, and precisely spherical as a great of philosophers believe it to be, but is uneven, rough, and full of cavities and prominences.

Galileo Galilei

The long desired possibility to classify the *scaling growth* of a rough surface in terms of *universality classes* has become a considerably ambitious task, not to say impossible in some cases.

This is particularly true, for instance, in the problem of a fluid filling a disordered medium –where the expression *disordered medium* applies both to a macroscopic porous medium [2] and a *microfluidic* device [142]. The point is that all the physical forces that play a role at the advancing front, such as the random capillarity of the medium, the surface tension of the interface or the viscous pressure, induce the roughness of the front to show a rich variety of scaling regimes, with the unavoidable presence of crossover effects. In addition, the so-called anomalous scaling [123], which reflects that the global scales of a rough surface behave in a different fashion as the corresponding local scales, makes difficult to find different physical situations that are described by exactly the same set of scaling exponents, which would make them belong to the same universality class. On the other hand, the characteristic intermittent *avalanche-like* behavior displayed by the front gives rise to an even more complicated dynamics, described in terms of *spatio-temporal complex dynamics*, as it is observed in many other disordered systems [132].

This thesis deals with the scaling properties and avalanche dynamics of interfaces moving in disordered media. Our main motivation in this work has been to understand the underlying physics that governs these complex phenomena, and to relate our findings to the large amount of experimental work carried out in fluid systems, ranging from the macroscopic Hele-Shaw cell to a microchannel (see Fig. 1.1).

1.1 Scaling growth and avalanches in macroscopic imbibition fronts

Imbibition is a process of fluid transport in a disordered medium, in which a viscous fluid that wets preferentially the medium displaces a less viscous resident fluid (typically air). The understanding of the different physical mechanisms competing at different scales at the liquid/air interface has revealed as an important issue in imbibition during the past two decades. In particular, only in the last few years it has been possible to achieve a satisfactory description based on a non-local model that takes into account all the forces that play a relevant role [2].

The experimental study carried out by Soriano *et al.* [134] at the University of Barcelona opened a completely new way to face up to the problem of imbibition in disordered media. The statistical properties of an oil/air interface (Fig. 1.1 shows two different examples) were extensively studied in terms of the scaling exponents, obtaining important results for which a satisfactory theoretical elaboration was needed. These scaling exponents give information, for instance, about the global width of the interface fluctuations or the correlation growth along the interface, and allow to completely characterize its morphology or roughness.

On the other hand, it is observed that the response of the interface to a slow external driving is given by cooperative motion along an extended region reflected in bursts or avalanches. Cooperative phenomena in general models of surface growth received considerable attention during the past decade [52, 106]. However, a clear picture of the avalanches in the non-local model of imbibition was unknown. In addition, up to very recently, detailed experimental results on avalanche dynamics and statistics in imbibition were not actually available. The recent work by Planet *et al.* [113] has allowed to have a first access to an experimental description of the avalanche dynamics in imbibition fronts.

1.2 Microfluidic fronts

The miniaturization of fluid systems up to the order of the microns has emerged during the last decade as an important and new field, called microfluidics [142], where different branches of Science, like biology, chemistry or medicine have found a considerable amount of technological applications [139, 149]. An example of these applications are the so-called lab-on-a-chip devices [20], which aim to integrate many biological, chemical or optical devices interconnected by microchannels.

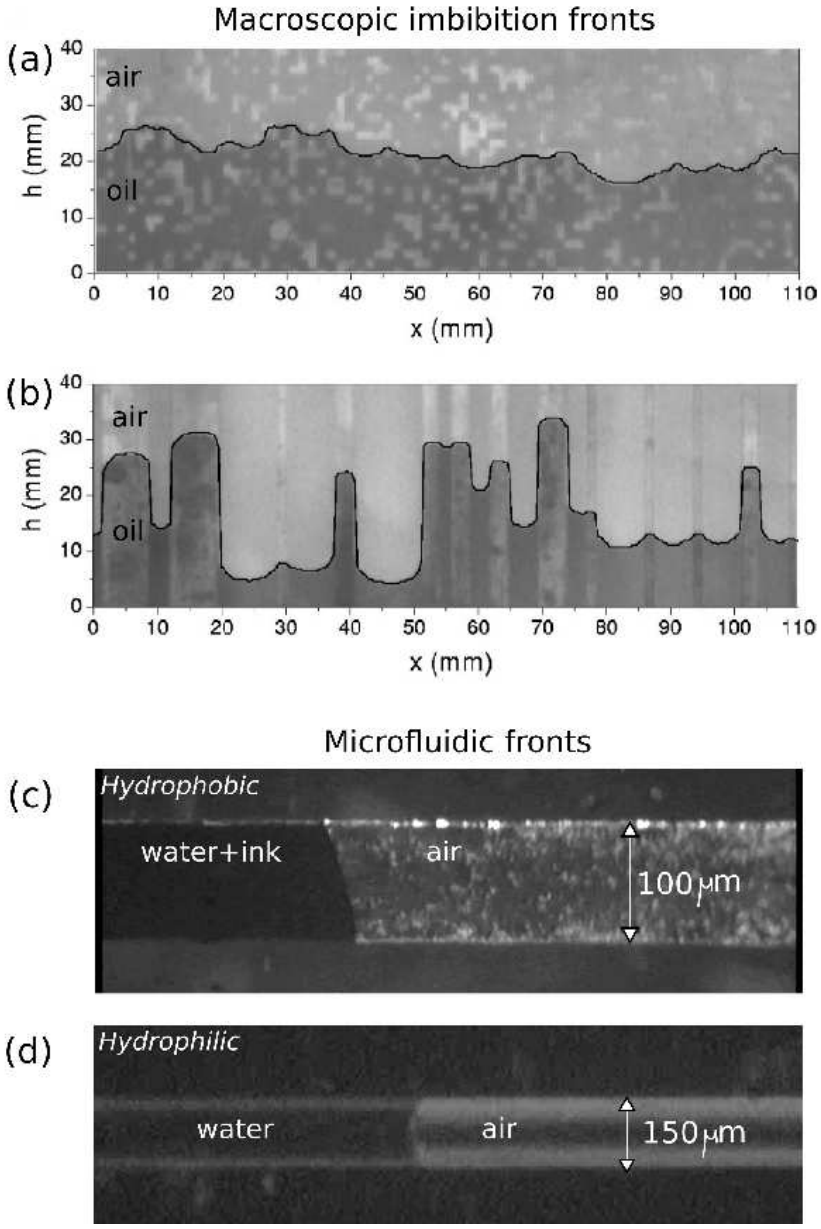

Fig. 1.1 Different examples of interfaces in disordered media studied in this thesis. (a) and (b) show imbibition fronts in a disordered Hele-Shaw cell with two different disorder configurations (Refs. [136, 138]). (c) and (d) show microfluidic fronts in a rectangular hydrophobic and cylindrical hydrophilic microchannel, respectively (courtesy by M. Queralt-Martín [120]).

It is therefore crucial to understand the physics governing the dynamics of fluids inside microfluidic devices, and in particular, there has been a great interest during the last years on how the roughness on the microchannel surfaces may affect either the wetting conditions or the filling process of the channel [34,35,66,75,77,131,140].

In this context, a series of experimental works in microchannels, carried out by Queralt-Martín *et al.* [120], has recently started in order to study the time evolution of a microfluidic front advancing in both hydrophobic and hydrophilic microchannels (see Fig. 1.1). The roughness of the surfaces of the channel, which would be irrelevant in larger systems, becomes crucial at these scales, and the concepts of pinning and avalanches are now applied in a microfluidic framework.

1.3 Thesis aims and structure

The aims of this thesis are to understand the morphology and dynamics of interfaces driven in disordered media by means of numerical and analytical work. The thesis mainly focuses in fluid systems, ranging from macroscopic to microscopic devices, and studies the physics underlying the process that brings the interface to show a spatio-temporal complex behavior. This includes the interfacial growth in terms of its scaling properties and avalanche dynamics. The structure of the thesis is then as follows.

This first Part of the thesis contains five Chapters, including this general introduction, that allows the reader to get the proper theoretical and experimental framework necessary to follow the results presented throughout the thesis. Chapter 2 introduces the basic concepts about capillarity and wetting phenomena, observed in systems where the surface tension effects are relevant. On the other hand, the formal mathematical description of such systems, called confined geometries, is given in Chapter 3, including the macroscopic Hele-Shaw cell and microfluidic devices. The imbibition problem is presented in Chapter 4 and the scaling theory used to describe general surface growth is given in Chapter 5.

Our original research is divided in the following three parts. Part II of the thesis is devoted to the scaling growth of interfaces described by both nonlocal and local models. Chapters 7, 8, and 9 theoretically study the morphology of imbibition fronts in different disorder configurations [as those shown in Fig. 1.1(a) and 1.1(b)], and are motivated by the experimental work by Soriano *et al.* [134]. We perform analytical studies of the interface scaling, and numerical work based on a diffuse interface model or phase field model, described in Ch. 4, which is found to be in very good agreement with the experimental results. A comparison between two different ways of using the numerical

phase field model is reported in Ch. 10. We study there how these models are affected by the disorder of the system. Finally, and motivated by imbibition phenomena, the last chapter of the second Part deals with the scaling properties in local models of surface growth with time-dependent crossover lengths.

Part III studies the avalanche dynamics of driven interfaces in disordered media. Chapter 13 introduces an avalanche theory valid in general models of surface growth, that allows to characterize the local dynamics and temporal correlations of avalanches defined through a spatio-temporal activity map. This theory is then applied in Chapter 14, in the case of forced-flow imbibition, where we find excellent agreement between analytical and numerical results. The last Chapter of the third Part deals with the characterization of avalanches by using a global magnitude that fluctuates in time. This allows to define the so-called global avalanches, obtaining excellent agreement with experimental results [113].

Finally, in Part IV, we focus on the subject of microfluidics, and in particular we study the dynamics of a liquid/air meniscus advancing through a disordered microchannel. We propose two different numerical methods in order to study the time evolution of a microfluidic front in a hydrophobic microchannel [see Fig. 1.1(c)]. Our results show that the pinning effects induced by the roughness of the hydrophobic surfaces affect the growth of the front, in agreement with experimental results [120].

Last, the thesis ends with a concluding part that contains the general conclusions of the thesis and future perspectives.

2
Capillarity and wetting phenomena

There are a lot of situations in nature where surface effects are very important. The spreading of a liquid over a solid is a clear example where surface tension plays an important role [1]. If a droplet of water is let on a solid substrate it is observed that the water spreads out getting a thin film or a perfect droplet depending on the material of the solid. This is an example of a fluid that shows wetting (*hydrophilic*) or nonwetting (*hydrophobic*) properties. Other examples are found in imbibition of liquids in porous media as a wetting process [2] or in the water repellency that some kind of leaves exhibit as a result of their high hydrophobicity, known as Lotus effect [7,78]. This chapter introduces some basic concepts to better understand such phenomena.

2.1
Contact angle and capillary pressure

In mechanical equilibrium, the wetting properties of a liquid over a solid substrate arises from a competition between the surface tensions of each interface. In Fig. 2.1 there are plot several examples of different wetting conditions. Typically, there is a solid phase in contact with two immiscible fluids (which usually are liquid and gas). Then, the wetting condition is determined by the equilibrium *contact angle* θ_e that appears at the contact line between the three phases, and is given by the Young-Dupré relation (see for instance Ref. [126]),

$$\cos\theta_e = \frac{\sigma_{sg} - \sigma_{sl}}{\sigma}, \tag{2.1}$$

where σ_{sg}, σ_{sl}, and σ are the surface tensions for the solid/gas, solid/liquid and liquid/gas interfaces respectively. The system is called hydrophilic for $\theta_e < 90^o$ and hydrophobic for $\theta_e > 90^o$.

Alternatively, an importance consequence of having an interface with a nonzero surface tension is that there exists a pressure difference Δp across

1) For general references on wetting phenomena see [38, 40] and also the recent review by Bonn *et al.* [12].

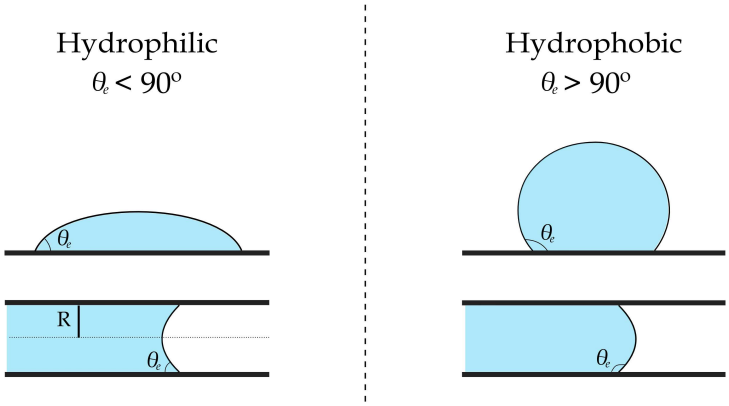

Fig. 2.1 Different examples of wetting (hydrophilic) and non-wetting (hydrophobic) situations. A droplet lying on a substrate (top) and a liquid meniscus inside a channel (bottom).

the interface. Consider a droplet of water with a spherical shape of radius R surrounded by air. If the water/air interface is increased by a radius variation δR, then the total energy of the system, which is given by the Gibbs free energy $\mathcal{F}$, changes as

$$\delta\mathcal{F} = -p_w \delta V_w - p_a \delta V_a + \sigma \delta A, \tag{2.2}$$

where p_w and p_a are the pressure at the water and air phases respectively, σ is the surface tension, $\delta V_w = 4\pi R^2 \delta R = -\delta V_a$ is the increased volume of the droplet, and $\delta A = 4\pi R \delta R$ is the increased area of the interface. In equilibrium, the condition $\delta\mathcal{F} = 0$ must hold, giving rise to the relation

$$p_w - p_a = \frac{2\sigma}{R}. \tag{2.3}$$

This relation indicates that there is a pressure difference across the interface related to the surface tension and the radius of the sphere and therefore, the pressure inside the droplet is higher than outside. For a general surface rested in equilibrium, Eq. (2.3) takes the form

$$\Delta p_c = \kappa\sigma, \tag{2.4}$$

that is, the pressure difference across the interface is given by the product of its surface tension and its curvature κ [2]. The sign convention used here is that convex surfaces have positive curvatures. Equation (2.4) is the so-called

2) The curvature of a general surface is given by the two principal radii of curvature $\kappa = 1/r_1 + 1/r_2$. For a spherical shape of radius R, the two principal radii are equal $r_1 = r_2 = R$, and then $\kappa = 2/R$, recovering Eq. (2.3)

Young-Laplace relation, and Δp_c is usually referred to as the capillary pressure.

2.2 Capillary length

It is of great importance to have a clear idea about the typical scales where capillary effects become relevant as compared to gravity effects. For instance in the channel depicted in Fig. 2.1, a particular length scale naturally arises when comparing capillary pressure $\sim \sigma/R$ [cf. Eq. (2.4)] to the hydrostatic pressure $\sim \rho g R$ at a depth R. In general terms, this length is denoted as κ^{-1} and is the so-called *capillary length*

$$\kappa^{-1} = \sqrt{\frac{\sigma}{\rho g}}, \tag{2.5}$$

where ρ is the density of the fluid and g the gravity field. It is shown then that capillary effects are relevant only for sizes $R < \kappa^{-1}$. Note that this length is usually of the order of a few mm. In the case of water for example, with $\rho \simeq 10^3$ Kg/m^3 and $\sigma \simeq 72 \cdot 10^{-3}$ N/m, the capillary length is about 2 mm. For systems with larger typical scales, gravity effects are more prominent and surface tension does not play any role. In the following section, an illustrative example where capillary effects become relevant is discussed.

2.3 Capillary rise in a tube

A particularly simple example of a liquid spreading over a solid is that of the capillary rise of a liquid into a small tube (capillary tube). This is actually a very common example of imbibition and has the grateful advantage that can be easily worked out. A capillary tube is actually the simplest porous medium that can be found, consisting only of one pore, and it is interesting because ideally reproduces the mean advancement of a liquid into a general porous medium. The example of capillary tube belongs to the group of confined geometries, whose mathematical treatment will be discussed in detail in next chapter. Notwithstanding, this section describes a simple derivation of the equilibrium height and time evolution of the one dimensional liquid/air meniscus position.

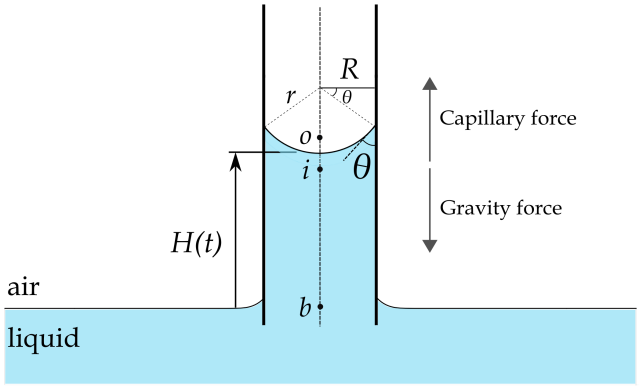

Fig. 2.2 Schematic representation of the capillary rise in a small tube. Since the contact angle $\theta < 90^\circ$ (hydrophilic condition), the induced curvature of the liquid meniscus is given by $\kappa = 2/r = 2\cos\theta/R$.

2.3.1 Equilibrium height

The simplest situation that can be imagined is when a cylindrical tube of radius R is vertically introduced into a liquid reservoir of density ρ and dynamic viscosity η. If the tube has a small enough radius ($R < \kappa^{-1}$), it is observed that the liquid raises into the tube up to an equilibrium height H_{eq}. Figure 2.2 shows a scheme of a liquid raising through a small tube. It shall be assumed here that the contact angle θ does not change during the liquid rising, and it is close to the equilibrium value $\theta \simeq \theta_e$. Then, due to the the hydrophilic wetting conditions ($\theta_e < 90^\circ$), the curvature induced at the liquid/air interface is $\kappa = 2\cos\theta_e/R > 0$, which, in turn, generates a pressure difference [capillary pressure, Eq. (2.4)] across the interface (points i and o in Fig. 2.2)

$$\Delta p_c \equiv p_o - p_i = \frac{2\sigma\cos\theta_e}{R}. \tag{2.6}$$

Therefore, the pressure p_o at the air phase is higher as compared to the pressure at the liquid phase $p_i = p_o - \Delta p_c$. Assuming that the pressure at the bottom of the tube (point b in Fig. 2.2) and at the air phase equal the atmospheric pressure, $p_b = p_o = p_{atm}$, the pressure difference along the liquid, $p_b - p_i = \Delta p_c$, makes the liquid to move into the tube. In equilibrium, such a pressure difference has to be balanced by the hydrostatic pressure of the column height $\Delta p_g = \rho g H_{eq}$, with

$$H_{eq} = \frac{2\sigma\cos\theta_e}{\rho g R}. \tag{2.7}$$

Note that the smaller radius the tube has the higher height the liquid reaches.

2.3.2 Time evolution of the liquid height

The dynamics of the liquid advancing through the capillary tube can be studied by considering the different forces that play a role on the liquid movement [40]. First, capillary pressure, Eq. (2.6), induces a capillary force

$$f_c = \pi R^2 \Delta p_c, \tag{2.8}$$

that causes the liquid to move inside the tube [3]. On the other hand, the weight of the liquid column $f_g = \rho g \pi R^2 H(t)$ and the friction viscous force f_η oppose to the movement. Then, the corresponding balance equation can be written as:

$$\frac{\mathrm{d}(MV)}{\mathrm{d}t} = f_c - f_\eta - f_g, \tag{2.9}$$

where the liquid mass depends on time as $M(t) = \pi R^2 \rho H(t)$, and $V(t) = \dot{H}(t)$ is the velocity of the interface. By making use of the Poiseuille's law [80], which states that the flow rate $Q = \pi R^2 V(t)$ in a tube is given by [4]

$$Q = \frac{\pi \Delta p}{8\eta H(t)} R^4, \tag{2.10}$$

we can therefore write the viscous force as

$$f_\eta = \pi R^2 \Delta p_\eta = 8\pi\eta H(t) V(t). \tag{2.11}$$

Then, by introducing each force expression in Eq. (2.9), we arrive at a general differential equation describing the temporal evolution of the capillary rise in a small tube

$$\frac{\mathrm{d}[H(t)V(t)]}{\mathrm{d}t} = \frac{2\sigma\cos\theta_e}{\rho R} - gH(t) - \frac{8\eta}{\rho R^2} H(t)V(t). \tag{2.12}$$

In the following, the above equation will be solved in two different scenarios.

Horizontal capillary tube. Wahsburn's law

In the case of having no gravity, the second term in the RHS of Eq. (2.12) vanishes and the solution reads as

$$H(t)V(t) = \frac{R\sigma\cos\theta_e}{4\eta}\left(1 - e^{\frac{t}{\tau_i}}\right). \tag{2.13}$$

3) Note that for hydrophobic walls ($\theta_e > 90^o$) the liquid would be ejected from the tube instead of being sucked.

4) Eq. (2.10) is actually being derived in next Chapter, for channel flows.

This equation shows that there exists a time scale $\tau_i = \frac{\rho R^2}{8\eta}$ that separates two different regimes:

- *Inertial regime*, $t \ll \tau_i$. Expanding the exponential term of Eq. (2.13) up to first order we observe that the interface position is given by

$$H(t) = \Big(\frac{2\sigma\cos\theta_e}{\rho R}\Big)^{1/2} t. \tag{2.14}$$

  During the initial times, the liquid grows linearly on time with an initial velocity $V_0 \sim \big(2\sigma\cos\theta_e/\rho R\big)^{1/2}$. Note that this regime is actually quite short in most of the capillary systems. For the capillary rise of water ($\eta \simeq 9\cdot 10^{-4}$ Pa $\cdot$ s, $\rho \simeq 10^3$ Kg/m^3) in a tube of $R \simeq 1$ mm, we have that $\tau_i \simeq 1$ s. Basically, this regime describes the moment when the liquid gets into the tube and therefore in the limit of $H(t) \to 0$. In this limit, the viscous term can be neglected and the dynamics is controlled by the inertia of the fluid.

- *Viscous regime*, $t \gg \tau_i$. At larger times, the inertia of the liquid is overcome by the viscous force and then the interface time evolution follows

$$H(t) = \sqrt{H_0^2 + \frac{R\sigma\cos\theta_e}{2\eta}t}, \tag{2.15}$$

  where the initial height H_0 can be approached as the height of the liquid at $t \sim \tau_i$. Eq. (2.15) is the so-called *Washburn's law* [148], and it is also found to be valid for the mean advancement of a liquid in porous media. For long enough times, it is reduced to $H(t) \sim t^{1/2}$, and then the velocity goes as $V(t) \sim t^{-1/2}$, indicating that the fluid has a slowing-down dynamics [44].

Note that the time scale $\tau_i \sim R^2/\rho\eta$ is a limitation of the Washburn's law at the initial times. However, in most of the capillary systems, the inertial regime is difficult to see experimentally, and only the Washburn's regime is usually observed. That is why in practice, the inertial effects can be neglected in solving Eq. (2.12) by simply assuming an initial height $H_0 > 0$.

Vertical capillary tube

For a vertically oriented tube, the gravity term of Eq. (2.12) has to be taken into account. As it has been shown in the last paragraph, the inertial effects are quickly overcome by viscous friction, and are only relevant during the initial times. Therefore, we shall neglect the inertial term when solving Eq. (2.12), and consider that the liquid started to grow from an initial height $H(t=0) =$

H_0. The dynamic equation reduces then to

$$\frac{\mathrm{d}H(t)}{\mathrm{d}t} = \frac{R\sigma\cos\theta_e}{4\eta H(t)}\Big[1 - \frac{H(t)}{H_{eq}}\Big], \tag{2.16}$$

where H_{eq} is the equilibrium height, Eq. (2.7). The solution of Eq. (2.16) is given by the transcendental equation

$$\frac{H(t) - H_0}{H_{eq}} + \ln\left[1 - \frac{H(t)}{H_{eq}}\right] - \ln\left[1 - \frac{H_0}{H_{eq}}\right] = -\frac{t}{\tau_g}. \tag{2.17}$$

It is straightforward to see that there also exists two different regimes separated by the time scale $\tau_g = \frac{8\eta H_{eq}}{\rho g R^2}$:

- *Washburn's regime*, $H(t) \ll H_{eq}$. During the initial times, when the meniscus height is still far from reaching the equilibrium height, the logarithmic terms in Eq. (2.17) can be expanded up to second order, recovering then Washburn's law, Eq. (2.15).

- *Exponential regime*, $H(t) \to H_{eq}$. When the liquid height is reaching the equilibrium height, the main contribution in the LHS of Eq. (2.17) comes from the logarithmic term $\ln[1 - H(t)/H_{eq}]$, obtaining the asymptotic behavior

  $$H(t) = H_{eq}\Big(1 - \mathrm{e}^{-\frac{t}{\tau_g}}\Big), \tag{2.18}$$

  with a characteristic time scale τ_g.

We therefore conclude that in the presence of gravity, the liquid initially grows following Washburn's law up to a typical time scale τ_g from then on, the equilibrium height is asymptotically reached.

Finally, it is important to remark that the behavior of a liquid rising through a vertical tube given by Eq. (2.17) ideally describes the behavior observed for the averaged liquid height in a general porous medium, such as for example, in a sheet of paper.

3
Fluid flow in confined geometries

This chapter introduces the mathematical description of the fluid motion in confined geometries. Here, a confined geometry shall be referred to as a three dimensional system that at least has one characteristic length scale of the order or smaller than the capillary length κ^{-1}, and therefore, capillary forces are expected to be prominent. Typical examples are closed channels of any shape, infinite-long parallel-plate channels or in general, any device used in microfluidics technology. Note that these kind of geometries have at least one submilimiter characteristic scale and therefore, typical fluid velocities inside the system are bound to keep slow. As it will be shown, these features allow to treat the fluid flow as a laminar flow and then easier to be analytically studied, something always desirable.

3.1
Governing equations

The most general description of the mechanical motion of an incompressible viscous fluid is given by the Navier-Stokes equation [80]

$$\rho\left[\frac{\partial \boldsymbol{u}}{\partial t} + (\boldsymbol{u}\cdot\boldsymbol{\nabla})\boldsymbol{u}\right] = -\boldsymbol{\nabla} p + \eta\nabla^2\boldsymbol{u}, \tag{3.1}$$

where $\boldsymbol{u} = (u_x, u_y, u_z)$ is the three-dimensional velocity field, ρ the density, η the dynamic viscosity, and p the pressure inside the fluid. The above equation together with the incompressibility condition $\boldsymbol{\nabla}\cdot\boldsymbol{u} = 0$ are the complete set of equations describing general viscous fluid flows. It is important to note that Eq. (3.1) is highly nonlinear and really complex to treat analytically. However, an important feature of Navier-Stokes equation appears when it is expressed in dimensionless units [80]. This means that we express all the physical variables in units of the characteristic scales. If the system has only one characteristic length scale b and velocity scale U, Eq. (3.1) can be rewritten as

$$Re\left[\partial'_t\boldsymbol{u'} + (\boldsymbol{u'}\cdot\boldsymbol{\nabla'})\boldsymbol{u'}\right] = -\boldsymbol{\nabla'}p' + \nabla'^2\boldsymbol{u'}, \tag{3.2}$$

where primes represent variables in dimensionless units. Here, $Re = \rho U b/\eta$ is the dimensionless *Reynolds number*, that separates a turbulent regime ($Re \gg 1$, nonlinear effects dominant) from a laminar regime ($Re \ll 1$, viscous effects dominant). In systems with a low characteristic velocity and small length scale, the low Reynolds number approximation reduces Eq. (3.2) to the linear Stokes equation

$$0 = -\boldsymbol{\nabla} p + \eta \nabla^2 \boldsymbol{u}, \tag{3.3}$$

expressed in the usual physical variables. The above equation can even be reduced to a simpler expression depending on the geometry of the system, as for example in a Hele-Shaw cell.

3.2 The Hele-Shaw cell

A Hele-Shaw cell [61] consists on two rectangular glass plates of dimensions $L_x \times L_y$ separated by a distance b which is much smaller than the other dimensions $b \ll L_x,\ L_y$. This is a very important setup that has been used to study several different problems such as interfacial instabilities [4,9,128,144], drainage from a porous medium [97], or imbibition phenomena [56,60,127,136,138]. The latter example corresponds actually to the physical phenomenon which this thesis is mainly based on, and the detailed experimental setup of a Hele-Shaw cell modeling imbibition in porous medium is discussed in next Chapter. For now, it only will be considered the flow of a viscous fluid in a *clean* Hele-Shaw cell, that is, without any kind of disorder between both plates. A schematic representation of a Hele-Shaw cell is depicted in Fig. 3.1. Note that the flow through the cell is characterized by two different length scales, b and L, instead of only one as we assumed in the previous section [1]. The procedure to get the dimensionless Navier-Stokes equation described above becomes then more involved [20], and has to be described in terms of the so-called aspect ratio $\varepsilon \equiv b/L$. In particular, an effective Reynolds number

$$\overline{Re} = \varepsilon Re = \frac{b}{L}\frac{\rho b U}{\eta}, \tag{3.4}$$

has to be replaced by the usual one in Eq. (3.2). In the limit of $\varepsilon \to 0$, the linear and inertial terms are neglected, and the main components contributing to the fluid flow are those lying on the plane parallel to the plates of the Hele-Shaw

1) It is assumed here that, although L_x and L_y are different in number, they can be considered to be of the same order of magnitude, and represented by a general characteristic scale L.

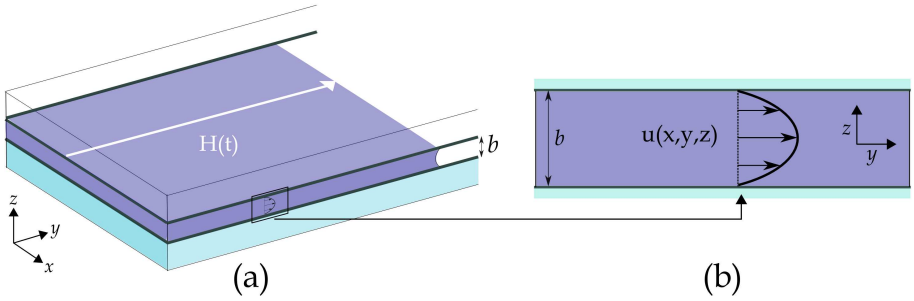

Fig. 3.1 (a) Schematic representation of a non-disordered Hele-Shaw cell in the stable case of a viscous fluid pushing air. The position of the interface separating both phases is denoted as $H(t)$. (b) Fluid flow in the liquid bulk of the cell is given by a Poiseuille profile.

cell, $\boldsymbol{u}_{\parallel} = (u_x, u_y)$ with $u_z \sim \mathcal{O}(\varepsilon^2)$. Therefore, the corresponding Stokes equation for the Hele-Shaw cell reads as

$$0 = -\boldsymbol{\nabla} p(x,y) + \eta \partial_z^2 \boldsymbol{u}_{\parallel}(x,y,z). \tag{3.5}$$

Note that the three-dimensional Laplacian term of equation (3.3) is expressed in dimensionless units as

$$\nabla'^2 \boldsymbol{u}'_{\parallel} = [\varepsilon^2(\partial_x'^2 + \partial_y'^2) + \partial_z'^2]\boldsymbol{u}'_{\parallel}, \tag{3.6}$$

and therefore only its z-component remains in the limit of $\varepsilon \to 0$. The procedure to derive Eq. 3.5 is actually known as the *lubrication approximation* and it is generally valid for confined geometries where flows have the transversal dimension much smaller than the others, something also very common for instance in thin film dynamics [69, 87, 103]. By integrating Eq. (3.5) along z-direction and using the *non-slip boundary condition* at the solid plates position, $\boldsymbol{u}_{\parallel}(x, y = \pm b/2) = 0$, the solution for the velocity profile is given by a Poiseuille flow (see Fig. 3.1)

$$\boldsymbol{u}_{\parallel}(x,y,z) = \frac{1}{2\eta}\left(z^2 - \frac{b^2}{4}\right)\boldsymbol{\nabla} p(x,y). \tag{3.7}$$

Since the flow along the component normal to the plane (x, y) is considered to be zero, the above equation can be averaged along the z direction. The resulting equation for the two-dimensional velocity field reads as

$$\boldsymbol{v}(x,y) \equiv \frac{1}{b}\int_{-b/2}^{b/2} \boldsymbol{u}_{\parallel}(x,y,z)\mathrm{d}z = -\frac{b^2}{12\eta}\boldsymbol{\nabla} p(x,y), \tag{3.8}$$

and corresponds to the so-called Darcy's law, which is a general law of fluid flow in porous media (see next Chapter). The ratio $b^2/12$ is the permeability K of the Hele-Shaw cell. Assuming that the fluid is incompressible, the continuity equation for the three-dimensional velocity field, $\boldsymbol{\nabla} \cdot \boldsymbol{u} = 0$, can be expressed as $\boldsymbol{\nabla} \cdot \boldsymbol{v} = 0$ for the averaged two-dimensional velocity. Therefore, Eq. (3.8) is also written as a Laplace equation for the pressure

$$\nabla^2 p(x, y) = 0. \tag{3.9}$$

In the case, for example, of having a liquid pushing air in a non-disordered Hele-Shaw cell, the interface separating both phases is stable and flat [2]. Then, the system is invariant along the x direction, and the flow is unidirectional, given by the y component of the velocity. We denote the interface position as $H(t)$, and by using Eqs. (3.8) and (3.9), one can easily find that the velocity at the interface position, $v_y(y = H) = \dot{H}(t)$, is given by

$$\dot{H}(t) = -\frac{b^2}{12\eta} \frac{\Delta p}{H(t)}, \tag{3.10}$$

where $\Delta p = p(H) - p(0)$ is the difference between the pressure at the interface position, $y = H(t)$, and at the origin of the cell, $y = 0$. As in the case of the capillary tube described in the preceding Chapter, the pressure at the interface will be given by the Young-Laplace equation [cf. Eq. (2.4)],

$$p(H) = p_{\text{air}} - \frac{2\sigma \cos\theta}{b}, \tag{3.11}$$

related to the curvature of the liquid/air meniscus along the z-direction [3]. p_{air} is the pressure at the air phase. If the pressure at the origin of the cell is kept constant, $p(0) = p_{\text{a}}$, the Washburn behavior, $H(t) \sim t^{1/2}$, is recovered when Eq. (3.10) is integrated.

3.3 Microfluidic devices

We discuss in this Section the fluid flow in microfluidic devices, and in particular we shall focus in microchannels. As before, the starting point is the Stokes equation (3.3) valid in the low Reynolds number approximation.

2) Note that this is not true in the opposed case of having air pushing liquid, where the interface becomes instable [128].

3) In a Hele-Shaw cell of gap spacing b, one of the two principal radii of curvature is infinite, and then the curvature is $\kappa = 2\cos\theta/b$, with θ the contact angle (see Ch. 2).

Consider the unidirectional flow in a rectangular microchannel with arbitrary aspect ratio of the cross-section, given by a width w and a height b. As occurred in the preceding Section, the z component of the velocity field $\boldsymbol{u}$ is assumed to be zero, and the only contribution to the flow is on the y-direction. Then, the corresponding Stokes equation for a rectangular channel is written as

$$\left[\partial_x^2 + \partial_z^2\right] u_y(x,z) = \frac{\Delta p}{\eta H(t)}, \tag{3.12}$$

with the non-slip boundary conditions at the channel surfaces [4]

$$u_y(\pm w/2, z) = 0 \qquad \text{and} \qquad u_y(x, \pm b/2) = 0. \tag{3.13}$$

We are assuming that the width is larger than the height, $w > b$. As in the preceding Section, the front position is given by $H(t)$, and $\Delta p = p(H) - p(0)$. The solution of the Eq. (3.12) is usually expressed in terms of a Fourier expansion (see for instance Ref. [20]), and reads as

$$u_y(x,z) = -\frac{\Delta p}{H(t)} \frac{4}{\eta w} \sum_{n=1}^{\infty} \frac{(-1)^{n+1}}{\beta_n^3} \left[1 - \frac{\cosh(\beta_n z)}{\cosh(\beta_n \frac{b}{2})}\right] \cos(\beta_n y), \tag{3.14}$$

where $\beta_n = (2n-1)\frac{\pi}{w}$. Then, the velocity of the front averaged over the cross-section of the channel

$$\dot{H}(t) = \frac{1}{wb} \int_{-b/2}^{b/2} \int_{-w/2}^{w/2} u_y(x,z) \mathrm{d}x\mathrm{d}z, \tag{3.15}$$

is given by the following relation:

$$\dot{H}(t) = -\frac{\Delta p}{H(t)} \frac{8}{\eta w^2} \sum_{n=1}^{\infty} \frac{1}{\beta_n^4} \left[1 - \frac{2}{\beta_n b} \tanh\left(\beta_n \frac{b}{2}\right)\right]. \tag{3.16}$$

The interesting point is that in the case of $w > b$, the above expression can be approximated as [20]

$$\dot{H}(t) = -\frac{b^2}{12\eta} \frac{\Delta p}{H(t)} \left[1 - 0.630 \frac{b}{w}\right], \tag{3.17}$$

which is basically the same relation for the Hele-Shaw cell, Eq. (3.10), multiplied by a geometric coefficient that depends on the cross-section aspect ratio

4) This is actually an important point in microfluidics, where the so-called *slip boundary condition* has been largely discussed (see for instance [39, 82, 146, 147]). In this derivation, however, we are not considering possible slip effects at the walls.

b/w, in such a way that in the limit of $b \ll w$ the Hele-Shaw behavior is recovered.

4
Imbibition in disordered media

Imbibition is a process of fluid transport in a porous medium, in which a viscous fluid that wets preferentially the medium displaces a less viscous resident fluid (typically air) [2]. It is really a very common phenomenon of daily life, observed for example when a sugar cube or a sheet of paper is introduced into a cup of coffee, or when an oil drop spreads without hesitating over a newly purchased sweater. Only with these simple examples an important feature of imbibition arises. The interface separating the liquid from the air is observed to be stable and become rough as the liquid gets into the porous medium. In particular, as a consequence of a competition of the different forces that play a role on the interface dynamics, such as random capillarity, surface tension or viscous pressure, the stable interface undergoes a kinetic roughening process with spatio-temporal correlations. To study the statistical and dynamical properties of the interface fluctuations belongs to an important problem of the nonequilibrium statistical physics and it is in which this thesis is mainly based on.

From a technological and industrial point of view, imbibition phenomena are also very common. Examples are found in different scenarios ranging from petroleum recovery and irrigation to retention of waste waters [2, 129], including applications in food industry or biological sciences (see Ref. [2] and references therein). In all the examples of imbibition processes, it is generally accepted that fluid flow over the porous medium is given by Darcy's law

$$\langle \boldsymbol{Q} \rangle = -\frac{K}{\eta}\Big(\boldsymbol{\nabla} p - \rho \boldsymbol{g}\Big), \tag{4.1}$$

which was discovered empirically by Darcy in 1854 [37]. Here, $\langle \boldsymbol{Q} \rangle$ is the average volume of fluid transported per unit time and per unit cross-section of the porous medium, K is the permeability of the medium, η the dynamic viscosity, ρ the density, p the pressure field of the viscous fluid, and $\boldsymbol{g}$ the gravity field. Eq. (4.1) is a general law for fluid flow in porous media, which in the absence of gravity is analogous, for instance, to the Ohm's law in the field of electrical networks, and results from an averaging procedure that ignores

the details on length scales smaller than the pores [1]. Recall from the preceding Chapter that Darcy's law in a Hele-Shaw cell came out when averaging along the transversal direction of the flow, obtaining there the permeability $K = b^2/12$.

It is important to remark that imbibition can be experimentally carried out in two different ways: a) *forced-flow imbibition* occurs when the invading fluid gets into the porous medium at a constant injection rate, and therefore at constant mean velocity, and b) *spontaneous imbibition* when the fluid is driven solely by capillary forces and the mean height of the interface $H(t)$ grows in time following the Washburn's law, $H(t) \sim t^{1/2}$.

This chapter describes the imbibition phenomenon both from an experimental and theoretical point of view.

4.1 Experimental setup

The most used experimental setup to reproduce imbibition phenomena has been the Hele-Shaw cell [61]. One of the first studies was carried out by Rubio *et al.* in a work appeared at the late eighty's [127]. The porous medium was modeled there by introducing glass beads of average diameter a randomly distributed between the two plates of the Hele-Shaw cell. Imposing then a constant flow velocity (forced-flow imbibition) the dynamics and the statistical properties of a growing water/air interface were studied.

Most recently, in the experimental work carried out by Soriano *et al.* [134], the porosity of the cell was modeled by attaching a fiberglass substrate with copper squares at the bottom cell. This new method allowed to have an excellent control of the disorder imposed into the cell, and different configurations such as for example columnar disorder were able to be studied. Figure 4.1 shows a detailed scheme of the Hele-Shaw cell with different disorder configurations. The dimensions of the copper squares can be either $1.50 \times 1.50 \times 0.06$ mm^3 or $0.4 \times 0.4 \times 0.06$ mm^3, and are randomly distributed overall space (x, y). In the case of columnar disorder, the fiberglass substrate contains a pattern of parallel copper tracks continuous in the y direction and randomly distributed along x. Each track has lateral size of 1.50 mm and is $d = 0.06$ mm high. The fraction of lattice sites occupied by copper is 35% in all the cases. The gap variation of the cell is then characterized by a dichotomic disorder that takes the values b or $b - d$. The viscous liquid (oil) gets into the cell from one of its short sizes and the displaced air leaves the cell at the other side. By using the Hele-Shaw cell, two different setups can be carried out depending on which kind of imbibition is desired to study.

1) For a general derivation of Eq. (4.1) see Ref. [129]

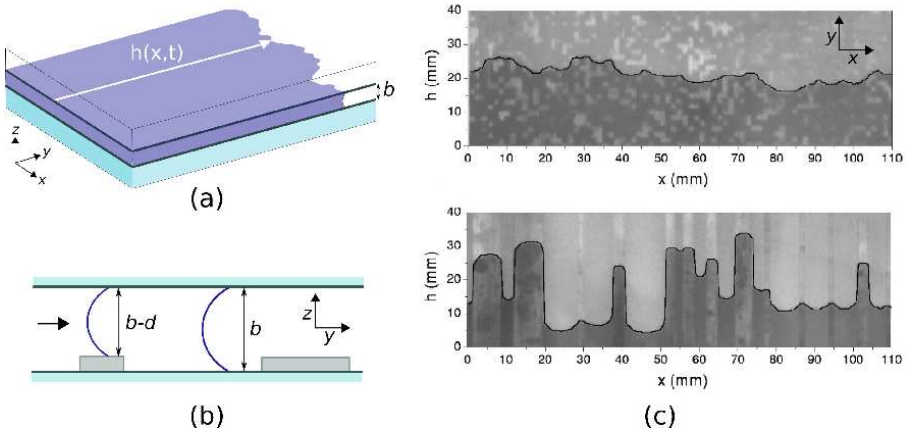

Fig. 4.1 (a) Schematic representation of the experimental setup of a disordered Hele-Shaw cell used in Refs. [136, 138]. (b) Gap variation due to the cooper obstacles induces different curvatures at the oil/air meniscus (blue lines). (c) Two examples of disorder configurations: squares (top) and tracks (bottom) (Ref. [136]).

- *Spontaneous imbibition.-* The pressure at the oil inlet is kept constant by using an oil container of selectable height H_c, measured with respect to the height of the air outlet. This fixes the pressure difference between the end of the cell and the liquid inlet as $\Delta p_a = \rho g H_c$, being ρ the density of the oil, and g the gravity.

- *Forced-flow imbibition.-* The oil is injected at constant flow rate by using a syringe pump that can be programmed to give flow rates Q in a given range.

4.2 Theoretical background

From a general point of view, imbibition phenomena belong to the problem of surface growth in disordered media. The first theoretical attempts to describe the physical mechanisms of an interface growing in a heterogeneous medium were actually based on general models of surface growth [5], given by a Langevin-like stochastic equation such as

$$\frac{\partial h}{\partial t} = \mathcal{G}(\nabla h) + F + \xi(\boldsymbol{x}, h), \tag{4.2}$$

where $h(\boldsymbol{x}, t)$ is the height of the interface at position $\boldsymbol{x}$ and time t. The functional $\mathcal{G}(\nabla h)$ depends on the specific model and should satisfy all the sym-

metries and conservation laws. F represents the driving force, and $\xi(\boldsymbol{x}, h)$ describes the random pinning forces of the medium acting on the surface, and it is called *quenched* disorder because does not change on time. One of the most acclaimed example of this kind of models was the so-called quenched Edwards-Wilkinson (QEW) model

$$\frac{\partial h}{\partial t} = \nabla^2 h + F + \xi(\boldsymbol{x}, h), \tag{4.3}$$

initially proposed as a suitable model to study the borders of magnetic domains in random field Ising model [19], and as a model for fluid moving in heterogeneous media [71]. However, although it has been found to be partially valid to statistically describe configurations of pinned fronts [143], Eq. (4.3) – and generally any model like Eq. (4.2) – turn out to be essentially incorrect to describe the physics of imbibition fronts. This is basically because the mass conservation of the liquid induces non-local effects that are not included in the above models. Different theoretical works [45, 64, 108] have actually arrived at the conclusion that the interface dynamics has to be described by a non-local and nonlinear equation that comes out when the transport of liquid from the reservoir is taken into account. This is what is called the *macroscopic description of imbibition* and it is derived in detail in the following Section.

4.3 Macroscopic description of imbibition

The starting-point to derive an equation for the interface dynamics in disordered media is the general Darcy's law, Eq. (4.1). For simplicity, the gravity effects shall be omitted in the following derivation. The experimental setup considered here is that from the Hele-Shaw cell used in the work by Soriano *et al.* [136, 138] with a randomly gap spacing $b + \delta b$. If we assume a smooth variation of the gap, $|\delta b| \ll 1$, the fluid flow can then be locally described by the Darcy's equation of the Hele-Shaw cell (see Ch. 3)

$$\boldsymbol{v}(x, y) = -\frac{b(x, y)^2}{12\eta} \boldsymbol{\nabla} p(x, y), \tag{4.4}$$

where now the permeability $K = b(x, y)^2/12$ is a random variable.

4.3.1 Capillarity versus permeability disorder

An important issue to start with is to realize that fluctuations of gap spacing $b + \delta b$ in the Hele-Shaw cell mainly give rise to two different kinds of disorder

acting on the interface [108], namely, the capillary disorder $p_c \sim 1/(b+\delta b)$ and the permeability disorder $K \sim (b+\delta b)^2$. However, it can be easily shown that both disorders act at different length scales separated by a typical crossover length, denoted as ℓ_K [2, 108]. An estimation of such crossover length can be obtained as follows.

Consider the two-dimensional normal velocity of the interface, given by the Darcy's equation projected normally ($\hat{n}$ direction) to the interface position

$$v_n = -\frac{K}{\eta}\partial_n p. \tag{4.5}$$

Let that permeability and pressure to be written in terms of fluctuating variables,

$$\begin{aligned} K &= K_0 + \delta K, \\ p &= p_0 + \delta p, \end{aligned} \tag{4.6}$$

where the disorder terms δK and δp come essentially from the gap variation δb, and they correspond to permeability and capillary pressure fluctuations, respectively,

$$\delta K = 2K_0\frac{\delta b}{b}, \tag{4.7}$$

$$\delta p = -\bar{p}_c\frac{\delta b}{b}, \tag{4.8}$$

with $K_0 = b^2/12$ and $\bar{p}_c = 2\sigma\cos\theta/b$ being the permeability and capillary pressure of the clean Hele-Shaw cell, respectively (see the preceding Chapter). Next, introduce the above expressions into Darcy's equation (4.5) and take linear orders in δb

$$v_n = \overline{v} + 2\overline{v}\frac{\delta b}{b} + \frac{K_0\bar{p}_c}{\eta}\partial_n\Big[\frac{\delta b}{b}\Big], \tag{4.9}$$

where $\overline{v} = -(K_0/\eta)\partial_n p_0$ is the mean velocity of the interface. Comparing both disorder terms at the above equation, one obtains the existence of a lateral length scale

$$\ell_K \simeq \frac{\sigma b}{12\eta}\frac{1}{\overline{v}}, \tag{4.10}$$

separating two regimes. At length scales below ℓ_K, the interface fluctuations are mainly caused by capillarity disorder – *capillary regime*. On the other hand, at length scales above ℓ_K, the interface roughness is produced by permeability disorder – *permeability regime*.

In the following we shall assume that the interface velocities are always low enough to ensure the crossover length of Eq. (4.10) to be always larger than the system lateral size, $\ell_K > L$. Therefore, the permeability disorder can be taken as a constant $K \sim K_0$ and we can assume that the main source of disorder essentially comes from the capillarity. Note that this is a quite reasonable approximation in the case of spontaneous imbibition, where the interface velocity is decreasing down in time. However, as it is shown in Chapter 8, for a very high applied pressure at the inlet of the cell, and then high initial velocities, the permeability disorder may start to be important.

Therefore, the macroscopic description of imbibition flows in a disordered Hele-Shaw cell will be given by the following set of equations

$$\begin{aligned} &v(x,y) = -\overline{K}_0 \boldsymbol{\nabla} p(x,y), \\ &\nabla^2 p(x,y) = 0, \\ &\Delta p_i = p_{\text{air}} - p(x,h) = \sigma\kappa + \xi(x,h), \end{aligned} \tag{4.11}$$

where we have applied the compressibility condition at the two-dimensional velocity field, $\boldsymbol{\nabla} \cdot v = 0$, giving rise to the pressure Laplace equation. As it was shown in Ref. [108] this condition only holds in the capillary regime, where the permeability K is assumed constant. The pressure jump across the interface Δp_i is given by the Young-Laplace relation [Eq. (2.4) in Ch. 2] that now contains also the local curvature κ in the cell plane due to the roughness of the interface. This curvature is expressed as

$$\kappa = \boldsymbol{\nabla} \cdot \hat{n} = \frac{\nabla^2 h}{(1 + |\nabla h|^2)^{3/2}}, \tag{4.12}$$

being $h(x,t)$ the interface position and $\hat{n}$ the normal vector to the interface. The quenched disorder term $\xi(x,h)$ in Eq. (4.11) comes from the curvature variation along the transversal direction and it represents the random capillarity of the system due to the gap fluctuations

$$\xi(x,h) = \frac{2\sigma\cos\theta}{b + \delta b}, \tag{4.13}$$

where we will suppose that the contact angle θ does not vary. We have also defined the term $\overline{K}_0 \equiv K_0/\eta$ in Eq. (4.11), which is called the mobility parameter.

4.3.2 Solving the macroscopic model

The purpose of this Section is to derive a dynamic equation describing the interface fluctuations. To this end, the macroscopic description, given by Eq.

(4.11), will be solved by using Green function formalism. We shall consider here the case of *spontaneous imbibition*, where the pressure at the origin of the system is kept constant to an applied pressure

$$p(x, y = 0) = p_{\mathrm{a}}. \tag{4.14}$$

Note that the above condition must be replaced by

$$\nabla p(x, y)|_{y=0} = -\frac{1}{K_0}\overline{v}\hat{y}, \tag{4.15}$$

in forced-flow imbibition, where the mean velocity $\overline{v}$ is kept constant by imposing a constant driving ($\hat{y}$ corresponds to an unit vector). A derivation of the interface equation in the case of forced-flow imbibition can be found in Refs. [64, 108].

Therefore, we need to work out a Laplace equation in a two-dimensional system (x, y) with moving boundary conditions. The procedure is based on standard Green function formalism (see for instance [8]), and our starting point is the following Green's identity:

$$\iint_{\Omega_L} d\boldsymbol{r}' \Big[p(\boldsymbol{r}')\nabla'^2 G(\boldsymbol{r}|\boldsymbol{r}') - G(\boldsymbol{r}|\boldsymbol{r}')\nabla'^2 p(\boldsymbol{r}') \Big] = \int_{S_L} d\boldsymbol{s}' \cdot p(s')\boldsymbol{\nabla}' G(s|s') - \int_{S_L} d\boldsymbol{s}' \cdot G(s|s')\boldsymbol{\nabla}' p(s'), \tag{4.16}$$

integrated over the volume of the liquid $\Omega_L = \{x, 0 \leq y \leq h(x,t)\}$, and along its surface S_L, where s is a tangential coordinate to the surface. The point now is to take the Green's function $G(\boldsymbol{r}|\boldsymbol{r'})$ defined in the positive half-plane $\Omega = \{x, y \geqslant 0\}$, and given by the equation

$$-\nabla^2 G(\boldsymbol{r}|\boldsymbol{r'}) = \delta(\boldsymbol{r} - \boldsymbol{r'}), \tag{4.17}$$

with homogeneous Dirichlet boundary conditions. The solution of the above equation at the half-plane geometry can be derived by using the method of image charges, obtaining

$$G(x, y|x', y') = \frac{1}{4\pi}\ln\left[\frac{(x-x')^2 + (y+y')^2}{(x-x')^2 + (y-y')^2}\right]. \tag{4.18}$$

Then, by evaluating the Green's identity, Eq. (4.16), at the interface position $\boldsymbol{r} = (x, h(x,t))$, and taking into account the Laplace equation for the pressure, we arrive at the following relation:

$$\frac{1}{2}p(x,h) = \int_{int} ds' \Big[G(s|s')\partial_n p(s') - p(s')\partial_n G(s|s') \Big] + \int_0 ds' p(s')\partial_n G(s|s'),$$

where we have applied the homogeneous boundary condition of the Green function $G(x,y|x,0) = 0$, and also considered that the integrals evaluated at $x \to \pm\infty$ cancel out. The factor $1/2$ in the LHS of the above equation comes from the Dirac delta function integral, which is integrated only up to the interface position. The subindex *int* and 0 mean that the integral is evaluated along the interface position $(x, h(x,t))$ and along the origin of the system $(x,0)$, respectively.

By making use now of a *planar approximation* for the interface, which is based on the condition $|\nabla h| \ll 1$, we can replace the tangential and normal coordinates by the usual cartesian coordinates, $s \sim x$ and $n \sim y$. Then, the above equation can be expressed as

$$\frac{1}{\overline{K}_0}\int_{-\infty}^{\infty} dx' \widehat{G}(x',h')\partial_t h(x',t) = \frac{1}{2}\Big[\sigma\nabla^2 h(x,t) + \xi(x,h)\Big] + \Lambda_S, \tag{4.19}$$

where we have made use of Darcy's equation (4.5) for the normal velocity of the interface, which is expressed as $\mathrm{d}s v_n = \mathrm{d}x\partial_t h(x,t)$. We have also considered the Young-Laplace relation for the pressure jump across the interface, Eq. (4.11), neglecting, for simplicity, the air pressure $p_{\mathrm{air}} \simeq 0$, and taking the interface curvature as $\kappa \sim \nabla^2 h(x,t)$. Here, we have defined $\widehat{G}(x',h') \equiv G(x,h|x',h')$, with $h' \equiv h(x',t)$, and the integral term

$$\Lambda_S = \int_{-\infty}^{\infty} dx' \Big\{ p_{\mathrm{a}} \partial_{y'} \widehat{G}(x',0) + \Big[\sigma\nabla^2 h(x,t) + \xi(x,h)\Big]\partial_{y'}\widehat{G}(x',h')\Big\}, \tag{4.20}$$

where the spontaneous imbibition condition, $p(x,0) = p_{\mathrm{a}}$, has been used. Therefore, we can conclude from Eq. (4.19) that interface fluctuations in spontaneous imbibition are described by a non-local and highly non-linear equation, that comes out when taking into account the mass conservation of the liquid.

Finally, making a linear expansion of the interface fluctuations around their mean value $H(t)$, Eq. (4.19) can be written in Fourier space as the following *linearized interface equation*:

$$\partial_t \hat{h}_k = \frac{1+\mathrm{e}^{-2|k|H}}{1-\mathrm{e}^{-2|k|H}}|k|\Big[-\sigma\overline{K}_0 k^2 \hat{h}_k - \dot{H}\hat{h}_k + \overline{K}_0\hat{\xi}_k\Big] + \delta(k)\left[\frac{\overline{K}_0 p_{\mathrm{a}}}{H} + \dot{H}\right]. \tag{4.21}$$

where $\delta(k)$ is the Dirac delta function, and the noise term in Fourier space is taken as $\tilde{\xi}_k = \int dx e^{-ikx}\xi(x,h(x,t))$. The above relation becomes more meaningful in the limit $|k|H(t) >> 1$, which means that during the kinetic roughening process, correlations of the interface fluctuations grow up in time slower

than the averaged interface position [2]. In this limit, we arrive at the final expression:

$$\boxed{\partial_t \hat{h}_k = -\sigma \overline{K}_0 |k| k^2 \hat{h}_k - \dot{H}|k|\hat{h}_k + \overline{K}_0 |k| \hat{\xi}_k.} \tag{4.22}$$

Note that the non-locality is reflected in the term $|k|$. If we take now the limit $k \to 0$ in Eq. (4.21) we obtain that the mean velocity is given by

$$\dot{H}(t) = \overline{K}_0 \frac{p_a + \langle \xi \rangle}{H}, \tag{4.23}$$

where $\langle \xi \rangle \sim 2\sigma \cos\theta / b$ is the spatially averaged capillary pressure at the interface. The above equation is the same equation obtained for the clean Hele-Shaw cell in Chapter 3, and reduces to the Washburn law for the mean height

$$H(t) = \sqrt{H_0^2 + 2at}, \tag{4.24}$$

where H_0 represents an initial height and $a = \overline{K}_0(p_a + \langle \xi \rangle)$. It is important to remark that the results presented in Refs. [64,108] show that the interface fluctuations in forced-flow imbibition are given by the same linearized equation (4.22). In that case, however, the mean interface velocity is constant $\dot{H} = \overline{v}$.

Finally, we can therefore see from Eq. (4.22) that the interface fluctuations due to the capillary disorder $\hat{\xi}_k$ are essentially damped by two different mechanisms. At small scales, the surface tension σ controls the fluctuations, while long scales are damped by the advancement of the front $\dot{H}(t)$. These two effects are separated by the typical crossover length:

$$\ell_\times \sim \left[\frac{\sigma \overline{K}_0}{\dot{H}(t)} \right]^{1/2}, \tag{4.25}$$

which increases in time, $\ell_\times \sim t^{1/4}$, in the case of spontaneous imbibition, and is fixed to a constant value, $\ell_\times \sim \overline{v}^{-1/2}$, in forced-flow imbibition. As it was pointed out by Dubé *et al.* [45], the importance of this crossover length in imbibition is that it acts as a *cut off* for the interface correlations (see next Chapter).

2) The important point in general surface growth is that there exists a correlation length growing in time as $\ell_c \sim t^{1/z}$. This is explained in detail in the following Chapter.

4.4 Phase field model for imbibition

The numerical resolution of the macroscopic model may involve important technical limitations, especially because the sharp interface needs to be tracked during all the system evolution. An alternative numerical approach useful to study imbibition fronts is by making use of the so-called *phase field model* or diffuse interface model. This model can be seen as a numerical tool that converts a moving boundary problem into a set of partial differential equations, allowing then an easier numerical treatment. The main aim of the phase field model is to write a dynamic equation for an order parameter, or phase field, without need to supply information on the interface position. Such an order parameter, denoted as ϕ, usually takes two limit values $\phi = \pm\phi_e$ representing the two different phases of the system. The physical interface is then located in the region where the parameter changes its value from ϕ_e to $-\phi_e$, defining a small region of width ϵ [see Fig. 4.2(a)]. Then, it is asked that in the *sharp interface limit* [49], when the width of the diffuse interface goes to zero, $\epsilon \to 0$, the resulting dynamics will be the same as in the macroscopic description.

These kind of models have been used during the last years in several contexts, such as for example in solidification phenomena [21, 31, 53, 81], Hele-Shaw flows [22, 54, 55, 63, 88] or biological membranes [26–29], among many others (see [17, 51, 57] for reviews). In the imbibition context, the phase field models were initially used by Dubé *et al.* [43, 45, 46] and A. Hernández-Machado *et al.* [64] (see also the review in [1]). The order parameter is chosen so that positive values represent the liquid phase and negative values the air phase, and can be understood as a global density function or total concentration field of the system.

4.4.1 Equilibrium solutions

The phase field model is based on a Ginzburg-Landau formulation, where the free energy of the system is given by

$$\mathcal{F}[\phi] = \int d\boldsymbol{r} f(\phi) = \int d\boldsymbol{r}\Big(V(\phi) + \frac{\epsilon^2}{2}|\nabla\phi|^2\Big), \tag{4.26}$$

where $f(\phi)$ represents the free energy density. The potential $V(\phi)$ is usually chosen to have a double-well form, which combined with the square gradient term ensures the existence of a well defined interface with a width of the order of ϵ. The chemical potential can also be defined as the change in $\mathcal{F}$ for a local

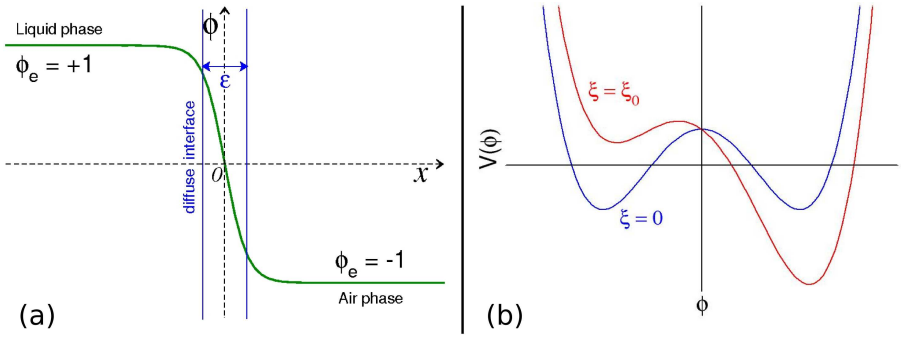

Fig. 4.2: (a) Schematic representation of the phase field profile, $\phi(x)$, in one dimension. The two limit values ± 1 represent the two phases of the system, and the phase field continuously goes from one to the other in a finite region, the diffuse interface. (b) The effect of adding a linear term $\xi\phi$ at the double-well potential, $V(\phi)$, is to destabilize one of the two phases.

change in concentration:

$$\mu \equiv \frac{\delta \mathcal{F}}{\delta \phi} = V'(\phi) - \epsilon^2 \nabla^2 \phi. \tag{4.27}$$

In equilibrium, the condition $\mu = 0$ gives rise to

$$V'(\phi_0) = \epsilon^2 \nabla^2 \phi_0, \tag{4.28}$$

where ϕ_0 represents the equilibrium solution for the phase field, also known as *kink* solution or Goldstone mode. In the case of a flat interface, and considering a double-well potential as

$$V(\phi) = V_0 - \frac{1}{2}\phi^2 + \frac{1}{4}\phi^4, \tag{4.29}$$

one can find the following solution:

$$\phi_0 = -\phi_e \tanh\left(\frac{u}{\epsilon\sqrt{2}}\right). \tag{4.30}$$

Note that by assuming the potential as in Eq. (4.29), the bulk value of the phase field is $\phi_e = 1$. In the above relation u represents a normal coordinate to the interface. An interesting and useful propertie of ϕ_0 is that in the sharp interface limit of $\epsilon \to 0$, the derivative of the kink solution can be approached by a Dirac delta function:

$$\lim_{\epsilon \to 0} \partial_u \phi_0 = -2\phi_e \delta(u) = -\Delta\phi\,\delta(u), \tag{4.31}$$

with $\Delta\phi = 2\phi_e$ being the miscibility gap.

Surface tension.- Consider the simple case of a flat interface. By multiplying Eq. (4.28) by $\partial_u \phi_0$ and integrating along u, we can write the relation:

$$\frac{\epsilon^2}{2}\Big(\frac{\mathrm{d}\phi_0}{\mathrm{d}u}\Big)^2 = V(\phi_0) - V(\phi_e), \tag{4.32}$$

where we have used the condition $\mathrm{d}_u\phi_0 = 0$ for $u \to \pm\infty$. Now, the free energy density $f(\phi)$ can be expressed as

$$f(\phi) = \epsilon^2\Big(\frac{\mathrm{d}\phi_0}{\mathrm{d}u}\Big)^2 + V(\phi_e). \tag{4.33}$$

The excess free energy per unit area, i.e. the surface tension is then given by

$$\sigma' = \epsilon^2 \int \mathrm{d}u \Big(\frac{\mathrm{d}\phi_0}{\mathrm{d}u}\Big)^2 = \epsilon \int_{-\phi_e}^{\phi_e} \mathrm{d}\phi \sqrt{2[V(\phi) - V(\phi_e)]}, \tag{4.34}$$

where we have used the prime to differentiate from the usual surface tension σ. If the arbitrary constant V_0 of the potential in Eq. (4.29) is chosen so that $V(\phi_e) = 0$, the above integral is finally reduced to [2,17]

$$\sigma' = \frac{2\sqrt{2}}{3}\epsilon. \tag{4.35}$$

Gibbs-Thomson relation.- It is interesting now to note that in the sharp interface limit, it is possible to obtain an equivalent Young-Laplace relation as a boundary condition for the chemical potential. To this end, we use a coordinate system (s, u) moving with the interface position, where s represents the arc length of the interface and u a coordinate perpendicular to the interface (see Sec. A.1 in Appendix A). The chemical potential evaluated in a surface of constant ϕ is then given by

$$\mu = V'(\phi) - \epsilon^2\partial_u^2\phi + \epsilon^2\kappa\partial_u\phi, \tag{4.36}$$

where κ is the interface curvature. Multiply now the above relation by $\partial_u\phi$, integrate along u, and apply the sharp interface limit, to obtain the following condition for the chemical potential at the interface position:

$$2\phi_e\mu|_{int} = -\Delta V - \kappa\sigma', \tag{4.37}$$

where $\Delta V = V(-\phi_e) - V(\phi_e)$. This relation is equivalent to the Young-Laplace equation for the pressure in the macroscopic model, Eq. (4.11), and it is called Gibbs-Thomson relation in the phase field model context [2,17]. The point now is to note that the capillarity effect can be included in the model by

adding a linear term in the potential:

$$V(\phi) = V_0 - \frac{1}{2}\phi^2 + \frac{1}{4}\phi^4 - \phi\xi(\boldsymbol{r}), \tag{4.38}$$

so that $\Delta V = 2\phi_e\xi(\boldsymbol{r})$. As it is shown in Fig. 4.2, this linear term destabilizes one of the two phases and therefore, for positive values of the quenched random field $\xi(\boldsymbol{r}) > 0$, the disorder favors the liquid (wet) phase, forcing the interface to advance at the expense of the air (dry) phase [45]. The disorder can also be chosen with negative values, modeling then a non-wetting or hydrophobic system.

4.4.2 Conserved dynamics

The dynamical evolution of the phase field is given by a generalized Cahn-Hilliard model [25] or model B in the Halperin-Hohenberg nomenclature [65], with a locally conserved order parameter

$$\frac{\partial\phi}{\partial t} = -\boldsymbol{\nabla}\cdot\boldsymbol{j}, \tag{4.39}$$

where the current is taken proportional to the gradient of the chemical potential

$$\boldsymbol{j} = -M(\phi)\boldsymbol{\nabla}\mu, \tag{4.40}$$

with $M(\phi)$ being the mobility coefficient, which may depend on the phase field. By using the expression for the chemical potential, Eq. (4.27), taking into account the potential form of Eq. (4.38), the resulting dynamic equation for the phase field reads

$$\boxed{\frac{\partial\phi}{\partial t} = \boldsymbol{\nabla}M(\phi)\boldsymbol{\nabla}\mu = \boldsymbol{\nabla}M(\phi)\boldsymbol{\nabla}\big[-\phi+\phi^3-\epsilon^2\nabla^2\phi-\xi(\boldsymbol{r})\big].} \tag{4.41}$$

In most of the results presented in this thesis, we have made use of the so-called *one-sided model*, where the mobility M is taken constant at the liquid phase ($\phi > 0$) and zero at the air phase ($\phi < 0$). A detailed comparison between this model and the *symmetric* model, where M is constant throughout the whole system, is given in Ch. 10.

It is also possible to calculate the normal velocity of the interface from the above equation. By using the curvilinear coordinate system (s, u) we have that

$$\frac{\partial\phi}{\partial t} = -v_n\frac{\partial\phi}{\partial u}, \tag{4.42}$$

where $v_n = -\partial_t u$ represents the normal velocity of the interface. Then by integrating Eq. (4.41) around a region $[-\epsilon, \epsilon]$ of the interface, and applying the sharp interface limit, we obtain

$$v_n = -\frac{M}{2\phi_e}\partial_u \mu. \tag{4.43}$$

This condition is completely equivalent to the macroscopic description for the pressure p based on the Darcy's law, Eq. (4.11). Actually, by making a matched asymptotic expansion in the sharp interface limit (see for instance Ref. [63]), it is possible to obtain a correspondence between the phase field parameters with the corresponding ones from the macroscopic description through the relations

$$p = \phi_e \mu_1, \quad \overline{K}_0 = \frac{M}{2\phi_e^2}, \quad \sigma = \frac{1}{2}\sigma', \tag{4.44}$$

where μ_1 is the first order in ϵ term of the chemical potential in the asymptotic expansion. Likewise, a detailed derivation of the interface equation (4.22) from the phase field equation (4.41) is provided in Appendix A.

Therefore, in order to numerically reproduce imbibition fronts in disordered media, Eq. (4.41) is integrated in a two-dimensional system of size $L_x \times L_y$ with a given disorder configuration $\xi(x, y)$. As it has been pointed out in [2, 46], the phase field equation can be put in dimensionless units by choosing all the parameters to unity, i.e. $\epsilon = 1$, $M = 1$. The interface position $h(x, t)$ is then given by interpolating the points where $\phi[x, h(x, t); t] = 0$. Figure 4.3 shows a numerical example of a liquid/air system in two different disorder configurations studied in this thesis.

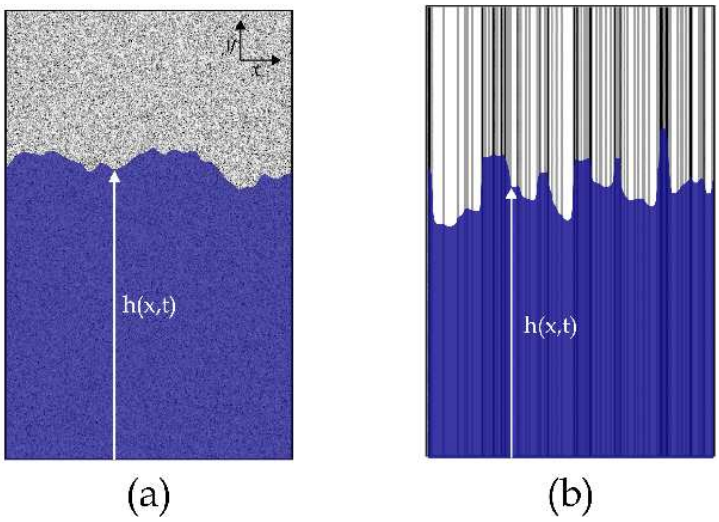

Fig. 4.3 Numerical example of a liquid/air system with a disorder $\xi(x,y)$ randomly distributed over the whole system (a), and a columnar disorder $\xi(x)$ (b).

5
Scaling theory of surface growth

The growth of fluctuating interfaces in disordered media has been a subject of much interest during the last twenty years. The study of the interface kinetic roughening is a fundamental problem of non-equilibrium statistical physics and has important applications in technological processes and material characterization. Examples of experimental studies are fracture surfaces [3, 11, 13, 95], the growth of thin films from an incoming flux of atoms [5, 73, 110], slow combustion fronts [100, 102], and fluid-air interfaces in porous media [56, 127, 135–138], among many others. The main common feature in such experiments is that one has a stable fluctuating interface that can be described in terms of scaling laws [5, 101]. The interface height at position $\boldsymbol{x}$ and time t is generally expressed with a single-valued function $h(\boldsymbol{r}, t)$ in $d+1$ dimensions. Usually, the growth starts with an initially flat interface that undergoes a kinetic roughening process until it reaches a saturated regime, in which the interface fluctuations become statistically independent of time and are scale-invariant up to some typical length scale of the system. This process is described in terms of the phenomenological Family-Vicsek scaling hypothesis [50], which supposes the presence of only one characteristic scale in the problem. This scale corresponds to the correlation length ℓ_c of the interface fluctuations, and it is expected to grow in time until it reaches the system size, $\ell_c = L$. Interfaces are then considered as random *self-affine* fractals, which means that they remain invariant under the anisotropic transformation:

$$h(\boldsymbol{r}) = b^{\alpha} h(b\boldsymbol{r}), \tag{5.1}$$

where α is called the *roughness exponent*. The above relation indicates that a self-affine function must be rescaled in a different way horizontally and vertically. For instance in $d = 1$, if the x axis is changed by a factor b, $x \to bx$, the height function must be rescaled by a factor b^{α}, $h \to b^{\alpha} h$, in order to preserve the function statistically invariant. In the especial case of $\alpha = 1$, one recovers an isotropic transformation, and then the function is referred to as *self-similar*.

This Chapter introduces several concepts concerning the statistical properties of the interface fluctuations in terms of scaling laws. To this end, the different types of scalings in which the interface may be classified are discussed,

which will be useful to follow the statistical analysis of fluctuating fronts presented in the following parts of the thesis.

5.1 Family-Vicsek scaling

In the Family-Vicsek scaling hypothesis [50], the lateral correlation length ℓ_c is expected to grow in time following a power-law as $\ell_c \sim t^{1/z}$ until it reaches the system size, $\ell_c = L$, which defines a saturation time $t_s \sim L^z$. In this context, z is the so-called *dynamic exponent*. One of the basic quantities to study the fluctuations of the growing interface is its global width or vertical correlation length (see Fig. 5.1), defined as

$$W(L,t) = \langle \overline{[h(x,t) - \overline{h}]^2} \rangle^{1/2}, \tag{5.2}$$

where $\langle .. \rangle$ denotes average over different noise realizations and the overbar is spatial average in the x direction.

Fig. 5.1 Example of a rough interface characterized by a lateral correlation length ℓ_c and the global width $W(L,t)$.

In most of cases, the interface is initially flat so that the global width is zero at $t = 0$. As the system evolves and the interface becomes rougher, the width increases in time as $W(L,t) \sim t^{\beta}$ for $t < t_s$ and becomes constant $W(L) \sim L^{\alpha}$ for $t > t_s$. Here, β is the *growth exponent*. Note that the saturation time is given by both $t_s \sim L^{\alpha/\beta}$ and $t_s \sim L^z$. Therefore, we can obtain the following scaling relation between the three exponents:

$$\beta = \frac{\alpha}{z}. \tag{5.3}$$

Alternatively, one might be interested in studying the correlations over a distance $\ell \ll L$ through the *local* interface width, defined as

$$w(\ell,t) = \langle \langle [h(x,t) - \langle h \rangle_\ell]^2 \rangle_\ell \rangle^{1/2} \tag{5.4}$$

where $\langle ... \rangle_\ell$ denotes an average over x in windows of size ℓ. In the Family-Vicsek scenario the above quantity is expected to grow in time as $w(\ell,t) \sim t^{\beta}$ until the local window ℓ gets saturated, $\ell_c \sim \ell$, defining then the local

saturation time $t_\ell \sim \ell^z$. Further on, the local width only depends on the lateral length ℓ as $w(\ell) \sim \ell^\alpha$. In general terms, these two asymptotic behaviors can be described by a single scaling function

$$w(\ell, t) = t^\beta f(\ell / t^{1/z}), \tag{5.5}$$

where $f(u)$ is a scaling function that behaves as

$$f(u) \sim \begin{cases} \text{const} & \text{if} \quad u \gg 1 \\ u^\alpha & \text{if} \quad u \ll 1. \end{cases} \tag{5.6}$$

Note that Eq. (5.5) is also valid by the global width behavior by simply replacing ℓ by L. It is important to remark that in the saturated regime, $t > L^z$, the only remaining scale that breaks scale-invariance symmetry is the size L of the system. Then, the interface width can be written in terms of a finite-size scaling $w(\ell, L) \sim \ell^\alpha f(\ell/L)$ with $f(u) \sim \text{const}$ for $u \ll 1$ and $f(u) \sim u^{-\alpha}$ for $u \simeq 1$. This basically means that the global interface width after saturation increases with the system size, $W(L) \sim L^\alpha$, with the same exponent as the local interface width observed at smaller window sizes $w(\ell \ll L) \sim \ell^\alpha$. This behavior is the main characteristic of the Family-Vicsek scaling. In contrast, as it is shown in next Section, when the interface is affected by *anomalous scaling* [67, 123], such an equivalence between global and local scales is not valid anymore, and the above scaling function needs to be generalized.

Another useful quantity also used to obtain the roughness exponent α is the structure factor or power spectrum of the interface $\mathcal{S}(k,t) = \langle \hat{h}_k(t) \hat{h}_{-k}(t) \rangle$, where $\hat{h}_k(t) = L^{-d/2} \sum_x [h(x,t) - \overline{h}] \exp(ikx)$ is the Fourier transform of the interface in a system of size L. In the Family-Vicsek assumption it scales as

$$\mathcal{S}(k,t) = k^{-(2\alpha+d)} s_{FV}(kt^{1/z}), \tag{5.7}$$

where s_{FV} is the scaling function

$$s_{FV}(u) \sim \begin{cases} \text{const} & \text{if} \quad u \gg 1 \\ u^{2\alpha+d} & \text{if} \quad u \ll 1. \end{cases} \tag{5.8}$$

Therefore, we can obtain the roughness exponent by looking at the power spectrum $\mathcal{S}(k,t) \sim k^{-(2\alpha+d)}$ for $k \gg k_c$ where $k_c \sim 1/\ell_c$.

The Edwards-Wilkinson equation.- One of the most famous models of surface growth, characterized by a Family-Vicsek scaling is the so-called Edwards-Wilkinson (EW) equation [47]:

$$\frac{\partial h}{\partial t} = \nabla^2 h + \xi(x,t), \tag{5.9}$$

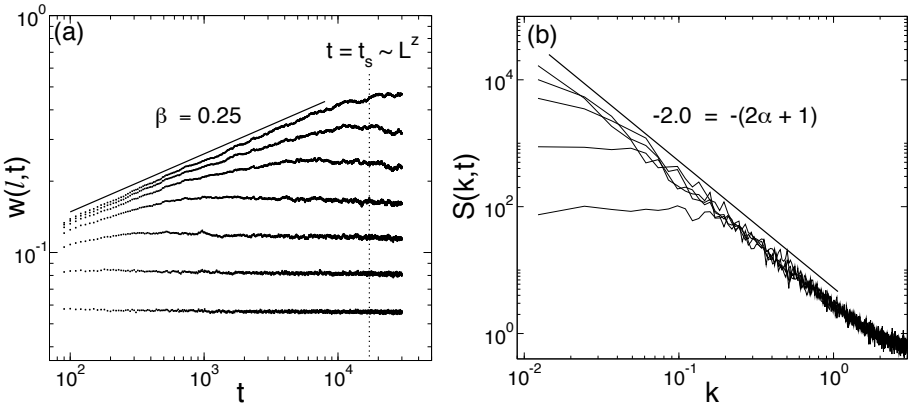

Fig. 5.2 Numerical resolution of the EW equation in a system of size $L = 512$. (a) Local interface width as function of time calculated at different lateral lengths, from $\ell = L/128$ up to $\ell = L$ (bottom to top). As expected in a Family-Vicsek scaling, the local scales $\ell \ll L$ saturate at the local time $t_\ell \sim \ell^z \ll L^z$. We obtain the exponent $\beta = 0.25(3)$ from the data fit, in perfect agreement with the theoretical prediction, Eq. (5.10). (b) Structure factor $\mathcal{S}(k,t)$ at different times giving a roughness exponent $\alpha = 0.50(5)$.

where $\xi(x,t)$ is a white noise with correlations $\langle \xi(x,t)\xi(x',t')\rangle \sim \delta(x - x')\delta(t - t')$. This model describes the process of random deposition with surface relaxation [5], and can be easily studied both numerically and analytically. Indeed, the scaling exponents can be obtained by imposing the above equation to be scale-invariant if the variables are rescaled as $x \to bx$, $t \to b^z t$, and $h \to b^\alpha h$ [5], obtaining:

$$z = 2, \qquad \alpha = \frac{2-d}{2}, \qquad \beta = \frac{2-d}{4}, \tag{5.10}$$

in $d + 1$ dimensions. As it is shown in Fig. 5.2, these exponents are in perfect agreement with numerical integrations of Eq. (5.9) in $d = 1$.

5.2 Anomalous scaling

Although the scaling proposed by Family and Vicsek [50], given by Eqs. (5.5) and (5.7), is found to be valid in a great variety of experiments or models, there are many other cases where this scaling is not suitable to describe the interface fluctuations. Basically, the finite-size scaling argument discussed in the preceding Section for the interface width turns out to be incorrect, and one needs to introduce a new *local roughness exponent* $\alpha_{\rm loc}$ in order to distinguish between the behavior at local scales $w(\ell) \sim \ell^{\alpha_{\rm loc}}$ and global scales $W(L) \sim L^\alpha$. This is the so-called anomalous scaling and has been observed in many

experimental results [32,95,135,138] and numerical models [67,90,141] during the last years. As pointed out by López [92], the presence of anomalous scaling is a consequence of a nontrivial dynamics shown by the mean local slope of the interface $\langle \nabla h \rangle$, and it is characterized by a lack of self-affinity [94].

A complete description of the anomalous scaling was given by Ramasco *et al.* [122, 123] on basis of a new scaling *ansatz* that generalizes the scaling form of the power spectrum given by Eq. (5.8), and include all the existing scaling behaviors in one single framework. Assuming that the Family-Vicsek hypothesis for the correlations growth, $\ell_c \sim t^{1/z}$ is still valid, the proposed generic ansatz is the following:

$$\mathcal{S}(k,t) = k^{-(2\alpha+1)} s_A(kt^{1/z}), \tag{5.11}$$

where now the scaling function has the general form

$$s_A(u) \sim \begin{cases} u^{2(\alpha-\alpha_s)} & \text{if} \quad u \gg 1 \\ u^{2\alpha+1} & \text{if} \quad u \ll 1, \end{cases} \tag{5.12}$$

being α_s the *spectral roughness exponent*. The above scaling behavior for the power spectrum allows to obtain the scaling for the local width by using the relation [67]

$$w(\ell,t)^2 \sim \int_{2\pi/L}^{\pi/a} \frac{\mathrm{d}k}{2\pi} [1 - \cos(kl)] \mathcal{S}(k,t), \tag{5.13}$$

where a is the lattice spacing. The resulting dynamic scaling for the local width reads as:

$$w(\ell,t) = t^{\beta} g(\ell/t^{1/z}), \tag{5.14}$$

with the corresponding scaling function

$$g(u) \sim \begin{cases} u^{\alpha_{loc}} & \text{if} \quad u \ll 1 \\ \text{const} & \text{if} \quad u \gg 1, \end{cases} \tag{5.15}$$

where α_{loc} is the rough local exponent and it characterizes the roughness at small scales $\ell \ll L$. Therefore, one of the main implications of the anomalous scaling is that the system has now three characteristic length scales: the system size L, the correlation length ℓ_c, and the observation scale ℓ. Consequently, there are three different time regimes:

$$w(\ell,t) \sim \begin{cases} t^{\beta} & \text{for} \quad t < \ell^z \\ t^{\beta^*} \ell^{\alpha_{\mathrm{loc}}} & \text{for} \quad \ell^z < t < L^z \\ \ell^{\alpha_{\mathrm{loc}}} L^{\alpha-\alpha_{\mathrm{loc}}} & \text{for} \quad t > L^z. \end{cases} \tag{5.16}$$

In the anomalous scaling, the local width saturates when the correlation length reaches the system size, i.e, at times $t_s \sim L^z$ and not at the local time $t_\ell \sim \ell^z$ as occurs in the Family-Vicsek scaling (see Fig. 5.2). There is an intermediate regime between t_ℓ and t_s when the local width grows as $w(\ell, t) \sim t^{\beta^*}$ where

$$\beta^* = \beta - \frac{\alpha_{loc}}{z}, \tag{5.17}$$

is the *local growth exponent*. An example of this behavior is plotted in Fig. 5.3. It is interesting to mention here that the scaling function for the local width can also be expressed as:

$$w(\ell, t) = \ell^{\alpha_{\rm loc}} g'(\ell / t^{1/z}), \tag{5.18}$$

with the scaling function

$$g'(u) \sim \begin{cases} u^{-(\alpha - \alpha_{loc})} & \text{if} \quad u \ll 1 \\ u^{-\alpha} & \text{if} \quad u \gg 1. \end{cases} \tag{5.19}$$

After saturation times, $t > L^z$, the local interface width scales as $w(\ell) \sim \ell^{\alpha_{\rm loc}}$ with a different exponent than the global width $W(L) \sim L^\alpha$.

Finally, it is important to remark that in order to characterize the anomalous scaling, we need three independent scaling exponents (α, z, $\beta = \alpha/z$, $\alpha_{\rm loc}$, $\beta^* = \beta - \alpha_{\rm loc}/z$). In addition, depending on the spectral roughness exponent α_s, different types of scaling arise when the integral of Eq. (5.13) is carried out [67,123]. The following scheme [123] summarizes all of them:

$$\begin{cases} \text{if} \quad \alpha_s < 1 \;\Rightarrow\; \alpha_{\rm loc} = \alpha_s \quad \begin{cases} \alpha_s = \alpha \;\Rightarrow\; \text{Family-Vicsek scaling} \\ \alpha_s \neq \alpha \;\Rightarrow\; \text{Intrinsic anomalous scaling} \end{cases} \\ \text{if} \quad \alpha_s > 1 \;\Rightarrow\; \alpha_{\rm loc} = 1 \quad \begin{cases} \alpha_s = \alpha \;\Rightarrow\; \text{Superroughening} \\ \alpha_s \neq \alpha \;\Rightarrow\; \text{Faceted surfaces} \end{cases} \end{cases}$$

The important point is that all the possible scalings are now described by the general anomalous scaling ansatz, Eq. (19.12). For instance, the Family-Vicsek scaling is recovered whenever $\alpha = \alpha_{\rm loc} = \alpha_s < 1$. In the following, each case of anomalous scaling will be discussed separately.

Intrinsic anomalous scaling.- For $\alpha_s < 1$ it is always accomplished that $\alpha_{loc} = \alpha_s$. Then, the intrinsic anomalous scaling appears if $\alpha \neq \alpha_{loc}$. If we replace

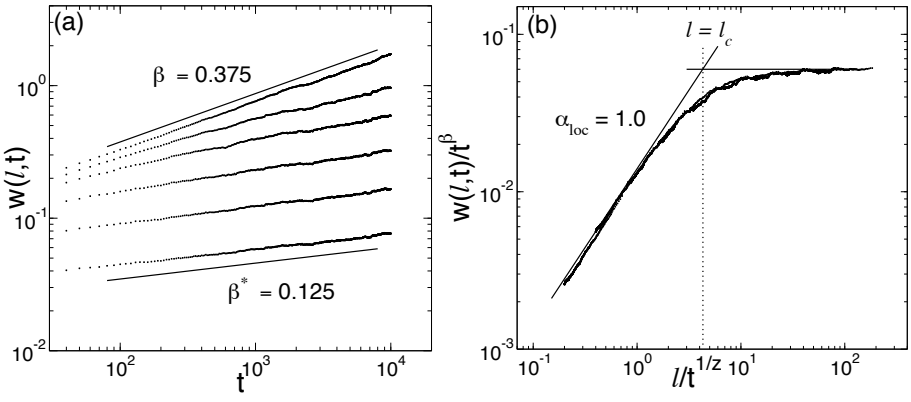

Fig. 5.3 Numerical resolution of the MBE equation in a system of size $L = 512$ showing a superroughening scaling. (a) Local interface width as function of time calculated at different lateral lengths, from $\ell = L/256$ up to $\ell = L$ (bottom to top). Due to the presence of the anomalous scaling ($\alpha_{\rm loc} \neq \alpha$), the local scales grow with the local growth exponent t^{β^*} and saturate at $t \sim L^z$. We obtain the exponents $\beta = 0.375(8)$ and $\beta^* = 0.125(6)$ from the data fit, in perfect agreement with the theoretical prediction, Eq. (5.23). (b) Data collapse of the local width $w(\ell, t)$ rescaled by t^{β}, using $\beta = 0.375$ and $z = 4$. According to Eq. (5.15), the scaling function $g(u)$ has the asymptotes $g(u) \sim u^{\alpha_{\rm loc}}$ for $u \ll 1$ and $g(u) \sim$ const for $u \gg 1$, giving a local roughness exponent $\alpha_{\rm loc} = 1.0(2)$ in agreement with the superroughening scaling. The inflexion point is given by taking $\ell = \ell_c$.

these conditions at the power spectrum function, we obtain that

$$\mathcal{S}(k,t) \sim \begin{cases} t^{2\theta} k^{-(2\alpha_{\rm loc}+d)} & \text{if} \quad k \gg k_c \\ t^{\frac{2\alpha+d}{z}} & \text{if} \quad k \ll k_c. \end{cases} \tag{5.20}$$

where $\theta = (\alpha - \alpha_{\rm loc})/z$. We can see that the power spectrum is characterized by showing up a temporal shift related to θ for $k \gg k_c$. Also, it is important to mention that the global roughness exponent α cannot be obtained directly from the power spectrum as occur for instance in the Family-Vicesk scaling. Then, it is usually required to calculate the local interface width and plot either the scaling function $g(u)$ [cf. Eq. (5.15)] or $g'(u)$ [cf. Eq. (5.19)] by means of a data collapse [see Fig. 5.3(b)]. As it will be shown in this thesis, this kind of scaling has been observed in imbibition fronts [116, 117, 135, 138].

Superroughness.- The global roughness exponent is now higher than one, and we have that $\alpha = \alpha_s > 1$. In addition the local roughness exponent is $\alpha_{\rm loc} = 1$. In this case, the power spectrum looks like

$$\mathcal{S}(k,t) \sim \begin{cases} k^{-(2\alpha+d)} & \text{if} \quad k \gg k_c \\ t^{\frac{2\alpha+d}{z}} & \text{if} \quad k \ll k_c. \end{cases} \tag{5.21}$$

Examples of this scaling are found in the quenched Edwards-Wilkinson model [89, 143] [see Eq. (4.3) in Ch. 4], imbibition fronts [45, 112] (see also the next parts of this thesis), and in the Molecular Beam Epitaxial (MBE) lineal model [5, 79, 150]. The latter example is interesting because can be easily solved numerically and analytically. The model is given by the following equation:

$$\frac{\partial h}{\partial t} = -\nabla^4 h + \xi(x,t), \tag{5.22}$$

where $\xi(x,t)$ is the same kind of noise as in the EW model. As before, the scaling exponents can be analytically calculated by imposing the above equation to be scale-invariant under the scaling transformation $x \to bx$, $t \to b^z t$, and $h \to b^\alpha h$, obtaining:

$$z = 4, \qquad \alpha = \frac{4-d}{2}, \qquad \beta = \frac{4-d}{8}, \tag{5.23}$$

in $d+1$ dimensions. Numerical integrations of Eq. (5.22) in $d = 1$ fully agree with these predictions (see Fig. 5.3).

Faceted surfaces.- This scaling appears when $\alpha_s > 1$ and $\alpha_s \neq \alpha$. In this case we also have that $\alpha_{\rm loc} = 1$, and the power spectrum reads as

$$\mathcal{S}(k,t) \sim \begin{cases} t^{\frac{2(\alpha-\alpha_s)}{z}} k^{-(2\alpha_s+d)} & \text{if} \quad k \gg k_c \\ t^{\frac{2\alpha+d}{z}} & \text{if} \quad k \ll k_c. \end{cases} \tag{5.24}$$

As in the case of intrinsic anomalous scaling, the power spectrum is affected by a temporal shift. Examples of interfaces showing this scaling are found, for instance, in the Kardar-Parisi-Zhang equation [70] with static columnar disorder $\eta(x)$ [141], and in experiments of electrodissolution of pure polycrystaline iron [32].

5.3 The crossover length in imbibition fronts

An important point which needs to be discussed here is concerning a particular aspect of the scaling of imbibition fronts. In particular, the presence of the crossover length $\ell_\times \sim 1/\sqrt{v}$ [cf. Eq. (4.25)] in the dynamic interface equation, has revealed during the last years as a crucial point in the kinetic roughening process [2]. More precisely, several numerical studies [2, 42, 45, 46, 84] have shown that the correlations of the interface are cut off by this crossover length. This basically means that the system reaches the steady state when the correla-

tion length catches up the crossover length, $\ell_c \sim \ell_\times$, defining a new saturation time as $t_\times \sim \ell_\times^z$. This point will be largely observed through out this thesis.

Part II Scaling growth in non-local and local models of surface roughening

6
Introduction

This second Part of the thesis is concerned about the study of the scaling properties in the non-local model for imbibition fronts, given by Eq. (4.22) in Ch. 4, and in local models of general surface growth with time-dependent coupling constants. Our main motivation is to study from a theoretical point of view some experimental work carried out by Soriano *et al.* [134], where the imbibition fronts are described in terms of the scaling theory explained in Ch. 5. It is shown that the interface fluctuations present a rich variety of scaling scenarios ranging from the Family-Vicsek to the anomalous scaling. By making use of the numerical phase field model described in Ch. 4, we present numerical results, accompanied by analytical work, describing the interface fluctuations in different contexts of imbibition.

Chapters 7 and 8 present a theoretical and experimental study, respectively, about the scaling properties of spontaneous imbibition fronts. Both studies are motivated by the disagreement observed between the experimental work by Soriano *et al.* [135] and the numerical work by Dubé *et al.* [45].

On the other hand, motivated by the interesting experimental results of Ref. [138], where is reported imbibition fronts in columnar geometries whose fluctuations are described by a phenomenological local model, we perform in Chapter 9, an analytical and numerical study of forced-flow and spontaneous imbibition in columnar geometries.

In Chapter 10 we present a study concerning the two different models that have been used during the last years to describe imbibition fronts. They are the one-sided model used as the first time by Hernández-Machado *et al.* [64] and the symmetric model used by Dubé *et al.* [45]. We focus on studying the effect of the disorder strength in these two models, and how the scaling properties of driven interfaces are modified.

Finally, one can easily observe from the results presented in all of these Chapters, that fluctuations of imbibition fronts are largely affected by the presence of crossover effects. In particular, in the case of spontaneous imbibition there is a time-dependent crossover length $\ell_\times(t)$ (see Ch. 4) that is responsible for the rich scaling behavior observed both experimentally and numerically.

Therefore, motivated by these phenomena, we present in Chapter 11 a general study of time-dependent crossover lengths in local models of surface growth.

7
Anomalous scaling in spontaneous imbibition

This Chapter deals with the morphology and scaling properties of the interface fluctuations observed in the spontaneous imbibition process of a viscous liquid invading a disordered medium. In particular, we study how different scaling scenarios emerge depending on several physical parameters, such as mean interface velocity or disorder strength. Let us recall that spontaneous imbibition occurs when a viscous liquid advances into the medium due to the capillarity (see Ch. 4). Then, as a consequence of liquid mass conservation, the mean interface position $H(t)$ grows asymptotically in time following the Washburn's law

$$H(t) = \sqrt{H_0^2 + 2at}, \tag{7.1}$$

where H_0 is the initial height of the liquid and a is a parameter that depends on the mean permeability of the medium K_0, the viscosity of the liquid η, the applied pressure at the origin p_a, and the mean capillary pressure at the interface $\langle \xi \rangle$. For long enough times, the above equation reduces to $H(t) \sim t^{1/2}$. On the other hand, we learned in Chapter 4 that for low enough velocities, the dynamics of the interface fluctuations is described by a linearized non-local equation that in Fourier space reads as

$$\partial_t \hat{h}_k = -\sigma \overline{K}_0 |k| k^2 \hat{h}_k - \dot{H}|k|\hat{h}_k + \overline{K}_0 |k| \hat{\xi}_k. \tag{7.2}$$

where $\widehat{\xi}_k$ are the Fourier components of the capillary disorder, σ the surface tension, and $\overline{K}_0 = K_0/\eta$. The relevant fact observed from the above equation is that fluctuations due to random capillarity are damped by two different mechanisms. While at small scales the surface tension controls the fluctuations with a dynamic exponent $z = 3$, the long scales are damped by the advancement of the front $\dot{H}(t)$. These two effects are separated by the crossover length:

$$\ell_\times = 2\pi \Big[\frac{\sigma \overline{K}_0}{\dot{H}(t)} \Big]^{1/2}. \tag{7.3}$$

The important point in spontaneous imbibition is that since the mean velocity is decreasing on time, $\dot{H}(t) \sim t^{-1/2}$, the above crossover length grows on time

as $\ell_\times \sim t^{1/4}$. This time-dependence becomes really crucial in spontaneous imbibition and there was actually an interesting debate regarding the role of the dynamic crossover length in the scaling observed in both simulations and experiments of imbibition [1].

7.1 Experimental and theoretical motivation

Our study is based mainly on the experimental work made by Soriano *et al.* [135], where an oil-air interface advances in a horizontal Hele–Shaw cell with a random gap spacing between both glass plates (see Ch. 4 for a detailed description of the cell). The gap thickness is $b = 0.46$ mm and gap fluctuations are provided by copper square obstacles of $d = 0.06$ mm high, that are randomly distributed over a fiberglass substrate filling the 35% of the total area. Traction due to capillarity is so strong that a negative pressure difference must be applied at the inlet of the cell. This experimental setup produces then very slow fronts that on average advance following the Washburn's law. The main result of this experimental work is that the interface fluctuations are described within the intrinsic anomalous scaling framework, with the scaling exponents $z = 3$, $\alpha \simeq 2$ and $\alpha_{\rm loc} \simeq 1$. The dynamical exponent $z = 3$ is consistent with the linear non-local model of Eq. (7.2), and indicates that the roughening process is mainly dominated by capillarity and surface tension terms.

In contrast, a previous numerical study of spontaneous imbibition carried out by Dubé *et al* [45], employing a phase field model (see Ch. 4), predicted the scaling exponents $z = 4$, $\alpha = 1.25$ and $\alpha_{\rm loc} \simeq 1$ within the superrough anomalous scaling. There is therefore a clear disagreement between previous numeric data and experiments. The main claim in the numerical work is that the crossover length of Eq. (7.3) acts as a *cut off* length, limiting then the growth of the interface correlations. This fact has also been observed in other numerical works of imbibition [2, 84], and the main reason is because the interface is always asymptotically flat on length scales larger than $\ell_\times$. The correlation growth follows then the growth of the crossover length, $\ell_\times \sim t^{1/4}$, giving rise to an *effective* dynamical exponent $z = 4$.

Therefore, while the difference on the dynamical exponent z observed numerically and experimentally can be explained in terms of a competition between the crossover length $\ell_\times(t)$ and the intrinsic correlation length of the problem $\ell_c(t)$, it is not clear under which conditions the imbibition fronts are expected to follow an intrinsic anomalous scaling or superroughening.

1) A general discussion about the role of having dynamic crossover lengths in general equations of surface growth is given in Chapter 11.

The purpose of this Chapter is then the following and the results reported here have been published in Ref. [116]. By using the phase field model we present a deeper numerical study of spontaneous imbibition fronts, accompanied with analytical results, in order to see under which conditions the numerical model can indeed reproduce both the intrinsic anomalous scaling and the dynamical exponent $z = 3$ observed in the experimental results. It is also desirable to understand the physical mechanisms that control the scaling type of the interface fluctuations.

7.2 Numerical method

The numerical study of spontaneous imbibition is made by means of the phase field method described in Chapter 4. The phase field equation

$$\frac{\partial \phi}{\partial t} = \nabla M \nabla \big[-\phi + \phi^3 - \epsilon^2 \nabla^2 \phi - \xi(r) \big], \tag{7.4}$$

is integrated in a rectangular lattice of $\Delta x = 1$ grid space, with periodic boundary conditions in the x direction. We have also considered smaller grid spaces up to $\Delta x = 0.5$ obtaining identical results. In order to ensure numerical convergence, we use a time step of $\Delta t = 0.01$ and the parameter $\epsilon = 1$. The interface position $h(x,t)$ is approached by a linear interpolation of the zero of the phase field, $\phi[x, h(x,t); t] = 0$. Here, we are using the so-called *one-sided* model, where the mobility is taken as $M = 1$ in the liquid phase ($\phi > 0$) and $M = 0$ in the air phase ($\phi < 0$) [2].

The quenched disorder $\xi(r)$ is taken as a dichotomic noise distributed in a two-dimensional system with the values:

$$\xi = \begin{cases} \xi_0 \\ \\ \frac{\xi_0}{1-\xi_A} \end{cases}, \tag{7.5}$$

and it is imposed in the same way as that in the experimental work of Ref. [135], in the sense that the sites with ξ_0 are randomly distributed filling 65% of the whole system. Even though in such experiments capillarity arises as a three-dimensional effect, we can relate our disorder parameters with Hele-Shaw gap spacing b (see Fig. 4.1 in Ch. 4) as

$$\xi_0 \sim 1/b \quad \text{and} \quad \xi_A \sim d/b, \tag{7.6}$$

2) A detailed comparison between this model and the *symmetric* one, where M is constant throughout the whole system, is given in Ch. 10.

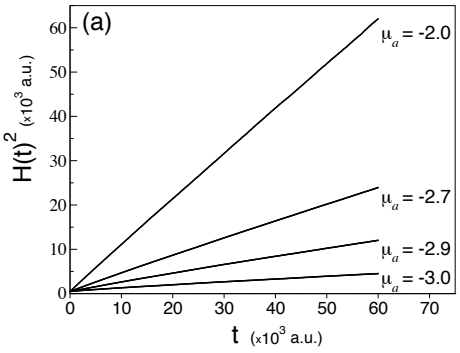

Fig. 7.1 Squared averaged interface height position, as function of time, follows Washburn law for different applied pressures μ_a.

so the ξ_A parameter controls the contrast between both noise values whereas the ξ_0 corresponds to the capillarity of the cell with a fixed gap.

It is important to mention that our numerical results are only focused on the case where capillarity is the dominant disorder and therefore, the permeability disorder is not taken into account in this phase field model. As it is explained in Chapter 4, this is a reasonable assumption as long as the typical velocity of the interface is low enough. However, as it will be shown in next Chapter, experiments carried out in a regime of very high velocities present interface fluctuations dominated by the permeability disorder, and then it would be necessary to introduce some kind of noise in the mobility parameter M of the phase field model, as it is done for example in [64, 85].

In order to reproduce spontaneous imbibition fronts, the chemical potential at the origin of the system is fixed to a constant value, $\mu(x, y = 0) = \mu_a$. It is worth to recall that the chemical potential in the phase field model plays the role of the macroscopic pressure. For this reason, the value μ_a will be called applied pressure throughout this Chapter. In all of our numerical integrations we will suppose an initial height $H_0 = 20$ to get a low initial velocity and the noise value $\xi_0 = 3.0$. All the results were averaged over 30 realizations. Our study is focused to obtain the different scaling exponents and its dependence on both the applied pressure μ_a and the contrast between noise values, ξ_A.

7.3 Variation in the applied pressure

Different applied pressures at the origin have been studied. In all of them the Washburn law, Eq. (7.1), is well accomplished as we can see from Fig. 7.1. As a first case to analyze, we choose the numerical parameters $\xi_A = 0.3$ and

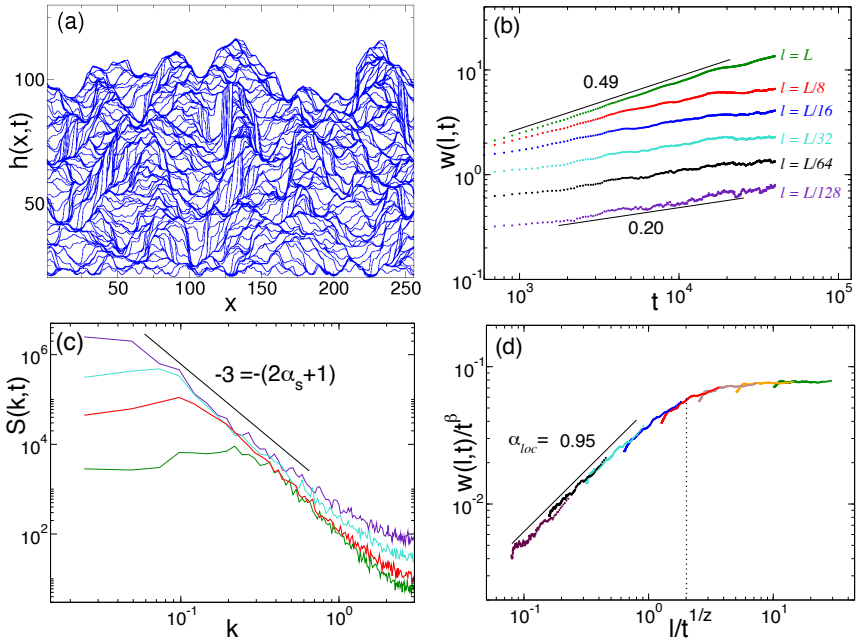

Fig. 7.2 Numerical results for spontaneous imbibition fronts at very low velocities ($\mu_a = -3.0$ and $\xi_A = 3.0$). (a) Temporal evolution of the interface at equal time intervals. (b) Log-log plot of the interfacial width as function of time in different windows sizes ℓ. The data fit shows a growth exponent $\beta = 0.49 \pm 0.03$ and the local one $\beta^* = 0.20 \pm 0.04$. (c) Power spectra of the interface $h(x,t)$ at different times. It shows that $\alpha_s = 1.0 \pm 0.1$. (d) Collapse of the interface local width function, $w(\ell,t)$, which is scaled by t^{β} versus $\ell/t^{\beta/\alpha}$, where $\alpha = 1.50 \pm 0.02$, and then $z = 3.0 \pm 0.1$ follows from $z = \alpha/\beta$. The picture also shows a local roughness exponent $\alpha_{\rm loc} = 0.95 \pm 0.03$.

$\mu_a = -3.0$. In Fig. 7.2(a) there is plotted the temporal evolution of the interface. Note that the applied pressure has the same value in module as the noise value ξ_0 and thus there are grid sites where the interface may rest locally pinned for a long time. In this situation, the interface has a slow motion and advances in avalanches [3]. Using the scaling concepts described in Ch. 5, we do a statistical description of the interface fluctuations, shown in Fig. 7.2. From the interface local width we obtain the global growth exponent $\beta = 0.49 \pm 0.03$ and the local one $\beta^* = 0.20 \pm 0.04$, clearly different from 0, indicating the existence of anomalous scaling. On the other hand, from the interface power spectrum we obtain the spectral roughness exponent $\alpha_s = 1.0 \pm 0.1$. The temporal shift observed in the power spectrum indicates that $\alpha > \alpha_s$ and since α_s is not greater than 1, the relation $\alpha_{\rm loc} = \alpha_s$ should be accomplished [123]. Therefore, the global roughness exponent α can not be achieved directly from the power

3) A characterization of the avalanche dynamics of imbibition fronts close to the pinning point is given in the next Part.

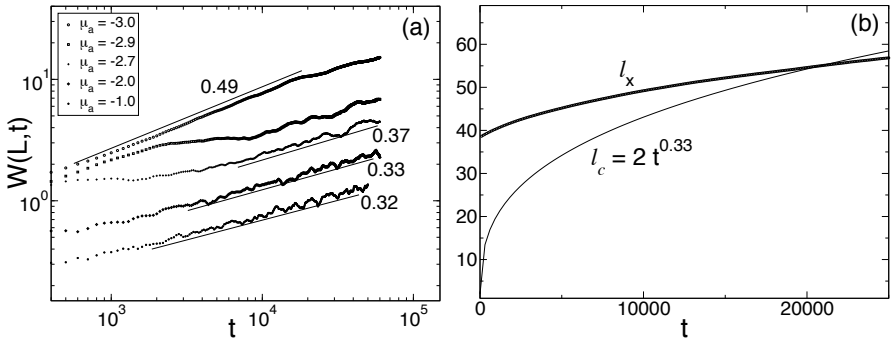

Fig. 7.3 (a) Global interface width $W(L,t)$ as function of time calculated at different applied pressure, $\mu_a = -3.0,\ -2.9,\ -2.7,\ -2.0,\ -1.0$ from top to bottom. The lines show a fit data corresponding to the growth exponent β. (b) Estimation of the crossover and correlation length when the dynamic exponent $z = 3$ is observed.

spectrum but it has to be obtained by means of a collapse of the interface local width function, Eq. (5.14) in Ch. 5 . The result of the best collapse is shown in Fig. 7.2(d) from which we obtain that $\alpha = 1.50 \pm 0.02$ and $z = 3.0 \pm 0.1$. This plot also shows a local roughness exponent of $\alpha_{\rm loc} = 0.95 \pm 0.03$, which is very close to the value of the roughness exponent, α_s. These sets of scaling exponents are compatible within the intrinsic anomalous scaling scenario, and they are clearly different from those obtained in Ref. [45].

Let us now increase the interface velocity by changing up the applied pressure, μ_a. Following the same statistical procedure as before, we compute the whole set of scaling exponents for different values of $\mu_a > -3.0$. Figure 7.3(a) shows the global width $W(L,t)$ in each case. We observe there a crossover from $\beta \simeq 0.5$ ($\mu_a = -3.0$) to $\beta \simeq 0.37$ ($\mu_a = -2.7$). In the specific case of $\mu_a = -2.7$, we obtain the different scaling exponents $\alpha = 1.5 \pm 0.02$, $z = 4.0 \pm 0.1$, $\beta = 0.37 \pm 0.03$, and $\alpha_{\rm loc} = 0.95 \pm 0.03$ (cf. Fig. 7.4). Finally, the results obtained in Ref. [45], $\alpha = 1.25$, $z = 4$, $\beta \simeq 0.32$ and $\alpha_{\rm loc} \simeq 1$, are recovered when we increase the applied pressure up to $\mu_a = -1.0$.

So it is important to remark that decreasing the applied pressure produces three important effects:

- The roughness exponent α changes from 1.25 to 1.5.
- The interface local growth change from a super-rough to an intrinsic anomalous scaling description.
- The dynamic exponent $z = 3$ obtained in experimental work is attained when the interface advances at low velocities.

In Table 7.1 we can see the different scaling exponents computed for different values of μ_a. The meaning of large and low velocities has to be understood as

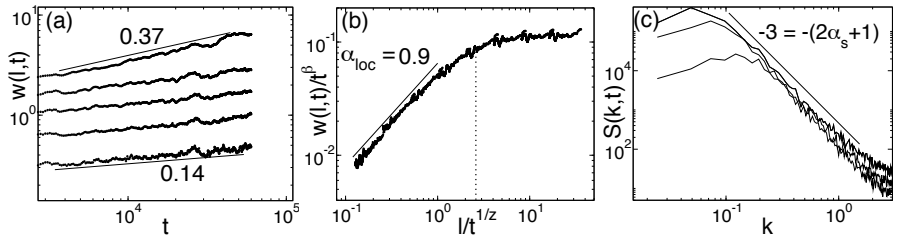

Fig. 7.4 Statistical description of interfaces when $\mu_a = -2.7$ and $\xi_A = 3.0$: (a) Log-log plot of the interfacial width as function of time in different windows sizes, $\ell = L,\ L/16,\ L/32,\ L/64,\ L/128$ from top to bottom. The data fit shows a growth exponent $\beta = 0.37 \pm 0.03$ and the local one $\beta^* = 0.14 \pm 0.04$. (b) Collapse of the interface local width function, $w(\ell, t)$, which is scaled by t^β versus $\ell/t^{\beta/\alpha}$, where $\alpha = 1.50 \pm 0.02$, and then $z = 4.0 \pm 0.1$ follows from $z = \alpha/\beta$. The picture also shows a local roughness exponent $\alpha_{\rm loc} = 0.95 \pm 0.03$. (c) Power spectra of the interface $h(x, t)$ at different times. It shows that $\alpha_s = 1.0 \pm 0.1$.

μ_a	α	z	β	β^*	α_s	Scaling
-1.0	1.25	4	0.32	0.10	1.25	SR
-2.0	1.34	4	0.33	0.12	0.9	IA
-2.7	1.5	4	0.37	0.14	0.9	IA
-3.0	1.5	3	0.49	0.20	0.9	IA

Tab. 7.1: Scaling exponents obtained when the applied pressure μ_a decreases. The contrast of the noise values is kept constant $\xi_A = 0.3$. SR and IA refer to superroughening and intrinsic anomalous scaling, respectively.

follows. The interface advances at low velocity when the pinning effects become important and the crossover length is large enough to observe an initial regime described by $z = 3$. Therefore, in this sense, we call low velocities the cases of $\mu_a < -2.0$ and large velocities the other ones, $\mu_a \geq -2.0$. Concerning the low velocities regime, there is some numerical inaccuracy in the determination of the interface position due to the slow advance of the interface. In order to check our numerical results, we have performed the case of $\mu_a = -3.0$ with a smaller grid space. We have used a $\Delta x = 0.5$ and no difference between the case of $\Delta x = 1.0$ has been observed.

The crossover and correlation length

So far we have seen that an initial regime, dominated by the surface tension term of Eq. (7.2), can be observed if the interface velocity is low enough. The point is that the correlation length $\ell_c = A \cdot t^{1/z}$ is smaller than the crossover length $\ell_\times$ during the time interval studied. In order to check it, we are interested in estimating the crossover and correlation length.

First, we suppose that in the case of $\mu_a = -2.7$, in the regime of $z = 4$, the crossover length, $\ell_\times = A \cdot t^{1/4}$, acts effectively as the correlation length as Dubé *et al.* have pointed out [45]. Then, the constant A can be approached from the inflection point of the width collapse, in Fig. 7.4(b), being $A \simeq 2.5$. Recall that the inflection point in the scaling function $s(u)$ of the data collapse corresponds to $u = \ell_c/t^{1/4} = A$, since we are assuming $\ell_c = \ell_\times$. On the other hand, we know that the crossover length has the expression

$$\ell_\times = C\Big(\frac{2}{a}\Big)^{1/4} \cdot t^{1/4}, \tag{7.7}$$

obtained from Eq. (7.3) in the limit $H_0^2 < 2at$, where a follows from Washburn law, Eq. (7.1), and can be obtained from the data fit in Fig. 7.1. With these two expression we can obtain the constant $C = (a/2)^{1/4}A \simeq 1.4$, which allows us to estimate the crossover length in its full expression, Eq. (7.3), when $\mu_a = -3.0$. In such case the correlation length grows up as $\ell_c = 2 \cdot t^{1/3}$, where now the parameter 2 has been obtained from the width collapse in Fig. 7.2(c). These results are depicted in Fig. 7.3(b), where we can observe that during the studied time interval, the condition $\ell_\times > \ell_c$ is accomplished, and thus the obtained dynamical exponent $z = 3$ is fully justified.

It should be noted from the equation for the mean interface growth $H(t) = \sqrt{H_0^2 + 2at}$, that the crossover length takes a certain time $\tau = H_0^2/2a$ to reach its asymptotic form $\ell_\times \simeq t^{1/4}$. This could produce some effect on the interface scaling as long as $t_\times \leq \tau$, where $t_\times$ is defined as the time when $\ell_c = \ell_\times$. As we can see in Fig. 7.3(a), in both cases of $\mu_a = -2.9$ and $\mu_a = -2.7$, there is a regime, during the transition from $z = 3$ to $z = 4$, where the interface global width does not increase. Therefore, by computing the parameter a from a fit of the Washburn law, we observe that the typical time $\tau \sim 2 \cdot 10^3$ and 10^3 for $\mu_a = -2.9$ and -2.7, respectively, indicating that $\tau \sim t_\times$ in both cases. For larger values of the applied pressure this effect occurs in an initial stage of the interface growth and it is not observed.

An interesting point to comment on from these numerical results is that the roughness exponent α does not change its value when the correlation length catches up the crossover length, that is, the growth exponent β varies accordingly with the change of the dynamic exponent from $z = 3$ to $z = 4$ keeping constant the α value [see Fig. 7.3(a)]. Therefore, it lead us to think that *the crossover length does not change the scaling properties of the interface except for the dynamic exponent* z. This fact can be very useful to extract information from the linear Eq. (7.2). Since the initial interface velocity has a finite value greater than zero, the condition $t_\times > 0$ is always accomplished and therefore there will be always an initial regime where fluctuations are dominated by the surface tension. Note that this initial regime could be very short for a high initial

velocity of the interface. Hence we can suppose that the scaling exponents α and $\alpha_{\rm loc}$, observed when the crossover length is controlling the fluctuations growth, are the same as those corresponding to the initial regime described by $z = 3$.

Intrinsic anomalous scaling in the low velocity regime

Our numerical results have shown the influence of the applied pressure on the scaling exponents. We have seen that the intrinsic anomalous scaling appears as the applied pressure is decreased. This can be understood in terms of the large local slopes observed when the interface velocity is decreased. Indeed, as it was pointed out by López [92], the origin of the anomalous scaling can be found in the non-trivial behavior of the interface local slopes.

Our purpose now is to derive analytically the interface scaling exponents observed in the case of low velocities. First, note that in this limit, the relevant terms of Eq. (7.2) are surface tension and capillarity. Then, assuming a columnar disorder $\xi(x)$ with correlations $\langle \xi(x)\xi(x')\rangle \simeq \delta(x - x')$, and rescaling the linear equation by the scaling transformation,

$$x \to bx \quad h \to b^{\alpha} h \quad t \to b^{z} t, \tag{7.8}$$

scale-invariance holds for the scaling exponents $\alpha = 1.5$, $z = 3$ and $\beta = 0.5$, which correspond to those observed numerically in the low velocities regime. Therefore, we can conclude that the interface feels an effective white columnar noise as the applied pressure is decreased. The roughness exponent $\alpha = 1.5$ is the same value obtained in the local quenched Edward-Wilkinson (QEW) model with columnar noise [93], and as it is shown in Ch. 9, numerical integrations of the phase field model with columnar disorder also give the same exponent. It should be pointed out that the assumption of columnar noise has to do with the number of sites where the interface is pinned; note that the fractions of the interface which are locally pinned increases as the applied pressure is decreased up to values lower than $\mu_a < -3.0$ where the interface does not advance at all. So in this sense, the roughness exponent $\alpha = 1.5$ is observed when the interface advances near a critical situation of pinning, which seems to indicate that the depinning transition in imbibition is not dominated by the non-linear terms coming from the quenched disorder $\xi(x, h)$. As it is shown in Ch. 14 of Part III, the same roughness exponent is also observed in slow forced-flow imbibition, close to the pinning point, $\overline{v} \to 0$.

On the other hand, when the applied pressure is increased and therefore we move further away from the critical situation we recover the results of $\alpha = 1.25$ corresponding to the value obtained in the local QEW model with quenched noise $\xi(x, h)$ [2, 89]. Therefore, the other observed roughness exponent $\alpha \simeq$

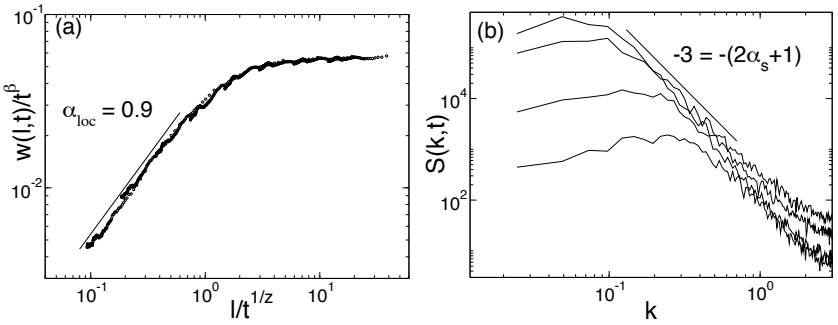

Fig. 7.5 Statistical description of interfaces described by Eq. (7.4) with a gaussian noise distributed at the 100% of the system with mean $\langle \xi \rangle = 3.0$ and strength $\Delta\xi = 0.6$. The applied pressure is $\mu_a = -2.5$. (a) Collapse of the interface local width function, $w(\ell, t)$, which is scaled by t^β versus $\ell / t^{\beta/\alpha}$, where $\alpha = 1.51 \pm 0.02$, $\beta = 0.51 \pm 0.03$ and then $z = 3.0 \pm 0.1$ follows from $z = \alpha/\beta$. The picture also shows a local roughness exponent $\alpha_{\rm loc} = 0.9 \pm 0.03$. (b) Power spectra of the interface $h(x, t)$ at different times. It shows that $\alpha_s = 1.0 \pm 0.1$.

1.34 can be understood as an intermediate regime between the value $\alpha = 1.25$ and $\alpha = 1.5$ when the applied pressure is decreased. Likewise, in the next section we will discuss an analytical approach which describes the quenched noise scaling in the high velocity regime, where the values $\alpha = 1.25$ and $\alpha = 1.33$ are also observed.

In order to check the validity of this numerical results, we have also performed the simulations with another kind of noise. We have used a gaussian field distributed at the 100% of the system with mean $\langle \xi \rangle = 3.0$ and strength $\Delta\xi = 0.6$. When the applied pressure is $\mu_a = -2.5$, the interface advances at low velocities and we recover the same results of $\alpha = 1.5$ and $z = 3$ within the intrinsic anomalous scaling, Fig. 7.5. Therefore, the columnar noise assumption is also correct when we use a different noise distribution.

Comparing to the experimental results, our $\alpha = 1.5$ differs from the value $\alpha = 2.0$ obtained in Ref. [135]. However, the other independent exponents, $\alpha_{\rm loc}$ and z are in perfect agreement. Such a discrepancy in the α exponent could be attributed to a three dimensional effect that becomes relevant at very low velocities, which would not be taken into account in the numerical integration of the phase field; however, it remains as an open question.

7.4 Variation in the capillary contrast

Another interesting issue to study is what happens when we increase the contrast between the two values of the noise keeping constant the applied pressure. This has to be similar to increasing the strongness of the capillarity of the

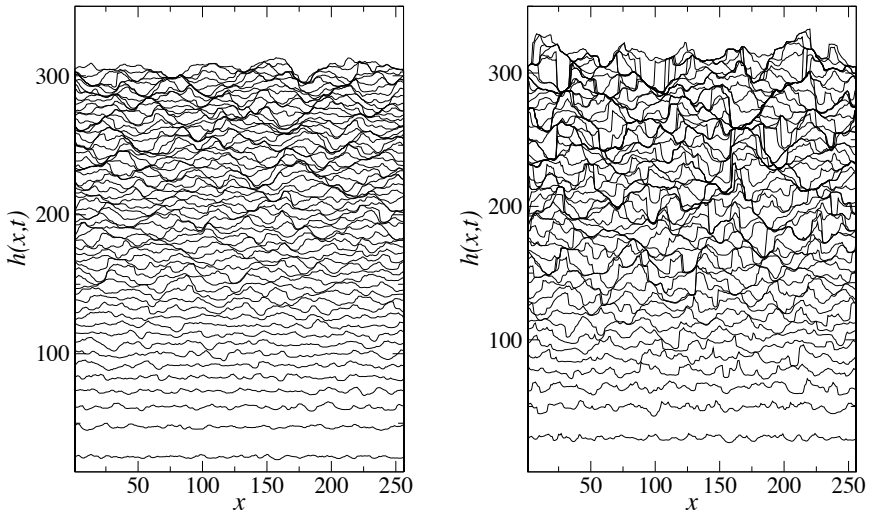

Fig. 7.6 Effect of increasing the contrast between the two values of the noise in the interface profile. The values used are: $\xi_A = 0.3$ (left) and $\xi_A = 0.5$ (right). The main difference is the switch from super-rough scaling to intrinsic anomalous one.

Hele-Shaw cell by decreasing the gap spacing, as it was experimentally done in the work by Soriano *et al.* [137] in a columnar disorder setup. So in this sense, we are interested to study the change of the scaling exponents when we increase the parameter ξ_A. Our starting point is the known results of superrough interfaces with $\alpha = 1.25$ and $z = 4$ obtained in the case of $\mu_a = -1.0$ and $\xi_A = 0.3$. Fig. 7.6 shows two different interface profiles with two different capillary contrasts, $\xi_A = 0.3$ and $\xi_A = 0.5$ respectively, where we can observe the morphological difference between both interfaces. While in the former case the interfaces are characterized by a smooth profile, large local slopes appear when the capillary contrast is increased. Note that due to numerical limitations, the capillary contrast is not able to be too large. Actually, for values $\xi_A > 0.6$ we have observed that the interface becomes unstable and a clear statistical description of the interface fluctuations cannot be performed.

The different scaling exponents for the case of $\xi_A = 0.5$ are given in Fig. 7.7 obtaining: $\alpha = 1.33 \pm 0.03$, $z = 4.0 \pm 0.1$, $\beta = 0.33 \pm 0.03$, $\beta^* = 0.16 \pm 0.04$ and $\alpha_{\mathrm{loc}} = 0.70 \pm 0.03$, which are compatible within the intrinsic anomalous scaling framework. In Table 7.2 we can see how the scaling exponents change by varying the noise contrast. While the global exponents (α, β, z) are quite similar in both cases, the interface local behavior changes from a superrough to an intrinsic anomalous description.

If we perform the same analysis by using a Gaussian noise instead of a dichotomic noise, we obtain a similar variation in the local scaling properties

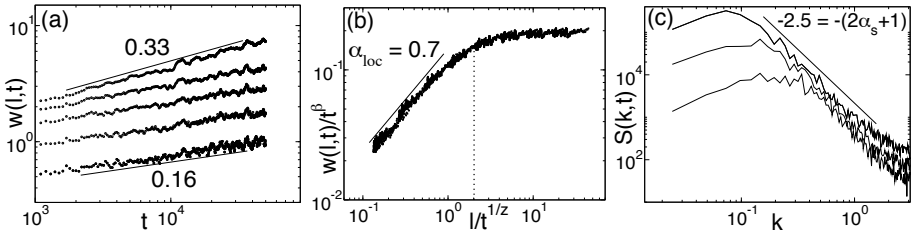

Fig. 7.7 Statistical description of the interface fluctuations with a high capillary contrast $\xi_A = 0.5$. (a) Lcal interface width as function of time in different windows sizes, $\ell = L,\ L/16,\ L/32,\ L/64,\ L/128$ from top to bottom. The data fit shows a growth exponent $\beta = 0.33 \pm 0.03$ and and the local one $\beta^* = 0.16 \pm 0.04$. (b) Collapse of the interface local width function, $w(\ell, t)$, which is scaled by t^β versus $\ell/t^{\beta/\alpha}$, where $\alpha = 1.33 \pm 0.03$, and then $z = 4.0 \pm 0.1$ follows from $z = \alpha/\beta$. The picture also shows a local roughness exponent $\alpha_{\rm loc} = 0.70 \pm 0.03$. (c) Power spectra of the interface $h(x, t)$ at different times. It shows that $\alpha_s = 0.75 \pm 0.05$.

of the interface fluctuations. It turns out that increasing the strength of the Gaussian noise, $\Delta\xi$, an intrinsic anomalous scaling of the interface fluctuations is observed. Therefore, there seems to be a relation between the capillary contrast of the dichotomic noise and the strength of the Gaussian field. Likewise, Laurila *et al.* [84] have observed a slightly dependence of the strength of Gaussian noise on the roughness exponent α in a similar way that our results of Table 7.2 when we change the capillary contrast of the dichotomic noise.

ξ_A	α	z	β	β^*	α_s	Scaling
0.3	1.25	4	0.32	0.10	1.25	SR
0.5	1.33	4	0.33	0.16	0.65	IA

Tab. 7.2: Scaling exponents for two different capillary contrast, ξ_A, with an applied pressure $\mu_a = -1.0$.

Scaling properties of the quenched noise

Our objective now is to try to determine *analytically* the global scaling exponents observed in each case of the studied capillary contrast. While the dynamic exponent z can be well understood from the different terms of the linear equation, Eq. (7.2), the roughness exponent α involves the knowledge of the scaling of the noise and this can be a more difficult task.

First, we assume the general form for the noise correlation

$$\langle \xi(x,h)\xi(x',h')\rangle \simeq f(x,x')g(h,h'). \tag{7.9}$$

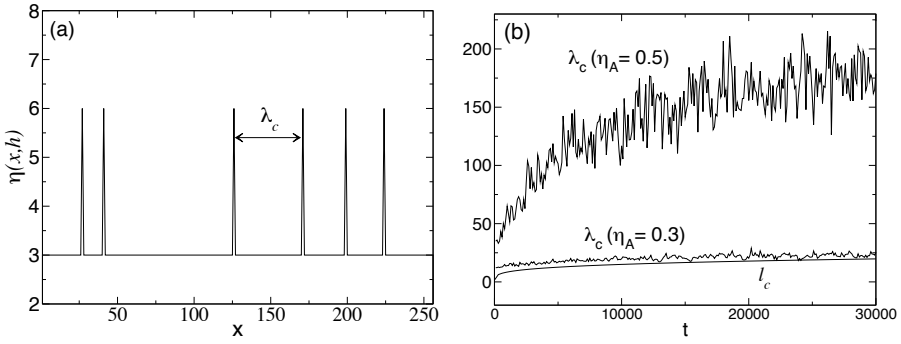

Fig. 7.8 (a) Dichotomic noise, $\xi(x,h)$, evaluated in a fixed interface $h(x,t_f)$ for each x in the case of the capillary contrast $\xi_A = 0.5$. λ_c represents an averaged length where the noise takes a constant value. (b) The length λ_c of the quenched noise is always greater than interface correlation length ℓ_c in both cases of $\xi_A = 0.3$ and 0.5.

In order to describe the scaling of the noise, we are interested in find out the expression for the functions $f(x,x')$ and $g(x,x')$. Consider first the case of $\xi_A = 0.5$ (Fig. 7.6). In this situation, an important feature of the interface velocity is that it has a great increase when the interface cross through the sites where the noise takes the largest value of Eq. (7.5). In some way, the interface seems to avoid these sites and it prefers to remain where the noise is lower, that is $\xi = \xi_0$. This leads to think about the existence of a lateral length λ_c below which the noise has a constant value. Since there is no imposed velocity but the interface moves only due to the capillarity of the media, this length $\lambda_c(t,\xi_A)$ is expected to increase with time and with the capillary contrast. An interpretation of λ_c can be seen in Fig. 7.8(a), where the values of the quenched noise $\xi(x,h)$ in a fixed interface $h(x,t_f)$ are plotted, being t_f an arbitrary chosen time. Note that λ_c has to be understood as an average length in such way that we can suppose the function $f(x,x') \simeq$ const for $|x-x'| < \lambda_c$ and $f(x,x') \simeq \delta(x-x')$ for $|x-x'| > \lambda_c$.

Since the only length scale characterizing the fluctuations growth in the x direction is the correlation length ℓ_c, two different scaling for the noise emerge depending if $\ell_c > \lambda_c$ or $\ell_c < \lambda_c$. In Fig. 7.8(b) there is plotted the length λ_c in the two cases of capillary contrast, $\xi_A = 0.3$ and $\xi_A = 0.5$, compared with the interface correlation length $\ell_c \simeq t^{1/4}$. We can see that in both cases $\lambda_c \gtrsim \ell_c$ and thus we can take the correlation of the noise along the x-direction as a constant.

Concerning the expression for the function $g(h,h')$, we will suppose the simplest case of $g(h,h') = \delta(h-h')$. However, note that two different kind of scaling are possible depending if the quenched noise is evaluated on the interface $\xi(x,h)$ or on the mean value of the interface, $\xi(x,h) \simeq \xi(x,H(t))$.

Therefore, we conclude that the quenched noise has to scale as

$$\xi(x,h) \rightarrow b^0 b^{-\frac{\alpha}{2}} \xi(x,h), \tag{7.10}$$

$$\xi(x,H) \rightarrow b^0 b^{-\frac{z}{4}} \xi(x,H), \tag{7.11}$$

when we rescale it by Eq. (7.8). The term with b^0 comes from the constant function $f(x,x')$. We have also assumed the Washburn law $H(t) \simeq t^{1/2}$.

It should be noted that these noise scalings are not valid when the interface movement is near a critical pinning situation (as in the previous section where $\mu_a \sim -3.0$) since in such a case there is an important number of sites where the interface is locally pinned and the effects of a columnar noise could become important.

Global scaling exponents

Once the scaling of the noise is derived, we can analytically compute the global scaling exponents for each case of capillary contrast, $\xi_A = 0.3$ and $\xi_A = 0.5$. We do a scaling analysis of the linear equation, Eq. (7.2), taking into account only the surface tension term. Imposing the noise scaling derived in Eq. (7.10), we obtain the exponent $\alpha = 1.33$, which is in accordance to the case of $\xi_A = 0.5$. On the other hand, if we suppose the noise scaling derived in Eq. (7.11), the exponent is then $\alpha = 1.25$, which adjusts the numerical value obtained in Ref. [45] and in our case of $\xi_A = 0.3$. Note that the exponent $\alpha = 1.33$ observed when $\xi_A = 0.5$ is the same than the value obtained in the Sec. 7.3, in the case of $\mu_a = -2.0$ (see Table 7.1), indicating that, in that case, the scaling of the noise has to follows also Eq. (7.10). Therefore, we analytically obtain the roughness exponents in the high velocity regime when we vary either the capillary contrast or the applied pressure.

Finally, since the crossover length controls the interface fluctuations in both cases, we conclude that the dynamic exponent has to be $z = 4$, and then we achieve the whole set of global scaling exponents described in Table 7.2.

7.5 Conclusions

This Chapter has presented analytical and numerical results of spontaneous imbibition using a phase field model. Our study has been focused on the dependence of the scaling exponents when we vary either the applied pressure imposed at the origin of the system or the capillary contrast of the dichotomic quenched noise.

By decreasing the applied pressure, we have got interfaces advancing at low velocities. In this situation of spontaneous imbibition, our results are in

good agreement with the experimental work made in Ref. [135]. Indeed, our numerical study confirms that there is a regime of low velocities where the growth of the interface fluctuations is controlled by the surface tension of the interface, following $\ell_c \simeq t^{1/3}$. We have also observed that the *cut off* crossover length, $\ell_\times$, acts as an effective correlation length when the initial interface velocity is higher, accordingly to the results of Dubé *et al.* [45].

On the other hand, our results show that the local scaling properties of the interface change as we decrease the applied pressure. More precisely, we obtain an intrinsic anomalous description at the regime of low velocities, where the interface is locally pinned. In addition, the roughness exponent we observe in such a situation is $\alpha = 1.5$ which is the same value obtained in the local QEW model with a columnar noise, $\xi(x)$.

It is also important to remark, however, that the intrinsic anomalous scaling is not related to the low velocity of the interface but to the capillary contrast of the noise. Indeed, when we increase the contrast between both noise values keeping constant the applied pressure, the local fluctuations description of the interface changes from a superrough to an intrinsic anomalous scaling, indicating the existence of a direct relation of the capillary contrast and the intrinsic anomalous scaling, which is something already observed experimentally [137] in the case of columnar geometries. In this sense, the presence of intrinsic anomalous scaling observed as the applied pressure is decreased can be related to the high contrast between the different forces acting on the interface, namely, the capillary pressure ξ and the opposite force due to the applied pressure μ_a. The dichotomic variation of the resulting force $\mu_a + \xi$ can be tunned as the applied pressure is modified and therefore change the local properties of the interface fluctuations.

Our numerical results have also found to be in agreement with analytical results obtained by assuming some scaling properties of the dichotomic quenched noise.

8
Pressure-dependent scaling scenarios in experiments of spontaneous imbibition

Following the theoretical analysis performed in the preceding Chapter, the purpose of this Chapter is to study if by changing some physical parameters on the experimental setup of Ref. [135], where spontaneous imbibition fronts were studied in a limit of very low velocities, the superrough anomalous scaling and the dynamical exponent $z = 4$ observed numerically can also be experimentally obtained. To this end, this Chapter presents experimental work carried out by Planet *et al.* [112] followed by a theoretical discussion.

8.1
Experimental results

Experimental setup.- The model porous medium used in this series of experiments is the same as in Ref. [135] (see Fig. 8.1). The pressure at the oil inlet is kept constant by using an oil container of selectable height H_c (measured with respect to the height of the air outlet). This fixes a pressure difference between the end of the cell and the liquid inlet as $\Delta p_a = \rho g H_c$. The used viscous liquid is a silicone oil (Rhodorsil 47 V) with kinematic viscosity $\nu = 50$ mm^2/s, density $\rho = 998$ kg/m^3, and oil–air surface tension $\sigma = 20.7$ mN/m at room temperature. Once the liquid gets into the model, the oil–air interface is recorded by two CCD cameras with an spatial resolution of 0.34 mm/pixel, and stored in a computer.

Spontaneous imbibition experiments were carried out at five different oil–column heights, H_c, corresponding to five different pressure differences. For each value of H_c four different disorder configurations were used and three runs for each configuration were performed.

By making use of the scaling theory of rough surfaces (see Ch. 5), each experiment has been analyzed in order to extract information about the statistical properties of the interface [112]. Table 8.1 and Fig. 8.2 present a summary of the complete set of scaling exponents for each case of applied pressure.

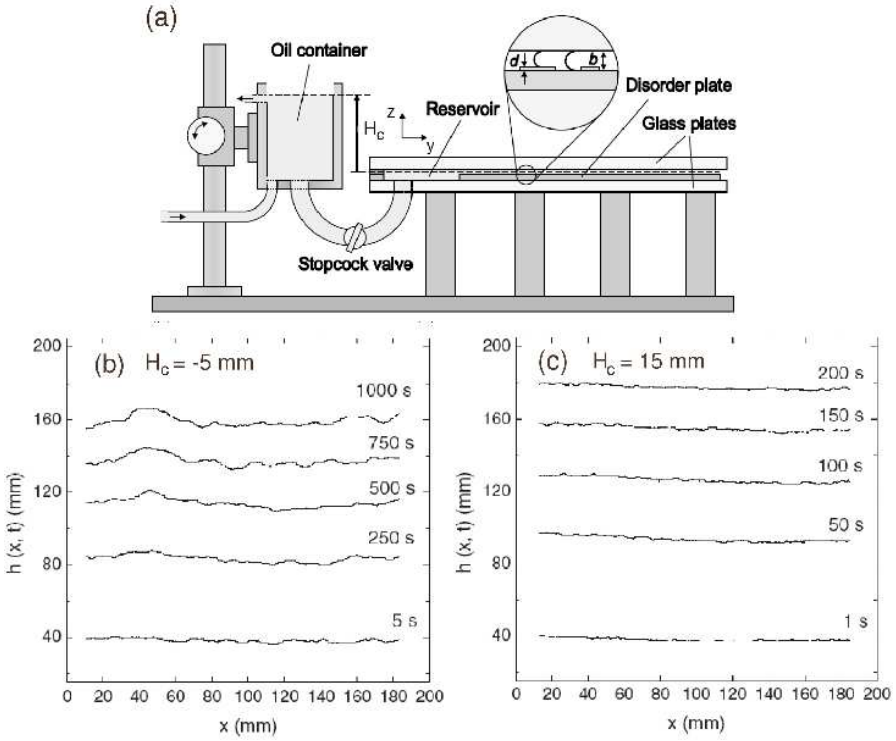

Fig. 8.1 (a) Experimental setup used to reproduce spontaneous imbibition fronts (Ref. [135]). Sequence of experimental interface profiles with an oil–column height $H_c = -5$ mm (b) and $H_c = 15$ mm (c), corresponding to a superrough scaling ($\alpha \simeq 1.25$) and a Family-Vicsek scaling ($\alpha \simeq 0.7$), respectively (Ref. [112]).

H_c (mm)	β	α	α_{loc}	β^*	z	Scaling
-9	0.64 ± 0.02	1.94 ± 0.20	0.94 ± 0.10	0.33 ± 0.03	3.0 ± 0.3	IA
-5	0.41 ± 0.02	1.25 ± 0.15	0.95 ± 0.30	0.10 ± 0.03	3.0 ± 0.4	SR
-4	0.42 ± 0.02	1.27 ± 0.15	0.97 ± 0.30	0.10 ± 0.03	3.0 ± 0.4	SR
10	0.34 ± 0.02	0.70 ± 0.15	0.64 ± 0.20	0.03 ± 0.02	2.1 ± 0.4	FV
15	0.36 ± 0.02	0.70 ± 0.15	0.59 ± 0.23	0.06 ± 0.03	1.9 ± 0.4	FV

Tab. 8.1: Summary of the experimental scaling exponents for each applied pressure difference $\Delta p_a = \rho g H_c$. IA refers to Intrinsic Anomalous scaling, SR to Superrough anomalous scaling and FV to Family-Vicsek.

8.2 Theoretical framework

The numerical results presented in the preceding Chapter were mainly focused in a regime of relatively low velocities, where the main disorder term

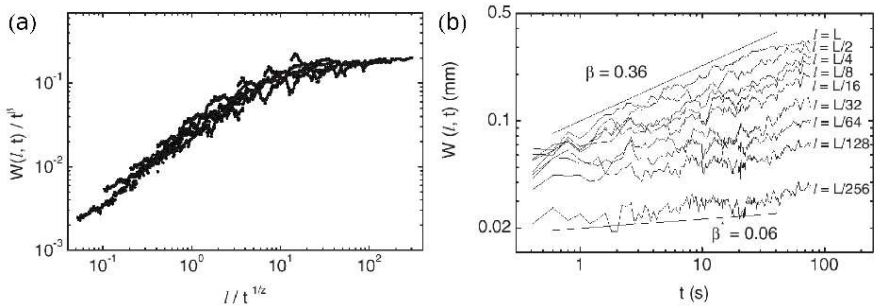

Fig. 8.2 (a) Experimental results [112] for the local width data collapse in the case of $H_c = -5$ mm with $\alpha = 1.25$ and $z = 3$. (b) Local width calculated at different window sizes in the case of $H_c = 15$ mm.

was supposed to be the capillarity. In this Chapter, however, in order to understand the results observed experimentally we need to keep in mind that, as it was explained in Chapter 4, fluctuations of gap spacing $b + \delta b$ in the Hele–Shaw cell mainly give rise to two different kinds of disorder acting on the interface, capillary disorder and permeability disorder. In order to justify then the experimental results, we need to study not only the crossover length

$$\ell_\times = 2\pi \Big[\frac{\sigma b^2}{12\eta \dot{H}(t)} \Big]^{1/2}, \tag{8.1}$$

but also the typical length scale

$$\ell_K = 2\pi \frac{\sigma b}{12\eta \dot{H}(t)}, \tag{8.2}$$

that separates two different regimes: for $\ell_c < \ell_K$, interface roughness is caused by capillarity (*capillary regime*), and for $\ell_c > \ell_K$, the roughness is produced by the permeability disorder (*permeability regime*). Therefore, we calculate the correlation length $\ell_c(t) = Bt^{1/z}$, the crossover length $\ell_\times(t)$ and the permeability length scale $\ell_K(t)$ for each case of applied pressure, Fig. 8.3. Furthermore, we can theoretically extract information concerning the dynamical exponent z by studying the deterministic part of the linearized interface equation

$$\partial_t \hat{h}_k = -\sigma \overline{K}_0 |k| k^2 \hat{h}_k - \dot{H}|k|\hat{h}_k. \tag{8.3}$$

By imposing the above equation to be scale-invariant under the transformation $x \to bx$, $h \to b^\alpha h$ and $t \to b^z t$, we obtain that $z = 3$ in the surface tension dominated regime (scales below the crossover length $\ell_\times$ and then taking into account the first term in the RHS) and $z = 2$ in the viscous pressure dominated

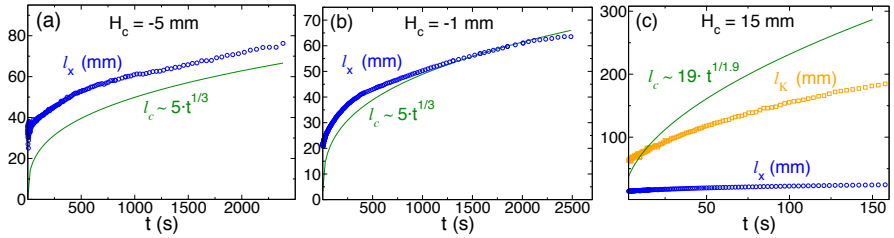

Fig. 8.3 Comparison of the different length scales that play a role in spontaneous imbibition. (a) Crossover length and correlation length versus time for a low applied pressure difference ($H_c = -5$ mm). (b) Crossover length and correlation length versus time for medium applied pressures differences ($H_c = -1$ mm). (c) Crossover length $\ell_\times$, permeability length ℓ_K, and correlation length ℓ for high applied pressure difference ($H_c = 15$ mm).

regime (scales above the crossover length $\ell_\times$ and then taking into account the second term in the RHS [1]).

Negative pressure differences.- For a negative pressure difference ($H_c = -5$ mm), the interface velocity is low enough to guarantee that $\ell_K \gg \ell_c$ and therefore, interface fluctuations are described in terms of the capillary disorder. The observed dynamical exponent $z = 3$ is the same obtained in Ref. [135] and also the same as in the lowest velocity case of the numerical results presented in the previous Chapter. This exponent basically means that interface fluctuations are controlled by surface tension. Fig. 8.3(a) shows that $\ell_\times \gtrsim \ell_c$ and therefore the observed exponents are well justified. The constant B of the correlation length, $\ell_c = Bt^{1/z}$, has been estimated from the inflexion point of the data collapse in Fig. 8.2(a).

When the applied pressure difference is increased up to $H_c = -1$ mm, the initial correlation length can catch up the crossover length [see Fig. 8.3(b)]. However a full description of the interface fluctuations cannot be obtained due to the presence of large crossover effects.

Positive pressure differences.- In the case of a large pressure difference ($H_c = 15$ mm), the interface fluctuations are described by the scaling exponents $z \simeq 1.9$, and $\alpha \simeq 0.7$ within the Family–Vicsek scaling description. Figure 8.3(c) shows that the relation $\ell_c \gtrsim \ell_K \gg \ell_\times$ is accomplished, therefore indicating that the permeability noise is more important or at least comparable to the capillary disorder. Here, the constant B of the correlation length has been calculated by imposing the condition $\ell_c(t_s) = L$, where $t_s \simeq 90$ s is the saturation time of the global interface width $W(L,t)$ [see Fig. 8.2(b)], and $L = 190$ mm is the system size.

1) Note that also Washburn's law, $\dot{H}(t) \sim t^{-1/2}$ has to be rescaled

8.3 Discussion and conclusions

The results presented in Table 8.1 show that the scaling description of the interface fluctuations is largely affected when the applied pressure is modified. In particular, three different scaling scenarios are observed. At an extremely large negative pressure difference the interface moves very slowly, under the competing influence of capillary forces that move the interface forward and the external pressure difference that tends to make the interface recede. In this regime capillary disorder is dominant and there is intrinsic anomalous scaling with a dynamic exponent $z = 3$, as reported in Ref. [135], and also in the numerical results presented in the preceding Chapter.

At larger but still negative pressure differences ($H_c = -5$ mm and $H_c = -4$ mm) capillary disorder is still the dominant force of the interface kinetic roughening. Our results show that the main difference with the case of very low velocities is observed at the local scales: intrinsic anomalous scaling has changed to a superrough anomalous scaling. As it was pointed out in the preceding Chapter, the presence of intrinsic anomalous scaling in spontaneous imbibition is related to the existence of a high contrast between the different forces acting on the interface: the dichotomic capillary disorder $p_c \sim 1/(b + \delta b)$, and the opposite force due to the applied pressure difference $\Delta p_a = \rho g H_c$. In this sense, increasing the applied pressure difference produces a decrease in the contrast between the two possible values of the resulting force of $p_c + \Delta p_a$ and, therefore, intrinsic anomalous scaling tends to disappear, giving rise to a superrough scaling instead. Concerning the global scales, the roughness exponent $\alpha \simeq 1.25$ measured in the experiments is in excellent agreement with the value found numerically in Ref. [45].

When the applied pressure difference is increased up to $H_c = 10$ mm and $H_c = 15$ mm the permeability disorder starts to be important in the roughening process ($\ell_c \gtrsim \ell_K$). The situation then becomes clearly different than in the capillary regime. First, the dynamical exponent changes to $z \simeq 2.0$, reflecting that surface tension is not the mechanism to damp the interface fluctuations. Note that the correlation length is much larger than the crossover length [cf. Fig. 8.3(c)] indicating that fluctuations are controlled by the second term in the right-hand side of Eq. (8.3) which is related to the advancement of the front. Taking into account only such a term in the interface equation one can obtain a dynamic exponent $z = 2$ by simple power-counting, which is very close to the value obtained experimentally. This is a situation never observed in spontaneous imbibition, and are in contrast with the numerical results presented in the previous Chapter, where only the capillary disorder was considered and a dynamic exponent $z = 4$ was obtained. Therefore, we conclude that the presence of the permeability disorder affects crucially the role of the crossover length scale $\ell_\times$. While in the capillary regime it is assumed that the crossover

length acts as a correlation length [45], giving rise then to $z = 4$, our results in the permeability regime show that this assumption is no longer valid.

9
Imbibition in columnar geometries

This Chapter presents analytical and numerical work concerning the dynamical scaling of imbibition fronts in a medium that is invariant along the flow direction [117]. We consider then a *columnar* disorder $\xi(x)$ that does not depend on the interface position $h(x,t)$.

9.1
Experimental motivation

Focusing the attention on columnar geometries, the experimental work by Soriano *et al.* [138] presented some years ago, studied the *forced-flow imbibition* in a Hele–Shaw cell with a columnar quenched disorder, produced by dichotomic variations in the thickness of the bottom plate (see Fig. 9.1). They found that the interfacial dynamics followed an intrinsic anomalous scaling with varying exponents that were incompatible with the expected results from the usual macroscopic model, that gives characteristic exponents of a non-local model. Instead, they obtained good agreement with an heuristic model of diffusively coupled columns presenting local interactions. The essential change of behavior, which pass to be dominated by non local to local interactions, is due to the persistence of the columnar disorder. The detailed physical mechanism, however, is not clear.

In the present Chapter, we perform numerical integrations of a phase-field model with columnar disorder to explore this behavior in both spontaneous and forced-flow imbibition. We obtain that both local and non-local behaviors can be observed in the numerical model through the variation of a parameter modeling the contrast between the different capillary values present in the system, that are given by the dichotomic variation of the Hele-Shaw cell gap. In addition, by imposing the columnar geometry of the interface motion at the macroscopic model, the heuristic local equation presented in Ref. [138] is analytically derived.

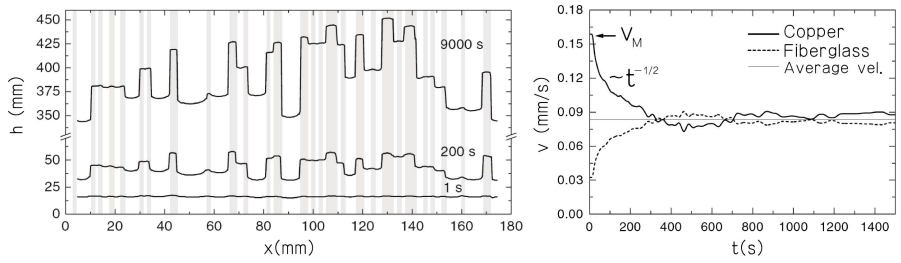

Fig. 9.1 (a) Experimental example of an interface advancing in a Hele-Shaw with columnar disorder, Ref. [138]. The interface profile is plotted at different times. (b) Average interface velocity $v_{\pm}$ over copper tracks $(+)$ and fiberglass $(-)$. It follows the relation $v_{\pm} = \overline{v} \pm (v_M - \overline{v})t^{-1/2}$, where v_M is the maximum of the average velocity over tracks (Ref. [138]).

9.2 Equations for the interface

As it is explained in Ch. 4, a dynamic equation describing the interface fluctuations can be derived within the macroscopic description of imbibition. The model is based on the Darcy's law, and takes into account the incompressibility of the liquid. The resulting interface equation can be obtained from the integro-differential equation

$$\iint_{\Omega_L} d\boldsymbol{r}' \left[p(\boldsymbol{r}')\nabla'^2 G(\boldsymbol{r}|\boldsymbol{r}') - G(\boldsymbol{r}|\boldsymbol{r}')\nabla'^2 p(\boldsymbol{r}') \right] = \int_{S_L} d\boldsymbol{s}' \cdot p(s')\boldsymbol{\nabla}' G(s|s') - \int_{S_L} d\boldsymbol{s}' \cdot G(s|s')\boldsymbol{\nabla}' p(s'). \tag{9.1}$$

This equation is integrated over the volume of the liquid $\Omega_L = \{x, 0 \leq y \leq h(x,t)\}$, and along its surface S_L. Here, p is the pressure field of the liquid and $G(s|s')$ corresponds to the Green function of the problem evaluated along the interface position, where s is the coordinate tangential to the interface. In this section, we study how the above equation is modified when the intensity of the quenched noise is changed. From an experimental point of view, this basically means that the gap between the Hele-Shaw cell plates is increased or decreased. The results are separated in two different cases.

Low capillary contrast. Linearized equations

For weak capillary disorder or low contrast between both values of the dichotomic disorder, we can assume that the quenched noise does not impose any special geometry, and the interface can be linearized around its averaged value, $H(t) = \langle h(x,t) \rangle_x$, as usual. The resulting equation is the well-known linearized interface equation, derived in Chapter 4, which written in Fourier

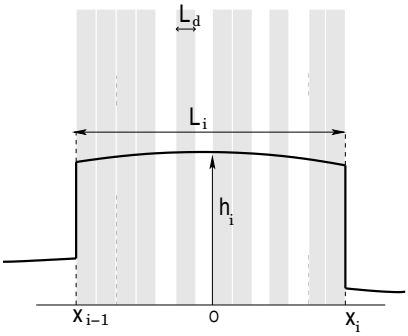

Fig. 9.2 Scheme of the interface $h_i(t)$ advancing through an effective channel L_i composed of several unit tracks L_d. The gray stripes correspond to tracks with a high capillary noise, $\xi = \xi_0/(1-\xi_A)$, and the white ones to tracks with a low capillary noise, $\xi = \xi_0$.

space reads as

$$\partial_t \hat{h}_k = -\sigma \overline{K}_0 |k| k^2 \hat{h}_k - \overline{v}|k|\hat{h}_k + \overline{K}_0 |k| \hat{\xi}_k. \tag{9.2}$$

where it is supposed that correlations do not grow up faster in time than the mean height of the interface, $|k|H(t) \gg 1$. As it has been shown in several theoretical works, under this limit, interface fluctuations follow the same Eq. (9.2) both for spontaneous and forced-flow imbibition [64, 108]. However, as it was observed in the previous Chapters, the presence of Washburn's law [$\overline{v}(t) \sim t^{-1/2}$] in spontaneous imbibition gives rise to dynamic crossover lengths and therefore, a rich variety of different scaling regimes are observed. In particular, the crossover length $\ell_\times \sim 1/\sqrt{\overline{v}}$, which can be seen as a balance between the surface tension term $\sigma \overline{K}_0 |k|^3$ and the drift term $|k|\overline{v}$ [45], becomes crucial for the interface scaling. In the forced-flow case, $\overline{v}$ is constant and thus the crossover length is just a static length scale separating two different regimes.

High capillary contrast. Coupled channel equations

The situation becomes quite different when the capillary contrast is increased. In the experimental work of Ref. [138], where forced-flow imbibition is studied for high capillary contrast, it is observed that the interface motion can be modeled through a phenomenological local equation. Our purpose now is to derive such an equation directly from the macroscopic model. To this end, we shall assume that the noise is so strong that the interface adopts the columnar geometry of the disorder. The procedure consists then on integrating Eq. (9.1) in a closed surface along the profile of the *i-th* effective channel. Here, an effective channel, or simply channel i, is defined as a group of single adjacent tracks of which the majority has the same disorder value, in such a way that the interface advances as a compact surface through each channel. An exam-

ple is depicted in Fig. 9.2, where the channel is composed of several tracks of which the majority has a high disorder value (gray tracks) and therefore, the averaged disorder of the channel ξ_i is larger than the mean disorder of the whole system $\langle\xi\rangle$. Note that the surrounding channels $i-1$ and $i+1$ must have a mean disorder value $\xi_i < \langle\xi\rangle$. The width of the channel is defined as L_i. An experimental and numerical example of these channels can be seen in Figs. 9.1 and 9.3, respectively.

We are considering the forced-flow imbibition case with the following boundary conditions at the top and the bottom of the channel:

$$\partial_y p(x,y)|_{y=h_i} = -\frac{1}{\overline{K}_0}\dot{h}_i(t) \tag{9.3}$$

$$\partial_y p(x,y)|_{y=0} = -\frac{\overline{v}}{\overline{K}_0}, \tag{9.4}$$

$$p(x,0) \sim \frac{H(t)\overline{v}}{\overline{K}_0} - \langle\xi\rangle, \tag{9.5}$$

where the pressure at the origin $p(x,0)$ has been estimated by using the relation

$$\frac{p_{int} - p(x,0)}{H(t)} = -\frac{\overline{v}}{\overline{K}_0},$$

which comes essentially from Eq. (9.4), taking that $p_{int} = -\langle\xi\rangle$ is the mean capillary pressure of the whole system. It means that the pressure at the origin is changing in time in order to get a mean constant velocity for the whole interface. Using these boundary conditions, and taking the general expression for the two-dimensional Green function

$$G(x-x'|y-y') = -\frac{1}{(2\pi)^2}\iint \mathrm{d}\boldsymbol{k}\frac{e^{i(x-x')k_x}\cdot e^{i(y-y')k_y}}{k_x^2+k_y^2},$$

we can evaluate the different boundary integrals of the top and bottom segments of Eq. (9.1) as

$$\int_{x_{i-1}}^{x_i}\mathrm{d}x\,\boldsymbol{n}\cdot\left[p(x,y)\boldsymbol{\nabla}\hat{G}(x,y)\right]_{y=h_i} = 0$$

$$\int_{x_{i-1}}^{x_i}\mathrm{d}x\,\boldsymbol{n}\cdot\left[\hat{G}(x,y)\boldsymbol{\nabla}p(x,y)\right]_{y=h_i} = \frac{L_i C}{\pi\overline{K}_0}\dot{h}_i(t),$$

$$\int_{x_i}^{x_{i-1}}\mathrm{d}x\,\boldsymbol{n}\cdot\left[p(x,y)\boldsymbol{\nabla}\hat{G}(x,y)\right]_{y=0} = \frac{H(t)\overline{v}}{2\overline{K}_0} - \frac{\langle\xi\rangle}{2},$$

$$\int_{x_i}^{x_{i-1}}\mathrm{d}x\,\boldsymbol{n}\cdot\left[\hat{G}(x,y)\boldsymbol{\nabla}p(x,y)\right]_{y=0} = \frac{h_i(t)\overline{v}}{2\overline{K}_0} - \frac{L_i C}{\pi\overline{K}_0}\overline{v},$$

where $C = \int_{\lambda}^{\infty} du \frac{sin(u/2)}{u^2}$, with $\lambda = L_i/L$ being a *cut off* due to the finite size L of the system. We have also supposed enough wide channels to ensure that $L_i > h_i(t)$, which means that we are taking the initial times, before the interface gets saturated. The nomenclature used for the Green function means that it is evaluated at the interface, $\hat{G}(x,y) \equiv G(0, h_i/x, y)$. Therefore, Eq. (9.1) can be written as

$$\begin{aligned}\frac{1}{2}p(0,h_i) = &\int_{h_i}^{0} dy' \Big[p(x,y')\partial_x \hat{G}(x,y') - \hat{G}(x,y')\partial_x p(x,y) \Big]_{x_i} \\ &- \int_{0}^{h_i} dy' \Big[p(x,y')\partial_x \hat{G}(x,y') - \hat{G}(x,y')\partial_x p(x,y) \Big]_{x_{i-1}} \\ &- a_i \dot{h}_i(t) + a_i \overline{v} - \frac{\langle \xi \rangle}{2}. \end{aligned} \tag{9.6}$$

The two first terms of the right-hand side are due to the flow between neighbor channels. We have defined the parameter $a_i \equiv \frac{L_i C}{\pi \overline{K}_0}$. In order to get an equation for the time evolution of the interface $h_i(t)$, we define the following coupling coefficients between channels as the ratio between channel flow and height differences

$$D_i \equiv \frac{\int_{h_i}^{0} dy' \Big[p(x,y')\partial_x \hat{G}(x,y') - \hat{G}(x,y')\partial_x p(x,y') \Big]_{x_i}}{a_i(h_{i+1} - h_i)},$$

$$D_{i-1} \equiv \frac{\int_{0}^{h_i} dy' \Big[p(x,y')\partial_x \hat{G}(x,y') - \hat{G}(x,y')\partial_x p(x,y') \Big]_{x_{i-1}}}{a_i(h_i - h_{i-1})}.$$

The coupling variable D_i has to be understood as a diffusion coefficient which depends on each channel i. As a general case, it may be taken as a random variable. Moreover, we shall assume that D_i does not vary in time during the initial times, before the interface gets saturated.
Then, we can write Eq. (9.6) as an inhomogeneous diffusion equation between channels:

$$\dot{h}_i(t) = \boldsymbol{\nabla} D_i \boldsymbol{\nabla} h_i + \overline{v} + \frac{1}{2a_i} \Big[- p_i(t) - \langle \xi \rangle \Big]. \tag{9.7}$$

where $p_i(t) \equiv p(0,h_i)$ corresponds to the pressure at the interface. We are assuming that the pressure at the interface is time-dependent, which is based on the experimental results reported in Ref. [138]. In such experimental work, the local velocity of the interface at each channel follows an expression similar to Washburn's law until it reaches the saturation value $\overline{v}$ (see Fig. 9.1). In order to take into account such behavior into the equation, we consider that the pressure at the interface can be expressed as $p_i(t) \sim -\Delta p_{int} - c u_i(t)$,

where the pressure difference Δp_{int} is given by the usual Young-Laplace relation $\Delta p_{int} = \sigma\kappa_i + \xi_i$, taking a negligible atmospheric pressure. The term $cu_i(t)$ is an effective kinetic term due to the local capillary forces at each channel, being c an arbitrary constant, and can be explained in terms of the mass conservation. When the interface goes through a channel i of a high capillary disorder ($\xi_i > \langle\xi\rangle$), its local velocity tends to initially increase up to a nominal value. In contrast, since we are imposing a constant velocity for the whole interface, the local velocity at the neighbor channel $i+1$ with a lower capillary disorder tends to decrease down to a nominal value. After reaching such nominal value in both cases, the local velocity decrease or increase asymptotically to the saturation value following the Washburn's behavior due to the capillary forces of each channel. Therefore, we are taking that $u_i(t) \sim \zeta_i t^{-1/2}$ for $t > 0$, where ζ_i is a random variable defined as

$$\zeta_i = \frac{\xi_i - \langle\xi\rangle}{|\xi_i - \langle\xi\rangle|},$$

which takes the values $\zeta_i = +1$ at the channel with the highest capillary value ($\xi_i > \langle\xi\rangle$), and $\zeta_i = -1$ at the channel with the lowest capillary value ($\xi_i < \langle\xi\rangle$). In addition, we also suppose that the curvature of the interface can be approximated as a constant value κ_0, and only its sign depends on each channel as $\kappa_i \sim \zeta_i\kappa_0$. Then, rewriting the last term on the right-hand side of Eq. (9.7), we get the final expression

$$\dot{h_i}(t) = \boldsymbol{\nabla} D_i \boldsymbol{\nabla} h_i + \overline{v} + \zeta_i\left(\overline{v}_i + \bar{a}_i t^{-1/2}\right), \tag{9.8}$$

where we have defined the new constants as $\overline{v}_i = (|\xi_i - \langle\xi\rangle| + \sigma\kappa_0)/2a_i$, and $\bar{a}_i = \sigma c/2a_i$. We thus conclude that when the capillary disorder is large enough, the columnar geometry of the system leads to a local description for the interface motion.

9.3 Numerical model and results

Our numerical results shall be performed using the phase-field model described in Ch. 4. The effect of an inhomogeneous capillarity is added by using a dichotomic capillary noise with the values:

$$\xi = \begin{cases} \xi_0 \\ \\ \frac{\xi_0}{1-\xi_A} \end{cases}. \tag{9.9}$$

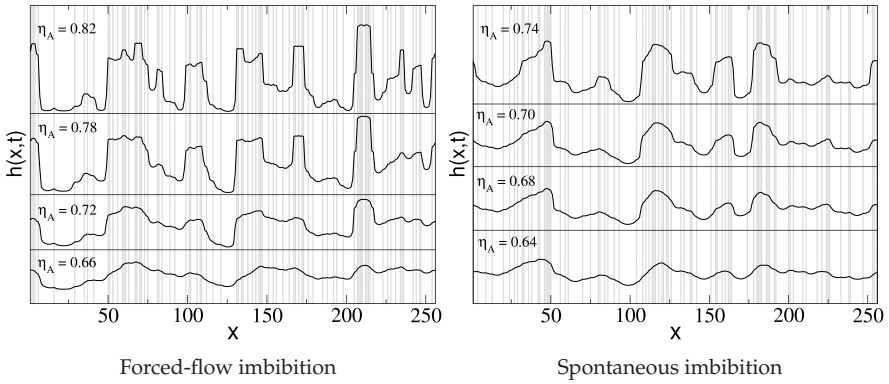

Fig. 9.3 Interface profiles at equal times but different values of capillary contrast ξ_A. The columnar disorder is also plotted: gray tracks are points where the dichotomic disorder takes its highest value of Eq. (9.9).

We consider a columnar disorder $\xi(x)$ defined by single tracks of lateral size L_d distributed along the x-direction in such a way that tracks with the high disorder value $\xi = \xi_0/(1-\xi_A)$ occupy 35% of the system length L. This is the same kind of disorder reported in the experimental work of Ref. [138]. Note that for a given disorder realization, tracks wider than L_d are obtained when two or more unit tracks are placed adjacently.

In our study, we will consider both situations of spontaneous and forced-flow imbibition by choosing conveniently the boundary conditions into the phase-field model [84]. For spontaneous imbibition an applied constant pressure is imposed at the origin of the cell $\mu(x, y=0) = \mu_a$. In contrast, a pressure gradient has to be imposed at the origin, $\overline{K}_0 \partial_y \mu|_{y=0} = -\overline{v}$, to reproduce forced-flow imbibition. Therefore, the main difference between both cases is found on the mean velocity of the interface. While in the forced-flow case, the interface evolves with the imposed constant velocity $\overline{v}$, in the spontaneous imbibition case, the averaged interfacial height $H(t)$ follows Washburn's law $H(t) \sim t^{1/2}$.

The numerical parameters used in all the numerical results have been $\epsilon = 1$, $M = 1$ in the liquid phase and $M = 0$ in the air phase (one-sided model), and $\xi_0 = 0.3$. The phase field equation [cf. Eq. (4.41) in Ch. 4] has been integrated over a system of lateral size $L = 256$ using a spatial grid $\Delta x = 1.0$ and a time step $\Delta t = 0.01$. The minimum length of the track disorder has been taken as $L_d = 2$.

9.3.1 Low capillary contrast

In this section we deal with the case of low capillary contrast in both forced-flow and spontaneous imbibition cases.

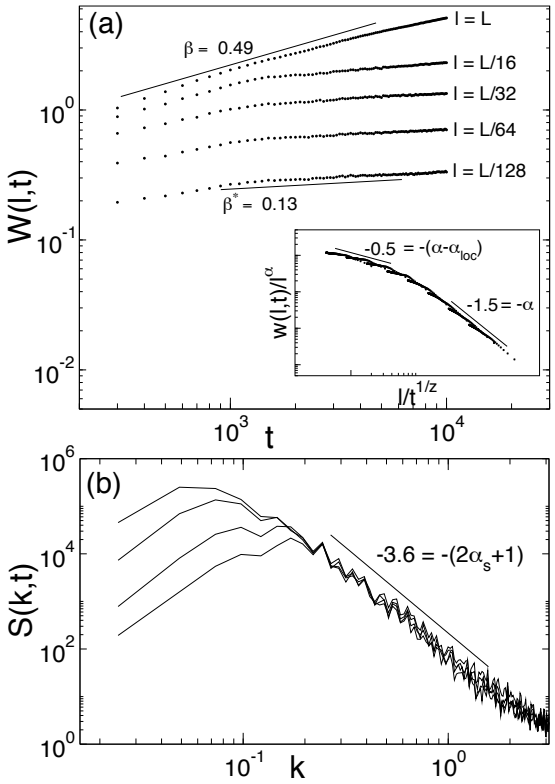

Fig. 9.4 Statistical analysis of the interface fluctuations in the forced-flow case with a low capillary contrast, $\xi_A = 0.66$. All the results were averaged over 25 disorder realizations. (a) Local width $w(\ell, t)$ evaluated at different window sizes. The global and local growth exponents can be measured directly from the data. The inset shows the best data collapse for the scaling function using the values of $z = 3.0$ and $\alpha = 1.5$. It also suggests a local roughness exponent of $\alpha_{\rm loc} = 1.0$. (b) Interface power spectrum calculated at different times. It shows a roughness exponent of $\alpha_s = 1.3 \pm 0.2$.

Forced-flow imbibition

We start to study a regime of low capillary pressures. The used value for the capillary contrast has been of $\xi_A = 0.66$ and the mean velocity has been fixed to $\overline{v} = 0.0025$. The shape of the interface for a given realization is shown in Fig. 9.3(a), case $\xi_A = 0.66$. We can see a smooth interface which is slightly correlated with the disorder. The results of the roughness analysis are shown in Fig. 9.4. From the local width $w(\ell, t)$ computed at different window sizes we can obtain the global and local growth exponents, $\beta = 0.49 \pm 0.05$ and $\beta^* = 0.13 \pm 0.05$. The best collapse of theses curves [shown at the inset of Fig. 9.4(a)] is obtained tuning the values of $z = 3.0$ and $\alpha = 1.5$. The slopes of the scaling function agree with the previously calculated exponents suggesting also a value for the local roughness exponent of $\alpha_{\rm loc} = 1$ which is corrobo-

rated at the power spectrum calculated at different times. Note that we are using here the scaling function given by Eq. (5.18) in Ch. 5. Since there is not any temporal shift between the lines of the power spectrum, we can assume that the interface fluctuations are described within the superrough anomalous scaling, and therefore $\alpha_{\rm loc} = 1$. In addition, the spectral roughness exponent obtained from the power spectrum $\alpha_s = 1.3 \pm 0.2$ corresponds to the global roughness exponent, which is in agreement with the value obtained previously. These measured exponents are compatible with those obtained by the linear Eq. (9.2) with a constant velocity $\overline{v}$. Rescaling such a linear equation by the usual transformation $x \to bx, t \to b^z t, h \to b^\alpha h$, we have trivially that $z = 3$ and $\alpha = 1.5$, and assuming superroughness ($\alpha_{\rm loc} = 1$), we get the remainder exponents as $\beta = \alpha/z = 0.5$, $\beta^* = \beta - \frac{\alpha_{\rm loc}}{z} = 0.17$, in agreement with the measured exponents. Therefore, we can conclude that this regime is well modelled by the non-local and linear equation (9.2), taking into account only the surface tension regime and with an uncorrelated columnar disorder.

If we increase the mean velocity of the interface, then the static crossover length $\ell_\times \sim 1/\overline{v}$ decreases, obtaining that interface fluctuations saturate earlier, at the time when the correlation length ℓ_c reaches the crossover length, $t_s \sim \ell_\times^z$, as it is observed in [2,84].

Spontaneous imbibition

In spontaneous imbibition, the crossover length scale, $\ell_\times \sim t^{1/4}$, becomes a dynamical scale and different regimes can be observed depending on the velocity of the interface (see previous Chapters). For low velocities, the initial correlation length $\ell_c \sim t^{1/z}$ is below the crossover length meaning that the relevant mechanism to damping the interface fluctuations is the surface tension with the characteristic dynamical exponent of $z = 3$. On the other hand, for higher velocities, the crossover length acts as an effective correlation length of the interface fluctuations, giving rise to the genuine exponent of $z = 4$. In order to study both regimes, we have controlled the initial velocity of the interface by choosing the initial height of the interface conveniently. We impose an initial height of $H_0 = 199$ to study a low velocity regime, whereas a higher velocity regime will be achieved by simply putting $H_0 = 1$.

Low velocity regime.- Typical shapes of interfaces in spontaneous imbibition are depicted in Fig. 9.3(b). In the low capillary regime, case of $\xi_A = 0.64$, the interface is weakly correlated with the disorder. A roughness analysis shown in Fig. 9.5 gives the exponents $\beta = 0.5 \pm 0.04$ and $\beta^* = 0.18 \pm 0.04$ from a direct measure of the growing local width. The best data collapse on these figures provides the exponents $z = 3.0$ and $\alpha = 1.5$. Likewise, the slope of the scaling function gives $\alpha_{\rm loc} = 1$, which is corroborated by the power spectrum shown in Fig. 9.5(b) , where we get a spectral roughness exponent of $\alpha = 1.35 \pm 0.2$,

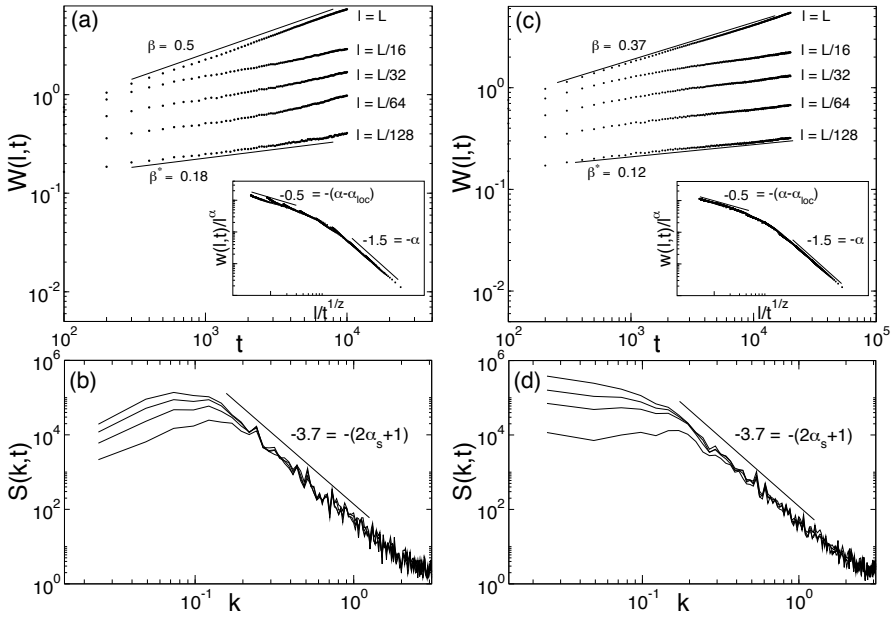

Fig. 9.5 Statistical analysis of the interface fluctuations in the spontaneous case with a low capillary contrast, both in a low velocity regime (left) and high velocity regime (right). All the results were averaged over 25 disorder realizations. (a) Local width $w(\ell, t)$ evaluated at different window sizes. The global and local growth exponents can be measured directly from the data. The inset shows the best data collapse for the scaling function using the values of $z = 3.0$ and $\alpha = 1.5$. It also suggests a local roughness exponent of $\alpha_{\rm loc} = 1.0$. (b) Interface power spectrum calculated at different times. It shows a roughness exponent of $\alpha_s = 1.35 \pm 0.2$. (c) Local width $w(\ell, t)$ evaluated at different window sizes, obtaining $\beta = 0.37(3)$ and $\beta^* = 0.12(3)$. The inset shows the best data collapse by using the values of $z = 4.0$ and $\alpha = 1.5$. It also suggests a local roughness exponent of $\alpha_{\rm loc} = 1.0$. (d) Interface power spectrum shows a roughness exponent of $\alpha_s = 1.35 \pm 0.2$.

without temporal shift between the curves, indicating we are dealing with a superrough scaling. Hence, the measured exponents are the same than those obtained in the forced-flow case. It was actually expected, since the relevant terms of Eq. (9.2) at low velocities are the same in both cases.

High velocity regime.- When the initial interface velocity is increased, the velocity-dependent term of Eq. (9.2) starts to be relevant and the new regime adopts the dynamics of the crossover length $\ell_\times \sim t^{1/4}$, getting then the expected dynamical exponent $z = 4$ [45], keeping the spatial structure with the same roughness exponent as before, $\alpha = 1.5$. The numerical results are presented in Fig. 9.5, obtaining $\beta = 0.37 \pm 0.03$, $\beta^* = 0.12 \pm 0.03$ and $\alpha_s = 1.35 \pm 0.2$ from direct measures, and $\alpha = 1.5$, $z = 4.0$, $\alpha_{\rm loc} = 1$ from the data collapse of the local widths, which are also in agreement with the linear description of Eq. (9.2).

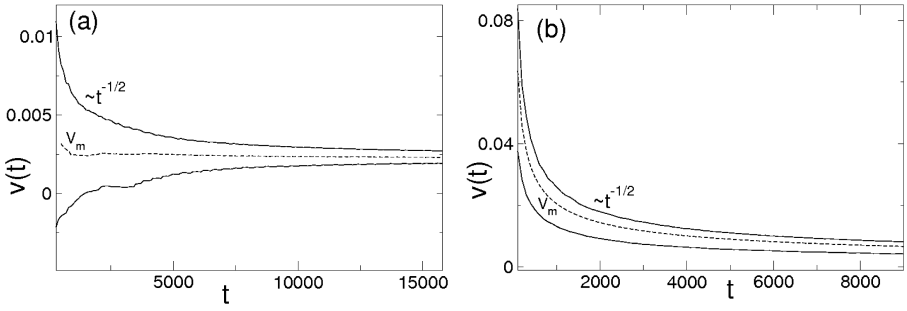

Fig. 9.6 Interface velocity $v(t)$ evaluated at two different points x of the system (solid lines) and the mean interface velocity $V_m = \overline{v}$ (dashed line) in both imbibition cases: (a) Forced-flow imbibition with $\overline{v} = 0.0025$, and (b) spontaneous imbibition within a high velocity regime. The curve above the mean velocity correspond to a channel with a high capillary disorder value (gray tracks in Fig. 2) and the curve below the mean velocity correspond to a channel with a low capillary disorder value (white tracks in Fig. 2).

9.3.2 High capillary contrast

As it is shown in Fig. 9.3, when the capillary contrast is increased the shapes of interfaces become sharper in both cases of imbibition. The effect of the disorder is so strong that a kind of columnar geometry is also imposed on the interface. As we will see, two important points of the dynamics of interface fluctuations arise as effect of increasing the capillary contrast. First, interface motion seems to be described by local effects instead of the non local effects observed in the case of low capillary contrast. Second, scaling type changes from superrough to intrinsic anomalous. As in the case of low contrast, forced-flow and spontaneous imbibition cases present distinct patterns of fluctuations and they need to be studied separately.

Forced-flow imbibition

We start to study the case of a capillary contrast $\xi_A = 0.72$ [cf. Fig. 9.3(a)]. In Fig. 9.6(a) there are plotted the local interface velocity at two different points x of the system (solid lines) and the mean velocity $\overline{v}$ (dashed line). The curve above the mean velocity corresponds to a channel i with a high disorder value, that is $\xi_i > \langle\xi\rangle$, being ξ_i the disorder of the channel i and $\langle\xi\rangle$ the mean disorder of the whole system. The curve below the mean velocity corresponds to the next channel $i+1$ with a lower disorder value, that is $\xi_{i+1} < \langle\xi\rangle$. We can see that both profiles can be locally described by Eq. (9.8) as

$$v_\pm \sim \overline{v} \pm (\overline{v}_\pm + \bar{a} t^{-1/2})$$

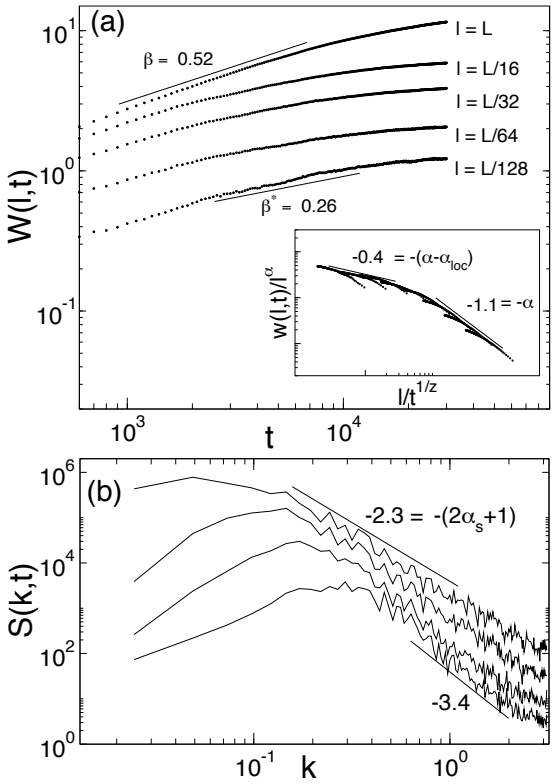

Fig. 9.7 Statistical analysis of the interface fluctuations in the forced-flow case with a high capillary contrast, $\xi_A = 0.72$. All the results were averaged over 25 disorder realizations. (a) Local width $w(\ell, t)$ evaluated at different window sizes. The global and local growth exponents can be measured directly from the data. The inset shows the best data collapse for the scaling function using the values of $z = 2.2$ and $\alpha = 1.1$. It also suggests a local roughness exponent of $\alpha_{\rm loc} = 0.7$. (b) Interface power spectrum calculated at different times. It shows a roughness exponent of $\alpha_s = 0.65 \pm 0.2$.

where $+$ and $-$ mean the channel with $\xi_i - \langle\xi\rangle > 0$ and $\xi_i - \langle\xi\rangle < 0$ respectively. Since the averaged velocity of the interface is low enough, the velocity v_- can be initially negative, as occurs in the experimental results shown in Fig. 9.1 [138].

As in the previous section we are interested in calculating the different scaling exponents. The scaling analysis is shown in Fig. 9.7. From direct measure of the interfacial local width slopes we get $\beta = 0.52 \pm 0.05$, and $\beta^* = 0.26 \pm 0.06$. The best data collapse is obtained using $\alpha = 1.1$ and $z = 2.2$. The power spectrum evolution changes with respect to the low contrast case since now there is a temporal shift between the curves, indicating the presence of inherent anomalous scaling. Hence, the spectral roughness exponent $\alpha_s = 0.65 \pm 0.2$ must be interpreted as the local roughness exponent, which is

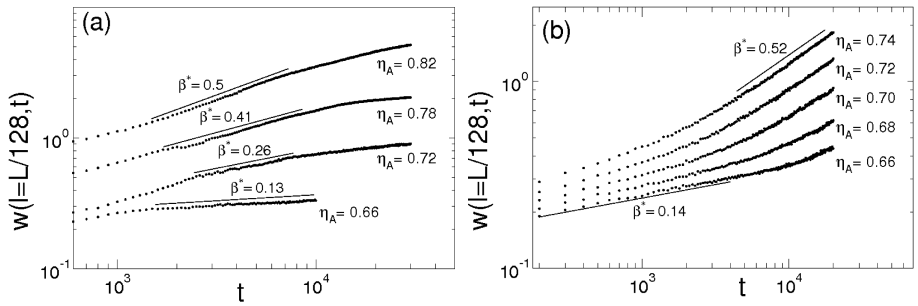

Fig. 9.8 Interface local width calculated in a small window of size $\ell = L/128$ for different capillary contrasts. The local growth exponent β^* can be obtained directly from the data. (a) Forced-flow imbibition, $\overline{v} = 0.0025$. (b) Spontaneous imbibition within a high velocity regime.

in agreement with the slopes of the collapsed scaling function. Note that these exponents are very close to the experimental exponents reported in Ref. [138], $\beta = 0.5 \pm 0.04$, $\beta^* = 0.25 \pm 0.03$, $\alpha = 1.0 \pm 0.1$. As shown in that reference, the shape of the interfaces and the analysis of fluctuations are well reproduced by Eq. (9.8), which takes into account strong diffusive coupled channels. Therefore, we can conclude that simple numerical integrations of the phase-field model reproduce both the shape and the scaling analysis of interfaces.

From low to high capillary contrast.- When we increase even more the values of the capillary contrast, interfaces become more correlated to the columnar disorder presenting quantitative changes on the scaling behavior. For instance, in Fig. 9.8(a) there is plotted the local width computed in a small window of length $\ell = L/128$. It allows us to calculate the local growth exponent β^* for different capillary contrasts. The complete set of scaling exponents is presented in Table (9.1). We can see that for high capillary contrasts ($\xi_A > 0.7$), interface fluctuations are always described by intrinsic anomalous scaling. In addition, the dynamics of the correlation is subdiffusive, ranging from $z = 2$ to $z \to \infty$ in the highest contrast value. We must interpret this extreme case as having fluctuations completely decoupled. It is characterized by the same local and global growth exponent $\beta = \beta^* = 0.5$, which implies a dynamic exponent of $z = \infty$, and it can be understood as a regime where the correlation length $\ell_c \sim t^{1/z}$ does not grow in time anymore. Experimentally, it has also been observed in the work carried out in Ref. [137]. It is worth noting that there are two exponents $\beta = 0.5$ and $\alpha_{\rm loc} = 0.5$ that remain constant.

Alternatively to the phase-field model results, this phenomenon can be reproduced by Eq. (9.8) taking a random diffusion coefficient $D(x)$ [93]. By choosing a probability density

$$P(D) = N_a D^{-a} f_c(D/D_{max})$$

ξ_A	α	α_{loc}	α_s	z	β	β^*	Scaling	Interaction
0.66	1.5	1	1.2	3	0.49	0.12	SR	Non-local
0.72	1.1	0.6	0.6	2.2	0.52	0.26	IA	Local
0.74	1.85	0.55	0.55	3.7	0.51	0.35	IA	
0.78	2.5	0.5	0.5	5.1	0.5	0.41	IA	
0.82	∞	0.5	0.5	∞	0.5	0.5	Decoupled	

Tab. 9.1: Complete set of scaling exponents for forced-flow imbibition when the capillary contrast ξ_A is increased. SR and IA refer to superroughening and intrinsic anomalous scaling, respectively.

where f_c represents a *cut off* function, Eq. (9.8) predicts a growth exponent $\beta = \alpha_{\text{loc}} = 0.5$ independently of the a value, a roughness exponent $1 \leq \alpha < \infty$, and a dynamic exponent $2 \leq z < \infty$, which is in accordance with the numerical values obtained using the phase-field model (see Table 9.1). In this sense, we can say that the diffusion coefficient D_i of Eq. (9.8) depends on the capillary contrast of the system. For very high capillary contrasts ($\xi_A > 0.8$) the coupling coefficient can be taken as $D_i \simeq 0$, obtaining then the decoupled state observed numerically. On the other hand, for lower capillary contrasts ($\xi_A \simeq 0.72$) the variations of D_i occur at scales larger than the correlation length and $D_i \simeq D$ can be taken as constant, obtaining then the regime described by $z \simeq 2$.

Spontaneous Imbibition

In Fig. 9.3(b) there is plotted four interface profiles evaluated at the same time but different capillary contrast. The velocity profiles of the interface are shown in Fig. 9.6(b). Since now there is not any imposed velocity, the velocity of the interface follows the Washburn's law in each channel of different noise value.

When we increase the parameter ξ_A a transition to a decoupled state ($\beta = \beta^* = 0.5$, $z = \infty$) also appears in the case of spontaneous imbibition. However, there is an important difference with the forced-flow case. As before, we calculate the local width in a small window size $\ell = L/128$ for different capillary contrasts [cf. Fig. 9.8(b)]. We observe that now, the local growth exponent β^* changes suddenly to $\beta^* = 0.5$, indicating that the interface advances completely decoupled. The transition to the decoupled state can be now discontinuous in time for each value of the capillary contrast. It seems that there exists a length $\ell_d(\xi_A)$ above which the fluctuations become decoupled. Therefore, for a given value of the capillary contrast, the clusters of interface with a size ℓ_d will become decoupled between each other at the time $t_d \sim \ell_d^z$, when corre-

lation length $\ell_c \sim t^{1/z}$ reaches the length ℓ_d. Above t_d, the local description is not valid anymore.

9.4 Conclusions

By means of numerical integrations of a phase-field model we find that there are strong differences between the dynamics of fluctuations in the cases of low and high capillary contrast with columnar disorder. Although these differences also exist in a case of quenched noise composed of squares, as described in Ch. 7, they are more dramatic when the quenched noise is of columnar type. It turns out that the persistence of the disorder in one direction forces the interface to adopt the same geometry, changing the nature of the interface motion.

In a low capillary contrast case, interfaces are superrough with a dynamics dominated by surface tension with exponents $z = 3$, when the mean velocity is nearly constant, or $z = 4$ when the mean velocity varies with Washburn's law. Furthermore, as interfaces are smooth and can be linearized around their mean value, a simple non local model for the interfacial evolution can be used to explain the observed dynamical scaling of fluctuations. On the other hand, when the capillary contrast is increased, interfaces are sharper and the correlation with disorder is more evident. The observed dynamical scaling corresponds then to an anomalous scaling description with a clear temporal shift at the power spectrum, and a subdiffusive behavior with dynamical exponents ranging from $z = 2$ to $z \to \infty$, depending on the strength of capillary forces. A prominent point to remark is that this behavior can be explained by a local model made of coupled channels with a fluctuating force following Darcy's law. One can interpret that in the high contrast case, the columnar disorder induces the existence of channels with more or less coupling, eliminating completely the non local character of imbibition in homogeneous geometries.

Finally, the difference between forced-flow and spontaneous imbibition has also been elucidated in the high capillary contrast regime. While in the forced-flow case the interface gets completely decoupled above a critical capillary contrast, in spontaneous imbibition the same decoupled state can be suddenly achieved for a given value of capillary contrast.

10
Influence of disorder strength on phase field models of interfacial growth

Phase field models of increasing complexity have in recent years been extensively used in studying interface roughening as well as microstructure formation [2, 48, 49, 65, 74, 125]. In particular, in modeling the problem of fluid imbibition into a disordered medium [2], two different ways to consider the mobility parameter in a Model B type of phase field model, called the *one-sided* and *symmetric* models, were used by Hernández-Machado *et al.* [64] and Dubé *et al.* [45, 46], respectively. The difference between these two cases is that in the symmetric model the mobility is constant throughout the system, while in the one-sided model it becomes zero in the phase which is being invaded.

The numerical results presented so far in this thesis have been obtained by using the one-sided phase field model. In this Chapter our aim is to carry out a detailed analysis [83] about the influence of the strength of the disorder in these two types of phase field models. Both cases can be described by a generalized Cahn-Hilliard equation or Model B with quenched disorder in the background medium (see Ch. 4). We shall focus here in the cases where the boundary conditions are used to couple the system to a reservoir of the invading phase with a constant mass flux. At the linear level of small front fluctuations, both phase field models can be analyzed through linearized interface equations, and the bulk diffusion fields implicit in this description cause the interface equation to become spatially non-local [45, 64]. It is thus of interest to examine how the models are influenced by varying disorder strength, which can be easily realized in the experiments. To this end, we first define a critical value of the disorder strength σ_c, above which the disorder becomes strong. We find that at weak disorder strengths ($\sigma \ll \sigma_c$) both models have the same interface scaling behavior given by superrough anomalous scaling, which is also predicted by the linear theory. We observe clear deviation from this scaling when the disorder strength comes close to σ_c, where superroughness disappears and weak intrinsic anomalous scaling arises. Furthermore, in the limit of strong disorder ($\sigma > \sigma_c$), the two models are no longer equivalent. The one-sided model can still be applied to describe forced-flow imbibition in good agreement with experimental results of Ref. [136]. However, in this limit

the symmetric model exhibits nucleation of the invading phase in front of the advancing interface.

The phase field model

As it is explained in Ch. 4, the phase field model is described by a Ginzburg-Landau formulation with a a quenched random field included in the double-well potential

$$V(\phi) = -\frac{1}{2}\phi^2 + \frac{1}{4}\phi^4 - \xi(\boldsymbol{r})\phi. \tag{10.1}$$

The dynamics is given by a continuity equation

$$\frac{\partial \phi}{\partial t} = \boldsymbol{\nabla} M(\phi)\boldsymbol{\nabla}\mu = \boldsymbol{\nabla} M(\phi)\boldsymbol{\nabla}\big[-\phi + \phi^3 - \epsilon^2\nabla^2\phi - \xi(\boldsymbol{r})\big], \tag{10.2}$$

where we consider a general mobility coefficient $M(\phi)$. We shall use a *gaussian* noise that is characterized by its average $\langle\xi\rangle$, and its standard deviation σ, which characterizes the disorder strength. The disorder also has a correlation length l_{corr}, which in our numerical scheme is set to the lattice spacing. Then, the standard deviation of ξ is σ when observed at scale l_{corr}.

The surface tension of this model can be calculated with the disorder-free *kink* solution ϕ_0, or Goldstone mode. The resulting dimensionless surface tension is $\gamma = \sqrt{2}/3 \simeq 0.47$ [49]. In order to avoid any confusion with the parameter σ, which in this Chapter refers to the standard deviation of the noise, the surface tension shall be exceptionally denoted as γ.

In the *sharp interface limit* $\epsilon \to 0$, the normal velocity of the interface can be obtained by integrating equation (10.2) in a region around the interface,

$$v_n \simeq M(\phi)\partial_n\mu|_+ - M(\phi)\partial_n\mu|_-, \tag{10.3}$$

where the subscripts $+$ and $-$ correspond to the two phases of the system. In our study, two different functional forms for the mobility $M(\phi)$ will be considered. First, we assume a *symmetric* parameter $M = M_0$ constant for the whole system independent of the field ϕ. In this case, the velocity of the interface is controlled by the difference between incoming and outgoing currents. Second, we will consider a *one-sided* parameter $M = M_0\theta(\phi)$, $\theta(\phi)$ being the Heaviside step function, which is zero in the phase where $\phi < 0$. Note that the normal velocity of the interface then reduces to $v_n \simeq -M_0\partial_n\mu|_-$, that is, it is only proportional to the outgoing current. As we will see in our numerical results, the two models can give different results and describe different physical situations depending on the strength of the disorder.

Here we consider the so-called driven case, where the mean velocity of the interface is fixed to a constant value. The relevant boundary condition is to impose a fixed gradient of the chemical potential at the bottom of the system, $\nabla\mu = -\overline{v}\hat{y}$. Combined with the initial condition of

$$\phi = \begin{cases} +1 & y < H_0; \\ -1 & y \geq H_0, \end{cases} \tag{10.4}$$

the boundary condition leads to phase $\phi = +1$ invading phase $\phi = -1$, and the interface moving with a constant average velocity $\overline{v}$. Here, H_0 represents an initial height. In the general context of the phase field model we will refer to these phases as A and B, respectively. In terms of liquid front invasion into a Hele-Shaw cell, these phases would be liquid and air, respectively, whereas in terms of phase separation they would be the phases rich in components A and B.

The linearized interface equation

Let us recall here that the dynamics of a front in the phase field model described above can also be considered in terms of an integro-differential equation for the interface (see Appendix A), given by the linearized equation

$$\partial_t \hat{h}(k,t) = -\frac{1}{2}\gamma|k|^3\hat{h}(k,t) - \dot{H}|k|\hat{h}(k,t) + \frac{1}{2}|k|\hat{\xi}(k), \tag{10.5}$$

where γ is surface tension, $\dot{H} = \overline{v}$ is the (constant) average front propagation velocity, and the disorder term is the Fourier transform of the two-dimensional disorder along the front, or $\hat{\xi}(k) = \int dx e^{-ikx}\xi(x, h(x,t))$. From the dispersion relation (10.5), one immediately obtains the crossover length scale

$$\ell_\times \sim \sqrt{\frac{\gamma}{\overline{v}}}, \tag{10.6}$$

when the two dispersion terms are equally strong.

Definition of disorder strength

In order to study the influence of disorder strength in the phase-field model of Eq. (10.2), we need to define a measure for the relative strength of the disorder. This can be achieved by comparing the disorder contribution in the dimensionless bulk free energy of Eq (10.1) to the surface energy. We do this by considering a domain of linear size r, where the local disorder average $\langle\xi\rangle_r$ is a stochastic variable with standard deviation $\sigma_r \propto r^{-1}\sigma$, where σ is the standard

deviation of a single disorder site, which is of linear size l_{corr}. Considering a circular domain of radius r, it is energetically favorable for this domain to be of the opposite phase than its surroundings if

$$2\pi r\gamma \leq \pi r^2 \Delta\phi \langle\xi\rangle_r, \tag{10.7}$$

where $\Delta\phi = 2\phi_e = 2$ is the miscibility gap. The LHS is the energy cost of the interface, whereas the RHS is the energy gain due to disorder. We consider the local disorder average $\langle\xi\rangle_r$ to be as large as its standard deviation $\sigma_r = \sigma\, l_{corr}/\sqrt{\pi}r$. Then Eq. (10.7) gives the condition

$$\sigma \geq \frac{\sqrt{\pi}}{l_{corr}}\gamma, \tag{10.8}$$

for when the disorder can locally dominate the bulk energy and thus is defined to be strong. The order of magnitude estimate for strong disorder in our dimensionless units ($l_{corr} = 1$, $\epsilon = 1$) is thus obtained as the variance being of the same order as the surface tension $\sigma = \sigma_c \approx \gamma$. Note in particular that no r dependence remains in the estimate, and thus the relative disorder strength will be the same *at all length scales* (larger than the interface width ϵ and disorder site size l_{corr}).

10.1 Numerical results

Our study will be focused on the influence of the disorder on the scaling behavior of the fluctuating interface for the two cases of the mobility M in the phase field model, that is, the one-sided model and the symmetric case. In our simulations we have used gaussian distributed disorder with zero mean $\langle\xi\rangle = 0$, and different disorder strengths (standard deviation of ξ) σ. In the numerical scheme the disorder will have a correlation length as long as the lattice spacing, meaning that the lattice spacing normalizes the standard deviation when dimensionless numbers in the numerical scheme are turned to physical units.

10.1.1 Weak disorder

For weak disorder, both models of the phase field (one-sided and symmetric) are expected to be equivalent, since the same linearized equation describes both cases in this limit. The weak disorder regime corresponds to $\sigma \ll \gamma$, where γ is the surface tension. In our dimensionless units [$\epsilon = 1$ in Eq. (10.2)] $\gamma \simeq 0.47$. Numerical solutions of the linearized interface equation (10.5) have

been performed in [84], obtaining the roughness and growth exponents of $\alpha \simeq 1.3$ and $\beta \simeq 0.4$, within the super-rough scaling description ($\alpha_{\rm loc} = 1$, $\alpha_s = \alpha$). This is in agreement with our results for both phase field models at weak disorder, which are shown in Figs. 10.1 and 10.2 on the top. From Figs. 10.2(a) and (d) we observe that $\alpha = \alpha_s$, since no temporal shift in the structure factor is present [unlike Fig. 10.2(c)]. Moreover, we observe that at small disorder strengths $\sigma < 0.2$ in accordance with $\sigma \ll \gamma$, the spectral roughness exponent saturates to the value predicted by Eq. (10.5), and is independent of the disorder strength (see Fig. 10.3).

10.1.2 Strong disorder

In the regime of strong disorder, $\sigma > 0.5$, different scenarios occur depending on which model is used. Below, we discuss the cases of the symmetric and two-sided models separately.

Symmetric model

According to the analysis of the disorder strength in the preceding Section, in this limit it is favorable for the phase field model to spontaneously create disperse domains of one phase (A) within the region that is initially of the other phase (B). Droplets of phase A will form in phase B, and this mixture will initially cover most of the system. However, local mass conservation must still be valid regardless of any nucleation events. This means that mass must be diffusively transported from the A phase to the location where it nucleates within the B phase to facilitate a growing droplet.

This is exactly what happens in the symmetric model (see Fig. 10.4), when one imposes the initial condition of Eq. (10.4). Since there is no characteristic scale for the domain creation, the droplets are not restricted by the crossover length $\ell_\times$, which acts as a *cutoff* for the interface fluctuations and therefore, the surface roughening at large scales is different respect to a weaker disorder strength. This is observed in Fig. 10.2(c), where the interface power spectrum is plotted for a higher disorder strength at different times using the symmetric model. We can see that the fluctuations are not saturated, indicating that the crossover length $\ell_\times$ (represented by the dashed line) is not acting anymore as an upper cutoff. In addition, our numerical results for the symmetric model at strong disorder show three differences to the weak disorder case.

- The local growth exponent β^* approaches the global exponent β [see Fig. 10.1(c)]
- The spectral roughness exponent decreases drastically to the range of $\alpha_s \simeq 0.5$ (see Fig. 10.3)

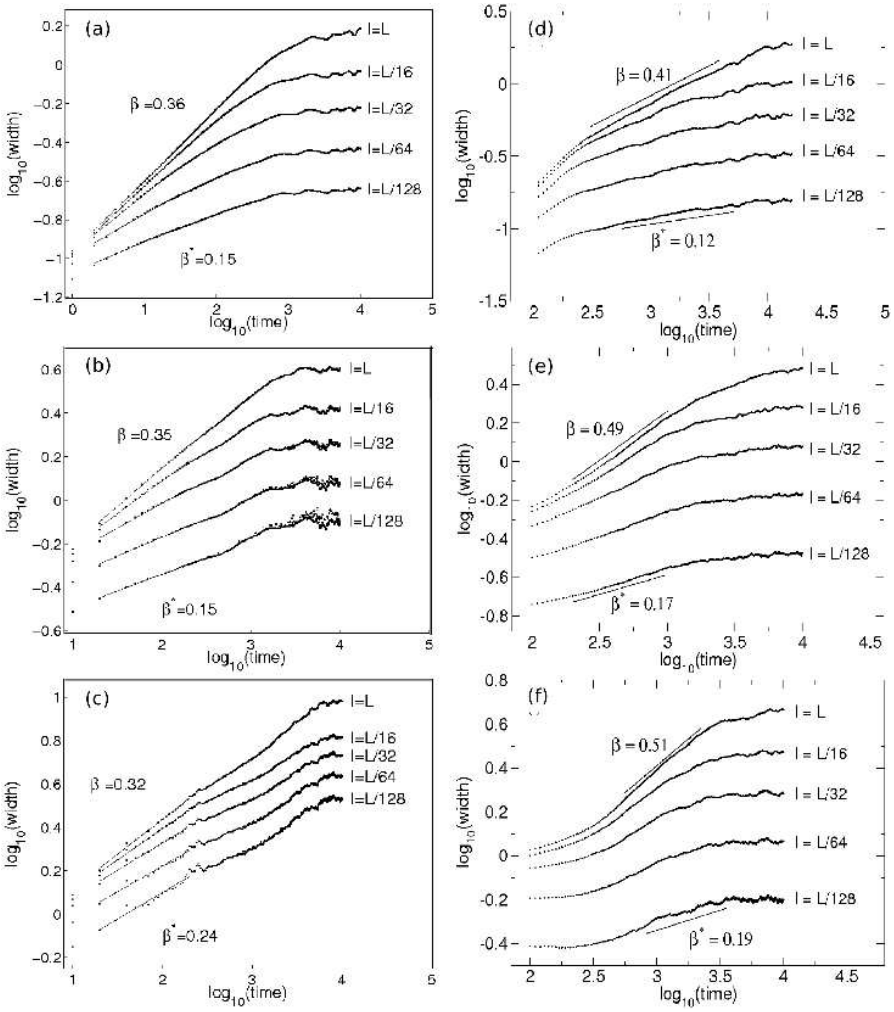

Fig. 10.1 Interface widths for the two models at different disorder strengths (in dimensionless units). Results from the symmetric and one-sided model are given on the left(a,b,c) and right(d,e,f) panels, respectively. Disorder strength is varied from top to down as: weak disorder ($\sigma = 0.2$), intermediate disorder ($\sigma = 0.5$), and strong disorder ($\sigma = 1$). Fitted growth exponents for the smallest and largest slopes are given in the figures, with solid lines representing the fits. (The numerical results from the symmetric model were performed by Laurila *et al.* [83]).

- A temporal shift appears in the power spectrum [see Fig. 10.2(c)]

We can thus conclude that the scaling picture of interface fluctuations changes from superrough to intrinsic anomalous scaling, where $\alpha_s \neq \alpha$.

The picture becomes problematic for strong disorder, however, because the interface becomes less and less representable by a single valued function $h(x,t)$. This is due to the interfacial area becoming more and more tattered

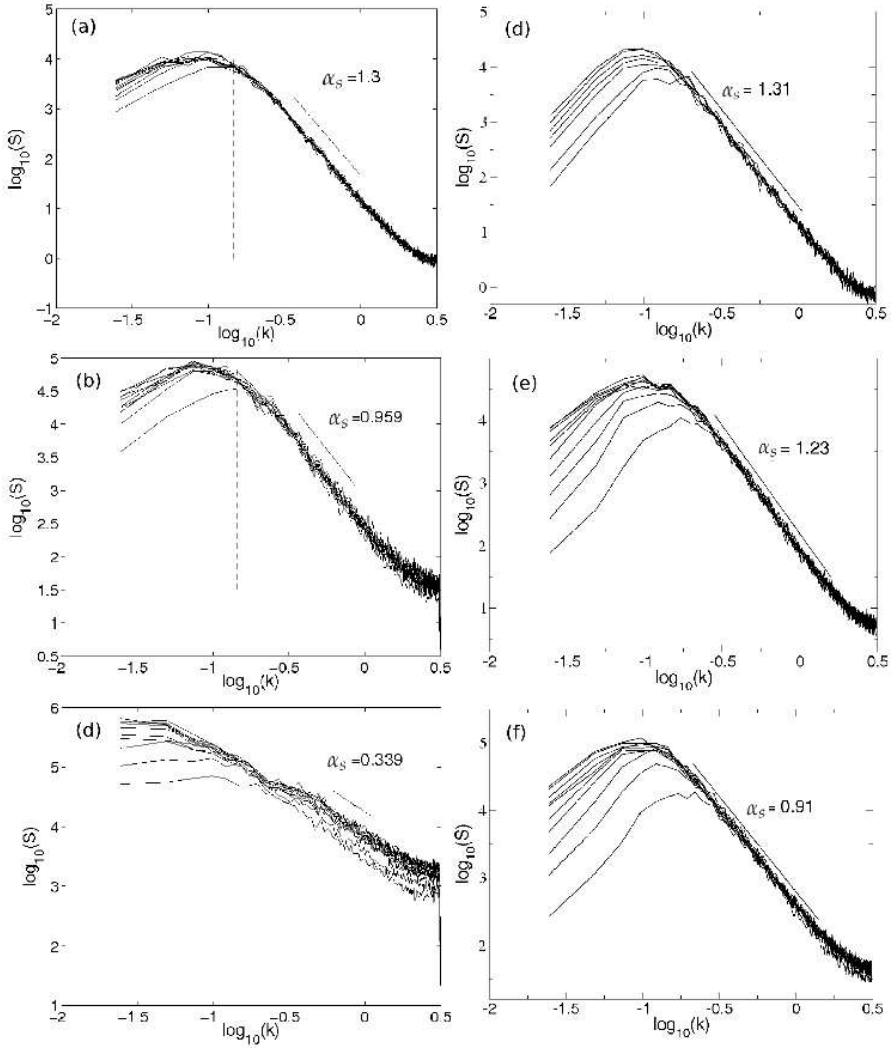

Fig. 10.2 Structure factors at ten equidistant time intervals for the two models at different disorder strengths (in dimensionless units). Results from the symmetric and one-sided model are given in the left(a,b,c) and right(d,e,f) panels, respectively. Disorder strengths are varied from top to down as weak ($\sigma = 0.2$), intermediate ($\sigma = 0.5$) and strong ($\sigma = 1$). Fitted roughness exponents are given in the figures, with solid lines corresponding to the fits. The dashed vertical line corresponds to the crossover point $k_\times = 2\pi/\ell_\times$ as obtained from the linearized interface equation. (The numerical results from the symmetric model were performed by Laurila *et al.* [83]).

by overhangs, droplets and bubbles. This also means that some numerical tricks are needed to distinguish the interface from these bubbles and droplets. This distinction is essentially made by finding a path for the phase bound-

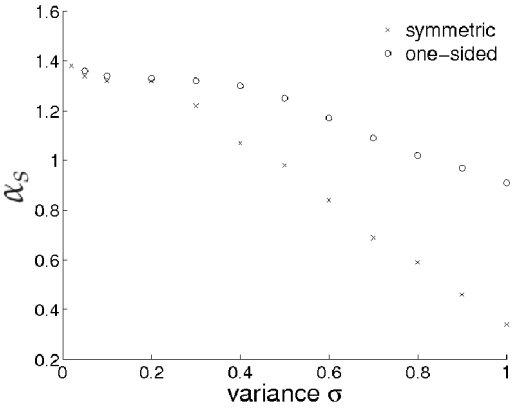

Fig. 10.3 Spectral roughness exponent α_S for both phase field models as a function of disorder strength.

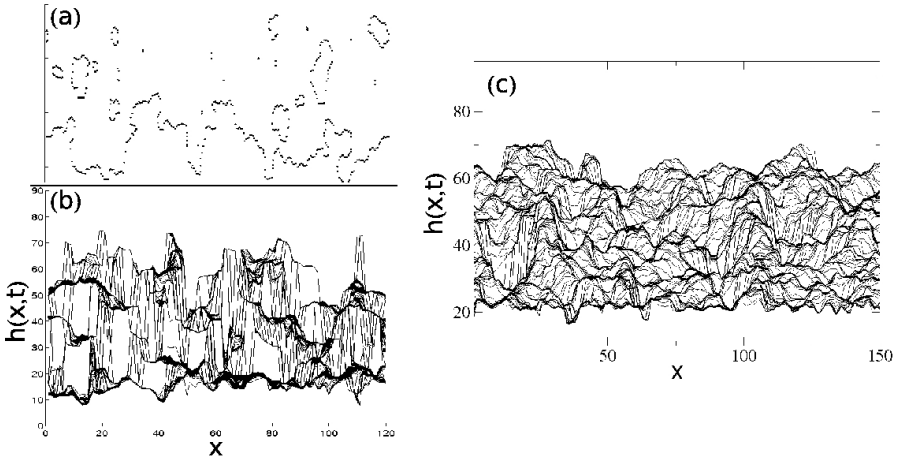

Fig. 10.4 An example of a set of rough fronts for strong disorder $\sigma = 1$ using both models. Symmetric model (left, b) and one-sided model (c). Figure (a) shows points of zero ϕ at fixed time in the symmetric model, demonstrating the nucleating domains. (The numerical results from the symmetric model were performed by Laurila *et al.* [83]).

ary across the system that locally has as small height jumps as possible. This works relatively well as long as the disorder is not much stronger than $\sigma = 1$ in our dimensionless units. However, note anomalous fluctuations in Fig. 10.1(c) around value 2.6 on the vertical axis, that are due to the abovementioned reason.

One-sided model

Using the one-sided model allows us to suppress the domain creation in phase B, where the mobility parameter is zero. Then, the position of the interface $h(x,t)$ can be found by taking the largest height where the phase A has advanced to at time t, coming from the phase B when the phase field is above zero. In Fig. 10.4 we show an example of the interface profile at different times for a strong disorder, $\sigma = 1.0$.

The growth exponent $\beta \simeq 0.5$ measured for strong disorder strength [see Fig. 10.1(e) and (f)] agrees with the experimental value of $\beta = 0.50 \pm 0.02$ reported in Ref. [136] for liquid front dynamics into a Hele-Shaw cell. Likewise, a similar variation in the spectral roughness exponent α_s, which changes from $\alpha_s \simeq 1.23$ to $\alpha_s \simeq 0.91$ when the disorder strength is increased (see Fig. 10.3), was also experimentally observed in the same reference, with a variation from $\alpha_s = 1.1 \pm 0.1$ to $\alpha_s = 0.9 \pm 0.1$ when the capillary forces of the Hele-Shaw cell were increased, by decreasing the gap spacing b. On the other hand, we numerically observe that the crossover length $\ell_\times$ still acts as a cutoff length for the interface fluctuations at strong disorder (see Fig. 10.2). These results indicate that the model can still describe the imbibition phenomenon at strong disorder.

10.2 Discussion and conclusions

In this Chapter, we have studied two different ways of considering the influence of the mobility parameter in a Model B type of phase field model with a Ginzburg-Landau type free energy. The main experimental context considered here is liquid front invasion into a Hele-Shaw cell with quenched disorder [136]. We have focused on the case of driven front invasion, where there is a forced constant mass flux into the system.The symmetric model, studied for example in Refs. [2, 45, 84], uses a constant mobility factor, whereas the one-sided model, studied for example in Refs. [64, 116], and in the work presented in the previous Chapters of this thesis, uses a mobility that is zero in the receding phase, which we call phase B.

We note that both models have previously been turned into non-local linear interface equations in the limit of small front fluctuations, which is equivalent to weak disorder [45, 64, 84]. These linearized equations are identical for both models, and therefore both models are expected to have identical scaling behavior at the weak disorder limit. This is verified by direct comparison of numerical simulations. Furthermore, these results also agree with the relevant Hele-Shaw experiments [136].

We give an estimate for the strong disorder limit by comparing the disorder contribution to bulk energy to the surface tension. We find that the linear weak disorder limit is found well below this disorder value, and that only in this limit, the roughness exponent obtained from both models does not depend on the disorder strength. This means that a well-defined region of universality only exists at the weak disorder limit.

Numerically we study the dependence of the growth and roughness exponents of the driven fronts as a function of the disorder strength. Our results are consistent with a (continuous) change of scaling behavior from superrough to intrinsic anomalous scaling, when the disorder strength is increased from weak to strong.

At strong disorder, the symmetric model is no longer found to correspond to the Hele-Shaw experiment due to domain creation of the invading phase in front of the propagating interface. As our analysis shows, the domain growth can occur at all length scales (larger than the disorder site size l_{corr} of the system) without any characteristic radius, which is a phenomenon observed in other experimental situations such as nucleation on dislocations [23] or binary mixtures [59]. In contrast, the results for the one-sided model do agree well with the Hele-Shaw experiments [136], even as the disorder strength is increased.

We hypothesize that the change in the scaling behavior observed as the disorder becomes strong is due to a decreased effect of surface tension and mass transport during interface roughening. In the limit of strong disorder, it has been argued that the disorder dominates over surface tension. Therefore, the interface scaling in the regime dominated by the surface tension (characterized by having a correlation length $\ell_c < \ell_\times$) should change for both models at strong disorder. In the one-sided model, mass transport still restricts interface roughening, and thus the crossover scale $\ell_\times$ persists. Conversely in the symmetric model the nucleated domains create roughening by avalanches that are not controlled by mass transport from the reservoir, and thus the crossover scale $\ell_\times$ becomes irrelevant.

11
Time-dependent crossover length scales in surface roughening

The studies presented in the previous Chapters reflected that imbibition phenomena show a rich variety of scaling regimes, mainly due to the presence of crossover lengths into the interface equations. This is particularly true in the case of spontaneous imbibition, where the scaling properties of the fluctuating interface are largely affected by the presence of the dynamic crossover length $\ell_\times \sim t^{1/4}$, that separates different physical mechanism of damping the interface fluctuations (see Ch. 7).

From a general point of view, the existence of crossover length scales and characteristic times in nonequilibrium surface roughening has only been studied in the case of time independent coupling parameters, where the analysis is actually relatively simple. However, little is known about the less common situations in which the couplings depend explicitly on time. In addition to spontaneous imbibition, such phenomena can also be found in other physical systems as for example in the problem of a stable phase growing at the expense of a metastable phase [62], among others. Therefore, not only for the clear motivation found in imbibition but also because it has a general interest in surface growth, the aim of this Chapter is to study how the scaling properties of a general growing interface are affected by the existence of characteristic length scales that depend on time. The general scaling analysis shall be exemplified with simple model systems in which dimensional analysis gives the exact exponents. Furthermore, in order to gain analytical understanding, the study is restricted to linear model examples that allow exact computation of the critical exponents. In addition, the analytical results will also be compared with numerical simulations [118].

11.1
General local models of surface growth

The details of the interactions in kinetic roughening are irrelevant in the mathematical description of the critical properties of the surface at long wavelengths, akin to critical point phenomena. Therefore, in the hydrodynamic limit, surface growth in $d+1$ dimensions can be described by the stochastic

equation

$$\frac{\partial h}{\partial t} = \mathcal{G}(\nabla h) + \xi(\mathbf{x}, t), \tag{11.1}$$

where $h(\mathbf{x}, t)$ is the height of the interface at substrate position $\mathbf{x}$ and time t. The functional $\mathcal{G}(\nabla h)$ depends on the specific model and should satisfy all the symmetries and conservation laws. The external noise $\xi(\mathbf{x}, t)$ describes the random driving forces acting on the surface, for instance the influx of particles in a deposition processes.

We are interested here in surface growth models with local coupling among degrees of freedom, *i.e*, growth equations that include only terms that depend on derivatives of the height, $\mathrm{Y} = \nabla h$. In the spirit of Ginzburg-Landau-Wilson theory of critical phenomena the functional $\mathcal{G}(\mathrm{Y})$ is constructed as the leading-order expansion in powers of the argument Y, its derivatives, and combinations thereof. One explicitly avoids to include terms that are incompatible with the symmetries of the problem. The corresponding expansion takes the form of a sum,

$$\mathcal{G}(\mathrm{Y}) = \sum_i \omega_i \Phi_i(\mathbf{x}, t), \tag{11.2}$$

where ω_i are the *coupling constants* and $\Phi_i(\mathbf{x}, t)$ are the *local operators* in the terminology of the renormalization group (RG). Local operators correspond to the combinations of degrees of freedom and its derivatives, which typically include surface diffusion $\nabla^2 h$, curvature diffusion $\nabla^4 h$, and in general higher-order diffusion terms $\nabla^{2m} h$. Also nonlinear terms usually appear, $(\nabla h)^{2n}$, $\nabla^{2n}(\nabla h)^{2m}$, and so on. The asymptotic long wavelength limit is governed by the most relevant terms in the RG sense. Higher-order terms are however important in describing crossover effects before the truly asymptotic behavior is reached. This leads to the existence of crossover length scales and characteristic times at which one can observe the true asymptotic scaling behavior of the system.

The problem we want to address here is to study the interplay between a crossover length scale growing in time and the dynamic correlation length characterizing the kinetic roughening process. As it will be shown, it turns out that the long time limit scaling behavior strongly depends on the nature of the phases that the dynamic crossover separates. We focus on three typical cases that cover the most important situations one can find: (i) Crossover between two different rough regimes, (ii) crossover from a rough to a flat regime, and (iii) the existence of a damping term, where scale-invariant fluctuations are damped over a certain length scale that varies with time.

11.1.1
Crossover between two different rough regimes

Consider a growing surface described by Eq. (11.1). Invariance under translation along the growth and substrate directions as well as invariance in the election of the time origin rule out an explicit dependence of $\mathcal{G}$ on h, $\mathbf{x}$ and t. These symmetry requirements alone lead to scale invariant growth in a generic way [5]. Let us consider the two most relevant terms in the leading-order expansion of $\mathcal{G}(\nabla h)$ in the hydrodynamic limit, so that we have $\mathcal{G} = \omega_{\rm I}\Phi_{\rm I}(x,t) + \omega_{\rm II}\Phi_{\rm II}(x,t) +$ higher-order terms. Let the $\Phi_{\rm I}$ term be more relevant (in the RG sense) than $\Phi_{\rm II}$.

We first discuss the case in which Eq. (11.1) exhibits crossover between two different rough regimes. This means $\omega_{\rm II}\Phi_{\rm II}(x,t)$ is relevant at short scales, while $\omega_{\rm I}\Phi_{\rm I}(x,t)$ becomes the most dominant in the long wavelength limit. Hence one expects to find an early times (short scales) regime with scaling exponents $\alpha^{(\rm II)}$ and $z^{(\rm II)}$ that crosses over to the true asymptotic regime, governed by the operator $\Phi_{\rm I}$, with exponents $\alpha^{(\rm I)}$ and $z^{(\rm I)}$. Dimensional analysis indicates that there exits a crossover length

$$\ell_\times \sim (\omega_{\rm II}/\omega_{\rm I})^{1/q}, \tag{11.3}$$

for some exponent q. This is the typical length above which the most relevant term $\omega_{\rm I}\Phi_{\rm I}$ takes over. This is likely the most common situation of crossover behavior in surface growth.

The question we wish to study here is how this picture is modified when the most relevant operator's coupling, $\omega_{\rm I}$, decreases in time. The most interesting situation naturally arises for a power-law decay of the coupling $\omega_{\rm I}(t) \sim t^{-\gamma}$, so that the term $\omega_{\rm I}(t)\Phi_{\rm I}$ gets effectively less relevant for longer times as compared with the $\omega_{\rm II}\Phi_{\rm II}$ term. In this case the crossover length diverges in time as a power-law, $\ell_\times(t) \sim t^{\gamma/q}$, and the interplay with the other relevant scale in the problem –namely, correlation length $\ell_c(t) \sim t^{1/z^{(\rm II)}}$, will give rise to an interesting behavior. On scales smaller than $\ell_\times(t)$ the less relevant term II dominates, while we expect a crossover to the asymptotic regime I for $\ell_c(t) \gg \ell_\times(t)$. The crossover then occurs when $t^{1/z^{(\rm II)}} \sim t^{\gamma/q}$. The point is now that the observable scaling regimes crucially depend on the exponent of the coupling γ. If $\gamma < q/z^{(\rm II)}$ the crossover does take place as described above. On the contrary, for $\gamma > q/z^{(\rm II)}$ the crossover length grows at an exponentially faster rate than the correlation length. Therefore, in this case the time-dependent coupling effectively takes the crossover length to scales much larger than those that can be correlated by the dynamics at any finite time. As a consequence the system will never cross over to regime I, and only the "less" relevant operator II governs the scaling regime observable for arbitrarily large system sizes.

To exemplify such a crossover behavior between different scaling regimes, a simple $1+1$ dimensional model is discussed. We consider Eq. (11.1) with $\Phi_{\rm I} = \nabla^2 h$ and $\Phi_{\rm II} = -\nabla^4 h$, describing diffusive coupling. Then we have the growth equation

$$\frac{\partial h}{\partial t} = \nu(t)\nabla^2 h - \nabla^4 h + \xi(x,t), \tag{11.4}$$

where we have rescaled all the couplings but $\nu(t)$ to unity. The noise is delta-correlated,

$$\langle \xi(x,t)\xi(x',t')\rangle = 2\delta(x-x')\delta(t-t'). \tag{11.5}$$

Higher-order diffusion terms, $\nabla^{2n} h$, might be present, but are irrelevant for the scaling behavior. Actually, even the $\nabla^4 h$ term is irrelevant as compared with $\nabla^2 h$ if the couplings are independent of time. Consider now a power-law decaying coupling [1] $\nu(t) \sim t^{-\gamma}$. Balancing the two gradient terms in Eq. (11.4) one finds that they become comparable at the typical crossover scale

$$\ell_\times(t) \sim t^{\gamma/2}, \tag{11.6}$$

with the exponent $q = 2$ in the previous analysis. Dimensional analysis tells us that the kinetic roughening process is governed by the fourth derivative term (that we label as II) on scales smaller than $\ell_\times$, while the diffusion term should dominate on much larger scales (that we label as regime I). Below the crossover, for $\ell_c(t) \ll \ell_\times(t)$, Eq. (11.4) has a correlation length $\ell_c(t) \sim t^{1/z^{(\rm II)}}$, where $z^{(\rm II)} = 4$, given by the $\nabla^4 h$ term dynamics. Crossover to the asymptotic regime I takes place when the correlation length reaches the crossover length $t^{1/z^{(\rm II)}} \sim t^{\gamma/2}$. Following the previous analysis, we expect that the regime I can only be reached if $\gamma < 2/z^{(\rm II)}$, *i.e*, $\gamma < 1/2$. On the contrary, for $\gamma > 1/2$ the crossover is wiped out and the less relevant operator II (in RG sense) does govern the scaling in the long wavelengths limit as well. By integrating numerically Eq. (11.1), we can see that this analysis is in excellent agreement with simulations, as it is shown in Figure 11.1.

Scaling properties for $\gamma < 1/2$

Let us now study the scaling properties in the case of $\gamma < 1/2$, where one expects two different regimes with different critical exponents. First, smaller scales, regime II, are simply governed by the dynamics of the curvature diffusion term $\nabla^4 h$. This regime is actually very well-known and can be exper-

1) An arbitrary small constant c is required to avoid the singularity at $t = 0$, so that $\nu \sim \nu_0(c+t)^{-\gamma}$. This has no significance for our analysis but it must be taken into account in numerical simulations.

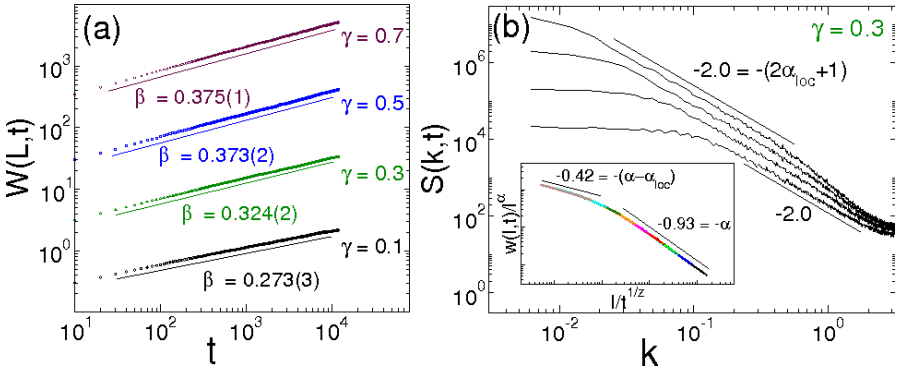

Fig. 11.1 Crossover from rough to rough. Numerical integration of Eq. (11.4) using a time step $\Delta t = 10^{-2}$ and $c = 10^{-3}$ in a system size $L = 1024$. All results were averaged over 200 realizations. (a) Global width of the interface, computed for different γ values. The theoretical prediction for the growth exponent $\beta^{(\mathrm{I})} = (1+\gamma)/4$ for $\gamma < 1/2$ fully agrees with simulations. For any $\gamma > 1/2$ we obtain $\beta = 3/8$, as expected. The curves are vertically shifted for clarity. (b) Power spectrum for $\gamma = 0.3$ evaluated at times 10, 10^2, 10^3, and 10^4. Anomalous scaling with a local roughness exponent $\alpha_{\mathrm{loc}}^{(\mathrm{I})} = 0.5$ is observed. The inset shows a data collapse of the local width data for $\alpha^{(\mathrm{I})} = 0.93(1)$ and $z^{(\mathrm{I})} = 2.86(4)$ to be compared with the predicted values given by Eq. (11.8), $\alpha^{(\mathrm{I})} = 0.928$ and $z^{(\mathrm{I})} = 2.857$ for $\gamma = 0.3$.

imentally found in molecular beam epitaxial growth [5, 79, 150] (see also Ch. 5), which is known to be described by a superrough surface with the global exponents

$$\alpha^{(\mathrm{II})} = \frac{3}{2}, \quad z^{(\mathrm{II})} = 4, \quad \beta^{(\mathrm{II})} = \frac{3}{8}, \tag{11.7}$$

and the local roughness exponent $\alpha_{\mathrm{loc}}^{(\mathrm{II})} = 1$, as expected in the superrough scaling in $d = 1$ dimension.

Intrinsic anomalous scaling in Regime I.- The interesting scaling occurs however, above the crossover length, $\ell_c(t) \gg \ell_\times$, when the system is expected to be in regime I, and therefore only governed by the diffusive term $\nabla^2 h$. By imposing scale invariance under the transformation $x \to bx$, $t \to b^z t$ and $h \to b^\alpha h$, one obtains the exact global exponents

$$\alpha^{(\mathrm{I})} = \frac{1+\gamma}{2(1-\gamma)}, \quad z^{(\mathrm{I})} = \frac{2}{1-\gamma}, \quad \beta^{(\mathrm{I})} = \frac{1+\gamma}{4}, \tag{11.8}$$

and the scaling relation $\alpha^{(\mathrm{I})} = z^{(\mathrm{I})}\beta^{(\mathrm{I})}$ is fulfilled. Figure 11.1 shows that this scaling analysis is in excellent agreement with a numerical integration of the model (11.4). In addition, we see that even for $\gamma < 1/2$ the asymptotic scaling behavior is nontrivial, since the time-dependent coupling $\nu(t)$ leads to anoma-

lous scaling of the local surface fluctuations. In order to study more clearly the local properties of the interface fluctuations, we need to calculate the structure factor (or spectral power spectrum), $\mathcal{S}(k,t) = \langle \widehat{h}(k,t)\widehat{h}(-k,t)\rangle$, where $\widehat{h}(k,t)$ is the Fourier transform of the surface in a system of lateral size L.

By neglecting the $\nabla^4 h$ term and expressing Eq. (11.4) in Fourier space, a solution for the interface position in Fourier space can be written in terms of the Green function of the problem

$$\widehat{h}(k,t) = \int_0^\infty \mathrm{d}t' G_k(t,t')\widehat{\xi}(k,t'), \tag{11.9}$$

where $\widehat{\xi}(k,t)$ is the Fourier transform of the noise and we have assumed that the interface is initially flat. Here, the Green function reads as

$$G_k(t,t') = \theta(t-t')\exp\Big[-\frac{k^2}{1-\gamma}\big(t^{1-\gamma} - t'^{1-\gamma}\big)\Big], \tag{11.10}$$

being $\theta(t-t')$ the Heaviside step function. For notation clarity, the constant c of $\nu(t) = (t+c)^\gamma$ has been omitted. The solution (11.9) allows then to calculate the interface power spectrum as

$$\mathcal{S}(k,t) = 2\int_0^t \mathrm{d}t' \exp\Big[\frac{2k^2}{1-\gamma}\big(t^{1-\gamma} - t'^{1-\gamma}\big)\Big], \tag{11.11}$$

where a delta-correlated noise, Eq. (11.5), has been taken. Finally, the above equation for the power spectrum can be rewritten in terms of a scaling function

$$\mathcal{S}(k,t) \sim k^{-2} t^\gamma s(k^2 t^{1-\gamma}), \tag{11.12}$$

where the scaling function $s(u)$ has the asymptotes, $s(u) \sim u$ for $u \ll 1$, and $s(u) \sim$ constant for $u \gg 1$. Note that Eq. (11.12) describes the surface scaling before saturation. For finite systems, the steady-state occurs at very long times, $t \sim L^{2/\gamma}$, when one recovers $S(k) \sim k^{-4}$. We are interested here in the intermediate regime before saturation is reached, in which both operators, k^{-2} and k^{-4}, play a role at different scales. In particular, Eq. (11.12) corresponds to the power spectrum calculated at the scales where the operator k^{-2} is the most relevant.

As it has been shown in Ch. 5, a temporal shift in the power spectrum implies intrinsic anomalous scaling of the local fluctuations. Here, the temporal shift is given by t^γ, and then, by following the theory of anomalous scal-

ing [67,92][cf. Eq. (5.20)], the scaling relation

$$\gamma = \frac{2(\alpha^{(\mathrm{I})} - \alpha_{\mathrm{loc}}^{(\mathrm{I})})}{z^{(\mathrm{I})}}, \tag{11.13}$$

must be fulfilled. We then conclude that, according to the spectral density (11.12), the scaling in the asymptotic regime (regime I) is anomalous in this case with a local roughness exponent $\alpha_{\mathrm{loc}}^{(\mathrm{I})} = 1/2$. Note that the local roughness exponent does not depend on the coupling exponent γ and self-affinity, $\alpha^{(\mathrm{I})} = \alpha_{\mathrm{loc}}^{(\mathrm{I})} = 1/2$, is recovered whenever the coupling is time independent ($\gamma = 0$). A comparison with numerical simulations for $\gamma = 0.3$ is shown in Figure 11.1.

11.1.2 Crossover from a rough to a flat regime

Another interesting situation occurs when the most relevant operator happens to lead to a flat surface. Here, a flat surface is understood in the sense that the interface fluctuations do not scale with the system size and therefore they become irrelevant in the thermodynamic limit. Accordingly, in this case the crossover is expected to take place from an early times (short scales) rough regime II, with roughness exponent $\alpha^{(\mathrm{II})} > 0$ to an asymptotic flat regime, where $\alpha^{(\mathrm{I})} \leq 0$. Again, a time dependent crossover length leads to nontrivial scaling properties in this case. Below the crossover we expect a rough phase dominated by the Φ_{II} term with exponents $\alpha^{(\mathrm{II})} > 0$ and $z^{(\mathrm{II})}$. Above the crossover length, however, surface correlations cannot evolve any longer since the operator Φ_{I} does not amplify surface fluctuations (note that $\alpha^{(\mathrm{I})} \leq 0$). This leads to an asymptotic roughness exponent identical to that in the early regime. Moreover, it is worth to stress here that the dynamical length scale $\sim t^{1/z^{(\mathrm{I})}}$ becomes a constant above the crossover (note that $z^{(\mathrm{I})} = 0$). Therefore, above the crossover length, the only relevant scale left in the problem scales as $\sim t^{\gamma/q}$. This must be identified with the correlation length $\ell_c(t)$ above the crossover. We therefore conclude that the time-dependent coupling leads to an asymptotic regime with exponents

$$\alpha = \alpha^{(\mathrm{II})}, \quad z = \frac{q}{\gamma}. \tag{11.14}$$

It is remarkable that, despite the most relevant term tends to flatten the surface, the time-dependent coupling conspires to produce a rough surface. The roughness exponent is inherited from the early time (short scale) phase. Meanwhile, the time-dependent crossover length becomes the only relevant scale above the crossover, which is to be associated with the dynamical exponent z of the system in the long times regime.

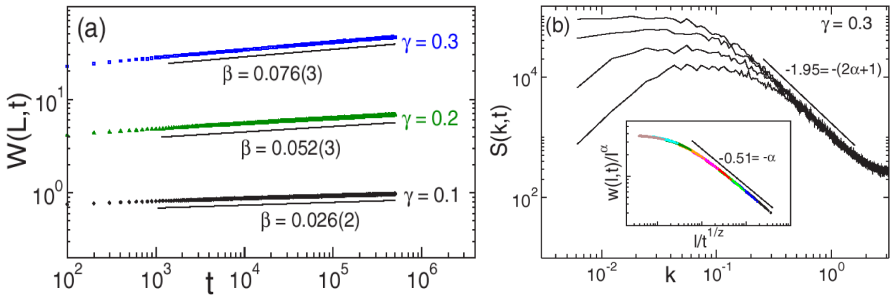

Fig. 11.2 Crossover from rough to flat. Numerical integration of Eq. (11.4) with conserved noise in a system size $L = 1024$. Results were averaged over 200 realizations. (a) Global width for different γ. The growth exponent was found to fit with the theoretical value $\beta = \gamma/4$. The curves are vertically shifted for clarity. (b) Power spectrum for $\gamma = 0.3$ at times 10^3, 10^4, 10^5, and 5×10^5. It shows a roughness exponent $\alpha = 0.48(3)$. The inset shows a data collapse of the local width data using $\alpha = 0.51(2)$ and $z = 6.63(4)$, which agrees with the scaling prediction $z = 2/\gamma$ for $\gamma = 0.3$.

To exemplify this general scaling analysis we now study a simple $1+1$ dimensional model system exhibiting a crossover between rough regime on short scales to a flat surface regime in the long wavelengths limit. Let us consider the same growth model as in (11.4), but the noise is now conserved,

$$\langle \xi_c(x,t)\xi_c(x',t')\rangle = -2\nabla^2\delta(x-x')\delta(t-t'). \tag{11.15}$$

Note that the surface diffusion operator $\nabla^2 h$ leads to flat surface fluctuations in the presence of conserved noise. On small scales the surface is expected to be dominated by the less relevant $\nabla^4 h$ term, so we obtain the exponents

$$\alpha^{(\mathrm{II})} = \alpha^{(\mathrm{II})}_{\mathrm{loc}} = \frac{1}{2}, \quad z^{(\mathrm{II})} = 4, \quad \beta^{(\mathrm{II})} = \frac{1}{8}, \tag{11.16}$$

in the early times (short scales) regime. On the other hand, above the crossover the $\nabla^2 h$ term governs the surface fluctuations and we find

$$z^{(\mathrm{I})} = \frac{2}{1-\gamma}, \quad \alpha^{(\mathrm{I})} = -\frac{1-3\gamma}{2(1-\gamma)}, \tag{11.17}$$

by simple power-counting as it has been done in the previously rough-to-rough section. Therefore, for values $0 < \gamma \leq 1/3$ we have the desired situation of a crossover from a rough to a flat regime ($\alpha^{(\mathrm{I})} \leq 0$). Therefore, according to our scaling argument, we expect scaling in the asymptotic regime with a roughness exponent

$$\alpha = \alpha^{(\mathrm{II})} = \frac{1}{2}, \quad z = \frac{2}{\gamma}, \quad \beta = \frac{\gamma}{4} \tag{11.18}$$

instead of the trivial values $\alpha^{(\mathrm{I})} = 0$ and $z^{(\mathrm{I})} = 0$ that would naively correspond to the $\nabla^2 h$ operator with conserved noise. A comparison with a numerical integration of the model for a time-dependent coupling with exponents $0 < \gamma < 1/3$ shows an excellent agreement with this analysis (see Figure 11.2).

11.1.3 Crossover to a damped regime

Finally, we discuss the case in which surface fluctuations become completely damped over a certain scale. This means that, for small deviations around the mean surface height, the terms $-h$, $-h^2$, ... have to be included in the growth equation. These terms break the $h \to h + c$ symmetry and therefore also break scale-invariance. Let us consider a growth model with the leading-order expansion $\mathcal{G} = -\omega(t)h(x,t) + \omega_{\mathrm{II}}\Phi_{\mathrm{II}}(x,t) +$ high-order terms, in such a way that the operator Φ_{II} is less relevant than the $-h$ damping term, but it would lead to scale-invariant behavior in the absence of damping. Following a scaling analysis similar to that of the previous sections, we find that for $z^{(\mathrm{II})} > q/\gamma$ the crossover to the damping regime will never take place. So, in all respects, the damping term is irrelevant and the surface will exhibit the scaling behavior corresponding to the operator II. On the other hand, if $z^{(\mathrm{II})} < q/\gamma$ the crossover then occurs when $\ell_c(t) \sim \ell_\times(t)$. The asymptotic regime in this case does exhibit scaling but with the nontrivial exponents

$$\alpha = \alpha^{(\mathrm{II})}, \quad z = \frac{q}{\gamma}, \tag{11.19}$$

for the same reasons as in the previously discussed rough-to-flat case. As a numerical example, the simple model

$$\frac{\partial h}{\partial t} = -\omega(t)h - \nabla^4 h + \xi(x,t), \tag{11.20}$$

is integrated with $\omega(t) \sim t^\gamma$. Note that in this example the crossover to the damping regime only occurs if $\gamma < z^{(\mathrm{II})}/4 = 1$. The predicted values for the scaling exponents are then

$$\alpha = \frac{3}{2}, \quad z = \frac{4}{\gamma}, \quad \beta = \frac{3\gamma}{8}, \tag{11.21}$$

which are in excellent agreement with the numerical results shown in Figure 11.3.

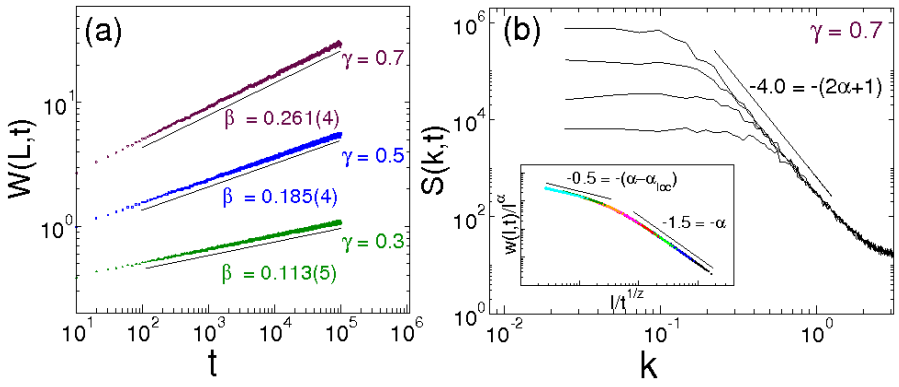

Fig. 11.3 Crossover from rough to a damped regime. Numerical integration of Eq. (11.20) in a system size $L = 256$. Results were averaged over 100 realizations. (a) Global width for different γ. The growth exponent was found to fit with the theoretical value $\beta = 3\gamma/8$. The curves are vertically shifted for clarity. (b) Power spectrum for $\gamma = 0.7$ at times 10^3, 10^4, 10^5, and 5×10^5. It shows a roughness exponent $\alpha = 1.50(3)$. The inset shows a data collapse of the local width data using $\alpha = 1.51(3)$ and $z = 5.73(4)$, which agrees with the scaling prediction $z = 4/\gamma$ for $\gamma = 0.7$.

11.2 Conclusions

We have shown that the presence of time-dependent coupling in non-equilibrium surface roughening has important implications in the scaling properties of the asymptotic regime. We have focused on local models that include the two most relevant terms separated by a crossover length scale growing in time, $\ell_\times(t) \sim t^{\gamma/q}$, which conspires with the correlation length of the system $\ell_c(t) \sim t^{1/z}$ to give highly nontrivial scaling properties. In the case of a crossover between two rough regimes, the surface may exhibit anomalous roughening, directly related to the value of $\gamma \neq 0$. On the other hand, in the case of a crossover from a rough to either a flat or damping regime, the dynamical crossover length $\ell_\times(t) \sim t^{\gamma/q}$ is the only relevant scale above the crossover and this immediately leads to an asymptotic rough regime with a dynamic exponent $z = q/\gamma$. A rough regime appears despite the most relevant term tends to flatten the surface. Remarkably, this is precisely the numerical result found in studies in spontaneous imbibition [2,45], presented in Ch. 7, where it was observed that the crossover length $\ell_\times \sim t^{1/4}$ gave rise to a dynamic exponent $z = 4$. This means that the term $\dot{H}|k|\hat{h}_k$ in the imbibition linearized equation (4.22) must produce flat surfaces above the crossover length. Our results show that these numerical results can be understood in the wider context of kinetic roughening in systems with time-dependent couplings.

Part III Avalanche dynamics in surface growth

12
Introduction

The results presented in the preceding Part have been mainly focused on the statistical properties of an interface involved in a kinetic roughening process. In particular, the interface fluctuations observed in imbibition have been extensively studied in terms of anomalous scaling scenarios, described by the roughness exponents α and α_{loc}, the growth exponents β and β^*, and the dynamical exponent z. Any study presented so far, however, has paid attention on the interface dynamics itself.

Likewise, little is known about avalanches in a non-local dynamics like the one that governs fluid flow in disordered media. Numerically, only the recent work by Rost *et al.* [125] has focused on the avalanche behavior but in a regime of relatively high velocities. On the other hand, and from an experimental point of view, a series of works carried out by Planet *et al.* [113] have recently started in order to study avalanches in experiments of forced-flow imbibition.

Precisely, our aim in this Part of the thesis is to study the spatio-temporal dynamics of an interface advancing into a disordered medium. To this end, we present several theoretical and numerical studies concerning the *avalanche dynamics* observed during imbibition in disordered media. Our main motivation in these studies is to get a connection between avalanche dynamics, velocity-fluctuation spectra and roughening exponents in a regime near the *depinning transition* or pinned state. Avalanches will be studied by using two different definitions. First, we define *local* avalanches from the spatio-temporal activity map, which allows to characterize an avalanche by means of a lateral extent, size and duration. On the other hand, *global* avalanches are defined from the temporal fluctuations of the spatially averaged velocity $\overline{v}(t)$, and are the result of the convolution of all the activity in the system at a given time.

Therefore, the structure of this third Part is as follows. Chapter 13 presents a theoretical framework to study avalanches in models of surface growth. In particular, several aspects concerning interface activity, avalanche motion an temporal correlations are studied. The theory is presented in a generic way to describe moving interfaces in disordered media, and will be applied in the case of forced-flow imbibition in Ch. 14. We present there an analytical and numerical study of forced-flow imbibition fronts, described in terms of a lo-

cal avalanche dynamics. Our results are also compared to the scaling theory derived in Ref. [125] which we find valid only in a regime of high velocities. Likewise, we show that a different and well defined scaling regime appears as the mean interface velocity is decreased. Finally, the last chapter of this Part deals with a different way of analysing the avalanche dynamics, based on the study of global fluctuations in forced-flow imbibition, and it is mainly motivated by the experimental work carried out in Ref. [113].

13
Avalanche theory of driven interfaces in disordered media

In many physical systems, the response to a slow external driving usually involves avalanches or bursts. Different examples are found in fracture cracks [11, 98], granular material [36], earthquakes [52], or imbibition of fluids in porous media [113, 125]. Having the main motivation in the latter example, we consider here the general problem of a moving interface driven into a disordered media. The interplay between the random pinning forces of the medium, the driving force and the interactions among the interface degrees of freedom, may give rise the interface to show a spatio-temporal complex dynamics over an extended macroscopic scale $\ell_\times$. In particular, a natural interesting situation in this context appears close to the *depinning transition*, where the driving force approaches a critical value below which the interface gets completely pinned. In this limit, typical velocities go to zero and correlations can extent up to the system size L, allowing collective transport phenomena to occur in terms of critical avalanches.

This Chapter presents several tools useful to completely characterize the dynamics of the interface, including activity statistics, avalanche scaling properties, interface temporal correlations and velocity fluctuations [96]. As it is shown, all the magnitudes are related to each other by scaling laws that we derive by means of simple scaling arguments. The theoretical framework is, in principle, expected to be valid for general models in $d+1$ dimensions[1], where surface roughness fluctuations are driven by local avalanches. It is also assumed that the interface height $h(\boldsymbol{r},t)$ at position $\boldsymbol{r}$ and time t, and the local interface velocity $v(\boldsymbol{r},t) \equiv \partial_t h(\boldsymbol{r},t)$ are well defined. In order to gain clarity and practicality, the end of this Chapter is provided with a table summarizing all the scaling relations derived here.

1) Let us note here that the scaling relations will be derived by assuming the simplest case of $d=1$. The resulting final equation, however, shall be expressed in $d+1$ dimensions.

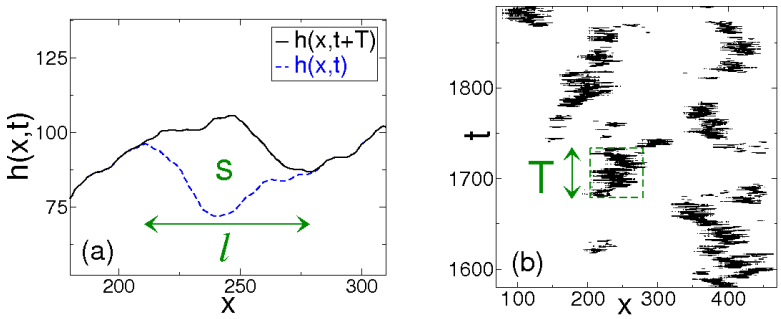

Fig. 13.1 Numerical example of forced-flow imbibition (see next Chapter). Typical avalanches of the front $h(x,t)$ in (a) are defined from the spatio-temporal activity in (b), and are characterized by the size s, lateral extent ℓ, and duration T.

13.1 Activity statistics

In order to study the avalanche dynamics of a moving interface, we first define the so-called *local activity map*. The *active sites* on the interface are defined as those where the local velocity takes values above some fixed threshold,

$$v(x,t) > c_{\text{th}}\overline{v}, \tag{13.1}$$

where c_{th} is some arbitrary constant, and $\overline{v}$ is the spatially averaged velocity along the whole system L

$$\overline{v} = \frac{1}{L}\int_L v(x,t)\mathrm{d}x. \tag{13.2}$$

This thresholding method allows to treat a continuum model in terms of a binary variable that takes the values 1 (active) or 0 (non-active). An example of activity pattern is shown in Fig. 13.1(b). Note that the activity map actually depends on the value of the constant c_{th}: the density of the activity points decreases as the constant is increased. We have to make sure, though, that our final results are not depending on such a threshold value. As it is explained in next Chapter, this dependency can be avoided by rescaling the variables.

For a model where activity is recurrent in time at any particular site, Maslov *et al.* [99] showed that the probability density function (PDF) for a site to become active after a time interval of inactivity, or waiting time interval t is given by the first-return time probability $\mathcal{P}_f(t)$, which is normalized

$$\int_{\delta T}^{\infty} \mathcal{P}_f(t)\mathrm{d}t = 1, \tag{13.3}$$

where the temporal resolution can be set to unity, $\delta T = 1$, without loss of generality. This probability describes the time intervals separating subsequent return points of activity at any given site. Then, the average number of return

points, $n(T)$, in a time interval T can be determined as follows. Note that the total length of inactivity in an interval T is given both by $T - n(T)$ and also by $n(T)\int_1^T t\mathcal{P}_f(t)\mathrm{d}t$. Therefore, we can write the following balance equation

$$n(T) = T - n(T)\int_1^T t\mathcal{P}_f(t)\mathrm{d}t. \tag{13.4}$$

Fractal activity.- In a critical system with long-range spatio-temporal correlations, as for example near the pinning/depinning critical transition ($\overline{v} \to 0$) or in growth models that self-organize to the critical state, the activity is expected to be scale-invariant (fractal) and therefore, the first-return time probability to scale as

$$\mathcal{P}_f(t) \sim t^{-\beta_f}, \tag{13.5}$$

for $t \gg 1$, with $\beta_f \in (1, 2]$. Consequently, Eq. (13.4) can easily be integrated, obtaining that the average number of return points in an interval $T \gg 1$ is

$$n(T) \sim T^{\theta}, \qquad \text{with} \qquad \theta = \beta_f - 1. \tag{13.6}$$

The fractal dimension θ of return points of activity at any site becomes therefore connected to the distribution of waiting times. Note that fractal activity implies an infinite average return time $\langle t \rangle = \int_1^{\infty} t\mathcal{P}_f(t)\mathrm{d}t \to \infty$, typical of critical dynamics.

Exponential activity.- If the system has an intrinsic typical scale $\ell_\times$ limiting the correlated extent, the first-return time probability is given then by a power-law exponentially cut off

$$\mathcal{P}_f(t) \sim t^{-\beta_f} \mathrm{e}^{-\frac{t}{t_0}}, \tag{13.7}$$

with a finite average return time $\langle t \rangle \sim t_0$. Applying again the balance equation (13.4), the average number of returns points becomes then

$$n(T) \sim \begin{cases} T^{\theta} & \text{for} \quad 1 \ll T \ll t_0, \\ \\ \overline{v}T & \text{for} \quad T \gg t_0, \end{cases} \tag{13.8}$$

where θ is given by Eq. (13.6), and $\overline{v} \sim 1/t_0$ is a finite average surface velocity, due to the existence of a finite average return time. Note that the limit $t_0 \to \infty$ (fractal activity) also implies $\overline{v} \to 0$.

13.2 Local avalanche dynamics

Local avalanches of forward moves can be monitored through the activity map of the interface. We define an avalanche as a connected cluster of active $[v(x,t) > c_{\rm th}\overline{v}]$ sites surrounded by non-active $[v(x,t) < c_{\rm th}\overline{v}]$ sites. Figure 13.1 shows how avalanches can be defined in an example of forced-flow imbibition (see next Chapter). Then, local avalanches are characterized by a lateral extent ℓ and a duration T, given directly by the lateral and vertical length of the activity cluster, and a typical size (volume) s, defined as

$$s = \int_{\ell} [h(x, t_i + T) - h(x, t_i)] \mathrm{d}x, \tag{13.9}$$

where t_i represents the initial time of the avalanche. It is important to remark here that we are considering local avalanches defined directly from the spatio-temporal activity pattern, and therefore different than those defined from a fluctuating global magnitude, such as for example the global mean velocity $\overline{v}(t)$ recently studied in a couple of imbibition works [113, 125]. Likewise, a detailed description of this alternative analysis is provided in Ch. 15.

For a given lateral correlation length $\ell_\times$ of the interface fluctuations, it is expected the average avalanche size to scale with the lateral extent as

$$\langle s(\ell) \rangle \sim \ell^D, \tag{13.10}$$

for $\ell \ll \ell_\times$, where D is the avalanche dimension exponent that can be easily related with the *local* roughness exponent $\alpha_{\rm loc}$. One has that the vertical extent of an avalanche of lateral length ℓ is of the order of the interface fluctuation width $w(\ell)$ (see Ch. 5). Therefore, we can write $\langle s(\ell) \rangle \sim \ell^d w(\ell) \sim \ell^d \ell^{\alpha_{\rm loc}}$, and then

$$D = d + \alpha_{\rm loc}, \tag{13.11}$$

in $d+1$ dimensions. In addition, we expect both the average avalanche lateral extent and average size to scale with the duration as

$$\langle \ell(T) \rangle \sim T^{1/z_{\rm av}}, \tag{13.12}$$

$$\langle s(T) \rangle \sim T^{\gamma}. \tag{13.13}$$

for $T \ll T_\times$, being $T_\times$ any typical time scale in the system. We have supposed here that the dynamics inside any avalanche is controlled by a *local dynamic exponent* $z_{\rm av}$ that could differ from the usual one z controlling the interface correlation growth. This would mean that the propagation of the interface correlations is decoupled from the avalanche dynamics. As it is shown in next Chapter, this behavior is observed to occur for example in short-ranged

correlated systems ($\ell_\times \ll L$), where the front motion can be decomposed in independent, spatially localized, avalanches of forward moves that can take place at the same time. Near a critical point, though, when long-range interface correlations fully coincide with avalanches of correlated events, the relation $z_{\rm av} = z$ should be recovered. In this situation, an avalanche occupies a significant fraction of lateral extent of the system and cooperative correlated motion over large scales does occur, expecting that only one avalanche occurs at a given time.

In any case, the exponent γ in Eq. (13.13) relating avalanche sizes with durations can generally be expressed as

$$\gamma = \frac{D}{z_{\rm av}} = \frac{d + \alpha_{\rm loc}}{z_{\rm av}}. \tag{13.14}$$

In the following, we shall assume that the dynamics of the front in the saturated regime is actually being dominated by its avalanche motion and therefore, either the condition $z_{\rm av} = z$ is fullfilled or not, the scaling relations involving avalanche dynamics will be generally expressed in terms of the local dynamic exponent $z_{\rm av}$.

It is worth to note here that in the case of fractal activity ($\ell_\times \to \infty$), the exponents $z_{\rm av}$ and $\alpha_{\rm loc}$ can be connected to the exponents θ and β_f from activity statistics in Eq. (13.6). One has that the avalanche size can be written in terms of the average number of return points of activity as

$$s \sim n(T)\ell^d \sim \ell^{\theta z_{\rm av}+d}. \tag{13.15}$$

Comparing to Eq. (13.10), we can conclude that

$$\theta = \frac{\alpha_{\rm loc}}{z_{\rm av}}, \qquad \beta_f = 1 + \frac{\alpha_{\rm loc}}{z_{\rm av}}, \tag{13.16}$$

which connects the local roughness of the interface $\alpha_{\rm loc}$ with the statistics of the first-return time probability $\mathcal{P}_f(t) \sim t^{-\beta_f}$.

Finally, it is also possible to define the front velocity $v(\ell)$ over a region ℓ spanned by the avalanche as the ratio between the vertical length of the avalanche and the elapsed time, $v(\ell) \sim w(\ell)/T$, which gives the relation

$$v(\ell) \sim \ell^{-\delta}, \qquad \text{with} \qquad \delta = z_{\rm av} - \alpha_{\rm loc}, \tag{13.17}$$

connecting avalanche dynamics with surface roughness. The exponent δ gives account of possible inter-events correlations. For instance, as it is shown in the following Chapter, in the case of exponential activity with uncorrelated avalanches ($\ell_\times \ll L$), the fluctuations of the avalanche velocity are Gaussian with $\delta = d/2$ [125].

Avalanche distributions

In order to study the statistics of the avalanche dynamics, it is usually required to calculate the probability density functions $\mathcal{P}(s)$, $\mathcal{P}(T)$ and $\mathcal{P}(\ell)$ for having avalanches of size s, duration T, and lateral extent ℓ, respectively. For systems with a diverging correlation length, these PDFs show criticality and are given by

$$\mathcal{P}(s) \sim s^{-\tau_s}, \quad \mathcal{P}(\ell) \sim \ell^{-\tau_\ell}, \quad \mathcal{P}(T) \sim T^{-\tau_T}. \tag{13.18}$$

Let us now consider the joint probability $\mathcal{P}(s, \ell, T)$ for having an avalanche of size s, extent ℓ, and duration T. Scale-invariant behavior implies that

$$\mathcal{P}(s, \ell, T) = b^{\sigma} \mathcal{P}(b^D s, b\ell, b^{z_{\rm av}} T), \tag{13.19}$$

for any scaling factor $b > 0$. Integrating then over two of the arguments one obtains each one of marginal PDFs

$$\begin{aligned}
\mathcal{P}(s) &= \int \mathcal{P}(s, \ell, T) \mathrm{d}\ell \mathrm{d}T = b^{\sigma - 1 - z_{\rm av}} \mathcal{P}(b^D s), \\
\mathcal{P}(\ell) &= \int \mathcal{P}(s, \ell, T) \mathrm{d}s \mathrm{d}T = b^{\sigma - D - z_{\rm av}} \mathcal{P}(b\ell), \\
\mathcal{P}(T) &= \int \mathcal{P}(s, \ell, T) \mathrm{d}s \mathrm{d}\ell = b^{\sigma - D - 1} \mathcal{P}(b^{z_{\rm av}} T).
\end{aligned}$$

Applying the expressions of Eq. (13.18) into the above relations, we finally get the scaling relations

$$\tau_T = 1 + \frac{D}{z_{\rm av}}(\tau_s - 1), \qquad \text{and} \qquad \tau_\ell = 1 + z_{\rm av}(\tau_T - 1), \tag{13.20}$$

that must be satisfied in the case of scale-invariant avalanche dynamics. They connect the avalanche activity exponents (τ_T, τ_s, τ_ℓ) with the avalanche dynamics ($z_{\rm av}$) and morphology (D).

Again, in a system with a finite correlation length $\ell_\times$ (exponential activity), the PDFs of Eq. (13.18) are not generically expected to be critical, but exponentially decaying functions:

$$\mathcal{P}(\varrho) \sim \varrho^{-\tau_\varrho} \exp\left(-\varrho/\varrho_\times\right), \tag{13.21}$$

where the index ϱ denotes the size s, lateral extent ℓ, or duration T of avalanches, and τ_ϱ is its characteristic exponent. The distribution cutoff $\varrho_\times$ will depend explicitly on the typical scales of the problem, in such a way that in the limit $\ell_\times \to \infty$ the critical behavior is recovered.

13.3 Heterogeneous growth and multiscaling

An additional tool to understand the dynamics inside avalanches is to study the height-height temporal correlations. As it was pointed out by Leschhorn *et al.* [91, 106], the presence of localized avalanches implies an heterogeneous growth which may give rise to multiscaling. Consider the height-height time correlation function in the saturated regime

$$C_q(t) = \left\langle \overline{|h(x,t+t') - h(x,t') - \overline{h(x,t+t') - h(x,t')}|^q}^{1/q} \right\rangle, \tag{13.22}$$

where t' represents an arbitrary time origin. Here, the overbar denotes average over x and $\langle..\rangle$ denotes average over time origin t' and disorder realizations. In the limit $q \to \infty$, only the site x with maximum height advance contributes to the infinite moment, and then we can write

$$C_\infty(t) \simeq \langle \max_x [h(x,t+t') - h(x,t')] \rangle \equiv \Delta h_{\max}(t). \tag{13.23}$$

During a time interval t, the maximum height advance $\Delta h_{\max}(t)$ corresponds to the typical height fluctuation produced by an avalanche. Then, for time intervals shorter than the mean avalanche duration, $t \ll T_\times$, the infinite moment can be related to the avalanche size as

$$C_\infty(t) \sim \frac{s(t)}{\ell^d} \sim t^{\beta_\infty}, \qquad \text{with} \qquad \beta_\infty = \frac{\alpha_{\text{loc}}}{z_{\text{av}}}, \tag{13.24}$$

where relation (13.12) has been applied. Therefore, we observe that by calculating the infinite moment $C_\infty(t)$ of the height-height time correlation we can obtain information about the local avalanche dynamics through the exponent $z_{\text{av}} = \alpha_{\text{loc}}/\beta_\infty$. This can be a really useful tool in experimental work, where one may have access to the interface position at different times $h(x,t)$. Since the local roughness exponent is usually determined by standard scaling tools (see Ch. 5), the local dynamic exponent simply comes from looking at $C_\infty(t)$.

On the other hand, the other moments $C_q(t)$ can be analytically estimated close to a critical point ($\ell_\times \to \infty$) by considering the following [91]. First, note that in this limit avalanches can extent up to the whole system and then it is expected that only one avalanche of lateral length ℓ is growing at a given time. Therefore, only the fraction $\ell/L \sim t^{1/z_{\text{av}}}/L$ of the interface is moving. Second, if we consider that the height advancement $\Delta h \equiv h(x,t+t') - h(x,t')$ scales

as $\Delta h \sim t^{\beta_\infty}$, we have

$$\begin{aligned} C_q(t) &= \left\langle \overline{|\Delta h - \overline{\Delta h}|^q}^{1/q} \right\rangle, \\ &= \left\langle |\overline{\Delta h^q} - q\overline{\Delta h^{q-1}}\,\overline{\Delta h} + \cdots + \overline{\Delta h}^q|^{1/q} \right\rangle \\ &\simeq \left\langle \left| \frac{t^{1/z_{\rm av}}}{L} t^{q\beta_\infty} - q\frac{t^{1/z_{\rm av}}}{L} t^{(q-1)\beta_\infty}\frac{t}{L} + \cdots + \frac{t^q}{L^q} \right|^{1/q} \right\rangle, \end{aligned} \tag{13.25}$$

where it has been supposed that $\overline{\Delta h}(t) \simeq t/L$ and $\overline{\Delta h^q} \simeq (\ell/L)t^{q\beta_\infty}$. In the regime of $t \ll L^{z_{\rm av}}$, the main contribution in the sum of the above equation comes from the first term [91], obtaining in $d+1$ dimensions

$$C_q(t) \sim t^{\beta_q}, \qquad \text{with} \qquad \beta_q = \beta_\infty + \frac{d}{qz_{\rm av}} = \frac{q\alpha_{\rm loc} + d}{qz_{\rm av}}, \tag{13.26}$$

for $t \ll T_\times$. It is also important to remark that the approximations used to derive the above expression could not be valid in systems with a short finite extent of the interface correlations ($\ell_\times \ll L$), where several uncorrelated avalanches may occur at the same time.

The different time scales involved in the problem are then characterized by the multiscaling of $C_q(t)$ for $t \ll T_\times$. This can be seen for instance in the time scale defined by $C_1(t) \sim t^{\beta_1}$ which is associated with the avalanche size growth $s \sim t^\gamma$, where γ is given by Eq. (13.14) and thus equals $\beta_1 = (\alpha_{\rm loc} + d)/z_{\rm av}$. Likewise, in the limit $q \to \infty$, the exponent β_∞ is directly related to the fractal dimension of return points in a given site, $\beta_\infty = \theta$, which in turn, can be related to the first-time probability exponent

$$\beta_f = \beta_\infty + 1. \tag{13.27}$$

This relation is important because allows us to associate a global observable (∞-correlation moment) with a local observable (distribution of return times of activity at any given site). Having a connection between global and local magnitudes is always something desirable since it is usually difficult to have direct experimental access to both of them. The following section presents another way to get this connection.

13.4 Velocity correlations

The last point we want to address, which is also related to the previous defined concepts, is the temporal correlations of the global mean interface velocity $\overline{v}(t) \equiv \partial_t \overline{h}(t)$. To this end, we shall study the power spectrum of the mean

interface velocity, $\mathcal{S}_{\bar{v}}(w) \equiv \langle|\widehat{\bar{v}}(w)|^2\rangle$. First, note that $\widehat{\bar{v}}(w) = -iw\widehat{\bar{h}}(w)$, and therefore the velocity fluctuation spectrum:

$$\mathcal{S}_{\bar{v}}(w) = w^2\langle|\widehat{\bar{h}}(w)|^2\rangle. \tag{13.28}$$

On the other hand, as it was explained in Ch. 5, the structure factor describing height-height correlations scales as

$$\mathcal{S}_h(k,t) = k^{-(2\alpha+d)}s_A(kt^{1/z_{\rm av}}), \tag{13.29}$$

where α is the global roughness exponent and $s_A(u)$ is a scaling function that takes the value $s_A(u) \sim u^{2\alpha+d}$ for $u \ll 1$. Then, in the limit $k \to 0$ we have

$$\langle|\widehat{\bar{h}}(w)|^2\rangle = \lim_{k\to 0}\mathcal{S}_h(k,w) \sim (1/w)^{\frac{2\alpha+d}{z_{\rm av}}+1}, \tag{13.30}$$

in the frequency domain. The above relation allows us to conclude that

$$S_{\bar{v}}(w) \sim w^{-\nu}, \qquad \text{with} \qquad \nu = \frac{2\alpha+d}{z_{\rm av}} - 1, \tag{13.31}$$

which relates the low-frequency behavior of the velocity power spectrum to the roughness of the growing interface. This formula generalizes an earlier analytical result [72], $\nu = (d+4)/z - 3$, valid for the Kardar-Parisi-Zhang equation [70]. Again, without loss of generality, we have assumed here that the front dynamics is mainly controlled by the avalanche motion and therefore by the local dynamic exponent $z_{\rm av}$.

Finally, an important scaling relation emerges if the exponent ν from the velocity power spectrum equals the exponent γ relating avalanche sizes *vs* durations, given by Eq. (13.14). In general terms we write

$$\nu = \gamma \quad \Leftrightarrow \quad z_{\rm av} = 2\alpha - \alpha_{\rm loc}. \tag{13.32}$$

The importance of this relation is that it establishes a connection between a global (ν) and local (γ) magnitude, and also connects the scaling of the interface roughness (α, $\alpha_{\rm loc}$) with the dynamics of the avalanches ($z_{\rm av}$).

13.5 Extremal dynamics

An interesting case where this theory can be applied is in the models exhibiting the so-called *extremal dynamics* [91, 106, 133]. In this kind of dynamics, there is only one lattice site where activity occurs at any given time step. Consequently, the avalanche size is proportional to the duration ($s \sim T^{\gamma}$ with

Exponents		Scaling relations
α, $\alpha_{\rm loc}$	interface roughness	$D = \alpha_{\rm loc} + d$
$z_{\rm av}$	avalanche dynamics	$\gamma = D/z_{\rm av}$
D	avalanche dimension	$\delta = z_{\rm av} - \alpha_{\rm loc}$
γ	avalanche size-duration	$\tau_T = 1 + \gamma(\tau_{\rm s} - 1)$
δ	avalanche velocity	$\tau_\ell = 1 + z_{\rm av}(\tau_T - 1)$
$\tau_{\rm s}$, τ_T, τ_ℓ	avalanche statistics	
β_f	first return probability	$\beta_f = 1 + \theta$
θ	activity returns	$\theta = \alpha_{\rm loc}/z_{\rm av}$
β_q	interface time correlation	$\beta_q = (q\alpha_{\rm loc} + d)/(qz_{\rm av})$
β_∞	infinite moment	$\beta_\infty = \alpha_{\rm loc}/z_{\rm av}$
ν	velocity power spectra	$\nu = (2\alpha + d)/z_{\rm av} - 1$
		$\gamma = \nu \;\Leftrightarrow\; z_{\rm av} = 2\alpha - \alpha_{\rm loc}$

Tab. 13.1: Summary of all the scaling relations derived in this Chapter for models of driven interfaces into disordered media in $d+1$ dimensions. All the scaling relations are expected to be valid within a critical extended region $\ell \ll \ell_\times$.

$\gamma = 1$) and therefore one has the relation

$$z_{\rm av} = \alpha_{\rm loc} + d, \tag{13.33}$$

which allows to conclude that the infinite moment of height-height correlation function is given by

$$\beta_\infty = 1 - \frac{d}{z_{\rm av}}, \tag{13.34}$$

with $T_\times \to \infty$ since the model is critical.

13.6 Conclusions

We have studied several aspects concerning the dynamics of a moving interface in disordered media. The avalanche dynamics has been described through the local activity map of the interface, which has allowed to completely characterize local avalanches in terms of its morphology (D), dynamics ($z_{\rm av}$, γ), and statistics (τ_s, τ_T, τ_ℓ), obtaining several scaling relations connecting to each other.

Our main hypothesis has been to assume an interface dynamics dominated by the local dynamics occurring inside the avalanches, given by the exponent

z_{av}. Such an exponent can actually differ from the usual z controlling interface correlation growth, and can be detected, for instance, by studying the infinite moment of the height-height time correlation function (β_∞).

Finally, we have also studied the correlations of the global velocity $\overline{v}(t)$ through its power spectra. In the event of the exponents from the power spectra and the avalanche size growth being equal, $\nu = \gamma$, we have derived an important scaling relation connecting avalanche motion with the scaling of the interface.

All the scaling relations have been summarized in Table 13.1. The theoretical framework presented in this chapter gives a complete way of characterize local avalanches, and will be applied in the case of forced-flow imbibition in the following Chapter.

14
Forced-flow imbibition fronts

This Chapter presents theoretical and numerical results concerning the dynamics and morphology of driven interfaces during fluid imbibition in disordered media. Let us recall that in the case of *forced-flow imbibition*, the spatially averaged velocity of the liquid-air interface $\overline{v}$ is kept constant by means of a constant injection rate. For relatively low velocities, the invading fluid advances then in the form of spatially localized events or *avalanches*, as occurs in many other disordered systems.

Avalanche dynamics in imbibition is expected to be responsible for the front velocity fluctuations. Rost *et al.* [125] have recently shown that in the case of imbibition, which is a locally conserved process, velocity fluctuations are controlled by the length scale $\ell_\times$ arising from fluid conservation. This characteristic length scale introduces a natural cutoff in the distribution of avalanche sizes and durations, which leads to non-critical avalanche distributions and is ultimately responsible for the lack of correlated fluctuations at large distances. Forced-flow imbibition described by avalanches with a fixed cutoff size has been experimentally observed in the recent works by Planet *et al.* [113] by means of analyzing the global velocity time series $\overline{v}(t)$, and Santucci *et al.* [130] by studying a local velocity map.

The results presented in this Chapter focuses on studying the statistics of local avalanches, interface roughness, temporal correlations, and velocity correlations in forced-flow imbibition. We analyze the mesoscopic behavior of the interface by monitoring locally active sites, *i.e.* those sites that are moving at a given time, which define the actual avalanche taking place in the system. Our study explores a regime of imbibition fronts close to the depinning transition ($\bar{v} \to 0$), never studied neither experimentally nor numerically in terms of the non-local model of imbibition. The singularity appearing as $\overline{v} \to 0$ affects the value of the critical exponents that characterize the front dynamics and morphology– namely, the avalanche exponents, as well as the roughness exponents. This leads to *effective* exponents due to crossover effects.

By making use of the scaling concepts explained in the preceding Chapter we are able to theoretically describe the dynamics of forced-flow imbibition fronts both in the static limit (long-range correlations, fractal activity) and also

in a regime of relatively high velocities (short-range correlations, exponential activity), obtaining excellent agreement with numerical results from a phase field model [119].

14.1 Theoretical description

The dynamics of the interface fluctuations $h(x,t)$ in slow forced-flow imbibition is given by the linearized equation derived in Chapter 4, which we rewrite here for convenience

$$\partial_t \hat{h}_k = -\sigma \overline{K}_0 |k| k^2 \hat{h}_k - \dot{H}|k|\hat{h}_k + \overline{K}_0 |k| \hat{\xi}_k. \tag{14.1}$$

where σ is surface tension, $\overline{K}_0$ is the mobility of the media, and $\hat{\xi}_k$ are the Fourier components of the capillary disorder at some coarse-grained scale. As it has been observed in several works [2, 45, 84] (see also the results presented in Part II of this thesis), the scaling properties in imbibition are largely depending on the crossover length

$$\ell_\times \simeq \left(\frac{\sigma \overline{K}_0}{\overline{v}} \right)^{1/2}, \tag{14.2}$$

that comes out when the surface tension and velocity terms in Eq. (14.1) are balanced. The main point is that interface fluctuations are uncorrelated above this typical scale [2], introducing then a natural cutoff in the system. Therefore, due to the existence of such a cutoff length, avalanches are expected to be power-law distributed with an exponentially decaying function. In the case of avalanche sizes, for instance, we have

$$\mathcal{P}(s) \sim s^{-\tau_s} \exp\left(-s/s_\times\right), \tag{14.3}$$

where the maximum avalanche size depends explicitly on $\overline{v}$ as

$$s_\times \sim \ell_\times^D \sim (\overline{v})^{-D/2}, \tag{14.4}$$

with $D = \alpha_{\mathrm{loc}} + d$. This cutoff diverges ($\ell_\times \to \infty$) as the control parameter $\overline{v} \to 0$, which renders critical avalanches expanding over the whole system. This divergence is very strong, $s_\times \sim (\overline{v})^{-1}$, already in $d = 1$, which, in turn, is expected to be reflected in long-tailed avalanche distributions even for finite values of $\overline{v}$. Forced-flow imbibition is therefore an interesting phenomenon because allows to study how the avalanche dynamics is modified in a model where the correlation length, given by $\ell_\times$, can be tunned toward pinning by

decreasing the mean interface velocity. Our theoretical and numerical results shall be mainly focused in the limit $\overline{v} \to 0$, and are to be contrasted to previous analytical work by Rost *et al.* [125] describing a regime of relatively high velocities.

Let us finally remark that although we study a regime referred to as *high velocities regime*, all the velocities considered here are low enough to guarantee that the permeability disorder does not play any role in the interface roughening (see Ch. 4 for more details about this point).

14.1.1 Scaling theory in the static limit

The interface scaling exponents in forced-flow imbibition can be obtained by a scaling theory which is expected to be valid in the *static* (pinned state) limit $\overline{v} \to 0$. In the pinned state the velocity-dependent term in Eq. (14.1) cancels and the geometric properties of the front can be described by the balance between surface tension and capillary disorder, which in real space can be written as

$$\sigma \nabla^2 h_{\rm p}(x) + \xi(x) \simeq 0 \tag{14.5}$$

where $h_{\rm p}(x)$ is the pinned state. Note that we are assuming here a columnar noise approximation as it has also been done in Chapter 7 when describing spontaneous imbibition fronts in a limit of low velocities. This is actually an approximation based on numerical evidences, which need to be corroborated by experiments carried out in the static limit.

Applying a scaling transformation, $x \to b\,x$ and $h_{\rm p} \to b^{\alpha}\, h_{\rm p}$ in Eq. (14.5), scale-invariance holds for a global roughness exponent $\alpha = 3/2$ for the pinned state configuration. Then, small perturbations of the pinned state δh_p are assumed to relax towards another of the infinitely many pinned configurations according to

$$\partial_t(\delta h_p) = \sigma \overline{K}_0 \nabla^2(\delta h_p) + \overline{K}_0 \xi(x), \tag{14.6}$$

which leads to the exact interface exponents

$$z = 2, \qquad \alpha = \frac{3}{2}, \qquad \alpha_{\rm loc} = 1, \tag{14.7}$$

at the critical point $\overline{v} = 0$ for $d = 1$. As we stated in the preceding Chapter, near the depinning transition an avalanche may occupy a significant fraction of lateral extent of the system and long-range correlations are expected to coincide with avalanches of correlated events. Local dynamics inside of the avalanche (described by $z_{\rm av}$) must coincide with interface correlations growth

and hence we have $z_{\rm av} = z = 2$. This set of exponents can now be replaced into the scaling relations derived in the previous Chapter (see Table 13.1) to obtain

$$\begin{aligned} &\tau_T = \tau_s, \qquad \tau_\ell = 2\tau_T - 1, \qquad \gamma = \nu = 1, \\ &\beta_\infty = \frac{1}{2}, \qquad \beta_q = \frac{1+q}{2q}, \qquad \beta_f = \frac{3}{2}, \end{aligned} \tag{14.8}$$

where we have used $D = d + \alpha_{\rm loc} = 2$ in $d = 1$. An interesting point to remark here is that avalanches in forced-flow imbibition near the depinning transition are described in terms of an *extremal dynamics* [91,106,133], reflected in the value $\gamma = 1$. As it was stated in the preceding Chapter, in this kind of dynamics only one site is growing at any given time. Consequently, the avalanche size is proportional to the duration ($\gamma = 1$) and therefore one has the relation

$$z_{\rm av} = \alpha_{\rm loc} + d. \tag{14.9}$$

In addition, if we consider the condition $\nu = \gamma$ [1], we can therefore conclude that the interface roughness exponents α and $\alpha_{\rm loc}$ must be related to each other as

$$\alpha = \alpha_{\rm loc} + \frac{d}{2} \quad \Leftrightarrow \quad \nu = \gamma. \tag{14.10}$$

In our case of forced-flow imbibition, the above relation is in perfect agreement with the values $\alpha = 3/2$ and $\alpha_{\rm loc} = 1$ in $d = 1$, obtained by assuming columnar disorder in Eq. (14.6).

Finally, it is also worth to mention that in the static limit, the different moments of the height-height time correlation function $C_q(t)$ give the information about all the typical growths of the interface. For instance, the first moment is related to the avalanche size growth, $\beta_1 = \gamma$, and the second moment to the usual global growth exponent for the interface fluctuations, $\beta_2 = \beta = \alpha/z$.

14.1.2 Scaling theory at high velocities

The scaling properties of the interface roughness in forced-flow imbibition in a regime of relatively high velocities have been studied in several works [2,84] (see also Ch. 10 of this thesis), all of them arriving at the conclusion that the

1) Recall that the exponent ν comes from the velocity power spectra $\mathcal{S}_{\bar{v}}(w) \sim w^{-\nu}$.

interface fluctuations are described by the exponents

$$z = 3, \qquad \alpha = \frac{5}{4}, \qquad \alpha_{\rm loc} = 1, \tag{14.11}$$

which are in agreement with the linearized equation (14.1). The main point in this regime is that the interface correlations are limited by the crossover length $\ell_\times$ and therefore non-critical avalanches are expected.

In a recent work by Rost *et al.* [125], it has been analyzed a regime of relatively high velocities for which the length scale $\ell_\times$ is very small as compared with system size L. In this regime avalanches are very narrow and one can decompose the front motion in independent, spatially localized, avalanches of forward moves. If simultaneous avalanches are narrow and independent, one should expect Gaussian fluctuations of the avalanche velocity

$$v(\ell) \sim \ell^{-\delta}, \qquad \text{with} \qquad \delta = \frac{d}{2}, \tag{14.12}$$

where it has been supposed an uncorrelated motion, $\langle v(\ell)v(\ell')\rangle \sim \delta(\ell - \ell')$ [125]. Therefore, by making use of the scaling theory of Table 13.1, one easily get that in $d = 1$

$$z_{\rm av} = \frac{3}{2}, \qquad \beta_\infty = \frac{2}{3}, \qquad \gamma = \nu = \frac{4}{3}, \tag{14.13}$$

expected to be valid only in a velocity regime such that the characteristic length scale is negligible as compared with the system size $\ell_\times \ll L$. Note that in this regime the propagation of the interface correlations is decoupled from the avalanche dynamics ($z_{\rm av} \neq z$). In addition, it is interesting to note that as in the static limit, the exponent $z_{\rm av}$ is also in agreement with the relation $z_{\rm av} = 2\alpha - \alpha_{\rm loc}$ since the condition $\gamma = \nu$ is still valid.

Let us recall that for lower front velocities, when $\ell_\times$ becomes comparable with the system size, the scaling exponents should tend to the values given by Eq. (14.8) instead of (14.13). In the following we compare these scaling results with numerical integrations of a phase field model as one approaches the singular point $\overline{v} = 0$.

14.2 Numerical results

Forced-flow imbibition is numerically studied with the phase field model described in Chapter 4. The phase field equation

$$\frac{\partial \phi}{\partial t} = \boldsymbol{\nabla} M \boldsymbol{\nabla} \big[-\phi + \phi^3 - \epsilon^2 \nabla^2 \phi - \xi(\boldsymbol{r}) \big], \tag{14.14}$$

is integrated in a two-dimensional system of lateral size $L = 512$ and 25 disorder realizations with $\epsilon = 1$, and the forced-flow boundary condition $\nabla\mu = -\bar{v}\hat{y}$ is imposed at the bottom of the system [84]. We have used a grid space $\Delta x = 1.0$ and time step $\Delta t = 0.01$. All the values for the average front velocity have been normalized to a reference value $v_0 = 0.002$, which corresponds to the highest value used in our study. We have used a dichotomic quenched disorder $\xi(x, y)$ taking the values $\xi_1 = 1.0$ and $\xi_2 = 1.6$ randomly distributed in such a way that sites with $\xi = \xi_2$ fill the 35 % of the whole system. All the data analysis has been performed in a statistically stationary state, after the interface fluctuations reach the saturated width.

Avalanche and activity statistics.- Local avalanches are defined through the activity map as it is described in the preceding Chapter (see Fig. 13.1). The clusters of connected active points give the information about avalanche lateral extent ℓ and duration T. The avalanche size is then defined by the area swept by the interface during a time interval T and along a lateral length ℓ.

Figures 14.1(a) and 14.1(b) show the avalanche size and duration statistics calculated using a threshold $c_{\rm th} = 3$. We observe that the probability distributions tend to a power-law as $\overline{v}$ is decreased, due to the divergent cutoff [cf. Eq. (14.4)]. We estimate the exponents $\tau_s \simeq 1.54(5)$ and $\tau_T \simeq 1.62(6)$ from the scaling of the data. Despite the smallest velocity we were able to reach $\overline{v} = v_0/40 = 5 \times 10^{-5}$ is still far from zero, the scaling region is reasonably good. According to our scaling theory of Eq. (14.8) both exponents should exactly coincide at the critical point, which is consistent with the numerical values within the error bars. We also plot a direct estimate of the divergent avalanche size cutoff in good agreement with Eq. (14.4).

An important point to check in our numerical results is that the exponents τ_s and τ_T from the avalanche size and duration PDFs, respectively, do not depend on the threshold value $c_{\rm th}$ we use. The inset of Fig. 14.1(b) and Fig. 14.1(c) show the PDFs of durations and sizes, respectively, for different choices of the arbitrary threshold from 3 to 20 in the case of $\overline{v} = v_0/40 = 5 \times 10^{-5}$. We can see that increasing the threshold just introduces an artificial cutoff $T_{c_{\rm th}}$ and $s_{c_{\rm th}}$ but does not change the exponent value. As it is shown in Fig. 14.1(d), this threshold dependency can actually be removed if we plot the avalanche size distribution normalized by the average size

$$\mathcal{P}(x) = a\, x^{-\tau_s} \exp(-bx), \qquad \text{with} \qquad x = \frac{s}{\langle s \rangle}, \tag{14.15}$$

where now a and b are constants that do not depend on the threshold cutoff [2].

2) This is not strictly true since the parameters a and b depend on integrals like $\int_\lambda^\infty y^{1-\tau_s} e^{-y} dy$, where $\lambda = s_m/s_{c_{\rm th}}$, with s_m being the

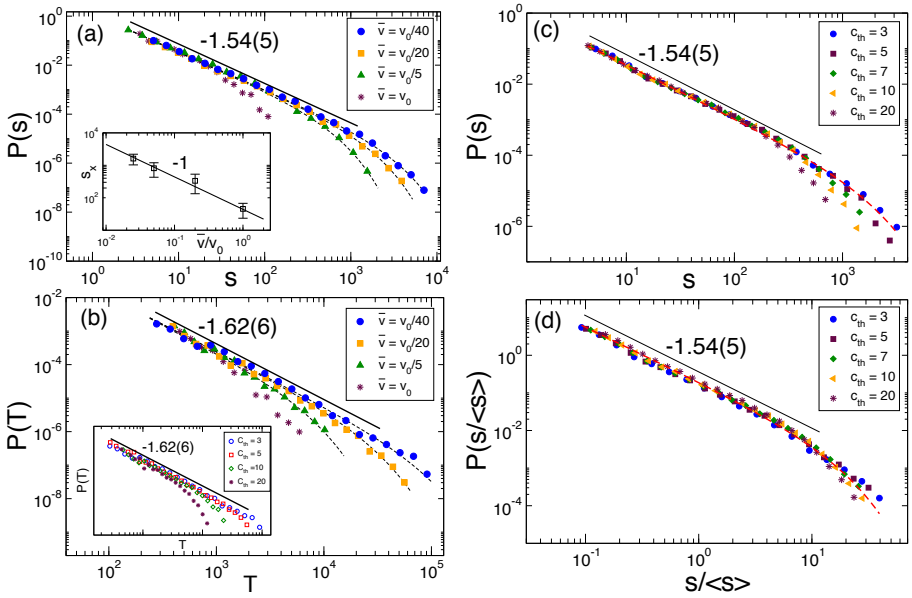

Fig. 14.1 (a) Distribution of avalanche size for different velocities. The dashed curves correspond to a data fit to $\mathcal{P}(s) = a\, s^{-\tau_s} \exp\left[-s/s_\times(\overline{v})\right]$. The solid line fits the power-law regime for the smallest velocity. The inset shows the cutoff $s_\times$ of the avalanche size distribution for each velocity with a guide-to-eye line of slope -1. (b) Distribution of avalanche durations. The inset shows a comparison for different choices of the arbitrary threshold $c_{\rm th}$ from 3 to 20 in the case of $\overline{v} = v_0/40 = 5 \times 10^{-5}$ a.u. (c) Distribution of the avalanche sizes for different choices of the arbitrary threshold in the same velocity case as (b). (d) Avalanche size distribution normalized by the average size $s/\langle s\rangle$. The dashed red line corresponds to a data fit to $\mathcal{P}(s/\langle s\rangle) = a\,(s/\langle s\rangle)^{-\tau_s} \exp\left[-b\, s/\langle s\rangle\right]$ with $\tau_s = 1.54(5)$.

We also find an excellent agreement with our prediction $\gamma = D/z_{\rm av}$ for the scaling relation between size and duration of an avalanche, $\langle s(T)\rangle \sim T^\gamma$. In Fig. 14.2 we plot both avalanche size and lateral extent *vs* time for two typical velocities. For the lowest velocity we studied $\overline{v} = v_0/40 = 5 \times 10^{-5}$ we estimate $\gamma \simeq 1.09(7)$, which is to be compared with $\gamma = 1$ from Eq. (14.8). This can also be compared with the scaling relation between avalanche exponents, $\tau_T = 1 + \gamma(\tau_s - 1)$. Substituting the numerical values $\gamma = 1.09$ and $\tau_T = 1.54$ we predict $\tau_T \simeq 1.60$ in good agreement with the numerical result (cf. Fig. 14.1). Note that the scaling theory is expected to be exact only at the critical point $\overline{v} = 0$, which is only approached with our phase-field model results. However, the singularity is strong enough to lead to effective exponents for velocities within a critical region $\overline{v} \leq L^{-2}$.

minimum avalanche size due to the numerical resolution, $s_m \sim \Delta x^2$. However, this dependency will not be relevant as long as $s_m \ll s_{c_{\rm th}}$.

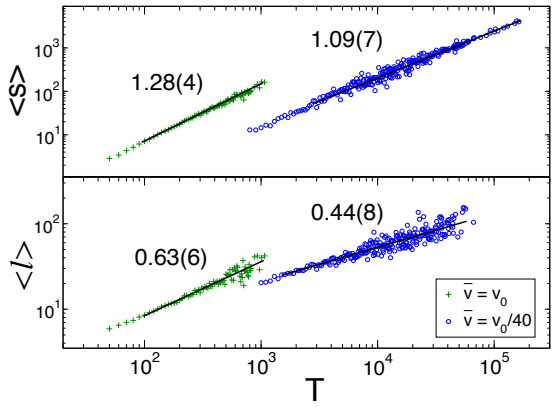

Fig. 14.2 Average avalanche size and lateral extent versus duration in a system of size $L = 512$ for two velocities in the different dynamical regimes discussed in this Chapter.

At variance with Rost *et al.* [125], who only monitored avalanches in the global velocity time series $\overline{v}(t)$, here we are actually looking at active sites that participate in an avalanche and, therefore, we are able to check the validity of the scaling law $\langle \ell \rangle \sim T^{1/z_{\rm av}}$. The typical lateral extent is predicted to scale with avalanche duration with an exponent $1/z_{\rm av} = 1/(\alpha_{\rm loc} + d/2) = 2/3$ in the high velocity regime for $d = 1$ [125], in excellent agreement with our numerical estimate in Fig. 14.2. However, for low velocities we predict $1/z_{\rm av} = 1/2$ with the dynamic exponent $z_{\rm av} = z = 2$ in the static limit. A strong proof of a distinctive behavior as the front velocity is decreased can be readily seen in Fig. 14.2. Our numerical simulations indicate that $\gamma \to 1$ and $\langle \ell \rangle \sim T^{1/2}$ as $\overline{v} \to 0$, pointing out that the dynamics is controlled by the static critical point at $\overline{v} = 0$.

The activity statistics has also been analyzed in terms of the first return probability $\mathcal{P}_f(t)$ describing the distribution of intervals t of inactivity at any site x. The results are shown in Fig. 14.3(c). We find that in the limit of very low velocities, $\overline{v} = v_0/40 = 5 \times 10^{-5}$, this distribution is given by a power-law with an exponent $\beta_f = 1.48(2)$, which is in excellent agreement with the theoretical value $\beta_f = 3/2$ from Eq. (14.8), predicted in the case of fractal activity. In contrast, in the case of high velocities, the first return probability is given by an exponential probability density, indicating that the activity is not scale-invariant anymore, due to the short-ranged correlations of the system.

Multiscaling.- An alternative method to detect the local dynamics inside the avalanches is by studying the height-height time correlation function $C_q(t)$, see Eq. (13.22) in the preceding Chapter. As it was shown there, we can directly calculate the local dynamic exponent $z_{\rm av}$ through the infinite moment $C_\infty(t) \sim t^{\beta_\infty}$ with $\beta_\infty = z_{\rm av}/\alpha_{\rm loc}$. Figures 14.3(a) and 14.3(b) show that $\beta_\infty = 0.53(4)$ for low velocities and $\beta_\infty = 0.64(5)$ for high velocities

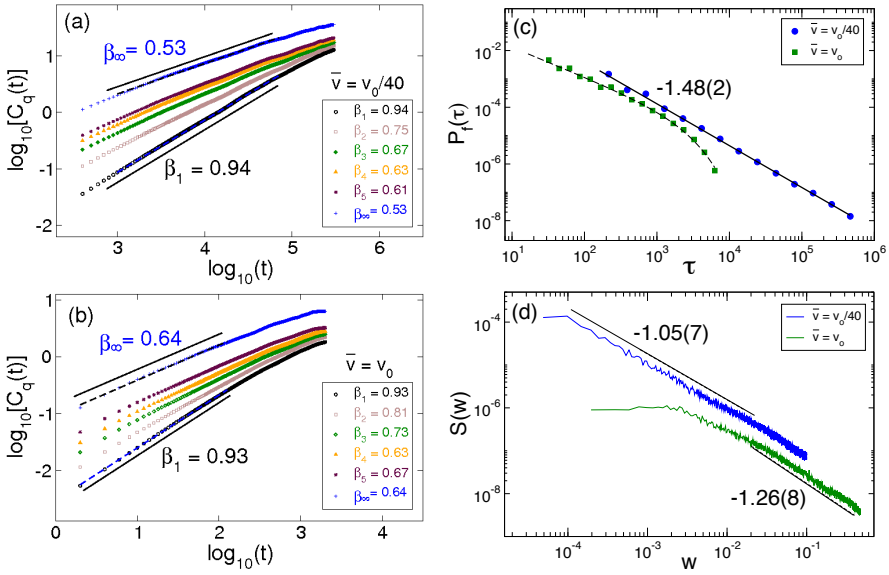

Fig. 14.3 (a),(b) Height-height time correlation function $C_q(t)$ for low and high velocities, respectively, calculated at different moments $q = 1, 2...\infty$. (c) First return probability calculated at two different velocities. The solid line corresponds to a data fit to $\mathcal{P}_f(t) = a\, t^{-\beta_f}$ with $\beta_f = 1.48(2)$, and the dashed line to $\mathcal{P}_f(t) = a\, t^{-\beta_f} \exp[-t/t_0]$ with $\beta_f \simeq 1$. (d) Velocity power spectrum $\mathcal{S}_{\bar{v}}(w) = \langle |\bar{v}(w)|^2 \rangle$ calculated at two different velocity regimes. The solid lines fit to the power-law regime in each case.

in excellent agreement with the theoretical predictions 0.5 and 0.66 in Eq. (14.8) and Eq. (14.13), respectively. In addition, all the moments β_q calculated from the numerical data at low velocities are also in excellent agreement with the theoretical prediction of Eq. (14.8). Accordingly, we find $\beta_1 = 0.94(3)$, $\beta_2 = 0.75(3)$, $\beta_3 = 0.67(3)$, and $\beta_4 = 0.63(3)$, to be compared with 1, 0.75, 0.66, and 0.625, respectively. At high velocities, however, the multiscaling exponents β_q are expected to be affected by strong crossover effects. Therefore, the relation for β_q derived in the preceding Chapter [Eq. (13.26)] fails to give the numerical estimated exponents in this case, although it certainly reproduces the trend.

Velocity correlations.- In order to check the validity of the condition $\gamma = \nu$, we have computed the power spectrum of the mean velocity $\mathcal{S}_{\bar{v}}(w) = |\widehat{\bar{v}}(w)|^2$ in the two typical velocities $\bar{v} = v_0$ and $\bar{v} = v_0/40$. The results are shown in Fig. 14.3(d), where it is observed that $\nu = 1.05(7)$ for low velocities and $\nu = 1.26(8)$ for high velocities that are to be compared with $\gamma = 1.09(7)$ and $\gamma = 1.28(4)$ (cf. Fig. 14.2), respectively. These numerical values are, in turn, in excellent agreement with the theoretical predictions of $\gamma = \nu = 1$ at low velocities [119] and $\gamma = \nu = 4/3$ at high velocities [125].

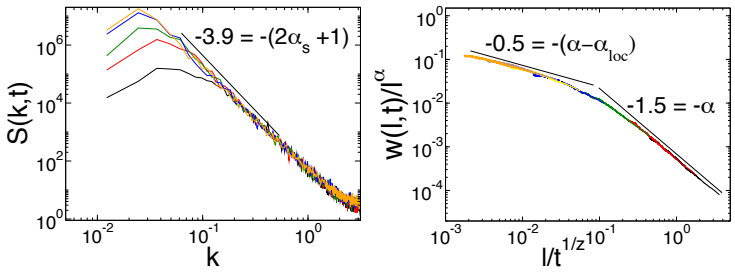

Fig. 14.4 Scaling of the front roughness in the phase-field simulations for $L = 512$ in the the low velocity $\overline{v} = v_0/40$ limit. (a) Structure factor $\mathcal{S}(k,t)$ at different times giving a spectral roughness exponent of $\alpha_s = 1.45(6)$. (b) Data collapse of the local width according to a super-rough scaling for $\alpha = 1.50(3)$, $\alpha_{\rm loc} = 1.0$, and $z = 2.09(6)$.

We must say that in order to properly compare the exponents γ and ν, the mean interface velocity has been defined as follows. First, note that only avalanches of forward moves are actually considered when the local activity map is defined, which is a consequence of the thresholding process. Possible backward moves [3] are not taken into account when calculating the γ exponent, but are indeed considered when the local interface velocity is averaged along the whole system. In order to avoid such an incongruity, which is expected to be relevant only at short times or high frequencies, the mean velocity is computed by considering only the points with a positive local velocity $v(x,t) > 0$. Sites with negative velocity are simply taken as $v(x,t) = 0$.

Interface roughness.- We have also estimated the scaling of the interfacial fluctuations for states close to the static limit. This provides an independent check of the validity of our scaling results in Eq. (14.8) and (14.7) connecting avalanche and roughness exponents. By calculating the structure factor $\mathcal{S}(k,t) = \langle |h_k(t)|^2 \rangle$ and local width $w(\ell,t)$ of the interface fluctuations before the saturated regime (cf. Fig. 14.4), we estimate the global, local, and spectral roughness exponents (see Ch. 5) $\alpha = 1.50(3)$, $\alpha_{\rm loc} = 1$, $\alpha_{\rm s} = 1.45(6)$, respectively, and the dynamic exponent $z = 2.09(6)$ in excellent agreement with our scaling theory for the pinned state [Eq. (14.7)].

Finally, we claim that the existence of a singular behavior as $\overline{v} \to 0$ and the extent of the critical region $\overline{v} \leq L^{-2}$ explain earlier numerical observations [2,84] that reported a dependence of the critical exponents $\alpha(\overline{v})$ and $z(\overline{v})$ with the velocity in numerical results of forced-flow imbibition in finite systems. Table 14.1 summarizes the different interfacial scaling exponents we observed for different velocities. We observe that as the static limit is approached the dynamic exponent $z \to 2$ and the roughness exponent $\alpha \to 3/2$, as corresponds to the pinned state.

3) Note that this is possible due to local mass conservation.

$\overline{v}$	$\ell_\times/L$	α	z	γ
v_0	0.1	1.33	3	1.28
$v_0/5$	0.23	1.35	2.8	1.21
$v_0/10$	0.31	1.37	2.6	1.18
$v_0/20$	0.48	1.41	2.3	1.13
$v_0/40$	0.64	1.50	2.09	1.09

Tab. 14.1: Correlation extent and effective scaling exponents from phase-field simulations at different velocities in a system of size $L = 512$. The fronts are always superrough with the usual local roughness exponent $\alpha_{\rm loc} = 1$.

14.3 Discussion and conclusions

We have studied avalanche dynamics in forced-flow imbibition. By making use of the scaling concepts of avalanche dynamics derived in the preceding Chapter, we have developed a scaling theory relating interface roughness and avalanche motion in the static limit of $\bar{v} \to 0$, obtaining excellent agreement with numerical results from a phase field model. This regime had never been studied before in forced-flow imbibition with a non-local model, and we show that the scaling regime that appears at very low velocities is different than that proposed by Rost *et al.* [125]. Indeed, we see that if we systematically decrease the front velocity, that is as we approach the pinned state, the physics of the system changes from short-ranged correlated fluctuations ($\bar{v} = v_0$, with correlations extending up to 10% of the system, see Table 14.1) to a long-ranged correlated problem ($\bar{v} = v_0/40$, with correlations extending up to 60% of the system). The numerical results reveal that as the mean velocity is decreased, the scaling exponents approach the ones predicted by our theory [cf. Eq. (14.8)]. This has an impact on the value of the exponents even relatively far from the pinned state, where effective exponents are observed (see Table 14.1), explaining then the effective increase of the roughness exponents for lower velocities observed in earlier numerical results [84].

From a experimental point of view, it would be of great interest to explore the pinning limit. In the experimental setup of a Hele-Shaw cell [113], this limit may be achieved by putting the cell at an angle so that gravity plays a role. This new setup should produce fronts near pinning. Note that already in the case of having a correlation length of about a 30% of the system size, the effect of the critical point should show up in a drift of the measured scaling exponents (see Table 14.1). Alternatively, fluctuations around the critical point $\overline{v} = 0$ could also be experimentally tested by setting the cell at an angle, so that the front is pinned, and then study how the system responds to a small angle variation. In this configuration we expect the front to jump from one pinned state to another following a relaxation dynamics described by Eq. (14.6) driven by avalanches described by the scaling exponents of Eq. (14.8).

Finally, let us remark that our study is based on the local activity of the interface, in contrast to the method used in both the numerical and experimental works of Ref. [125] and [113] respectively, where the avalanche dynamics was analyzed through the time fluctuations of the global velocity $\overline{v}(t)$ (see next Chapter). Work is in progress in order to properly compare recent experimental work [111, 130] with the results presented in this Chapter, by using the same avalanche definition.

15
Global fluctuations analysis

The present Chapter deals with the analysis of global quantities in forced-flow imbibition. In contrast to the preceding Chapter, we shall study here the avalanche dynamics by means of a global analysis, based on the time fluctuations of the mean interface velocity [113, 125].

In general terms, a global quantity or *global observable* is defined as the spatial average of a local quantity measured at different times in a large enough system. Note that such observables are actually very common in physical sciences since they give information about macroscopic properties of the system and usually are well accessible from an experimental point of view (see Ref. [30] for a recent review on global fluctuations). Then, the resulting signal $V(t)$ is observed to fluctuate on time showing a complex behavior. In particular, when a system is pushed slowly, it is observed to respond in spatially extended avalanches, giving rise to an intermittent and *burst-like* dynamics of the global signal $V(t)$. This is observed, for instance, in the phenomenon of *crackling noise* [132] in fracture and the Barkhausen noise [33, 109] in magnetic systems.

When the system is formed by many independent degrees of freedom, the fluctuations of the global magnitude are given by a Gaussian probability density function. This is a direct consequence of the Central Limit Theorem (CLT) which states that the sum of a large number of independent and identically distributed random variables is normally distributed (see for example [6]). However, when the system presents correlations over a macroscopic scale $\ell_\times$ the fluctuations of global quantities might display a non-Gaussian statistics [10, 15]. Basically the system cannot be divided into domains that are statistically independent and therefore the basic premise of the CLT is not satisfied. Indeed, a huge number of experimental and numerical works have reported global fluctuations which are described by non-Gaussian distributions in the context of turbulence [16, 114], magnetization of an XY model [16, 115], liquid crystals [68, 145], forced-flow imbibition [113, 125] and microfluidic fronts (see next Part of this thesis), among many others [see also the recent paper by Bramwell [14] and references therein].

As it is stated in the preceding Chapter, the avalanche dynamics in imbibition fronts is expected to be responsible for the front velocity fluctuations. Our study presented in this Chapter is mainly motivated by the recent experimental work about forced-flow imbibition carried out by Planet *et al.* [113], where the spatially averaged velocity has been studied in a regime of relatively high velocities. The experimental setup consists there on a horizontal Hele-Shaw cell where the disorder is provided by a random distribution of copper square patches $l_d^2 = 0.40 \times 0.40\,\mathrm{mm}^2$ on a fiberglass board attached to the bottom plate of the cell (see also Ch. 4 for a detailed description of the cell). The imbibition fronts are then monitored by making use of a high–resolution camera. They have found that avalanches defined from the global velocity signal are power-law distributed in both sizes and durations, obtaining a scaling relation between them which is in agreement with previous numeric data [125]. In addition, the velocity fluctuations are found to follow an asymmetric, non-Gaussian distribution (referred to as generalized Gumbel distribution [58,115]) when the velocity is averaged over length scales comparable to the correlation length of the system [15].

The purpose of this Chapter is therefore to numerically study such global fluctuations (cf. Fig. 15.1) in terms of an avalanche description, and directly compare to the experimental results. To this end, our analysis shall be restricted in a regime of relatively high velocities (cases from $\bar{v} = v_0$ to $\bar{v} = v_0/10$ in the preceding Chapter). We use the same phase field model as before, integrated in a system of size $L = 512$, with the same numerical parameters. All the values for the average front velocity have been normalized to a reference value $v_0 = 0.002$, which corresponds to the highest value used in our

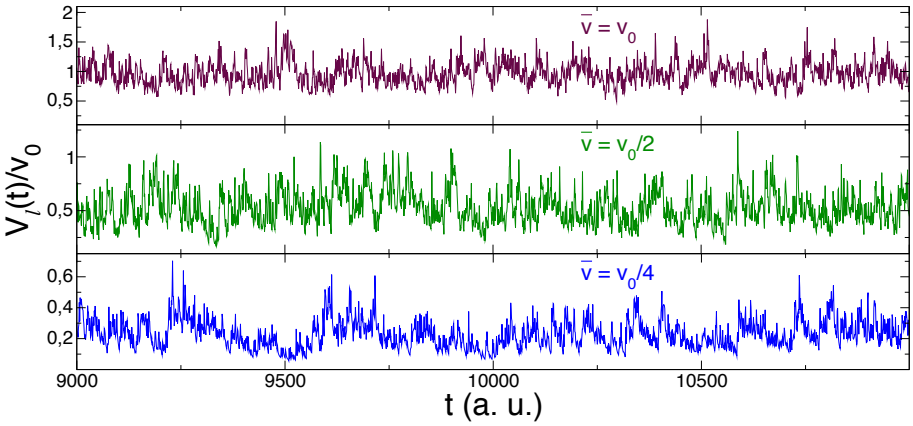

Fig. 15.1 Global velocity of the interface normalized to the nominal value $V_l(t)/v_0$, averaged along the whole system, $l = L = 512$. The typical velocity $\bar{v}$ is decreasing from top to bottom.

study. All the data analysis has been performed in a statistically stationary state, after the interface fluctuations reach the saturated width.

15.1
Global avalanche definition

The global magnitude under study is defined as the local interface velocity averaged along a window of length l

$$V_l(t) = \frac{1}{l}\int_l v(x,t)\mathrm{d}x = \bar{v} + \delta V_l(t), \tag{15.1}$$

where $\delta V_l(t)$ represents the fluctuations around a mean value $\bar{v}$. Figure 15.1 shows an example of these fluctuations when taking the averaging window as the system size, $l = L$, for different mean velocities $\bar{v}$. As expected, the signal $V_l(t)$ shows an intermittent behavior with large fluctuations as a consequence of the avalanche-like dynamics of the interface and the finite size of the system.

Avalanches or bursts from the velocity signal are then defined by using standard procedures based on a thresholding process [86]. Figure 15.2 shows a schematic representation of how a global avalanche is characterized by a size A and a duration T.

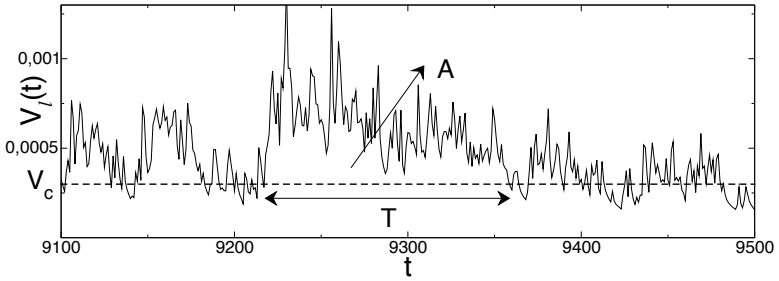

Fig. 15.2 Global avalanches are defined as fluctuations above some given threshold V_c (dashed line).

We consider fluctuations of $V_l(t)$ above some arbitrary threshold V_c. Then the avalanche size is defined as

$$A = \int_T \Big[V_l(t) - V_c\Big]\mathrm{d}t, \tag{15.2}$$

where $V_l(t) - V_c > 0$ during the whole time interval or avalanche duration T, and $V_c = c_v \langle V_l \rangle$ being c_v an arbitrary constant [1]. Note that, as it occurred in

1) We are using here a slightly different threshold as compared to the experimental work by Planet *et al.* [113], where they use

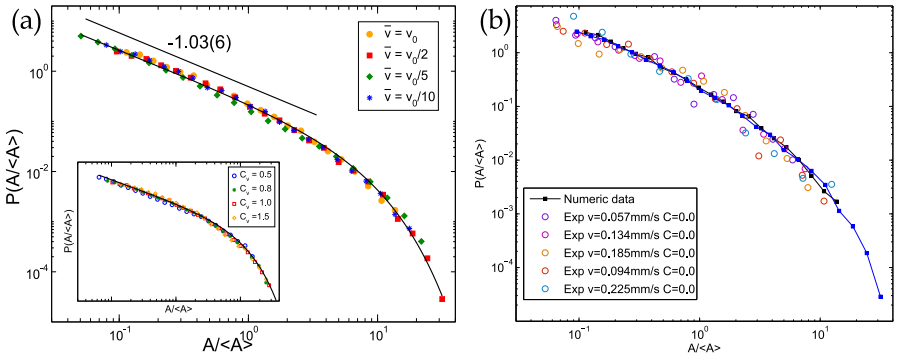

Fig. 15.3 (a) Avalanche size distribution $\mathcal{P}(A/\langle A\rangle)$ rescaled by the average size $\langle A\rangle$ for different velocities using a constant $c_v = 1.0$. The solid line corresponds to a data fit to $\mathcal{P}(x) = a\,x^{-\tau_A}\exp[-bx]$, with $x = A/\langle A\rangle$. The inset shows the same distribution in the case of $\bar{v} = v_0/2$ for different choices of the arbitrary constant c_v from 0.5 to 1.5. (b) Direct comparison of numerical data (solid lines) to experimental results at different velocities (open circles) of forced-flow imbibition carried out in a Hele-Shaw cell (courtesy by R. Planet [113]).

the local avalanche definition used in the two previous Chapters, this global avalanche definition depends also on an arbitrary threshold. As before, we have to make sure that our results do not depend on the constant c_v.

15.2 Avalanche dynamics

Avalanches defined through the velocity signal $V_l(t)$ with $l = L = 512$, and characterized by a size A and a duration T are numerically studied. In order to properly compare to the experimental work of Ref. [113], we study the burst size and duration distributions $\mathcal{P}(A/\langle A\rangle)$ and $\mathcal{P}(T/\langle T\rangle)$, rescaled by the average size $\langle A\rangle$ and average duration $\langle T\rangle$, respectively.

Figure 15.3(a) shows the statistics of sizes A for different mean velocities $\bar{v}$ and the same threshold $c_v = 1.0$. We observe that the data collapse into a single distribution, following a power-law with an exponential cutoff

$$\mathcal{P}(A/\langle A\rangle) = a\left[\frac{A}{\langle A\rangle}\right]^{-\tau_A}\exp\left[-b\frac{A}{\langle A\rangle}\right], \tag{15.3}$$

with an exponent $\tau_A = 1.03(5)$. As it can be shown in Fig. 15.3(b), this distribution is in excellent agreement with the experimental work, where an exponent $\tau_A = 1.00(6)$ was reported [113]. Actually, both numeric and experimental data seems to collapse into the same distribution when plotted together [cf.

$V_c = \langle V_l\rangle + c\sigma$ with $\langle V_l\rangle$ the time average, σ^2 the variance of $V_l(t)$, and c an arbitrary clip level.

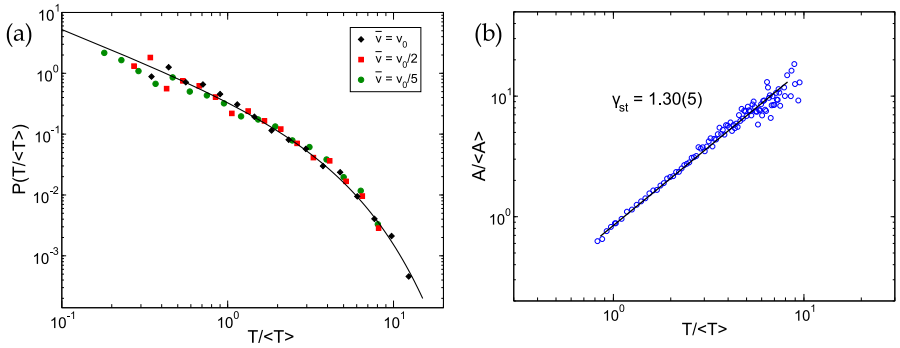

Fig. 15.4 (a) Avalanche duration T distribution $\mathcal{P}(T/\langle T\rangle)$ normalized by the average duration $\langle T\rangle$ for different velocities.The solid line corresponds to a data fit to $\mathcal{P}(x) = a\,x^{-\tau_T}\exp[-bx]$, with $x = T/\langle T\rangle$, and $\tau_T \simeq 1.1$. (b) Avalanche size $A/\langle A\rangle$ *vs* duration $T/\langle T\rangle$ in the case of $\bar{v} = v_0/2$ with $c_v = 1.0$.

15.3(b)]. In addition, the results show that such distribution is robust and independent of both the mean velocity and the arbitrary choice of the threshold c_v.

We also find that the duration distribution is given by a power-law with an exponential cutoff [cf. Figure 15.4(a)]. The obtained exponent is $\tau_T = 1.10 \pm 0.11$ which is slightly different (within error bars) from the exponent reported experimentally, $\tau_T = 1.31 \pm 0.15$. This is attributed to the fact that the duration distribution is mostly exponential, and therefore it is difficult to extract clear information about the power-law regime.

Finally, we have also checked that the relation between avalanche sizes and durations

$$A \sim T^{\gamma_{st}}, \tag{15.4}$$

is well accomplished, obtaining the value $\gamma_{st} = 1.30 \pm 0.05$ in agreement with both the numerical work by Rost *et al.* [125] and the experimental results [113], who reported a value of 1.33 and 1.31 ± 0.21, respectively.

15.3
Spatially averaged velocity fluctuations

The last point we want to address here is concerning the statistical properties of the global velocity fluctuations $V_l(t)$. Let us recall first that forced-flow imbibition is characterized by having a fixed correlation length $\ell_\times$, that depends on the mean interface velocity as $\ell_\times \sim 1/\sqrt{\bar{v}}$. A natural arising question is then how the statistical properties of the velocity signal are modified depending on the averaging length l. In particular, we are considering here two

different cases corresponding to a global velocity averaged along a correlated window $l \sim \ell_\times$ or along a non-correlated window $l \gg \ell_\times$.

Let us consider the normalized variable

$$x = \frac{V_l(t) - \langle V_l(t) \rangle}{\sigma}, \tag{15.5}$$

where $\langle .. \rangle$ denotes average over time and σ^2 is the variance of $V_l(t)$. The probability density functions of x are shown in Fig. 15.5. We observe that when the global velocity is averaged along a correlated window $l = \ell_\times$, the variable x follows an asymmetric, non-Gaussian distribution, with an exponential long tail characterizing the large fluctuations of the signal, in agreement with the experimental work [113]. In particular, global fluctuations follow the so-called BHP distribution, found for the first time by Bramwell-Holdsworth-Pinton [16] in the context of turbulence and XY Ising Model, and it is given by [15]

$$\mathcal{P}(y) = K(\mathrm{e}^{y-\mathrm{e}^y})^a \quad \text{with} \quad y = -b(x+s), \tag{15.6}$$

and the numerical parameters $b = 0.938$, $s = 0.374$, $K = 2.14$, and $a = \pi/2$. On the other hand, when the global velocity is averaged along a non-correlated window, the fluctuations tend to be Gaussian distributed

$$\mathcal{P}(x) = \frac{\mathrm{e}^{-\frac{x^2}{2}}}{\sqrt{2\pi}}, \tag{15.7}$$

as a consequence of the Central Limit Theorem.

15.4 Conclusions

We have performed a numerical study concerning the global fluctuations in forced-flow imbibition. The global observable $V_l(t)$, defined as the local interface velocity averaged along a window of length l, has been studied in terms of an avalanche dynamics and statistical methods. In order to properly compare to the experimental results reported in Ref. [113], our study has focused in a regime of relatively high velocities, characterized by having correlations extend up to 30% of the system.

Our numerical results have shown that avalanches defined from the velocity signal are power-law distributed with an exponential cutoff, in excellent agreement with experiments. Actually, the numeric avalanche size distribution has been observed to collapse nicely with the experimental data.

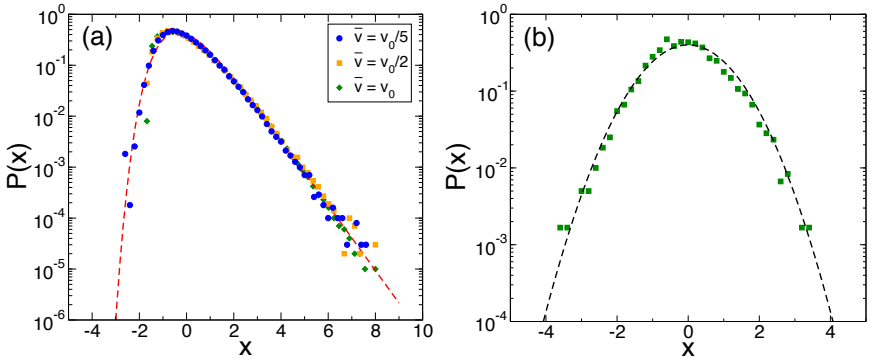

Fig. 15.5 Numerical results for the probability density function of $x = (V_l - \langle V_l \rangle)/\sigma$ at two typical situations discussed in this Chapter. (a) Global velocity V_l averaged along a correlated window for the cases of mean velocities $\bar{v} = v_0$, $\bar{v} = v_0/2$, and $\bar{v} = v_0/5$, with $l = \ell_\times \simeq 50, 70,$ and 110, respectively, in a system of size $L = 512$. The numerical data are compared to a BHP distribution (dashed red line).(b) Global velocity averaged along a system of size $L = 4096$ with a correlation length $\ell_\times \simeq 50$ corresponding to the case with mean velocity $\bar{v} = v_0$. Numerical data are compared to a Gaussian distribution (black dashed line).

In addition, we have observed that when the velocity is averaged at length scales comparable to the correlation length of the system, the fluctuations of the signal $V_l(t)$ follow a BHP distribution [16], consisting of an asymmetric, non-Gaussian distribution with a long exponential tail, reflecting the avalanche motion of the interface occurring at these scales. In contrast, global fluctuations tend to be Gaussian distributed when the velocity is averaged along a non-correlated window. In this situation, the velocity signal is formed by a large sum of domains statistically independents, and therefore the Central Limit Theorem applies.

Part IV Microfluidics

16
Pinning effects in microchannels

Controlling the advancement of a fluid inside a microchannel is one of the main issues in microfluidics. The huge amount of technological, biological and medical applications found in the miniaturization of fluidic systems has brought an important part of the scientific community to put a considerable effort in understanding the physics underlying microfluidics devices [20, 139, 142]. In particular, to study the effect of the wetting conditions and the roughness of the surface channel on the dynamics of the fluid has revealed as a fundamental problem in this field [34, 35, 66, 75, 77, 131, 140].

This last Part of the thesis deals with the dynamics of a liquid/air meniscus when it is driven into a microchannel. The aim is to see how the geometry and the wetting conditions of the channel may affect the time evolution of the interface. In a limit of very low driving forces the advancement of the liquid is affected by local pinning-depinning movements at the contact line level which induce cooperative correlated motion, reflected as a *burst-like* dynamics of the meniscus. In this limit, it can be assumed that the interface has a slow dynamics and previous defined concepts such as global avalanche motion or non-Gaussian fluctuations (see Ch. 15) are now applied in a microfluidic framework.

This Chapter presents numerical results in order to study the front dynamics observed in experiments carried out in a microchannel, where the spatially averaged height of a *microfluidic front* $H(t)$ and its mean velocity $V(t)$ are studied. We propose two different numerical studies. First, by making use of the two dimensional phase field model described in Chapter 4, we study the dynamics of an interface growing in a disordered *hydrophobic* medium when a constant pressure is applied at the origin of the system. Note that this model is actually based on the macroscopic description of imbibition fronts, and therefore does not take into account the microscopic details inside the microchannel. However, this two-dimensional study turns out to be suitable to describe the spatially averaged magnitudes $H(t)$ and $V(t)$ studied in experiments of microchannels. On the other hand, in order to study the dynamics of the meniscus inside the microchannel, we introduce a generalized three dimensional phase field model that takes into account the wetting effects of the

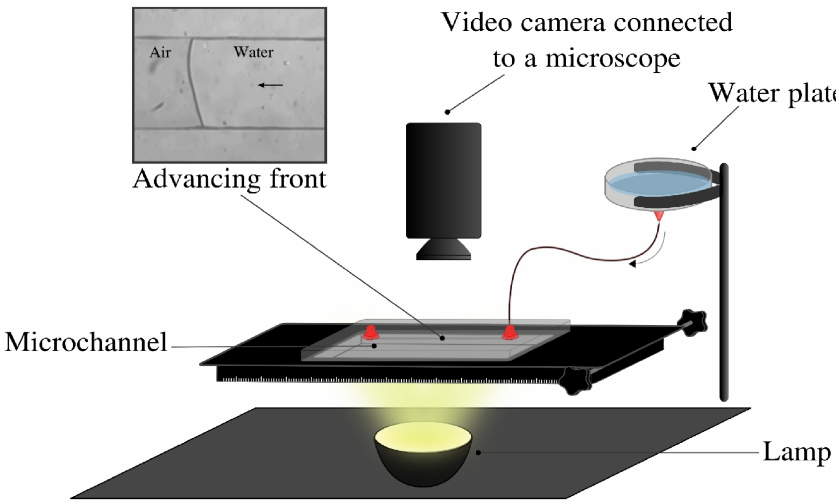

Fig. 16.1 Setup of the experimental work in microchannels (courtesy by M. Queralt-Martín [120]).

walls. Then, by modeling disordered walls we are able to follow the pinning-depinning mechanisms at the contact line level. Our numerical and theoretical work is focused there on channels patterned with parallel grooves placed perpendicular to the flow and randomly distributed along the flow.

16.1 Experimental results in a hydrophobic microchannel

The results presented in this Section have been carried out by Queralt-Martín *et al.* [120,121]. The experimental setup consists there on a rectangular closed microchannel with a cross section of $L = 100\ \mu m$ wide and $b = 7\ \mu m$ high. The channels are manufactured in such a way that can show either hydrophilic or hydrophobic properties by using different materials, and they are filled of water by imposing a constant pressure at the origin of the channel (see Fig. 16.1). The small dimensions of the channel make the intrinsic roughness of the wall, which would be irrelevant for larger systems, to play an important role on the fluid flow. Such an intrinsic roughness is assumed to be important enough to affect the interface dynamics of the front.

During the filling of the channel, the position of the liquid/air interface is monitored at several times by a CCD camera situated on the top of the channel. This allows to calculate the mean height position, denoted as $H(t)$, and then the mean interface velocity as $V(t) = \mathrm{d}H(t)/\mathrm{d}t$. The experimental work is then focused on studying the time evolution of both the mean height and velocity of the interface when the applied pressure and the wetting properties

of the channel are changed. The results presented in this Chapter, however, mainly focus on hydrophobic channels.

Time evolution of the mean height

It is important to remark that the experimental setup used during the filling process –that is, with an applied constant pressure at the origin of the cell– is actually the same than in the spontaneous imbibition case described in Chapter 4. It could be therefore expected the mean advancement of the microfluidic front to advance following the Washburn's law, $H(t) \sim t^{1/2}$, as it is observed in the macroscopic Hele-Shaw cell. As a general case, we assume that the height growth is given by

$$H(t) \sim t^{\lambda}, \tag{16.1}$$

where λ is an effective exponent that takes the value $\lambda = 1/2$ for the Washburn behavior. Experiments carried out in a hydrophobic channel (Fig. 16.2) have shown that the exponent λ decreases as the applied pressure is decreased. In particular, the exponent changes from a regime described by the Washburn exponent ~ 0.56 (high pressures) to a new, and different exponent ~ 0.38 (low pressures), that differs from the classic value $1/2$.

Statistics of the mean velocity

Another interesting aspect studied in the experimental work has been the time fluctuations of the mean velocity of the front

$$V(t) \sim V_0(t) + \delta v(t), \tag{16.2}$$

where $V_0(t) \sim t^{\lambda-1}$ is the mean temporal dependency that comes from Eq. (16.1). The fluctuating term $\delta v(t)$ is attributed to the pinning effects at the interface induced by the roughness present at the surfaces of the channel. The point is to study how these fluctuations behave when the applied pressure is modified.

The statistical description of the velocity signal for an hydrophobic channel at low applied pressures is shown in Fig. 16.3. It is observed that the global velocity signal shows large fluctuations and are non-Gaussian distributed. As it was stated in Chapter 15, this behavior is a typical signature of a burst-like dynamics. The velocity distribution is then given by a Generalized-Gumbel distribution, which has been reported in several different works [14], and in particular in macroscopic imbibition fronts [113]. The general form of this

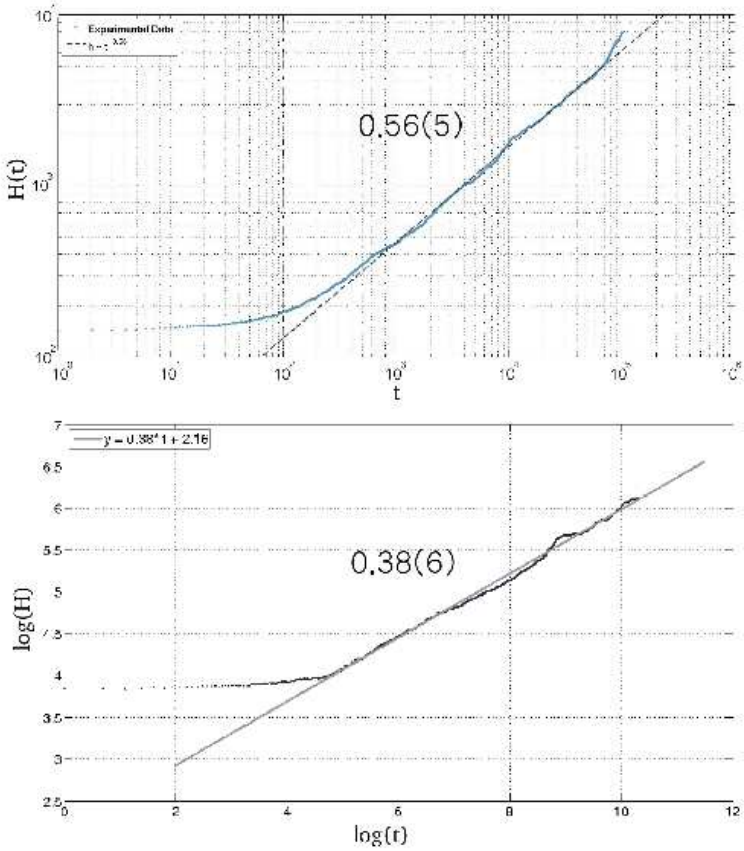

Fig. 16.2 (a) Experimental results for the evolution of the mean height $H(t)$ (μm) as function of time t (s) in a hydrophobic microchannel at two typical applied pressures, high (top) and low (bottom). It is shown that both cases follow a power law, $H(t) \sim t^{\lambda}$, with $\lambda \simeq 0.56$ at high pressures and $\lambda \simeq 0.38$ at low pressures, respectively (courtesy by M. Queralt-Martín [120]).

distribution is given by

$$\mathcal{P}(x) = \frac{a^a b_a}{\Gamma(a)} \exp\left(-a\{b_a(x+s_a) + \exp\left[-b_a(x+s_a)\right]\}\right), \tag{16.3}$$

where x is the normalized variable

$$x = \frac{\delta v - \langle \delta v \rangle}{\sigma}. \tag{16.4}$$

As a difference with the global velocity signal reported in Chapter 15, where fluctuations were around a constant value, here, it is necessary to substract the mean temporal dependency $V_0(t)$ at the global signal. Then the fluctuations

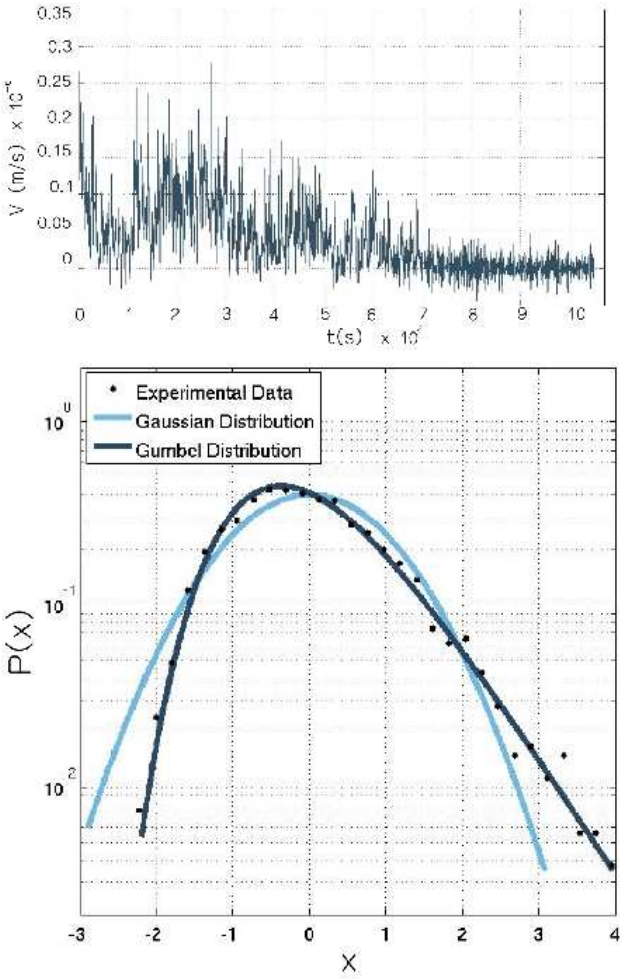

Fig. 16.3 Statistical analysis of the global velocity $V(t)$ (top). PDF of the variable x shows global fluctuations non-Gaussian distributed (bottom). The experimental data are compared both to a generalized-Gumbel and Gaussian distribution (courtesy by M. Queralt-Martín [120]).

under study are given by $\delta v(t)$ with the average over time $\langle \delta v \rangle$ and variance σ^2. The only free parameter at the above equation is a, since b_a and s_a are given by

$$b_a = \frac{\sqrt{\frac{\mathrm{d}^2 \ln \Gamma(a)}{\mathrm{d}a^2}}}{\sigma_x}, \qquad s_a = \langle x \rangle + \frac{\ln a - \frac{\mathrm{d} \ln \Gamma(a)}{\mathrm{d}a}}{b_a}, \tag{16.5}$$

where $\Gamma(a)$ is the gamma function and $\langle x \rangle = 0$ and $\sigma_x = 1$ in our case. The BHP distribution [16], observed in our numerical results presented in Chap-

ter 15 can actually be considered an especial case of the above generalized-Gumbel distribution by taking the specific value $a = \pi/2$.

These experimental results show that the advancement of the microfluidic front into hydrophobic microchannels can be studied in terms of a global avalanche-motion. In addition, the fact that in the limit of very low velocities the mean height growth does not hold with the typical Washburn behavior $\sim t^{1/2}$ but is given by a lower exponent ~ 0.38, reveals that pinning effects might become really crucial.

16.2 Two dimensional description

Our first numerical approach to study microfluidic fronts, as those reported in the experiments, is based on the two-dimensional (2D) phase field model derived in Ch. 4 and used to study macroscopic imbibition fronts (see Parts II and III). Our purpose is to model an interface advancing through a disordered media that contains blocking sites (hydrophobic defects) randomly distributed. We are taking into account here that the aspect ratio of the system is actually quite small, $\varepsilon = b/L \simeq 0.07 \ll 1$, and therefore a 2D approach is still expected to be valid to describe the spatially averaged quantities $H(t)$ and $V(t)$. Also, note that the experimental results shown in Fig. 16.3 reflect a critical behavior similar to that observed in macroscopic disordered media (see Ch. 15). Therefore, we shall consider that at a 2D level, the dynamics of the growing microfluidic front is given by the already well-known equation for imbibition fronts [cf. Eq. (4.22) in Ch. 4]. The numerical data will be then studied in terms of a global analysis for the velocity fluctuations as it was made in Ch. 15 to study forced-flow imbibition fronts, but now with the particularity that the mean velocity of the front is decreasing on time, Eq. (16.2).

Let us also remark, however, that by using this two dimensional model we are actually loosing information about the microscopic details of the meniscus inside the microchannel (transversal direction to the flow), something that might indeed become crucial at these scales. To this end, next Section introduces some preliminary studies based on a three dimensional model that accounts the wetting effects at the walls, and therefore is able to study the meniscus dynamics inside the channel.

16.2.1 Numerical method

The phase field equation [cf. Eq. (4.41)] is integrated in a two dimensional system of size $L = 256$ with a dichotomic quenched disorder $\xi(x, y)$ that takes the values $\xi_1 = -0.4$ and $\xi_2 = -0.65$ randomly distributed in such a way that the

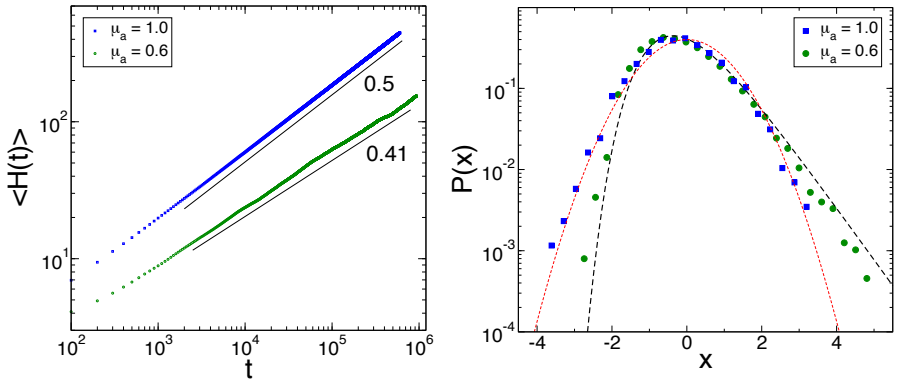

Fig. 16.4 Numerical results obtained by using the two-dimensional phase field model in a system of size $L = 256$. (a) Mean height of the interface averaged over 15 disorder realizations $\langle H(t) \rangle \sim t^{\lambda}$ for two typical applied pressures μ_a. At low applied pressures, the exponent λ differs form the usual $1/2$ expected for Washburn behavior. (b) PDF of $x = (\delta v - \langle \delta v \rangle)/\sigma$ for two applied pressures are compared to a Gaussian (red dashed line) and BHP (black dashed line) PDF.

sites with $\xi = \xi_2$ fill the system with a probability $p = 0.3$. The negative values of the disorder model the hydrophobicity of the medium. The numerical integration is made by taking the usual grid space and time step of $\Delta x = 1.0$ and $\Delta t = 0.01$, respectively, and periodic boundary conditions are applied at the x direction. We are assuming here that the possible boundary effects at the sides of the closed channel do not affect the global dynamics of the microfluidic front. The driving force is then provided by a constant applied pressure [1] at the origin of the system [spontaneous imbibition conditions, $\mu(x,0) = \mu_a$]. We study how the dynamics of the front varies when the applied pressure is changed from 0.5 up to 1.0.

16.2.2 Results

Figure 16.4 shows the numerical results for two different applied pressures. We observe that at high applied pressures ($\mu_a = 1.0$), the advancement of the interface is given by the usual Washburn behavior with $H(t) \sim t^{0.5}$. Also, by studying the fluctuations of the normalized variable x [cf. Eq. (16.4)], we observe that they are basically Gaussian distributed. In the context of macroscopic imbibition fronts, this can be understood as having short-range correlations at the interface. Recall that in the 2D model for imbibition, interface correlations are given by the typical crossover length $\ell_\times$ separating a regime

1) Let us recall that in the phase field model framework, the pressure field of the fluids is given by the chemical potential μ (see Ch. 4 for more details).

controlled by surface tension from a regime controlled by the viscous pressure

$$\ell_\times \sim \frac{1}{\sqrt{V(t)}} \sim t^{\frac{1-\lambda}{2}}. \tag{16.6}$$

At high pressures and then high velocities this correlation length grows very slowly, and then it is expected that $\ell_\times \ll L$ during all the experiment. Basically, the saturated regime ($\ell_\times \sim L$) is never reached. Hence, in this limit, the averaged velocity can be considered as a sum of domains statistically independents and, as a consequence of the Central Limit Theorem, Gaussian distributed.

On the other hand, as the applied pressure is decreased the pinning point is approached. In particular, it is observed that for values of $\mu_a < 0.6$, the interface gets completely pinned and does not advance at all [2]. Close to this limit, the interface is dominated by a burst-like dynamics reflected in the large fluctuations of the mean velocity, giving rise then to an asymmetric Generalized Gumbel PDF. In Fig. 16.4 there is observed that the distribution of the global velocity fluctuations approaches the BHP distribution [see Eq. (15.6) in Ch. 15]. In addition, the mean height growth of the interface is given by an exponent $\nu \sim 0.41$ lower than that observed at high applied pressures, in agreement with the experimental results reported in hydrophobic microchannels.

16.3 Three dimensional description

In order to numerically study the advancement of a fluid inside a microchannel, the phase field model used in the preceding Section has to be modified by a three-dimensional model that takes into account the wetting properties at the walls. The free energy for the order parameter is then modified by adding an extra term due to the presence of solid/fluid interactions [24]. This extra term allows to introduce the wetting effects into the model.

16.3.1 Phase field model with wetting boundary conditions

Free energy of the system

Consider a system of two different fluids in contact with a solid wall located at $x = 0$, being $\hat{\boldsymbol{x}}$ its normal direction. In the bulk region, the free energy per

2) Note that this also would occur by increasing the fraction p of blocking points for a given applied pressure. This study, however, has not been performed

unit area for a flat surface is written as

$$\mathcal{F} = f_s(\phi_s) + \int_0^\infty \mathrm{d}x \Big[V(\phi) + \frac{\epsilon}{2} \Big(\frac{d\phi}{dx} \Big)^2 \Big], \tag{16.7}$$

where $V(\phi) = \frac{1}{4}(1-\phi^2)^2$ is the usual double well potential [3]. The term f_s is added to take into account the energy of the surface wall [24], and it will be taken as

$$f_s = A_s \phi_s, \tag{16.8}$$

where $\phi_s = \phi(x=0)$, and the parameter A_s describes the preference of the wall for either the liquid ($A_s > 0$) or the air ($A_s < 0$) phase. The equilibrium solution of Eq. (16.7) is then given as follows. Taking a perturbation around the equilibrium solution $\phi = \phi_0 + \lambda\phi_1$, the variational calculus tells us that

$$\frac{d\mathcal{F}[\phi_0 + \lambda\phi_1]}{d\lambda}\Big|_{\lambda=0} = \int_0^\infty \mathrm{d}x \phi_1 \Big[V'(\phi_0) - \epsilon \frac{d^2\phi_0}{dx^2} \Big] + \Big[\phi_1 \Big(\frac{df_s}{d\phi_s} - \epsilon \frac{d\phi_0}{dx} \Big) \Big]_{x=0} = 0. \tag{16.9}$$

By taking an arbitrary function ϕ_1 which vanishes at the boundaries, the equilibrium equations, written in a general system, are:

$$V'(\phi) = \epsilon \nabla^2 \phi, \tag{16.10}$$

$$\frac{df_s}{d\phi}\Big|_s = \epsilon \Big[\hat{\boldsymbol{n}} \cdot \boldsymbol{\nabla}\phi \Big]_s, \tag{16.11}$$

where the condition (16.11) is the so-called *natural boundary condition* of the problem [24].

Surface tensions and contact angle

We are interested in calculating the equilibrium contact angle of the interface liquid/air with the substrate, given by the Young-Dupré relation

$$cos(\theta_e) = \frac{\sigma_{sg} - \sigma_{sl}}{\sigma_{lg}}. \tag{16.12}$$

From the equilibrium equations of the system, Eqs. (16.10) and (16.11), we can calculate the different surface tensions solid/liquid and solid/gas. By

3) We are taking here, for convinience, the square gradient term of the free energy multiplied by ϵ, instead of being multiplied by ϵ^2 as it was taken in the phase field model described in Ch. 4.

considering a flat surface, we use the relation

$$\frac{d}{dx}\Big[\Big(\frac{d\phi}{dx}\Big)^2\Big] = 2\frac{d\phi}{dx}\frac{d^2\phi}{dx^2}, \tag{16.13}$$

to integer Eq. (16.10) along x direction,

$$\frac{\epsilon}{2}\Big[\frac{d\phi}{dx}\Big]^2 = V(\phi) - V(\phi_e), \tag{16.14}$$

where it has been used that $d_x\phi(x \to \infty) = 0$ and $\phi(x \to \infty) = \phi_e = \pm 1$. From the boundary condition Eq. (16.11) and from Eq. (16.14) we can obtain the continuity equation:

$$V(\phi_s) - V(\phi_e) = \frac{1}{2\epsilon}\Big[\frac{df_s}{d\phi_s}\Big]^2 = \frac{A_s^2}{2\epsilon}, \tag{16.15}$$

which gives a relation for the value of the phase field at the wall, ϕ_s. Note that such a value depends on which phase is the wall in contact. The surface tension at the solid/fluid interface is evaluated from Eq. (16.7) and using Eq. (16.14) we obtain

$$\sigma_{sf} = f_s(\phi_s) + 2\int_0^\infty \mathrm{d}x V(\phi) = f_s(\phi_s) + \sqrt{2\epsilon}\int_{\phi_s}^{\phi_e}\mathrm{d}\phi\sqrt{V(\phi)}. \tag{16.16}$$

Therefore, the surface tensions for each fluid are:

$$\sigma_{sg} = f_s(\phi_{sg}) + \sqrt{2\epsilon}\int_{\phi_{sg}}^{-1}\mathrm{d}\phi(1-\phi^2) = \sqrt{\frac{\epsilon}{2}}\Big[-\frac{2}{3} - (1-h)\phi_{sg} + \frac{1}{3}\phi_{sg}^3\Big], \tag{16.17}$$

$$\sigma_{sl} = f_s(\phi_{sl}) + \sqrt{2\epsilon}\int_{\phi_{sl}}^{+1}\mathrm{d}\phi(\phi^2-1) = \sqrt{\frac{\epsilon}{2}}\Big[-\frac{2}{3} + (1+h)\phi_{sl} - \frac{1}{3}\phi_{sl}^3\Big], \tag{16.18}$$

where we have defined the parameter $h = \sqrt{\frac{2}{\epsilon}}A_s$. ϕ_{sg} and ϕ_{sl} correspond to the value of the phase field at the surface in contact with gas or liquid respectively. These values can be obtained from Eq. (16.15), taking that $\phi_{sg} < 0$ with $1 - \phi_{sg}^2 > 0$, and $\phi_{sl} > 0$ with $1 - \phi_{sl}^2 < 0$. Finally, using the Young-Dupré relation (16.12), we obtain [18, 24, 41, 107]

$$\cos\theta_e = \frac{1}{2}\Big[(1+h)^{3/2} - (1-h)^{3/2}\Big], \tag{16.19}$$

where we have used the usual expression for the liquid-gas surface tension $\sigma_{lg} = \frac{4}{3}\sqrt{\frac{\epsilon}{2}}$ derived in Chapter 4.

Conserved dynamics

The dynamics for the order parameter is then assumed to be conserved and is given by

$$\frac{\partial \phi}{\partial t} = \nabla M \nabla \mu = \nabla M \nabla [-\phi + \phi^3 - \epsilon \nabla^2 \phi], \tag{16.20}$$

where $\mu = \delta \mathcal{F} / \delta \phi$ is the chemical potential, and it will play the role of the pressure field. The above equation is then numerically integrated in a three dimensional system by considering the wetting boundary condition, Eq. (16.11), at the wall positions.

16.3.2 Results

Although the experimental setup is an actual three-dimensional system, we shall use here a simplified two-dimensional version with two disordered walls that resembles a three-dimensional channel translationally invariant along the direction perpendicular to the flow. This has to be taken as a first step to characterize the time evolution of the height meniscus inside a real disordered microchannel.

The phase field equation (16.20) has been integrated in a two dimensional system $L_y \times L_z$ with the wetting boundary condition, Eq. (16.11), applied at the wall positions. To perform a similar analysis as in the experiments, a constant pressure is imposed at the origin $\mu(y = 0, z) = \mu_a$. The numerical parameters have been fixed to $M = 1$ and $\epsilon = 2$. The grid space and time step are the usual $\Delta x = 1$ and $\Delta t = 0.01$.

Flat walls

Numerical results of a liquid filling a smooth channel are shown in Figure 16.5. We observe that in both hydrophilic ($A_s = 0.5$) and hydrophobic ($A_s = -0.5$) wetting conditions, the advancement of the mean liquid/air interface, denoted as $H(t) = \langle H(z,t) \rangle_z$, is given by Washburn's law $H(t) \sim t^{1/2}$. These results show that any deviation from the classical Washburn behavior must be given by the disorder present in the system.

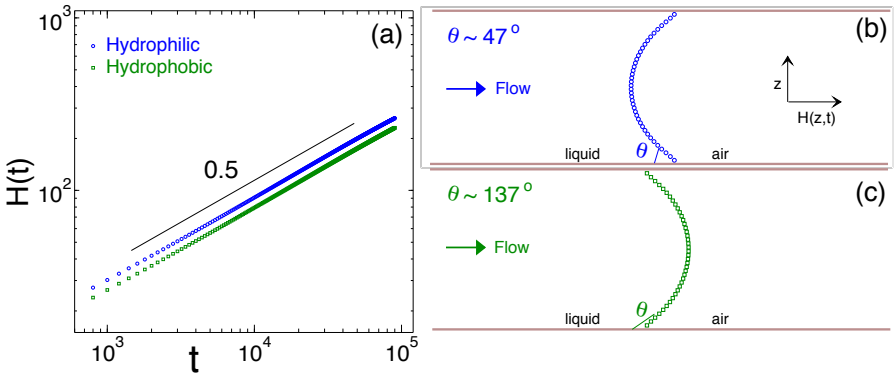

Fig. 16.5 Numerical example of a liquid meniscus advancing through a channel with flat walls. Equation (16.20) has been integrated by choosing $A_s = 0.5$ (hydrophilic condition) and $A_s = -0.5$ (hydrophobic condition). (a) Time evolution of the mean height, $H(t) = \langle H(z,t)\rangle_z$. A guide-to-eye line of slope 0.5 reflects that Washburn's law, $H(t) \sim t^{1/2}$, is well accomplished in both wetting conditions. (b) and (c) show the interface profiles for the hydrophilic and hydrophobic cases respectively. Here, the numerical contact angles 47 and 137 are obtained by fitting a semi-circle to the interface profile, and are found to be in agreement with the predicted values 42 and 137, given by Eq. (16.19) with $A_s = 0.5$ and $A_s = -0.5$, respectively, and $\epsilon = 2$.

Disordered walls

The situation becomes more involved in the case of disordered or topologically patterned walls. We consider here a channel with grooves that are translationally invariant perpendicular to the flow, and randomly distributed along the flow. The problem is then reduced to a two-dimensional system as it is shown in Fig. 16.6. The grooves have a fixed depth $h_d = 6$ and a length l_d that takes values from 2 to 14 randomly distributed.

Our study is mainly focused on superhydrophobic channels with an equilibrium contact angle $\theta_e \sim 145°$. Then the wetting boundary condition, Eq. (16.11), with a value $A_s = -0.7$ is applied at the walls at each side of the groove. In particular, the normal derivative at the edges of the grooves has been taken as

$$\hat{n} \cdot \nabla\phi = \frac{1}{\sqrt{2}}(\partial_x + \partial_y)\phi. \tag{16.21}$$

We focus then on studying how the time evolution of the interface changes as the applied pressure is modified. In Figure 16.7 there is plot the mean advancement of the front for two typical applied pressures . We observe that the mean height growth can be described by a general law $H(t) \sim t^{\lambda}$, where the exponent λ only corresponds to $1/2$ for high applied pressures. In the limit of very low velocities, the height growth is given by an effective exponent $\lambda \sim 0.4$ which is in agreement with the experimental one (~ 0.38), and also with our value obtained by using the 2D model.

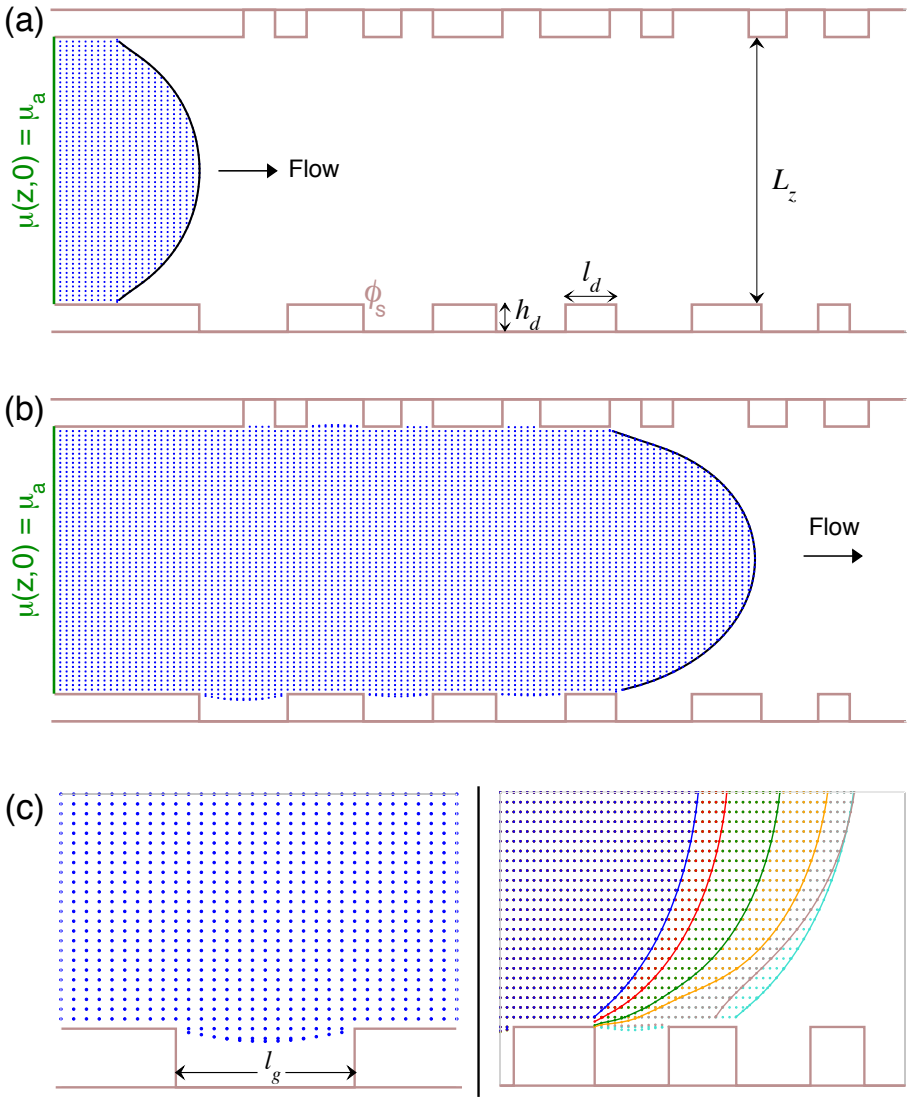

Fig. 16.6 Numerical simulation of a liquid advancing into a hydrophobic disordered microchannel by making use of the phase field model described in this Chapter. (a) The disordered walls are defined with rectangular grooves with a fixed depth $h_d = 6$ and a length l_d, that takes values from 2 to 14 randomly distributed along the channel. The size of the system in the vertical direction is $L_z = 60$. A constant chemical potential is applied at the origin of the system $\mu(z,0) = \mu_a$. The wetting boundary condition, Eq. (16.11), is applied at the walls, setting there the value of the phase field ϕ_s. (b) As the liquid goes through the channel, the hydrophobic disordered walls let the fluid not to penetrate into the grooves [(c), left] leaving the liquid volume in the so-called Wenzel state. This is a clear manifestation that the disorder may affect the wetting conditions. The dynamics of the contact line is governed by a pinning-depinning mechanism as it is shown in (c), right.

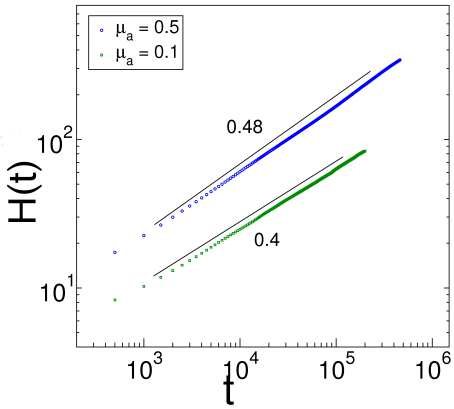

Fig. 16.7 Numerical results for hydrophobic disordered channels, averaged over 15 disorder realizations. Mean height growth $H(t)$ in a hydrophobic channel for two different pressures.

An interesting point to remark is that due to the hydrophobic condition of the wall, as the liquid goes through the disordered microchannel, a composite liquid/air interface is formed in the grooves, leaving space free of liquid inside [see Fig. 16.6(c)]. This is the so-called Wenzel state reported in several works [34, 35, 76, 131, 151]. At higher pressures, the liquid may occupy the groove space.

16.4 Theoretical discussion

From the experimental and numerical work, we can conclude that the Washburn's behavior is not observed in hydrophobic microchannels for very low applied pressures. In order to better understand such behavior in the three dimensional model, we propose a simple theoretical description, based on the averaged Darcy's law for the mean height in a channel (see Ch. 3)

$$\frac{dH(t)}{dt} = M\left[\frac{p_\mathrm{a} - p_\mathrm{i}}{H(t)}\right]. \tag{16.22}$$

Here, M is the mobility parameter, p_a the applied pressure at the origin and p_i the pressure at the interface position. From the Young-Laplace relation, we know that the pressure drop across the interface is given by

$$p_\mathrm{i} = p_\mathrm{air} - \sigma\overline{\kappa}, \tag{16.23}$$

where $\overline{\kappa}$ represents the mean curvature of the meniscus height. Our approximation is based on assuming that the geometry of the channel induces an ef-

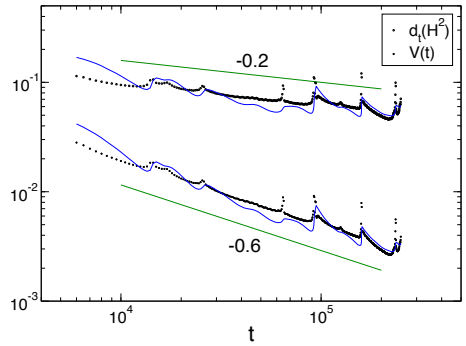

Fig. 16.8 Numerical results for $\mathrm{d}H^2(t)/\mathrm{d}t$ (circle points) and $V(t)$ (star points) are compared to $p_{\mathrm{ap}} - \sigma\overline{\kappa}(t)$ and $[p_{\mathrm{ap}} - \sigma\overline{\kappa}(t)]/H(t)$ (blue solid lines) respectively.

fective mean curvature that depends on time $\overline{\kappa}(t)$. Then, by neglecting the atmospheric pressure and introducing the above equation into the Darcy's law, one arrives at the equation

$$\frac{dH(t)}{dt} = M\left[\frac{p_{\mathrm{a}} - \sigma\overline{\kappa}(t)}{H(t)}\right], \tag{16.24}$$

that can also be reduced to

$$\frac{1}{2}\frac{dH^2(t)}{dt} = M\Big[p_{\mathrm{a}} - \sigma\overline{\kappa}(t)\Big]. \tag{16.25}$$

The actual time-dependence of the curvature is something that is not known *a priori* and must contain the main physical mechanism that bring the interface to have local pinning-depinning movements [as those shown in Fig. 16.6(c)]. From the numerical data, it is possible to check the validity of Eqs. (16.25) and (16.24) by calculating the average curvature of the meniscus and the time derivative of the squared mean height. The results are shown in Fig. 16.8. In the case of very low pressures, the mean height is found to growth with an exponent of $\lambda \sim 0.4$ implying that

$$p_{\mathrm{a}} - \sigma\overline{\kappa}(t) \sim t^{2\lambda-1} = t^{-0.2}, \tag{16.26}$$

$$V(t) \sim t^{-0.6}, \tag{16.27}$$

which agrees with the averaged curvature calculated from the numerical data (see Fig. 16.8). These results show that in this three dimensional model a description based on the Darcy's law is valid.

16.5 Conclusions

We have studied microfluidic fronts by means of two different numerical approaches. First, by integrating a two dimensional phase field model with hydrophobic disorder, we have studied how the mean time evolution of the front is modified as the applied pressure approaches the pinning value below which the interface gets completely pinned. Our results have shown that near the pinned state, the interface advances with a burst-like dynamics reflected in the non-Gaussian distribution of the global velocity fluctuations. In addition, the mean height growth is observed to scale with time with an exponent ~ 0.4, smaller than the usual Washburn exponent 0.5 expected in this kind of configuration. Interestingly, this numerical results are in agreement with experimental results carried out in a hydrophobic microchannel. On the other hand, as the applied pressure is increased, and then getting away the pinned state, the Washburn behavior is recovered with global fluctuations Gaussian distributed. In this limit, the quenched disorder due to disordered channel can be approached by a thermal noise $\xi(x,h) \sim \xi(x,t)$, meaning that the pinning effects of the front are overcome by the driving force.

On the other hand, by making use of a generalized phase field model that takes into account the wetting boundary conditions at the channel surfaces, we have been able to model the pinning-depinning motion of the contact line due to the disorder of the walls. Here we are actually assuming that the meniscus has a slow dynamics, in the sense the contact angle variations from equilibrium are essentially due to the geometric conditions of the channel. Our results have shown that the mean height growth is also depending on the applied pressure. In particular, we observe that at very low applied pressures, the pinning effects may give rise to a scaling law $H(t) \sim t^{0.4}$ different than the Washburn behavior observed at high applied pressures. Our numerical results are in agreement with a Darcy's law for the mean height that contain a time-dependent curvature, as a consequence of the pinning-depinning motion of the contact line.

Let us finally remark that these numerical results are actually the first step before going further and consider an actual three dimensional system disordered in both directions of the flow plane. In addition, it is worth to mention that the experimental work carried out in hydrophilic microchannels [120] have shown that the mean height growth is always observed to follow the classic Washburn behavior. This actually agrees with the behavior observed in the macroscopic Hele-Shaw cell with hydrophilic conditions, where it was always observed the Washburn behavior even at very low velocities (see Ch. 7). Moreover, such hydrophilic experiments also show that the velocity fluctuations are always given by a Gaussian distribution. This seems to indicate that the pinning effects due to the roughness of the microchannel surfaces are not

so important as in the case of hydrophobic microchannels. However, a clear theoretical framework on this question is still not clear; should be therefore interesting to perform a detailed analysis of hydrophilic channels by using the three-dimensional model presented in this Chapter.

Part V Conclusions

17
General conclusions

Understanding the physics underlying interfaces moving in disordered media has been the main aim in the work presented in this thesis, and in particular, we have focused on the topics of imbibition and microfluidic fronts. We have studied both the morphology and dynamics of the interface in terms of a scaling growth and avalanche dynamics, obtaining very good agreement with experimental results. The original results have been presented in three different parts and a summary of all the conclusions is given as follows.

In Part II we studied the scaling growth in non-local and local models of surface roughening. We characterized the interface fluctuations in terms of scaling exponents in both the non-local model describing imbibition fronts and local models of surface growth that included time-dependent coupling constants.

In Ch. 7 we have studied spontaneous imbibition by using a phase field model in a two dimensional system with a dichotomic quenched noise. We have focused on studying the scaling properties of the interface fluctuations when some physical parameters are changed. In particular, by decreasing the applied pressure, and therefore the interface velocity, we have studied a regime where the interface advances at low velocities, obtaining the scaling exponents $z = 3.0 \pm 0.1$, $\alpha = 1.50 \pm 0.02$ and $\alpha_{loc} = 0.95 \pm 0.03$ within the intrinsic anomalous scaling scenario. These results are found to be in quite good agreement with experimental data reported in Ref. [135]. Likewise, we have observed that the local properties of the interface changed from a super-rough to an intrinsic anomalous description when the contrast between the two values of the dichotomic noise is increased. In addition, from a linearized interface equation we have been able to analytically derive the different global scaling exponents, which have found to be comparable to the numerical results.

Motivated by the numerical work reported in Ch. 7, we have presented in Ch. 8 experimental results of spontaneous imbibition fronts in a Hele-Shaw cell. The objective was to study how the scaling properties of the interface are changed when the applied pressure difference at the inlet of the Hele-Shaw cell is modified. We have seen that the interface fluctuations change

from obeying intrinsic anomalous scaling at large negative pressure differences, to being superrough with the same dynamic exponent $z \simeq 3$ at less negative pressure differences, to finally obey ordinary Family-Vicsek scaling with $z \simeq 2$ at large positive pressure differences. This rich scenario reflects the relative importance on different length scales of capillary and permeability disorder, and the role of surface tension and viscous pressure in damping interface fluctuations. All of these experimental results are in agreement with the theoretical non-local model proposed for imbibition.

We have studied in Ch. 9 the dynamical scaling of imbibition in columnar geometries. By using the phase field model with a dichotomic columnar disorder, we have found that two distinct behaviors are possible depending on the capillary contrast between both values of disorder. In a high contrast case, where interface evolution is mainly dominated by the disorder, an inherent anomalous scaling is always observed. Moreover, in agreement with experimental work reported in Ref. [138], the interface motion has to be described through a local model. This local model has also been derived analytically. On the other hand, in a lower contrast case, interface is dominated by surface tension and can be well modeled by the usual non-local model of imbibition. We have studied both spontaneous and forced-flow imbibition situations, giving a complete set of scaling exponent in each case.

The results presented in Ch. 10 have focused on studying the influence of the disorder strength on the interface roughening process in two different phase field models that have been used separately to describe imbibition fronts. The one-sided model, used throughout of this thesis has been compared to the symmetric model used in Refs. [45, 84]. We have found that in the limit of weak disorder, both models are completely equivalent and can reproduce the physical process of a forced-flow imbibition, where superrough scaling of the interface fluctuations occurs. On the other hand, increasing disorder causes the scaling properties to change to intrinsic anomalous scaling. In the limit of strong disorder this behavior prevails for the one-sided model, whereas for the two-sided case, nucleation of domains in front of the invading front are observed.

Finally, in Ch. 11 we have studied general local models of surface roughening with time-dependent crossover lengths. The motivation was clearly the spontaneous imbibition phenomenon, where one has the crossover length $\ell(t) \sim t^{1/4}$. We have shown that time dependent couplings included in non-equilibrium kinetic roughening models may lead to nontrivial scaling properties of the surface fluctuations of the asymptotic regime. We have studied three typical situations. In the case of a crossover between two different rough regimes, the time-dependent coupling may result in anomalous scaling for scales above the crossover length. In a different setting, for a crossover from a rough to either a flat or damping regime, the time dependent crossover length

may conspire to produce a rough surface, despite the most relevant term tends to flatten the surface.

Therefore, the general conclusions of Part II can be summarized as follows:

- The numerical results obtained from a phase field model describing the scaling properties of interface fluctuations are in very good agreement with experimental results performed in a Hele-Shaw cell, obtaining in both cases that several scaling scenarios emerge depending on the physical parameters of the system.

- We have numerically seen that increasing the strength of the disorder induce an intrinsic anomalous scaling in both spontaneous and forced-flow imbibition, and also with both quenched and columnar disorder.

- In the case of columnar disorder, analytical and numerical results show that increasing the strength of the disorder change the behavior of the interface, which pass to be dominated by non local to local interactions, in agreement with previous experimental data [138].

- Both numerical and experimental results have shown that spontaneous imbibition fronts change from an intrinsic to a superrough anomalous scaling when the applied pressure difference is increased, changing then from a regime of very low to a moderate velocities. At very high velocities, experimental results have shown that the anomalous scaling tends to disappear, observing then the usual Family-Vicsek instead.

- Anomalous scaling is observed numerically and experimentally only when the interface fluctuations are produced by the capillarity disorder. In contrast, the experimental results show that the Family-Vicsek scaling is only observed in a regime where the permeability disorder is the relevant.

- The presence of time-dependent crossover lengths in both local and non-local models has important consequences on the dynamical scaling of the interface fluctuations.

In Part III we have focused on the avalanche dynamics in surface growth. Chapter 13 has presented a general theoretical framework to study avalanche dynamics in driven interfaces in disordered media, relating several magnitudes such as local avalanche statistics with interface roughness, temporal correlations, and the global mean velocity $\overline{v}$. This theory has been applied to the case of forced-flow imbibition in Ch. 14. We have explored there both a regime of high velocities and the depinning transition, $\overline{v} \to 0$, by using a phase field model and analytical analysis. The numerical results have found

to be in excellent agreement with the scaling theory presented in the previous Chapter. Finally, in Ch. 15 we have studied avalanches by using a global definition based on the time fluctuations of the spatially averaged interface velocity, obtaining excellent agreement with the experimental work reported in [113].

The general conclusions of Part III can be summarized as follows:

- Our analytical and numerical results show that the depinning transition in forced-flow imbibition is governed by an extremal dynamics given by the characteristic exponents $\alpha = 1.5$, $z = 2$, and $\gamma = 1$.
- The local dynamics inside the avalanches is affected by the correlation length $\ell_\times(\overline{v})$. At high velocities and therefore short-ranged correlations, the system show spatially localized and independent avalanches occurring at the same time, giving rise to a local dynamics described by $z_{\rm av} = 3/2$, and decoupled from the propagation of the interface correlations $z = 3$. At low velocities and therefore long-range correlations, the system is expected to show only one avalanche at the same time and both dynamics are given by the same exponent $z = z_{\rm av} = 2$.
- Global fluctuations defined from the spatially averaged velocity are described by a non-Gaussian distribution that corresponds to the so-called BHP distribution [16] when the velocity signal is averaged along a correlated window.

Finally, in Part IV we have studied theoretically and numerically the dynamics of an interface advancing into a hydrophobic microchannel. By making use of two different numerical approximations, we have explored a regime of low driving forces, obtaining that the pinnings effects become very important. The general conclusions of this Part can be summarized as follows:

- We have used a two dimensional phase field model with hydrophobic quenched disorder. In the limit of very low applied pressures, the mean advancement of the microfluidic front is given by $H(t) \sim t^\lambda$ with the exponent $\lambda \simeq 0.4$ different from the classic Washburn value $1/2$. In addition, the fluctuations of the mean velocity $V(t)$ have been observed to be non-Gaussian distributed, accordingly to a generalized-Gumbel distribution. All of these results are in agreement with experimental data carried out in microchannels.
- By making use of a three dimensional model that takes into account the wetting boundary condition, we have been able to follow the pinning-depinning motion occurred at the contact line level.

18
Future perspectives

In this Chapter we briefly discuss some of open questions for future research encountered along the thesis.

18.1
Permeability disorder in the phase field model

The experimental results presented in Ch. 8 have reported that the scaling properties of spontaneous imbibition fronts at very high velocities are described by the Family-Vicsek scaling with a dynamical exponent $z = 2$. This has been theoretically argued by taking into account that the dominant disorder on the interface fluctuations is that coming from the permeability term. Therefore, it would be interesting to numerically explore this regime by adding a disorder term in the mobility parameter [64] of the phase field equation

$$\frac{\partial \phi}{\partial t} = \boldsymbol{\nabla} M(\boldsymbol{r}) \boldsymbol{\nabla} \big[-\phi + \phi^3 - \epsilon^2 \nabla^2 \phi - \xi(\boldsymbol{r}) \big], \tag{18.1}$$

where now $M(\boldsymbol{r})$ is taken as random. The competition between both disorder terms, $M(\boldsymbol{r})$ and $\xi(\boldsymbol{r})$, would give rise to a richer behavior that could be suitable to reproduce the experimental results at high velocities.

18.2
Avalanche dynamics with gravity and thermal noise

At the conclusions of Ch. 14, we noted that another way of study pinned interfaces is by taking into account gravity effects. As it is explained in [43], the gravity term in the phase field model can be implemented by adding a convective term in the phase field equation

$$\frac{\partial \phi}{\partial t} - g \frac{\partial \phi}{\partial y} = \boldsymbol{\nabla} M \boldsymbol{\nabla} \big[-\phi + \phi^3 - \epsilon^2 \nabla^2 \phi - \xi(\boldsymbol{r}) \big], \tag{18.2}$$

where g plays the role of gravity. By imposing the spontaneous imbibition condition, the interface will get completely pinned when capillary pressures are balanced by hydrostatic pressures. Then, fluctuations around the pinned state could be achieved by the following options:

- Once the interface gets pinned, decrease slightly the gravity field and study how the new configuration relax to another pinned state.
- Adding some kind of thermal noise in order to get local depinning. In the one-sided model, where the mobility parameter depends on the phase field, $M(\phi)$, the correct description in order to add an additive conservative thermal noise into the phase field equation is given by [124]

$$\frac{\partial \phi}{\partial t} - g\frac{\partial \phi}{\partial y} = \nabla M \cdot \nabla \mu - \frac{\beta^{-1}}{2}\nabla \cdot \left[\nabla \frac{\delta M}{\delta \phi}\right] + \xi_c(\mathbf{r}, t), \tag{18.3}$$

  where ξ_c represents a conservative thermal noise of amplitude β^{-1}, and μ is the usual chemical potential. Integrating numerically the above equation, one could then study pinned fronts with thermal fluctuations.

18.3 Disorder effects in avalanche dynamics

There is a current experimental work [111, 130] studying forced-flow imbibition fronts in terms of a local description. Their preliminary results carried out in a regime of relatively high velocities (correlations extending up to 10% of the system size) show that the interface growth is actually being affected by some kind of anisotropy, giving rise then to a local dynamic exponent $z_{\mathrm{av}} \simeq 1$, different than the numerical results at high velocities ($z_{\mathrm{av}} \simeq 1.5$). Wether this anisotropy becomes relevant at the depinning transition or not is something for now unknown, and could be numerically studied by changing the disorder configuration, for example, introducing some correlations at the disorder.

18.4 Microfluidics

The results presented in Part IV have opened a new line of work in the field of microfluidics, where the three-dimensional model described there could apply. In particular the following points are to be studied:

- In order to properly describe the dynamics of the meniscus inside a real microchannel, the three-dimensional model should take into account geometrical disorder at the hydrophobic walls, both in the perpendicular

and parallel direction of the flow. This could be achieved by decorating the walls with *holes* or posts of given dimensions, randomly distributed throughout the surfaces. The resulting rough contact line will show interesting phenomena induced by the combination of hydrophobicity and disordered walls.

- To study the meniscus advancement in a microchannel with grooves placed parallelally to the flow, as it has been experimentally studied in [104, 105], and analytically in Ref. [131]. In this situation, there is not pinning effects, but it would be interesting to study the interface formed inside the grooves (Wenzel state) and how it changes in time.
- As it is stated in Ch. 16, it is also desired to study disordered hydrophilic microchannels in order to better understand the wetting effects on the meniscus dynamics.

Part VI Resum en català

19
Introducció

Una important motivació alhora d'estudiar el creixement d'una superfície rugosa ha estat la possibilitat de poder caracteritzar-la en termes de classes d'universalitat. Avui dia però, això s'ha convertit en una tasca força ambiciosa per no dir impossible. Un exemple n'és el cas d'un fluid que avança a través d'un medi desordenat – on el terme medi desordenat pot referir-se bé a un medi porós qualsevol [2], o bé a un dispositiu microfluídic [142]. El punt està en què el conjunt de forces que actuen al nivell del front que avança, com per exemple la capil·laritat del medi, la tensió superficial o le pressió viscosa, provoquen que la interfície mostri un comportament complex, descrit per varis règims d'escala i una dinàmica intermitent caracteritzada per allaus.

El principal objectiu d'aquesta tesi és estudiar la dinàmica i morfologia d'interfícies que avancen en un medi desordenat. La motivació ha estat entendre els processos físics que governen aquests fenòmens complexes i poder relacionar els nostres resultats amb la gran quantitat de treball experimental realitzat en sistemes de fluids, com per exemple la cel·la de Hele-Shaw o un microcanal.

En aquest capítol introduirem alguns conceptes útils per poder seguir els resultats presentats en el pròxim capítol d'aquest Resum.

19.1
Imbibició en medis porosos

El fenomen d'imbibició apareix en moltes situacions de la vida quotidiana (veure [2] per un article extens sobre imbibició). Des d'una gota de cafè o te que és absorbida per un terròs de sucre fins a l'aigua que es filtra pel subsòl, passant clar per la sempre inoportuna taca que es forma en el teu jersei favorit quan una gota d'oli cau mentre et menges un bon pa amb tomàquet. Totes elles tenen la particularitat que un fluid viscós penetra en un medi porós formant una interfície entre dos fluids que tenen un alt contrast de viscositats, car se suposa que el fluid que hi ha inicialment dins el medi porós és aire. Tècnicament hi ha dos tipus d'imbibició. La *imbibició espontània* es produeix quan el fluid avança degut a la capil·laritat del medi i té la peculiaritat que

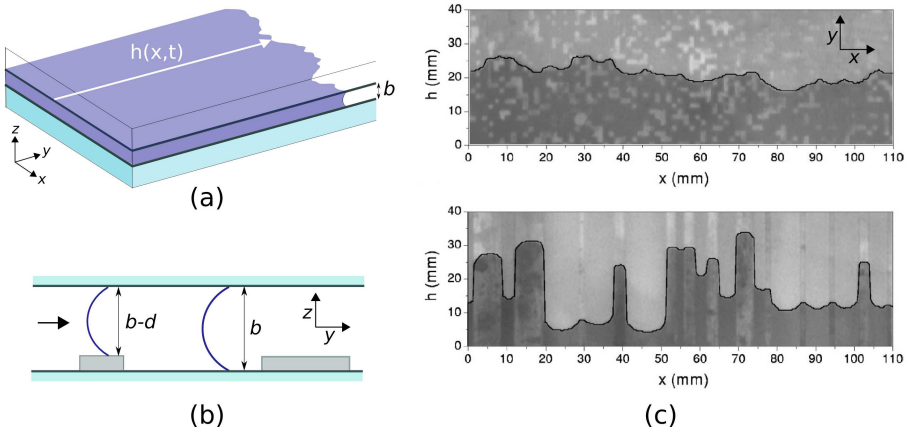

Fig. 19.1 (a) Exemple experimental de la cel·la de Hele-Shaw utilitzada en els experiments duts a terme per Soriano *et al.* [136, 138]. (b) Variació de la distància entre plaques deguda als obstacles. (c) Dos exemples de configuracions del desordre utilitzat: quadrats (superior) i columnes (inferior).

l'altura promig de la interfície avança seguint una llei clàssica coneguda com la llei de Washburn, $H(t) \simeq t^{1/2}$ [148]. Clar que aquesta llei es vàlida suposant que no hi ha evaporació per part del fluid viscós i que el fluid avança en un medi horitzontal i per tant no hi actua la gravetat. Tanmateix, el que sí és cert és que la velocitat de la interfície decreix amb el temps, i en alguns casos es para en un temps finit (quan hi ha gravetat o evaporació) i en d'altres disminueix assimptòticament a zero (cas horitzontal). D'altra banda, l'anomenada *imbibició a flux forçat* es produeix quan s'imposa una velocitat mitja de la interfície constant.

Experimentalment, la imbibició es pot reproduïr mitjançant l'anomenada cel·la de Hele-Shaw, la qual consisteix en dues plaques de vidre de mida $L_x \times L_y$, separades per una distància b molt inferior a l'allargada de qualsevol dels costats de les plaques (veure Fig. 19.1). Introduint obstacles repartits aleatòriament per tota la cel·la es poden aconseguir interfícies rugoses que en promig creixen seguint la llei de Washburn o linealment en el temps.

Les equacions macroscòpiques que descriuen els fluxos en cel·les de Hele-Shaw són les següents:

$$\begin{aligned} &\boldsymbol{v}(x,y) = -\overline{K}_0 \boldsymbol{\nabla} p(x,y), \\ &\nabla^2 p(x,y) = 0, \\ &\Delta p_i = p_{\text{air}} - p(x,h) = \sigma\kappa + \tilde{\xi}(x,h), \end{aligned} \tag{19.1}$$

on hem suposat que el desordre principal és degut a la capil·laritat del medi i per tant la permeabilitat és constant. $v(x,y)$ representa el camp de velocitats

dos dimensional del liquid, p la pressió i $\overline{K}_0 = b^2/12\eta$ és la mobilitat amb η la viscositat. S'ha fet ús de la relació de Young-Laplace per la diferència de pressions al llarg de la interfície, Δp_i, on κ representa la corbatura en el pla de la cel·la deguda a la rugositat de la interfície. En el l'aproximació d'interfície plana ve donada per:

$$\kappa \sim \nabla^2 h(x,t), \tag{19.2}$$

on $h(x,t)$ representa la posició de la interfície. Finalment el terme capil·lar $\xi(x,h)$ és degut a la corbatura en la direcció transversal del fluxe i ve donada per:

$$\xi(x,h) = \frac{2\sigma\cos\theta}{b+\delta b}, \tag{19.3}$$

on θ és l'anomenat angle de contacte que suposarem constant i σ és la tensió superficial. Les equacions macroscòpiques es poden projectar al nivell de la interfície per obtenir una equació integro-diferencial no local per les fluctuacions de la interfície (veure Cap. 4 de la tesi, i també [2, 64, 108]). L'equació resultant, linealitzada al voltant del valor mig de les fluctuacions de la interfície, i expresseda en l'espai de Fourier és:

$$\partial_t \hat{h}_k = -\sigma\overline{K}_0|k|k^2\hat{h}_k - \dot{H}|k|\hat{h}_k + \overline{K}_0|k|\hat{\xi}_k. \tag{19.4}$$

El punt important d'aquesta equació és que mostra com les fluctuacions del desordre de la capil·laritat venen controlades per dos mecanismes diferents. A escales petites, la tensió superficial amorteix les fluctuacions interficials. D'altra banda, les escales grans venen controlades per la pressió viscosa. Aquests dos règims estan separats per una longitud típica:

$$\ell_\times \sim \left[\frac{\sigma\overline{K}_0}{\dot{H}(t)}\right]^{1/2}. \tag{19.5}$$

Tal i com s'ha vist en molts resultats numèrics [2, 45, 84] i en els resultats presentats en aquesta tesi, aquesta longitud és molt important en els fenòmens d'imbibició perquè caracteritza una extensió màxima de correlació.

Finalment, és important remarcar que els dos tipus d'imbibició esmentats es diferencien bàsicament per les condicions de contorn aplicades a l'origen del sistema. Per reproduïr la imbibició espontània s'ha d'aplicar una pressió constant $p(x,0) = p_a$, i per reproduïr imbibició a fluxe constant s'ha d'imposar un gradient de pressions constant $\nabla p(x,y)|_{y=0} = -\frac{1}{\overline{K}_0}\bar{v}\hat{y}$, on $\overline{v}$ és la velocitat mitja.

19.2
El model de camp de fase

Una alternativa al model macroscòpic d'interfíce abrupta és fer ús dels anomenats models de camp de fase, els quals introdueixen una amplada finita ϵ i de caràcter difós a la interfície, de tal forma que en el límit d'interfície abrupta es recuperi la descripció macroscòpica, Eq. (19.1) (veure [1,51,57] per referències generals). Des d'un punt de vista numèric aquests models són molt més fàcils d'implementar ja que eviten el problema de tenir un contorn mòbil, fent que la posició de la interfície es pugui calcular d'una forma molt senzilla.

Aquests models es basen en una formulació a l'estil Ginzburg-Landau per un paràmetre d'ordre ϕ, l'energia lliure del qual ve donada per

$$\mathcal{F}[\phi] = \int d\boldsymbol{r}\Big[V(\phi) + (\frac{\epsilon}{2}\nabla\phi)^2\Big]. \tag{19.6}$$

El potencial s'acostuma a escollir de tipus doble-pou amb un terme lineal:

$$V(\phi) = -\frac{1}{2}\phi^2 + \frac{1}{4}\phi^4 - \xi(\boldsymbol{r})\phi, \tag{19.7}$$

on $\xi(\boldsymbol{r})$ jugarà el paper del desordre capil·lar del medi. La dinàmica del paràmetre d'ordre se suposa conservada i correspon al Model B [65]

$$\begin{aligned}\frac{\partial\phi}{\partial t} &= \boldsymbol{\nabla} M \boldsymbol{\nabla}\big[V'(\phi) - \epsilon^2\nabla^2\phi\big] \\ &= \boldsymbol{\nabla} M \boldsymbol{\nabla}\big[-\phi + \phi^3 - \epsilon^2\nabla^2\phi - \eta(\boldsymbol{r})\big],\end{aligned} \tag{19.8}$$

on μ és el potencial químic i representa el paper de la pressió dins el marc de la imbibició. El paràmetre M és la mobilitat. Per reproduïr fronts d'imbibició, doncs, s'integra numèricament l'equació anterior i es busquen els punts on $\phi(x, h(x,t); t) = 0$, els quals representen la posició de la intefície.

19.3
Escalament dinàmic de superfícies rugoses

Les propietats estadístiques d'una interfície $h(x,t)$ es caracteritzen generalment, mitjançant un estudi de les seves fluctuacions. El punt important es basa en la hipòtesi d'escala de Family-Vicsek [50]. Aquesta ens assegura l'existència d'una longitud de correlació lateral ℓ_c que creix amb el temps de la forma $\ell_c \simeq t^{1/z}$, sent z l'exponent d'escala dinàmic, fins que assoleix la longitud total del sistema $\ell_c(t_s) = L$, definint així el temps de saturació t_s per sobre del qual les fluctuacions estan completament correlacionades. D'altra banda, la longitud de correlació vertical o amplada global de la interfície ve definida

com

$$W(L,t) = \langle \overline{[h(x,t) - \overline{h}]^2} \rangle^{1/2}, \tag{19.9}$$

la qual, per $t < t_s$, augmenta amb el temps seguint la llei $W(L,t) \simeq t^{\beta}$, on β és l'exponent d'escala de creixement, i per $t > t_s$ esdevé constant $W(L,t) \simeq L^{\alpha}$, sent α l'exponent de rugositat. Tots aquests exponents estan relacionats mitjançant la relació $\alpha = z\beta$. La notació utilitzada en l'expressió (19.9) és la següent: $\langle .. \rangle$ significa promig per diferents realitzacions del desordre i la ratlla significa promig espaial al llarg de la coordenada x. Alternativament, hom pot també estudiar les correlacions al llarg de finestres de mida $\ell < L$ a través de l'amplada local de la interfície definida com $w(\ell,t) = \langle \langle [h(x,t) - \langle h \rangle_\ell]^2 \rangle_\ell \rangle^{1/2}$. En el cas d'un escalament de tipus Family-Vicsek, les escales locals i globals es comporten de la mateixa forma i es poden obtenir tots els exponents mitjançant l'amplada local.

Una altra eina força útil per calcular l'exponent de rugositat és a través de l'espectre de la interfície $S(k,t) = \langle \tilde{h}_k(t) \tilde{h}_{-k}(t) \rangle$, on $\tilde{h}_k(t)$ correspon a la transformada de Fourier de la interfície. En l'escalament de Family-Vicsek aquest escala com

$$S(k,t) = k^{-(2\alpha+1)} s_{FV}(kt^{1/z}), \tag{19.10}$$

on s_{FV} és la funció d'escala

$$s_{FV}(u) \sim \begin{cases} \text{const.} & \text{si} \quad u \gg 1 \\ u^{2\alpha+1} & \text{si} \quad u \ll 1. \end{cases} \tag{19.11}$$

Encara que aquest tipus d'escalament descriu força sistemes, últimament han aparegut diferents experiments i models numèrics que presenten un altre tipus d'escalament. És l'anomenat escalament anòmal, en el qual les escales locals i globals es comporten de diferent forma, de manera que s'ha d'introduir un nou exponent α_{loc} que descrigui la rugositat a escales locals $\ell \ll L$. En aquest sentit, es necessita un nou *ansatz* per la funció d'escala, el qual va ser proposat per Ramasco *et al.* [123], i es tracta d'una generalització de la funció d'escala de Family-Vicsek, equació (19.11), de la forma

$$S(k,t) = k^{-(2\alpha+1)} s_A(kt^{1/z}), \tag{19.12}$$

on ara la funció d'escala té la forma general

$$s_A(u) \sim \begin{cases} u^{2(\alpha-\alpha_s)} & \text{si} \quad u \gg 1 \\ u^{2\alpha+1} & \text{si} \quad u \ll 1, \end{cases} \tag{19.13}$$

essent α_s l'exponent de rugositat espectral. Aquest tipus d'escalament per l'espectre de la interfície dóna lloc al següent escalament dinàmic per l'amplada local

$$w(\ell, t) = t^{\beta} g(\ell / t^{1/z}), \tag{19.14}$$

amb la corresponen funció d'escala

$$g(u) \sim \begin{cases} u^{\alpha_{loc}} & \text{si} \quad u \ll 1 \\ \text{const.} & \text{si} \quad u \gg 1. \end{cases} \tag{19.15}$$

Una de les implicacions que comporta l'escalat anòmal és que l'amplada local satura al mateix temps t_s que l'amplada global i no al temps local $t_\ell \simeq \ell^z$ com passa en l'escalat de Family-Vicsek. Diguem que hi ha un règim intermedi entre t_ℓ i t_s en el qual l'amplada local creix com $w(\ell, t) \sim t^{\beta^*}$ amb $\beta^* = \beta - \alpha_{loc}/z$.

Depenent dels valors dels exponents d'escala poden haver-hi diferents tipus d'escalament. Per $\alpha_s < 1$ sempre es compleix que $\alpha_{loc} = \alpha_s$; en aquest cas, l'escalament de Family-Vicsek s'obté quan $\alpha = \alpha_{loc}$. En cas contrari, per $\alpha \neq \alpha_{loc}$, estem en el cas d'un escalament anòmal intrínsec. D'altra banda, en el cas en què $\alpha_s > 1$, el valor de l'exponent local de rugositat és sempre $\alpha_{loc} = 1$ i si es compleix que $\alpha = \alpha_s$, llavors estem en el cas d'un escalament anòmal super-rugós.

20
Resultats

En aquest capítol farem un resum dels diferents resultats obtinguts en aquesta tesi. El treball está dividit en tres parts. En al primera hem realitzat un estudi de les propietats d'escala d'interfícies descrites per models no-locals com el de la imbibició [cf. Eq. (19.4)], i per models locals generals de creixement de superfícicies amb coeficients que depenen del temps. En segon lloc, hem estudiat la dinàmica d'allaus observada en la imbibició i finalment en l'última part, ens hem centrat en fronts que avancen en microcanals.

20.1
Escalament dinàmic en la imbibició espontània

En els capítols 7 i 8 hem presentat un estudi teòric i experimental per caracteritzar les fluctuacions interfícials en la imbibició espontània [112, 116]. Una de les principals motivacions per dur a terme aquest treball ha estat el desacord trobat entre el treball numèric realitzat per Dubé *et al.* [45], en el que s'observaven fronts descrits per un escalament super-rugós amb exponents $\alpha = 1.25$ i $z = 4$, i el treball experimental dut a terme per Soriano *et al.* [135], on els fronts seguien un escalament anòmal intrínsec amb $\alpha = 2$ i $z = 3$. En aquest sentit, el nostre estudi s'ha centrat en veure com canvien les propietats d'escala de la interfície quan els paràmetres físics del sistema, com ara la pressió aplicada o la intensitat de les forces capil·lars, són modificats.

Primerament, en el Cap. 7 hem utilitzat un model de camp de fase per estudiar fronts d'imbibició espontània. Hem imposat un soroll dicotòmic i hem estudiat com canvien les propietats d'escala del front quan la pressió aplicada μ_a a l'origen i el contrast entre els dos valors del desordre ξ_A s'han modificat. En la Fig. 20.1 hi ha un exemple de fronts d'imbibició que avancen en un límit de velocitats molt baixes. En aquest límit, que de fet seria el mateix que el règim estudiat experimentalment [135], els nostres resultats mostren interfícies descrites per un escalament anòmal intrínsec amb un exponent dinàmic $z = 3$, obtenint doncs un bon acord amb els resultats experimentals. A mesura que la pressió aplicada s'augmenta, observem com l'escalament anòmal canvia d'intrínsec a super-rugós i l'exponent dinàmic de $z = 3$ a $z = 4$, obtenint els

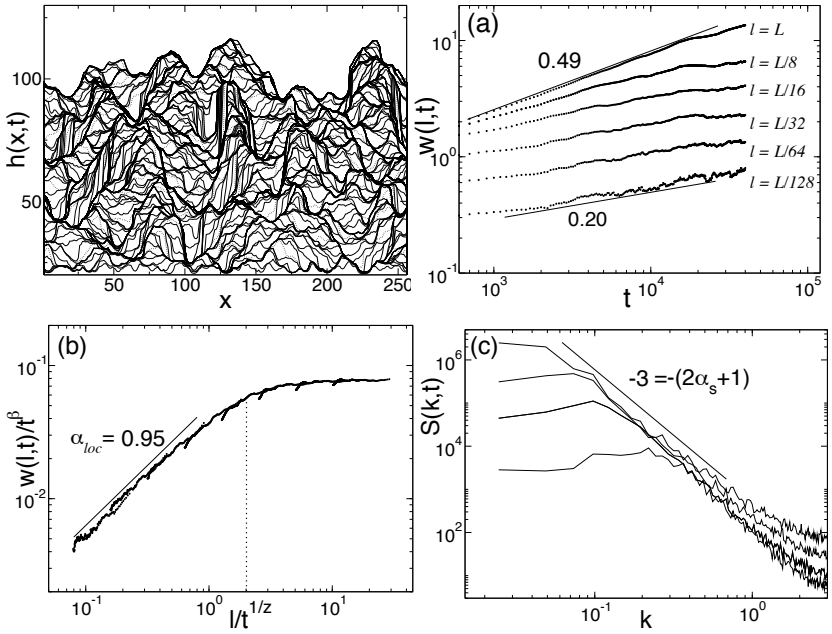

Fig. 20.1 Resultats numèrics per fronts d'imbibició espontània en un règim de velocitats molt baixes. A dalt a l'esquerra, evolució temporal de la interfície, pintada a intervals de temps equidistants. (a) Amplada local en funció del temps calculada a diferents finestres. L'ajust de les dades mostra un exponent de creixement global $\beta = 0.49 \pm 0.03$ i local $\beta^* = 0.20 \pm 0.04$. (b) Espectre de potències de la interfície a diferents temps. Mostra un exponent $\alpha_s = 1.0 \pm 0.1$. (c) Col·lapse de les dades de l'amplada local rescalada per t^β vs. $\ell/t^{\beta/\alpha}$, on $\alpha = 1.50 \pm 0.02$, i per tant $z = 3.0 \pm 0.1$ segueix de $z = \alpha/\beta$. La gràfica mostra també un exponents local de rugositat $\alpha_{loc} = 0.95 \pm 0.03$.

resultats numèrics de Dubé *et al.* [45]. D'altra, també hem vist que canviant el contrast entre els dos valors del soroll dicotòmic mantenint fixada la pressió aplicada a l'origen, les propietats d'escala local de les fluctuacions interficials canvien d'un escalament anòmal super-rugós a un d'anòmal intrínsec quan el contrast s'augmenta. Els valors dels exponents es mostren en la següent taula:

ξ_A	α	z	β	β^*	α_s	Escalament
0.3	1.25	4	0.32	0.10	1.25	SR
0.5	1.33	4	0.33	0.16	0.65	AI

Tab. 20.1: Exponents d'escala que s'obtenen al canviar el contrast capi·lar, ξ_A, amb una pressió aplicada constant.

Finalment, en el Cap. 8 hem presentat resultats experimentals d'imbibició espontània duts a terme per Planet *et al.* [112], acompanyats d'una discussió

teòrica. L'estudi s'ha centrat en veure com canvien els diferents exponents d'escala al augmentar la pressió aplicada. La taula següent mostra els valors obtinguts:

H_c (mm)	β	α	α_{loc}	β^*	z	
-9	0.64 ± 0.02	1.94 ± 0.20	0.94 ± 0.10	0.33 ± 0.03	3.0 ± 0.3	AI
-5	0.41 ± 0.02	1.25 ± 0.15	0.95 ± 0.30	0.10 ± 0.03	3.0 ± 0.4	SR
-4	0.42 ± 0.02	1.27 ± 0.15	0.97 ± 0.30	0.10 ± 0.03	3.0 ± 0.4	SR
10	0.34 ± 0.02	0.70 ± 0.15	0.64 ± 0.20	0.03 ± 0.02	2.1 ± 0.4	FV
15	0.36 ± 0.02	0.70 ± 0.15	0.59 ± 0.23	0.06 ± 0.03	1.9 ± 0.4	FV

Tab. 20.2: Sumari dels diferents exponents d'escala obtinguts experimentalment quan la diferència de pressions a l'origen $\Delta p_a = \rho g H_c$ és modificada. IA es refereix a Anòmal Intrínsec, SR a Super-Rugós i FV a Family-Vicsek.

Veiem doncs que el tipus d'escalament depèn àmpliament de la pressió aplicada. Per poder justificar des d'un punt de vista teòric aquesta sèrie de resultats, hem de tenir en compte les diferents longituds típiques que hi ha en la imbibició espontània. Hem parlat en la introducció de la longitud $\ell_\times(t)$ que separa un règim dominat per la tensió superficial (i per tant $z = 3$), d'un règim dominat per la pressió viscosa. Una altra longitud no esmentada és aquella que separa un règim on les fluctuacions venen donades pel soroll capil·lar d'un altre règim en què les fluctuacions venen donades pel soroll de la permeabilitat [108]. Aquesta longitud té la forma:

$$\ell_K = 2\pi \frac{\sigma b}{12\eta \dot{H}(t)}. \tag{20.1}$$

Si calculem d'una banda la longitud de correlació $\ell_c(t)$ i d'una altra banda les longituds de separació $\ell_\times(t)$ i $\ell_K(t)$ veiem el següent. A pressions baixes ($H_c < -4$ mm) es compleix que $\ell_c < \ell_\times \ll \ell_K$ i per tant, veiem un règim dominat per la tensió superficial i el desordre capil·lar. A pressions moderades ($H_c \sim 0$ mm) tenim que $\ell_c \sim \ell_\times$ i per tant no es pot extreure un conclusió clara. A pressions molt altes ($H_c > 10$ mm), el desordre en la permeabilitat es fa important i tenim que $\ell_\times \ll \ell_c \sim \ell_K$.

20.2 Imbibició en medis columnars

Dins el mateix context d'imbibició, en el Cap. 9 hem estudiat els casos d'imbibició espontània i forçada en un medi que és invariant al llarg de la

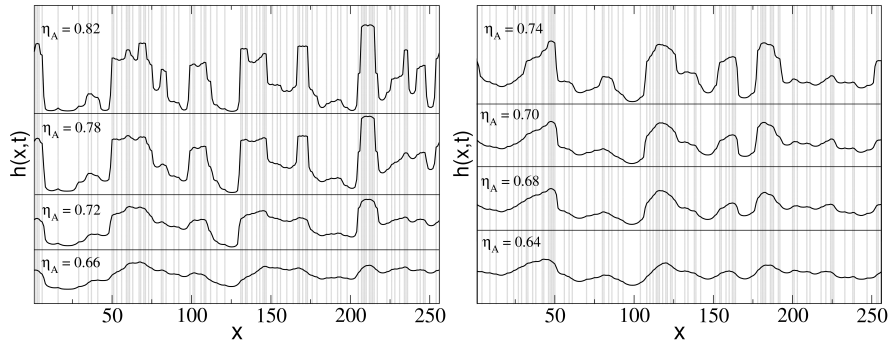

Imbibició a fluxe constant Imbibició espontània

Fig. 20.2 Perfils de les interfícies dibuixades a temps iguals però per diferents contrasts ξ_A.

direcció de propagació; o dit d'una altra forma, en un medi en què el desordre és columnar $\xi(x)$.

La motivació d'aquest estudi és essencialment deguda a un treball experimental dut a terme per Soriano *et al.* [138], en el què s'obtenia un escalament anòmal intrínsec en fronts d'imbibició descrits per una equació local enlloc de l'equació no-local, Eq. (19.4). L'objectiu doncs en el nostre estudi [117] és veure si es pot justificar teòricament les interaccions locals observades en l'experiment i descriure d'una forma quantitativa els tipus d'escalament que presenta la imbibició en medis columnars.

Fent ús del model de camp de fase amb un desordre columnar dicotòmic, hem estudiat numèricament les propietats d'escala de la imbibició quan el contrast entre els dos valors del soroll ξ_A s'augmenta. La Fig. 20.2 mostra com la forma de les interfícies va canviant a mesura que el contrast capil·lar es va augmentant.

Primerament hem calculat analíticament l'equació per la interfície quan el contrast és molt alt. En aquest límit, les interfícies adopten una forma columnar, tal i com es pot veure en la Fig. 20.2, i l'equació resultant és:

$$\dot{h_i}(t) = \boldsymbol{\nabla} D_i \boldsymbol{\nabla} h_i + \bar{v} + \zeta_i \left(\bar{v}_i + \bar{a}_i t^{-1/2} \right), \tag{20.2}$$

recuperant doncs els resultats experimentals en què s'observava un comportament local. D'altra banda, els resultats numèrics han mostrat que al augmentar el contrast les propietats d'escala canvien de super-rugós a anòmal intrínsec. A més a més, en un límit de contrast alt, les interfícies creixen de forma desacoblada entre canals. La forma d'arribar en aquest desacoblament depèn del tipus d'imbibició. Pel cas forçat, s'observa una trancisió contínua al augmentar el contrast capil·lar, mentre que pel cas espontàni, la transició és discontínua i pot passar per a qualsevol valor del contrast capil·lar.

20.3
Influència del desordre en models de camp de fase

El model de camp de fase utilitzat en els resultats presentats en les seccions anteriors és l'anonemnat model *one-sided*, en què el paràmetre de la mobilitat M en l'equació (19.8) és zero en la fase d'aire i constant en la fase líquida.

En el Cap. 10 hem fet un estudi quantitatiu [83] comparant el model *one-sided* amb l'anomenat model *symmetric*, on la mobilitat és constant en tot el sistema. Els nostres resultats mostren que per intensitats del desordre molt gran, el model symmetric presenta problemes de nucleació en la fase d'aire. En particular, apareixen dominis de la fase líquida dins de la fase d'aire, provocant una difícil caracterització de les interfícies. D'altra banda, hem vist que aquest problema es pot solucionar justament fent ús del model one-sided, en què l'evolució del paràmetre d'ordre resulta ser suprimida a través de la mobilitat, i per tant no es permet la creació de dominis.

20.4
Creixement de superfícies amb acoblaments dinàmics

Motivats pels fenòmens d'imbibició, on les fluctuacions de la interfície es veuen modificades per la presència de longituds típiques que canvien amb el temps, en el Cap. 11 hem estudiat models locals generals de creixement de superfícies rugoses [118]. En particular, ens hem centrat en resoldre equacions del tipus:

$$\frac{\partial h}{\partial t} = \nu(t)\nabla^2 h - \nabla^4 h + \xi(x,t), \tag{20.3}$$

on $\nu(t) \sim t^{\gamma}$ i per tant, es tenen dos termes que actuen a escales diferents, el qual defineix dos règims separats per una longitud típica de separació $\ell_\times(t) \sim t^{\gamma/2}$ que canvia amb el temps segons una llei de potències. El primer cas que hem estudiat ha estat considerant que els dos règims són rugosos, això és, ambdós estan bén caracterizats per exponents d'escala. En aquest cas hem obtingut que les fluctuacions interficials del règim d'escales grans (o temps llargs) es veuen afectades per la presència d'un escalat anòmal intrínsec, que depèn de l'exponent γ.

En segon lloc hem estudiat un cas en què el règim de temps llargs és pla. Això simplement vol dir que els exponents de rugositat són zero o negatius amb la conseqüència que les fluctuacions no es veuen amplificades. Per tant, en el cas que la longitud de separació dels dos règims fòs constant, hom veuria com les fluctuacions saturen en el moment en què la longitud de correlació iguala la longitud de separació $\ell_c \sim \ell_\times$. En el nostre cas, en què aquesta longitud de separació creix amb el temps, observem que les correlacions no

saturen sinó que creixen seguint el ritme de $\ell_\times(t)$. La importància d'aquest cas és que correspon al mateix comportament observat en la imbibició espontània. Per tal d'aconseguir un règim pla, el terme de soroll en l'equació (20.4), s'ha de substituir per un soroll conservat $\xi_c(x,t)$ amb la propietat $\langle \xi_c(x,t)\xi_c(x',t')\rangle = -2\nabla^2\delta(x-x')\delta(t-t')$.

Finalment hem estudiat un últim cas en que el règim per sobre de la longitud de separació $\ell_\times$ trenca alguna simetria i per tant es trenca la invariància d'escala. Això s'aconsegueix, per exemple, amb una equació de l'estil:

$$\frac{\partial h}{\partial t} = \nu(t)h - \nabla^4 h + \xi(x,t), \tag{20.4}$$

on ara el terme $\nu(t)h$ trenca la simetria $h \to h + c$. Al igual que en el cas anterior, hem vist que les fluctuacions creixen al ritme de la longitud de separació.

20.5 Dinàmica d'allaus en medis desordenats

Així com en els resultats presentats en la segona part de la tesi es centraven en la morfologia de les interfícies, els resultats presentats en la tercera part, han estudiat la dinàmica dels fronts d'imbibició en termes d'una dinàmica d'allaus. Depenent de la forma de definir les allaus, els resultats es resumeixen en dues subseccions.

Dinàmica d'allaus local

En els capítols 13 i 14 hem estudiat la dinàmica d'allaus observada en la imbibició forçada. Les allaus locals es defineixen a través de l'anomenat mapa d'activitat local, que consisteix en el següent. En primer lloc definim els punts actius de la interfície com aquells en què la velocitat local és superior a un cert llindar, $v(x,t) > c_{\text{th}}\overline{v}$, on c_{th} és una constant arbitrària i $\overline{v}$ la velocitat promitjada espaialment. Aplicant aquesta regla a cada punt x per diferent temps, aconseguim un mapa espai-temps que descriu l'activitat de la interfćie (veure Fig. 20.3). A partir d'aquest mapa podem definir les allaus com clusters conectats de punts actius. Per tant, les allaus estan caracteritzades per una longitud lateral ℓ, una mida o volum s i una durada T.

Els nostre estudi s'ha centrat en el límit de velocitats molt baixes (l'anomenat punt d'anclatge en el qual $\overline{v} \to 0$). En aquest límit el sistema està totalment correlacionat i hom espera que les magnituds que descriuen les allaus es distribueixin segons una llei de potències:

$$\mathcal{P}(s) \sim s^{-\tau_s}, \quad \mathcal{P}(\ell) \sim \ell^{-\tau_\ell}, \quad \mathcal{P}(T) \sim T^{-\tau_T}. \tag{20.5}$$

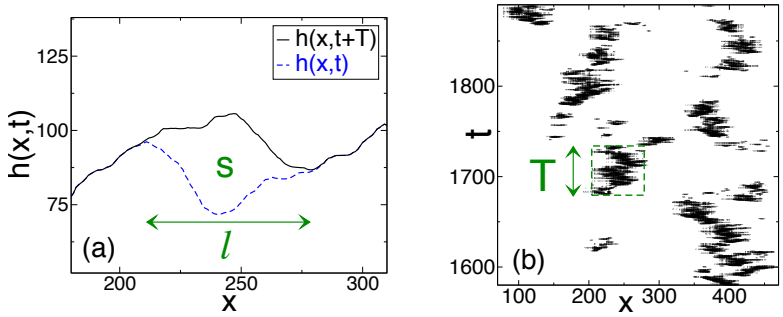

Fig. 20.3 Definició local d'una allau (a) utilitzant el mapa d'activitat del front (b). Les allaus queden caracteritzades per una longitud ℓ, una mida s i una durada T.

A més, existeixen relacions d'escala entre elles. Per exemple, la mida de l'allau es pot relacionar amb la longitud lateral com $s \sim \ell^D$ on $D = \alpha_{\rm loc} + d$ és la dimensió fractal de l'allau en un sistema de dimensions $d+1$. D'altra banda, també tenim que:

$$\langle \ell(T) \rangle \sim T^{1/z_{\rm av}}, \tag{20.6}$$

$$\langle s(T) \rangle \sim T^{\gamma}, \tag{20.7}$$

on $z_{\rm av}$ és l'exponent dinàmic de l'allau i $\gamma = D/z_{\rm av}$.

En el límit de velocitats molt baixes, podem escriure una teoria d'escala que ens permeti calcular analíticament els exponents de rugositat de la interfície. En el punt crític de $\overline{v} = 0$ els termes que depenen amb la velocitat en l'equació linealitzada (19.4) cancel·len, i la configuració d'equilibri per l'estat d'interfície parada $h_{\rm p}(x)$ vindrà donat per un balanç entre la tensió superficial i la capil·laritat:

$$\sigma \nabla^2 h_{\rm p}(x) + \xi(x) \simeq 0. \tag{20.8}$$

Aquí hem fet ús d'una aproximació de soroll columnar, en principi vàlida només en aquest límit. Si apliquem ara la transformació d'escala $x \to b\,x$ i $h_{\rm p} \to b^{\alpha}\, h_{\rm p}$, podem trobar l'exponent de rugositat $\alpha = 3/2$. Assumint que les fluctuacions al voltant de l'estat parat relaxaran a una nova configuració segons la llei:

$$\partial_t(\delta h_p) = \sigma K_0 \nabla^2(\delta h_p) + K_0 \xi(x), \tag{20.9}$$

podem trobar analíticament els exponents

$$z = 2, \qquad \alpha = \frac{3}{2}, \qquad \alpha_{\rm loc} = 1, \tag{20.10}$$

els quals ens permeten trobar $\gamma = 1$ i $D = 2$. Aquí hem suposat que la dinàmica de les allaus és la mateixa que la de la interfície i per tant tenim que $z = z_{\rm av} = 2$. Aquesta teoria s'ha comparat amb resultats numèrics d'un model de camp de fase, obtenint un excellent acord, tal i com es mostra en la següent taula:

$\overline{v}$	$\ell_\times / L$	α	z	γ
v_0	0.1	1.33	3	1.28
$v_0/5$	0.23	1.35	2.8	1.21
$v_0/10$	0.31	1.37	2.6	1.18
$v_0/20$	0.48	1.41	2.3	1.13
$v_0/40$	0.64	1.50	2.09	1.09

Tab. 20.3: Fracció del sistema correlacionada i els diferents exponents obtinguts de simulacions del model de camp de fase per diferents velocitats. A mesura que la velocitat decreix, els valors dels exponents s'aproximen als establerts per la teoria, Eq. (20.10).

Dinàmica d'allaus global

Alternativament als resultats descrits en la secció anterior, hom pot definir una allau a través de la senyal global de la velocitat $\overline{v}(t)$. La presència d'allaus en el moviment de la interfície és la responsable que la velocitat promitjada en l'espai mostri grans fluctuacions. Així doncs, i motivats pel treball experimental dut a terme per Planet *et al.* [113], en el Cap. 15 hem estudiat la dinàmica d'allaus definida a través de la velocitat global. En la Fig. 20.4 s'hi mostra un exemple de com es defineix una allau global.

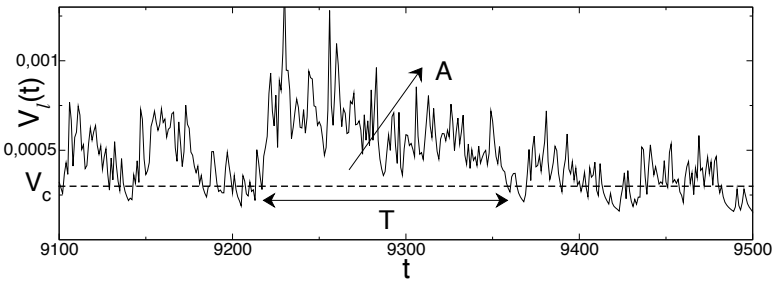

Fig. 20.4 Les allaus globals es defineixen a través de les fluctuacions temporals de la velocitat mitja de la interfície $\overline{v}(t)$, i queden caracteritzades per una durada T i una mida A.

Fent ús del model de camp de fase, hem estudiat estadísticament fronts d'imbibició forçada. Els nostres resultats han mostrat que les mides i durades de les allaus globals estan distribuïdes segons una llei de potències amb un

truncament exponencial:

$$\mathcal{P}(A) \sim A^{-\tau_A} \exp(-A/A_\times). \tag{20.11}$$

Pel cas de les mides A, la distribució obtinguda numèricament està en ple acord amb els resultats experimentals [113], obtenint el mateix exponent $\tau_A \simeq 1.0$.

D'altra banda, estudiant les propietats estadístiques de la senyal global de la velocitat, hem vist que les fluctuacions es distribueixen segons una PDF assimètrica i no-Gaussiana. En particular, hem definit la senyal global com la velocitat local promitjada al llarg d'una finestra de longitud l:

$$V_l(t) = \frac{1}{l}\int_l v(x,t)\mathrm{d}x = \bar{v} + \delta V_l(t). \tag{20.12}$$

Els resultats numèrics han mostrat que en el cas de promitjar al llarg d'una finestra totalment correlacionada, és a dir $l = \ell_\times$ on $\ell_\times$ representa la longitud de correlació, les fluctuacions de la senyal global es distribueixen segons l'anomenada distribució BHP [16]:

$$\mathcal{P}(y) = K(\mathrm{e}^{y-\mathrm{e}^y})^a \quad \text{amb} \quad y = -b(x+s), \tag{20.13}$$

on x és la variable normalitzada

$$x = \frac{V_l(t) - \langle V_l(t)\rangle}{\sigma}. \tag{20.14}$$

Aquest distribució és del tipus Gumbel generalitzada i s'ha trobat en molts contextos diferents de la física, en particular en experiments d'imbibició forçada [113].

Contràriament, quan promitgem al llarg d'una finestra totalment descorrelacionada $l \gg \ell_\times$, les fluctuacions segueixen una distribució Gaussiana, tal i com s'espera pel Teorema Central del Límit. En la Fig. 20.5 podem veure aquests dos casos.

20.6 Fronts microfluídics

Finalment, en l'última part d'aquesta tesi hem estudiat la dinàmica d'un líquid que avança en un microcanal. Aquest és un problema d'un gran interest actual degut a la gran quantitat d'aplicacions tecnològiques (veure per exemple [20]). El problema que nosaltres hem adreçat ha estat el de veure com les propietats rugoses i de mullat de les parets del microcanal poden afectar l'avanç del front microfluídic.

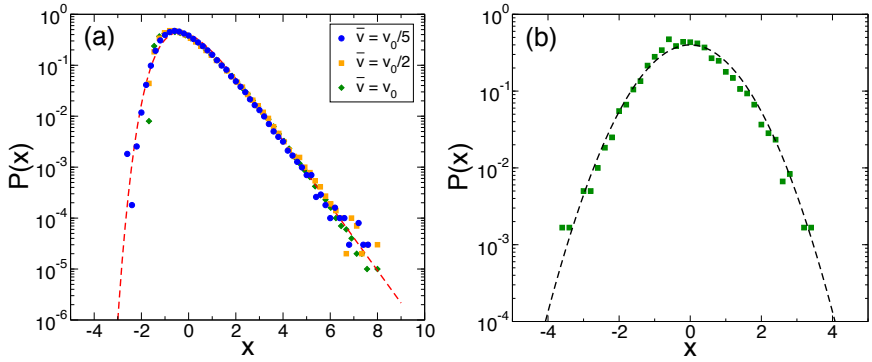

Fig. 20.5 Resultats numèrics per la PDF de $x = (V_l - \langle V_l \rangle)/\sigma$ en dues situacions típiques. (a) Velocitat global V_l promitjada al llarg d'una finestra correlacionada per differents velocitats. Els resultats són comparats amb la distribució BHP. (b) Velocitat global promitjada al llarg d'una finestra descorrelacionada.

En primer lloc hem proposat el model de camp de fase utilitzat en la imbibició per tal d'estudiar una interfície que avança a través d'un medi hidrofòbic, en el sentit que s'ha d'aplicar una pressió a l'origen del sistema per tal que el fluid avanci. D'aquesta manera, ens trobem en un cas en què la interfície es veu afectada per punts de bloquieg. En un límit de pressions aplicades molt baixes, els nostres resultats numèrics han mostrat que l'avanç mitjà del front segueix una llei

$$H(t) \sim t^{\lambda}, \tag{20.15}$$

amb un exponent $\lambda \simeq 0.4$, diferent del valor clàssic de Washburn. Aquest valor es recupera al augmentar la pressió aplicada i per tant allunyant-se del punt d'anclatge, en el qual la interfície està totalment parada. Així mateix, estudiant les fluctuacions de la velocitat global, hem observat que es distribueixen segons una PDF no-Gaussiana, assimètrica, que reflexa una dinàmica d'allaus. Els resultats numèrics estan d'acord amb resultats experimentals obtinguts en un microcanal [120].

D'altra banda, a partir d'un model tres-dimensional que té en compte les propietats de mullat a les parets, hem estudiat la dinàmica d'una superfície líquid/aire que avança a través d'un microcanal desordenat. La Fig. 20.6 mostra la simulació numèrica d'un menisc avançant en un microcanal.

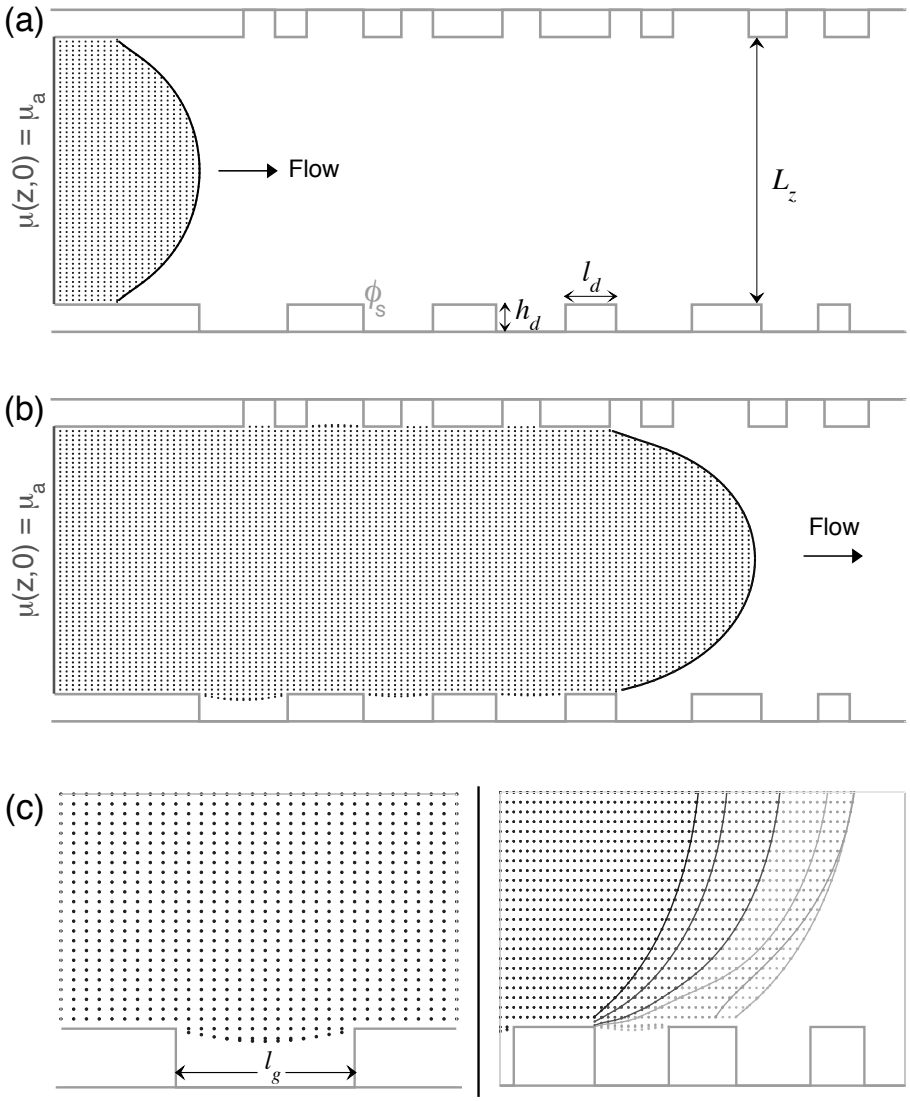

Fig. 20.6 Simulació numèrica d'un líquid avançant a través d'un microcanal desordenat hidrofòbic. (a) El desordre de les parets està definit amb solcs rectangulars de profunditat fixa $h_d = 6$ i una longitud l_d, que pren valors entre 2 i 14 distribuïts aleatòriament al llarg del canal. La mida del sistema en la direcció vertical és de $L_z = 60$. El potencial químic a l'origen del sistema està fixat a un valor constant. $\mu(z,0) = \mu_a$. A les parets s'hi aplica una condició pel paràmetre d'ordre que hi fixa el seu valor ϕ_s, donant lloc a propietats de mullat. (b) Així que el el líquid avança a través del canal, les parets hidrofòbiques no deixen que el fluid entri dins dels solcs, deixant lliure un espai d'aire. Aquest estat s'anomena estat de Wenzel, i és una clara manifestació de com el desordre pot arribar a afectar les propietats de mullat. La dinàmica de la línea de contacte està governada per un mecanisme d'anclatge-desanclatge tal i com es mostra en la figura (c) a la dreta.

21
Conclusions

La principal motivació d'aquesta tesi ha estat d'intentar entendre els mecanismes físics que regeixen la dinàmica d'interfícies en medis desordenats. Els nostres estudis s'han centrat principalment en el problema d'un fluid que avança a través d'un medi porós tipus cel·la de Hele-Shaw o d'un microcanal, centrant-nos en estudiar tant la morfologia com la dinàmica de la interfície líquid/aire.

Els resultats presentats en aquesta tesi han mostrat que les propietas d'escala dels fronts d'imbibició es veuen àmpliament afectats pels paràmetres físics del sistema. Per exemple, diferents tipus d'escalament com ara el superrugós o l'anòmal intrínsec poden ser observats en un experiment d'imbibició espontània simplement canviant la pressió aplicada. Això és principalment degut a la presència de longituds de separació que canvien amb el temps, donant lloc a una rica varietat d'exponents d'escala.

D'altra banda, la dinàmica complexa descrita en termes d'allaus ha estat estudiada en el límit de velocitats molt baixes, on hom espera que les correlacions divergeixin. És important fer notar que aquest límit mai havia estat estudiat en un model no-local com aquell que descriu la imbibició. Els nostres resultats, tant teòrics com numèrics, mostren que les fluctuacions interficials en el punt crític vénen descrites per un terme de soroll que de forma efectiva és columnar. Aquesta suposició ens ha permès el·laborar tota una teoria d'escala que ha estat comprovada amb simulacions numèriques. Finalment, també hem estudiat la dinàmica de fronts microfluídics obtenint un bon ajust entre resultats numèrics i experimentals duts a terme en un microcanal.

Per acabar, és important de remarcar que els resultats numèrics obtinguts utilitzant un model de camp de fase estan en molt bon acord amb experiments realitzats en una cel·la de Hele-Shaw, la qual cosa indica que els models de camp de fase són una eina molt potent per aquest tipus de problemes.

A
Projection to an interface equation from the phase field model

In this Appendix we discuss the details of the sharp interface projection to obtain the linearized interface equation, Eq. (4.22), from the phase field model equation:

$$\frac{\partial \phi}{\partial t} = \boldsymbol{\nabla} M(\phi) \boldsymbol{\nabla} \mu. \tag{A.1}$$

We focus on the spontaneous imbibition case where the chemical potential is kept constant at the origin of the system. For a derivation of the interface equation in forced-flow imbibition see [84].

The procedure will be the same as in the macroscopic model resolution, based on a Green's formalism. Since the mobility parameter $M(\phi)$ depends on the phase field, our starting point is the following identity

$$\begin{aligned} &\nabla' \Big[G(\boldsymbol{r}|\boldsymbol{r}') M \nabla' \mu(\boldsymbol{r}') \Big] - M \nabla' \Big[\mu(\boldsymbol{r}') \nabla' G(\boldsymbol{r}|\boldsymbol{r}') \Big] = \\ &G(\boldsymbol{r}|\boldsymbol{r}') \nabla' M \nabla' \mu(\boldsymbol{r}') - M \mu(\boldsymbol{r}') \nabla^2 G(\boldsymbol{r}|\boldsymbol{r}'), \end{aligned} \tag{A.2}$$

where the Green function is defined as

$$-\nabla^2 G(\boldsymbol{r}|\boldsymbol{r'}) = \delta(\boldsymbol{r} - \boldsymbol{r'}), \tag{A.3}$$

in the positive half-plane $\Omega = \{x, y > 0\}$ with homogeneous Dirichlet boundary conditions, and has the explicit expression:

$$G(x, y|x', y') = \frac{1}{4\pi} \ln \left[\frac{(x - x')^2 + (y + y')^2}{(x - x')^2 + (y - y')^2} \right]. \tag{A.4}$$

Integrate now Eq. (A.2) over the volume Ω and take into account that $M = 1$ in the liquid volume Ω_L and $M = 0$ in the air volume Ω_A. The resulting equation reads

$$\int_\Omega \mathrm{d}\boldsymbol{r'} \sqrt{\det(g')} G(\boldsymbol{r}|\boldsymbol{r'}) \frac{\partial \phi(\boldsymbol{r'}, t)}{\partial t} = -\frac{1}{2} \mu(\boldsymbol{r}) + \Lambda, \tag{A.5}$$

where g represents the metric of the coordinate system, and the surface term Λ is given by

$$\Lambda = \int_{S_L} \mathrm{d}\boldsymbol{s} \cdot \mu(\boldsymbol{r}')\nabla' G(\boldsymbol{r}|\boldsymbol{r}'). \tag{A.6}$$

As it occurred during the resolution of the macroscopic model, the factor $1/2$ in the chemical potential term comes from the integral

$$\int_{\Omega_L} \mathrm{d}\boldsymbol{r}'\mu(\boldsymbol{r}')\delta(\boldsymbol{r}-\boldsymbol{r}'), \tag{A.7}$$

which is evaluated only over the liquid volume.

The next step is to consider a single-valued interface $h(x,t)$ and transform to a coordinate system moving with the interface position, given by an arc length coordinate s and a perpendicular coordinate u, so that the interface position corresponds to the points where $\phi(s, u=0) = 0$.

A.1 Curvilinear coordinates

The Cartesian coordinates $\boldsymbol{r} = (x,y)$ are connected to a curvilinear system through the relationship

$$\boldsymbol{r} = \boldsymbol{R}(s) + u\hat{n}(s), \tag{A.8}$$

where $\hat{n}$ is the normal vector and $\boldsymbol{R}$ is the distance from the origin of the (x,y) coordinate system to a position along the interface. The metric for the coordinate transformation can be obtained using

$$\frac{\partial \boldsymbol{r}}{\partial u} = \hat{n} \tag{A.9}$$

$$\frac{\partial \boldsymbol{r}}{\partial s} = \hat{t}(1+u\kappa), \tag{A.10}$$

where $\hat{t}$ is tangent to the interface and κ is the curvature defined as $\partial\theta/\partial s$, being θ the angle between the y axis and the normal. The metric of the transformation is then

$$g = \begin{bmatrix} 1 & 0 \\ 0 & (1+u\kappa)^2 \end{bmatrix} \tag{A.11}$$

obtaining a Jacobian $J = \sqrt{\det(g)} = 1 + u\kappa$. Therefore, we can obtain the Laplacian, expressed in the small curvature approximation, as

$$\nabla^2 \simeq \frac{\partial^2}{\partial u^2} + \frac{\partial^2}{\partial s^2} + \kappa \frac{\partial}{\partial u}. \tag{A.12}$$

A.2 The sharp interface projection

We want to project Eq.(A.5) to the interface position. To this end, we shall assume that near the interface, the phase field can be approached by the equilibrium 1D kink solution given by

$$\partial_u^2 \phi_0 = V'(\phi_0). \tag{A.13}$$

In the sharp interface limit, $\epsilon \to 0$, the above solution has the propertie that $\partial_u \phi_0(u) \to -2\delta(u)$. Therefore, multiplying Eq. (A.5) by $\partial_u \phi_0(u)$ and integrating along u we obtain

$$4 \int \mathrm{d}s' G(s, 0; s', 0) v_n(s') = \sigma\kappa + \xi(s, 0) + 2\Lambda|_{u=0}, \tag{A.14}$$

where σ is the surface tension defined by Eq. (4.44). We have also used the Gibbs-Thomson relation for the chemical potential, Eq. (4.37), and that $\partial_t \phi(s, u, t) = -v_n(s)\partial_u \phi$. Transforming back to the Cartesian coordinate system using $\mathrm{d}s v_n(s) = \mathrm{d}x \partial_t h(x, t)$ we finally arrive to the interface equation

$$\int \mathrm{d}x' G(x, h|x', h')\partial_t h(x', t) = \frac{1}{4}\Big[\sigma\kappa + \xi(x, h)\Big] + \tag{A.15}$$
$$\int \mathrm{d}x' \frac{1}{2}\Big[\sigma\kappa + \xi(x', h')\Big]\partial_{y'} G(x, h|x', h') + \frac{\mu_\mathrm{a}}{2} \int \mathrm{d}x' \partial_{y'} G(x, h|x', 0).$$

where we have imposed the spontaneous imbibition boundary condition for the chemical potential: $\mu(x, y = 0) = \mu_\mathrm{a}$.

The linearized interface equation

Equation (A.15) is a nonlocal integro-differential equation which describes the interface fluctuations. If we linearize it around the mean value of the interface, $h(x, t) \simeq H(t) + \delta h$, and then transforming to the Fourier space, we obtain that

$$\partial_t \hat{h}_k = \frac{1 + \mathrm{e}^{-2|k|H}}{1 - \mathrm{e}^{-2|k|H}} \frac{|k|}{2} \Big[-\sigma k^2 \hat{h}_k - 2\dot{H}\hat{h}_k + \hat{\xi}_k \Big] + \delta(k) \left[\frac{\mu_\mathrm{a}}{2H} + \dot{H} \right] \tag{A.16}$$

which is the same equation derived from the macroscopic model [cf. Eq. (4.21)] taking into account that $\overline{K}_0 = M/2\phi_e^2 = 1/2$. If we take the limit $|k|H \gg 1$ we then recover the linearized interface equation, Eq. (4.22).

B
List of publications

- *Intrinsic versus superrough anomalous scaling in spontaneous imbibition*
  M. Pradas, and A. Hernández-Machado
  Physical Review E **74**, 041608 (2006).

- *Time-dependent coupling and crossover length scales in nonequilibrium surface roughening*
  M. Pradas, J. M. López, and A. Hernández-Machado
  Physical Review E (Rapid Communication) **76**, 010102(R) (2007).

- *Pressure-dependent scaling scenarios in experiments of spontaneous imbibition*
  R. Planet, M. Pradas, A. Hernández-Machado, and J. Ortín
  Physical Review E **76**, 056312 (2007).

- *Dynamical scaling of imbibition in columnar geometries*
  M. Pradas, A. Hernández-Machado, and M. A. Rodríguez
  Physical Review E **77**, 056305 (2008).

- *Influence of disorder strength on phase-field models of interfacial growth*
  T. Laurila, M. Pradas, A. Hernández-Machado, and T. Ala-Nissila
  Physical Review E **78**, 031603 (2008).

- *Avalanche dynamics in fluid imbibition near the depinning transition*
  M. Pradas, J. M. López, and A. Hernández-Machado
  (submitted, 2009).

- *Activity statistics, avalanche kinetics, and velocity correlations in surface growth*
  J. M. López, M. Pradas, and A. Hernández-Machado
  (preprint, 2009).

- *Pinning and avalanches in hydrophobic microchannels*
  M. Queralt-Martín, M. Pradas, R. Rodríguez-Trujillo, M. Arundell, E. Corvera-Poiré, and A. Hernández-Machado
  (preprint, 2009)

Bibliography

1 Ala-Nissila, T., S. Majaniemi, and K. Elder (2004). Phase-field modeling of dynamical interface phenomena in fluids. *Lect. Notes Phys. 640*, 357.

2 Alava, M., M. Dubé, and M. Rost (2004). Imbibition in disordered media. *Adv. Phys. 53*, 83.

3 Alava, M., P. Nukala, and S. Zapperi (2006). Statistical models of fracture. *Adv. Phys. 55*, 349.

4 Álvarez-Lacalle, E., J. Ortín, and J. Casademunt (2004). Nonlinear saffman-taylor instability. *Phys. Rev. Lett. 92*, 054501.

5 Barabasi, A. L. and H. E. Stanley (1995). *Fractal concepts in surface growth*. Cambridge: Cambridge University Press.

6 Barlow, R. J. (1989). *Statistics: A guide to the use of statistical methods in the physical sciences*. John Wiley & Sons.

7 Barthlott, W. and C. Neinhuis (1997). Purity of the sacred lotus or escape from contamination in biological surfaces. *Planta 202*, 1.

8 Barton, G. (1989). *Elements of Green's functions and propagation : potentials, diffusion, and waves*. New York: Oxford University Press.

9 Bensimon, D., L. P. Kadanoff, S. Liang, B. I. Shraiman, and C. Tang (1986). Viscous flows in two dimensions. *Rev. Mod. Phys. 58*, 977.

10 Bertin, E. (2005). Global fluctuations and gumbel statistics. *Phys. Rev. Lett. 95*, 170601.

11 Bonamy, D., S. Santucci, and L. Ponson (2008). Crackling dynamics in material failure as the signature of a self-organized dynamic phase transition. *Phys. Rev. Lett. 101*, 045501.

12 Bonn, D., J. Eggers, J. Indekeu, J. Meunier, and E. Rolley (2009). Wetting and spreading. *Rev. Mod. Phys. 81*, 739.

13 Bouchard, E. (1997). Scaling properties of cracks. *J. Phys. Cond. Matt. 9*, 4319.

14 Bramwell, S. T. (2009). The distribution of spatially averaged critical properties. *Nature phys. 5*, 443.

15 Bramwell, S. T., K. Christensen, J.-Y. Fortin, P. C. W. Holdsworth, H. J. Jensen, S. Lise, J. M. López, M. Nicodemi, J.-F. Pinton, and M. Sellitto (2000). Universal fluctuations in correlated systems. *Phys. Rev. Lett. 84*, 3744–3747.

16 Bramwell, S. T., P. C. W. Holdsworth, and J.-F. Pinton (1998). Universality of rare fluctuations in turbulence and critical phenomena. *Nature (London) 396*, 552–554.

17 Bray, A. J. (2002). Theory of phase ordering kinetics. *Adv. Phys. 51*, 481.

18 Briant, A. J., P. Papatzacos, and J. M. Yeomans (2002). Lattice boltzamn simulations of contact line motion in a liquid-gas system. *Phil. Trans. Roy. Soc. A 360*, 486.

19 Bruinsma, R. and G. Aeppli (1984). Interface motion and nonequilibrium properties of the random-field ising model. *Phys. Rev. Lett. 52*, 1547.

20 Bruus, H. (2007). *Theoretical microfluidics*. New York: Oxford University Press.

21 Caginalp, G. (1984). Surface tension and supercooling in solidification theory. In L. Garrido (Ed.), *Applications of Field Theory to Statistical Mechanics*, pp. 216. Berlin: Springer.

22 Caginalp, G. (1989). Stefan and hele-shaw type models as asymptotic limits of the phase field equations. *Phys. Rev. A 39*, 5889.

23 Cahn, J. W. (1957). Nucleation on dislocations. *Acta Metall. 5*, 169.

24 Cahn, J. W. (2007). Critical point wetting. *J. Chem. Phys. 66*, 3667.

25 Cahn, J. W. and J. E. Hilliard (1958). Free energy of a nonuniform system. i. interfacial energy. *J. Chem. Phys. 28*, 258.

26 Campelo, F. (2008). *Shapes in cells. Dynamics instabilities, morphology, and curvature in biological membranes*. Ph. D. thesis, Universitat de Barcelona, Barcelona, Spain.

27 Campelo, F. and A. Hernández-Machado (2006). Dynamic model and stationary shapes of fluid vesicles. *Eur. Phys. J. E 20*, 37.

28 Campelo, F. and A. Hernández-Machado (2007). Model for curvature-driven pearling instability in membranes. *Phys. Rev. Lett. 99*, 088101.

29 Campelo, F. and A. Hernández-Machado (2008). Polymer-induced tubulation in lipid vesicles. *Phys. Rev. Lett. 100*, 158103.

30 Clusel, M. and E. Bertin (2008). Global fluctuations in physical systems: a subtle interplay between sum and extreme value statistics. *Int. J. Mod. Phys. B 22*, 3311.

31 Collins, J. B. and H. Levine (1985). Diffuse interface model of diffusion-limited crystal growth. *Phys. Rev. B 31*, 6229.

32 Córdoba-Torres, P., T. J. Mesquita, I. N. Bastos, and R. P. Nogueira (2009). Complex dynamics during metal dissolution: From intrinsic to faceted anomalous scaling. *Phys. Rev. Lett. 102*, 055504.

33 Cote, P. J. and L. V. Meisel (1991). Self-organized criticality and the barkhausen effect. *Phys. Rev. Lett. 67*, 1334.

34 Cottin-Bizonne, C., C. Barentin, E. Charlaix, L. Bocquet, and J.-L. Barrat (2004). Dynamics of simple liquids at heterogeneous surfaces: Molecular-dynamics simulations and hydrodynamic description. *Eur. Phys. J. E 15*, 427.

35 Cottin-Bizonne, C., J.-L. Barrat, L. Bocquet, and E. Charlaix (2003). Low-friction flows of liquid at nanopatterned interfaces. *Nature Mater. 2*, 237.

36 Daerr, A. and S. Douady (1999). Two types of avalanches behavior in granular media. *Nature (London) 299*, 241.

37 Darcy, H. (1856). *Les fontaines publiques de la ville de Dijon*. Paris: Libraire des Corps Imperiaux des Ports et Chaussees et des Mines.

38 de Gennes, P. G. (1985). Wetting: statics and dynamics. *Rev. Mod. Phys. 57*, 827.

39 de Gennes, P. G. (2002). On fluid/wall slippage. *Langmuir 18*, 3413.

40 de Gennes, P.-G., F. Brochard-Wyart, and D. Quéré (2003). *Capillarity and wetting phenomena. Drops, bubbles, pearls, waves*. New York: Springer.

41 Desplat, J.-C., I. Pagonabarraga, and P. Bladon (2001). Ludwig: A parallel lattice-boltzmann code for complex fluids. *Comput. Phys. Commun. 134*, 273.

42 Dubé, M., C. Daneault, V. Vuorinen, M. Alava, and M. Rost (2007). Front roughening in three-dimensional imbibition. *Eur. Phys. J. B. 56*, 15.

43 Dubé, M., S. Majaniemi, M. Rost, M. Alava, K. R. Elder, and T. Ala-Nissila (2001). Interface pinning in spontaneous imbibition. *Eur. Phys. J. B 64*, 051605.

44 Dubé, M., M. Rost, and M. Alava (2000). Conserved dynamics and interface roughening in spontaneous imbibition: A critical overview. *Eur. Phys. J. B 15*, 691.

45 Dubé, M., M. Rost, K. R. Elder, M. Alava, S. Majaniemi, and T. Ala-Nissila (1999). Liquid conservation and nonlocal interface dynamics in imbibition. *Phys. Rev. Lett. 83*, 1628.

46 Dubé, M., M. Rost, K. R. Elder, M. Alava, S. Majaniemi, and T. Ala-Nissila (2000). Conserved dynamics and interface roughening in spontaneous imbibition: A phase field model. *Eur. Phys. J. B 15*, 701.

47 Edwards, S. F. and D. R. Wilkinson (1982). The surface statistics of a granular aggregate. *Proc. R. Soc. Lond. A 381*, 17.

48 Elder, K. R., F. Drolet, J. M. Kosterlitz, and M. Grant (1994). Stochastic eutectic growth. *Phys. Rev. Lett. 72*, 677.

49 Elder, K. R., M. Grant, N. Provatas, and J. Kosterlitz (2001). Sharp interface limits of phase-field models. *Phys. Rev. E 64*, 021604.

50 Family, F. and T. Vicsek (1985). Scaling of the active zone in the eden process on percolation networks and the ballistic deposition model. *J. Phys. A 18*, L75.

51 Fife, P. C. (2000). Models for phase separation and their mathematics. *Electron. J. Differ. Equ. 48*, 1.

52 Fisher, D. (1998). Collective transport in random media: from superconductors to earthquakes. *Phys. Rep. 301*, 113.

53 Fix, G. J. (1983). Phase field models for free boundary problems. In A. Fasan and M. Primicerio (Eds.), *Free boundary problems, Theory and Applications*, Volume 2, pp. 580. Boston (MA): Pitman.

54 Folch, R., J. Casademunt, and A. Hernández-Machado (1999a). Phase field model for Hele-Shaw flows with arbitrary viscosity contrast. i. theoretical approach. *Phys. Rev. E 60*, 1724.

55 Folch, R., J. Casademunt, and A. Hernández-Machado (1999b). Phase field model for Hele-Shaw flows with arbitrary viscosity contrast. ii. numerical study. *Phys. Rev. E 60*, 1734.

56 Geromichalos, D., F. Mugele, and S. Herminghaus (2002). Nonlocal dynamics of spontaneous imbibition fronts. *Phys. Rev. Lett. 89*, 104503.

57 González-Cinca, R., R. Folch, R. Benítez, L. Ramírez-Piscina, J. Casademunt, and A. Hernández-Machado (2004). Phase-field models in interfacial pattern formation out of equilibrium. In R. C. and (Ed.), *Advances in condensed matter and statistical physics*, pp. 203–236.

58 Gumbel, E. J. (1958). *Statistics of extremes*. New York: Columbia University Press.

59 Gunton, J., M. S. Miguel, and P. Shani (1983). In C. Domb and J. :ebowitz (Eds.), *Phase Transitions and Critical Phenomena*, pp. 267. Academic New York.

60 He, S.-J., G. L. M. K. S. Kahanda, and P. Wong (1992). Roughness of wetting fluid invasion fronts in porous media. *Phys. Rev. Lett. 69*, 3731.

61 Hele-Shaw, H. S. (1898). The flow of water. *Nature 58*, 33.

62 Hernández-Garía, E., T. Ala-Nissila, and M. Grant (1993). Interface roughening with a time-varying external driving force. *Europhy. Lett. 21*, 401.

63 Hernández-Machado, A., A. M. Lacasta, E. Mayoral, and E. Corvera-Poiré (2003). Phase-field model of Hele-Shaw flows in the high-viscosity contrast regime. *Phys. Rev. E 68*, 046310.

64 Hernández-Machado, A., J. Soriano, A. M. Lacasta, M. A. Rodríguez, L. Ramírez-Piscina, and J. Ortín (2001). Interface roughening in Hele-Shaw flows with quenched disorder: Experimental and theoretical results. *Europhy. Lett. 55*, 194–200.

65 Hohenberg, P. C. and B. I. Halperin (1977). Theory of dynamic critical phenomena. *Rev. Mod. Phys. 49*, 351.

66 Hyvaaluoma, J. and J. Harting (2008). Slip flow over structured surfaces with entraped microbubbles. *Phys. Rev. Lett. 100*, 246001.

67 J.M. López, M. R. and R. Cuerno (1997). Power spectrum scaling in anomalous kinetic roughening of surfaces. *Physica A 256*, 329.

68 Joubaud, S., A. Petrosyan, S. Ciliberto, and N. B. Garnier (2008). Experimental evidence of non-gaussian fluctuations near a critical point. *Phys. Rev. Lett. 100*, 180601.

69 Kalliadasis, S. and C. Bielarz (2000). Steady free-surface thin film flows over topography. *Phys. Fluids 12*, 1889.

70 Kardar, M., G. Parisi, and Y.-C. Zhang (1986). Dynamic scaling of growing interfaces. *Phys. Rev. Lett. 56*, 889.

71 Koplik, J. and H. Levine (1985). Interface moving through a random background. *Phys. Rev. B 32*, 280.

72 Krug, J. (1991). 1/f noise for driven interfaces. *Phys. Rev. A 44*, R801.

73 Krug, J. (1997). Origins of scale invariance in growth processes. *Adv. Phys. 46*, 139.

74 Kuittu, K. L. M.-P., C. Tong, S. Majaniemi, and T.Ala-Nissila (2005). Phase-field modeling of wetting on structured surface. *J. Chem. Phys. 123*, 194702.

75 Kunert, C. and J. Harting (2007). Roughness induced boundary slip in microchannel flows. *Phys. Rev. Lett. 99*, 176001.

76 Kusumaatmaja, H., M. L. Blow, A. Dupuis, and J. M. Yeomans (2007). The collapse transition on superhydrophobic surfaces. *Europhys Lett. 81*, 36003.

77 Kusumaatmaja, H., C. M. Pooley, S. Girardo, D. Pisignano, and J. M. Yeomans (2008). Capillary filling in patterned channels. *Phys. Rev. E 77*, 067301.

78 Lafuma, A. and D.Quéré (2003). Superhydrophobic states. *Nature Mater. 2*, 457.

79 Lai, Z.-W. and S. D. Sarma (1991). Kinetic growth with surface relaxation: Continuum versus atomistic models. *Phys. Rev. Lett. 66*, 2348.

80 Landau, L. D. and E. M. Lifshiftz (1987). *Fluid Mechanics*. Oxford: Pergamon Press.

81 Langer, J. (1986). In G. Grinstein and G. Mazenko (Eds.), *Directions in condensed matter physics*. World Scientific.

82 Lauga, E., M. P. Brenner, and H. A. Stone (2007). In J. Foss, C. Tropea, and A. Yarin (Eds.), *Handbook of experimental fluid dynamics*. Springer.

83 Laurila, T., M. Pradas, A. Hernández-Machado, and T. Ala-Nissila (2008). Influence of disorder strength on phase-field models of interfacial growth. *Phys. Rev. E 78*, 031603.

84 Laurila, T., C. Tong, I. Huopaniemi, S. Majaniemi, and T. Ala-Nissila (2005). Dynamics and kinetic roughening of interfaces in two-dimensional forced wetting. *Eur. Phys. J. B 46*, 553–561.

85 Laurila, T., C. Tong, S. Majaniemi, and T. Ala-Nissila (2006). Interface equations for capillary rise in random environment. *Phys. Rev. E 74*, 041601.

86 Laurson, L., X. Illa, , and M. Alava (2009). The effect of thresholding on temporal avalanche statistics. *J. Stat. Mech.: Theo. Exp. 0901*, P01019.

87 Ledesma-Aguilar, R., A. Hernández-Machado, and I. Pagonabarraga (2008). Dynamics of driven three-dimensional thin films: From hydrophilic to superhydrophobic regimes. *Phys. Fluids 20*, 072101.

88 Ledesma-Aguilar, R., M. Quevedo-Reyes, E. C. Poiré, and A. Hernández-Machado (2005). Lateral instability in normal viscous fingers. *Phys. Rev. E 71*, 16312.

89 Leschhorn, H. (1993). Interface depinning in a disordered medium - numerical results. *Physica A 195*, 324.

90 Leschhorn, H. and L.-H. Tang (1993). Self-organized interface depinning. *Phys. Rev. Lett. 70*, 2973.

91 Leschhorn, H. and L.-H. Tang (1994). Avalanches and correlations in driven interface depinning. *Phys. Rev. E 49*, 1238.

92 López, J. (1999). Scaling approach to calculate critical exponents in anomalous surface roughening. *Phys. Rev. Lett. 83*, 4594.

93 López, J. and M. A. Rodríguez (1995). Growth of interfaces with strong quenched disorder: columnar media. *Phys. Rev. E 52*, 6442.

94 López, J. and M. A. Rodríguez (1996). Lack of self-affinity and anomalous roughening in growth processes. *Phys. Rev. E 54*, R2189.

95 López, J. and J. Schimttbuhl (1998). Anomalous scaling of fracture surfaces. *Phys. Rev. E 57*, 6405.

96 López, J. M., M. Pradas, and A. Hernández-Machado (2009). Activity statistics, avalanche kinetics, and velocity correlations in surface growth. preprint.

97 Løvoll, G., Y. Méheust, R. Toussaint, J. Schmittbuhl, and K. J. Måløy (2004). Growth activity during fingering in a porous Hele-Shaw cell. *Phys. Rev. E 70*, 026301.

98 Måløy, K. J., S. Santucci, J. Schmittbuhl, and R. Toussaint (2006). Local waiting time fluctuations along a randomly pinned crack front. *Phys. Rev. Lett. 96*, 045501.

99 Maslov, S., M. Paczuski, and P. Bak (1994). Avalanches and 1/f noise in evolution and growth models. *Phys. Rev. Lett. 73*, 2162.

100 Maunuksela, J., M. Myllys, O.-P. Kähkönen, J. Timonen, N. Provatas, M. Alava, and T. Ala-Nissila (1997). Kinetic roughening in slow combustion of paper. *Phys. Rev. Lett. 79*, 1515.

101 Meakin, P. (1998). *Fractals, Scaling and Growth far from equilibrium*. Cambridge: Cambridge University Press.

102 Merikoski, J., J. Maunuksela, M. Myllys, J. Timonen, and M. Alava (2003). Temporal and spatial persistence of combustion fronts in paper. *Phys. Rev. Lett. 90*, 024501.

103 Oron, A., S. H. Davis, and S. G. Bankoff (1997). Long-scale evolution of thin liquid films. *Rev. Mod. Phys. 69*, 931.

104 Ou, J., B. Perot, and J. Rothstein (2004). Laminar drag reduction in microchannels using ultra-hydrophobic surfaces. *Phys. Fluids 16*, 4635.

105 Ou, J. and J. Rothstein (2005). Direct velocity measurements of the flow past drag-reducing ultra-hydrophobic surfaces. *Phys. Fluids 17*, 103606.

106 Paczuski, M., S. Maslov, and P. Bak (1996). Avalanche dynamics in evolution, growth, and depinning models. *Phys. Rev. E 53*, 414.

107 Papatzacos, P. (2002). Macroscopic two-phase flow in porous media assuming the diffuse-interface model at pore level. *Trans. Porous Media 49*, 139.

108 Pauné, E. and J. Casademunt (2003). Kinetic roughening in two-phase fluid flow through a random Hele-Shaw cell. *Phys. Rev. Lett. 90*, 144504.

109 Perković, O., K. Dahmen, and J. P. Sethna (1995). Avalanches, barkhausen noise, and plain old criticality. *Phys. Rev. Lett. 75*, 4528.

110 Pimpinelli, A. and J. Villain (1998). *Physics of Crystal Growth*. Cambridge: Cambridge University Press.

111 Planet, R. (2009). *Estudi experimental de la dinàmica d'un front fluid en un medi desordenat*. Ph. D. thesis, Universitat de Barcelona, Barcelona, Spain.

112 Planet, R., M. Pradas, A. Hernández-Machado, and J. Ortín (2007). Pressure-dependent scaling scenarios in experiments of spontaneous imbibition. *Phys. Rev. E 76*, 056312.

113 Planet, R., S. Santucci, and J. Ortín (2009). Avalanches and non-gaussian fluctuations of the global velocity of imbibition fronts. *Phys. Rev. Lett. 102*, 094502.

114 Portelli, B., P. C. W. Holdsworth, and J.-F. Pinton (2003). Intermittency and non-gaussian fluctuations of the global energy transfer in fully developed turbulence. *Phys. Rev. Lett. 90*, 104501.

115 Portelli, B., P. C. W. Holdsworth, M. Sellitto, and J.-F. Pinton (2001). Universal magnetic fluctuations with a field-induced length scale. *Phys. Rev. E 64*, 036111.

116 Pradas, M. and A. Hernández-Machado (2006). Intrinsic versus superrough anomalous scaling in spontaneous imbibition. *Phys. Rev. E 74*, 041608.

117 Pradas, M., A. Hernández-Machado, and M. A. Rodríguez (2009). Dynamical scaling of imbibition in columnar geometries. *Phys. Rev. E 77*, 056305.

118 Pradas, M., J. M. López, and A. Hernández-Machado (2007). Time-dependent couplings and crossover length scales in nonequilibrium surface roughening. *Phys. Rev. E 76*, 010102(R).

119 Pradas, M., J. M. López, and A. Hernández-Machado (2009). Avalanche dynamics in fluid imbibition near the depinning transition. submitted.

120 Queralt-Martín, M. (2009). Fluid fronts in hydrophilic and hydrophobic microchannels. Master Thesis, Universitat de Barcelona.

121 Queralt-Martín, M., M. Pradas, R. Rodríguez-Trujillo, M. Arundell, E. Corvera-Poiré, and A. Hernández-Machado (2009). Pinning and avalanches in hydrophobic microchannels. preprint.

122 Ramasco, J. J. (2002). *Invariancia de escala en el crecimiento de superficies e interfases*. Ph. D. thesis, Universidad de Cantabria, Santander, Spain.

123 Ramasco, J. J., J. M. López, and M. A. Rodríguez (2000). Generic dynamic scaling in kinetic roughening. *Phys. Rev. Lett. 84*, 2199.

124 Ramírez-Piscina, L., A. Hernández-Machado, and J. M. Sancho (1993). Fluctuations in domain growth: Ginzburg-Landau equations with multiplicative noise. *Phys. Rev. B 38*, 119.

125 Rost, M., L. Laurson, M. Dubé, and M. Alava (2007). Fluctuations in fluid invasion into disordered media. *Phys. Rev. Lett. 98*, 054502.

126 Rowlinson, J. S. and B. Widom (1926). *Molecular theory of capillarity*. New York: Dover Publications.

127 Rubio, M., C. Edwards, A. Dougherty, and J. Gollub (1989). Self-affine fractal interfaces from immiscible displacements in porous media. *Phys. Rev. Lett. 63*, 1685.

128 Saffman, P. G. and G. Taylor (1958). The penetration of a fluid into a porous medium or Hele-Shaw cell containing a more viscous liquid. *Proc. R. Soc. London A 245*, 312.

129 Sahimi, M. (1993). Flow phenomena in rocks: from continuum models to fractals, percolation, cellular automata, and simulated annealing. *Rev. Mod. Phys. 65*, 1393.

130 Santucci, S., R. Planet, K. J. Måløy, and J. Ortín (2009). Local avalanche dynamics of imbibition fronts: towards critical pinning. *(submitted)*.

131 Sbragaglia, M. and A. Prosperetti (2007). A note on the effective slip properties for microchannel flows with ultrahydrophobic surfaces. *Phys. Fluids 19*, 043603.

132 Sethna, J., K. Dahmen, and C. Myers (2001). Crackling noise. *Nature 410*, 242.

133 Sneppen, K. (1992). Self-organized pinning and interface growth in a random medium. *Phys. Rev. Lett. 69*, 3539.

134 Soriano, J. (2003). *Roughness experiments of viscous fluid interfaces in disordered Hele-Shaw cells*. Ph. D. thesis, Universitat de Barcelona, Barcelona, Spain.

135 Soriano, J., A. Mercier, R. Planet, A. Hernández-Machado, M. A. Rodríguez,

and J. Ortín (2005). Anomalous roughening of viscous fluid fronts in spontaneous imbibition. *Phys. Rev. Lett. 95*, 104501.

136 Soriano, J., J. Ortín, and A. Hernández-Machado (2002). Experiments of interfacial roughening in Hele-Shaw flows with weak quenched disorder. *Phys. Rev. E 66*, 031603.

137 Soriano, J., J. Ortín, and A. Hernández-Machado (2003). Anomalous roughening in experiments of interfaces in Hele-Shaw flows with strong quenched disorder. *Phys. Rev. E 67*, 056308.

138 Soriano, J., J. J. Ramasco, M. A. Rodríguez, A. Hernández-Machado, and J. Ortín (2002). Anomalous roughening of Hele-Shaw flows with quenched disorder. *Phys. Rev. Lett. 89*, 026102.

139 Squires, T. M. and S. R. Quake (2005). Microfluidics: Fluid physics at the nanoliter scale. *Rev. Mod. Phys. 77*, 977.

140 Steinberger, A., C. Cottin-Bizonne, P. Kleimann, and E. Charlaix (2007). High friction on a bubble mattress. *Nature Mater. 6*, 665.

141 Szendro, I., J. M. López, and M. A. Rodríguez (2007). Localization in disordered media, anomalous roughening, and coarsening dynamics of faceted surfaces. *Phys. Rev. E 76*, 011603.

142 Tabeling, P. (2005). *Introduction to microfluidics*. New York: Oxford University Press.

143 Tang, L.-H. and H. Leschhorn (2003). Pinning by direct percolation. *Phys. Rev. A 45*, R8309.

144 Torralba, M., J. Ortín, A. Hernández-Machado, and E. Corvera-Poiré (2006). Fluctuations in saffman-taylor fingers with quenched disorder. *Phys. Rev. E 73*, 046302.

145 Tóth-Katona, T. and J. T. Gleeson (2003). Distribution of injected power fluctuations in electroconvection. *Phys. Rev. Lett. 91*, 264501.

146 Tretheway, D. C. and C. D. Meinhart (2002a). Apparent fluid slip at hydrophobic microchannels walls. *Phys. Fluids 14*, L9.

147 Tretheway, D. C. and C. D. Meinhart (2002b). A generating mechanism for apparent fluid slip in hydrophobic microchannels. *Phys. Fluids 16*, 1509.

148 Washburn, E. W. (1921). The dynamics of capillary flow. *Phys. Rev. 17*, 273–283.

149 Whitesides, G. M. (2006). The origins and the future of microfluidics. *Nature (London) 442*, 368.

150 Wolf, D. E. and J. Villain (1990). Growth with surface diffusion. *Europhys. Lett. 4*, 651.

151 Ybert, C., C. Barentin, C. Cottin-Bizonne, P. Joseph, and L. Bocquet (2007). Achieving large slip with superhydrophobic surfaces: Scaling laws for generic geometries. *Phys. Fluids 19*, 123601.